FUNDAMENTAL STUDIES OF ULTRA-HIGH DUCTILITY MULTI-PHASE MG-LI BASED ALLOYS FOR BIODEGRADABLE TRACHEAL STENT APPLICATION

by

Jingyao Wu

B.S. in Materials Science and Engineering,

University of Science and Technology of China, 2011

Submitted to the Graduate Faculty of

Swanson School of Engineering in partial fulfillment

of the requirements for the degree of

Doctor of Philosophy

University of Pittsburgh

2018

UNIVERSITY OF PITTSBURGH

SWANSON SCHOOL OF ENGINEERING

This dissertation was presented

by

Jingyao Wu

It was defended on

September 12, 2018

and approved by

David Chi, MD, Associate Professor
Department of Otolaryngology

Youngjae Chun, Ph.D., Associate Professor
Department of Industrial Engineering, Bioengineering

William R. Wagner, Ph.D., Professor
Department of Surgery, Bioengineering and Chemical Engineering

Dissertation Director: Prashant N. Kumta, Ph.D., Edward R. Weidlein Chair Professor
Departments of Bioengineering, Mechanical Engineering and Materials Science, Chemical
and Petroleum Engineering

FUNDAMENTAL STUDIES OF ULTRA-HIGH DUCTILITY MULTI-PHASE MG-LI BASED ALLOYS FOR BIODEGRADABLE TRACHEAL STENT APPLICATION

Jingyao Wu, Ph.D.

University of Pittsburgh, 2018

Airway obstruction though uncommon in the pediatric age group is however, extremely difficult and challenging to handle. Current gold standard treatment therapies include tracheal intubation with prolonged mechanical ventilation, implementation of surgical procedures, and intraluminal airway stents. All the current treatment options are associated with high complications and failure rates. Commercially available airway stents provide immediate relief and reduced morbidity and risks, albeit are unsatisfactory in long-term effectiveness. Due to the obvious deficiencies of currently available treatment options, there is a significant clinical need for the generation and use of a biodegradable medical device, which maintains airway patency while safely degrading overtime. Previous preclinical and clinical studies have focused on designing polymeric scaffolds as extraluminal splint or intraluminal stents. Despite the promising clinical results, an open surgery is always required to place the extraluminal stents. As for intraluminal stents, one of the major pitfalls is that the remnants of the degraded stents might migrate to the bronchi causing progressing dyspnea.

The objectives of this dissertation were to explore the feasibility of a biodegradable magnesium alloy-based tracheal stents. Six ultra-high ductility multi-phase Mg-Li-Zn-(Al) alloys were accordingly designed and fabricated. These alloys display ultra-high ductility due to the co-

existence of both α (HCP) and β (BCC) phases. Further characterization of the six alloys for microstructure, mechanical properties and in vitro degradation demonstrated superior overall performance of the Mg-Li-Zn-(Al) alloys. In addition, all the selected alloys exhibited high cell viability and low cell apoptosis although possibly inhibiting the proliferation of human bronchial epithelial cells due arrest of cells in the G2/M phase. In vivo subcutaneous implantation of all the six alloys in mouse further proved the efficacy of these alloys demonstrating low corrosion rate and excellent tissue compatibility of the Mg-Li-Zn-(Al) alloys. Finally, prototype stents were fabricated and evaluated both in a bioreactor system and in a rabbit airway model. The stents showed significantly higher corrosion resistance under flow environments in vitro and safely degraded in vivo without affecting further growth of the rabbit airway. Both the alloy matrix and degradation products were well tolerated by the airway tissue without exhibiting noticeable local and systematic toxicity. In conclusion, the studies demonstrated the feasibility of using Mg-Li-Zn-(Al) alloy biodegradable magnesium alloy for tracheal stent application. It is anticipated that this novel approach and the promising results of the study will likely lead to a new treatment method for airway obstruction.

TABLE OF CONTENTS

LIST OF TABLES

LIST OF FIGURES

PREFACE

Firstly, I would like to express my sincere gratitude to my dissertation adviser, Professor Prashant Kumta, PhD, for his continued support and invaluable mentorship throughout my PhD training here at the University of Pittsburgh. Dr. Kumta was kind enough to accept me as his graduate student when my previous advisor, Dr. Thomas Gilbert, left and allowed me to transfer and continue my previous research project which I have a passion for. I am grateful for Dr. Kumta's willingness to provide tremendous resource, efforts and patience to me to restart my research from the scratch in the new lab. Beyond the advice on research, Dr. Kumta has always encouraged me to participate the entrepreneurship activities and develop the skills that help me bridge the gap between fundamental research and technology translation. Without the experience in Dr. Kumta's lab during my PhD training, I wouldn't be the person who I am today.

I would like to thank the rest of my PhD thesis committee – Dr. David Chi, Dr. Young Chun, and Dr. William Wagner, for their time and valuable feedback on my thesis. The collaboration and interaction I had with my committee members have took my research to a brand-new level from which I benefit a lot, not as a researcher but also as a person.

I am especially grateful to Dr. Thomas Gilbert for offering me a chance to join the Department of Bioengineering at the University of Pittsburgh in the beginning, and providing tremendous support during my transition to Dr. Kumta's lab when he decided to leave and join Acell Inc. Even after my transition, Dr. Gilbert has continually offering mentorship and support as external advisor of my research project over the past six years.

1.0   INTRODUCTION

1.1   TRACHEA AND TRACHEAL OBSTRUCTION

1.1.1   Anatomy of trachea

Trachea, as key component of respiratory system, is a flexible air tube that extends from the larynx to the thorax. The normal size of trachea is about 2.5 cm in diameter and 10 cm in length. The major function of trachea is to serves as a conduit for air transportation and conditioning inspired air. (Figure 1.1)

To fulfil the function of airway, the wall of the trachea consists of four layers: (1) mucosa, which is composed of a ciliated, pseudostratified epithelium and an elastic, fiber-rich lamina propria, (2) submucosa, which is composed of a slightly denser connective tissue than the lamina propria, (3) cartilaginous layer, which is composed of C-shaped hyaline cartilages and keeps the trachea from collapsing, (4) adventitia, which is composed of connective tissue that binds the trachea to adjacent structures.

For mucosa, the tracheal epithelium mainly contains ciliated columnar cells, goblet cells, and basal cells. The ciliated columnar cells are the major cell type in epithelium which extended through the epithelium layer. As shown in Figure 1.1, the cilia appear as short and hair-like profiles facing toward the surface of trachea. With approximately 250 cilia for each cell, the

1

ciliated columnar cells function as a 'mucociliary escalator' which continuously providing upward motion to the mucous to pharynx. Goblet cells was named based on the goblet-like shape of the cells. The main role of tracheal goblet cells is to secrete mucus and maintain a continuous mucus layer. Beneath the trachea epithelium is a dense layer of collagenous fibers called basement membrane. And lamina propria is under basement membrane and appears as a typical loose connective tissue.

The submucosa is hard to distinguish from lamina propria with similar loose connective tissue. The submucosa contains the larger vessels and lymphatics as well as submucosal glands which are numerous in posterior cartilage-free portion of the tracheal wall.

The tracheal cartilages and trachealis muscle are the layer between submucosa and adventitia. Normal human usually has 16-20 C-shaped tracheal cartilages. This special structure enables the flexibility of the air tube while providing mechanical support to maintain the patency.

The adventitia, the outer layer, binds the trachea to adjacent structures in the neck and mediastinum and contains the largest blood vessels and nerves that supply the tracheal wall, as well as the larger lymphatics that drain the wall.
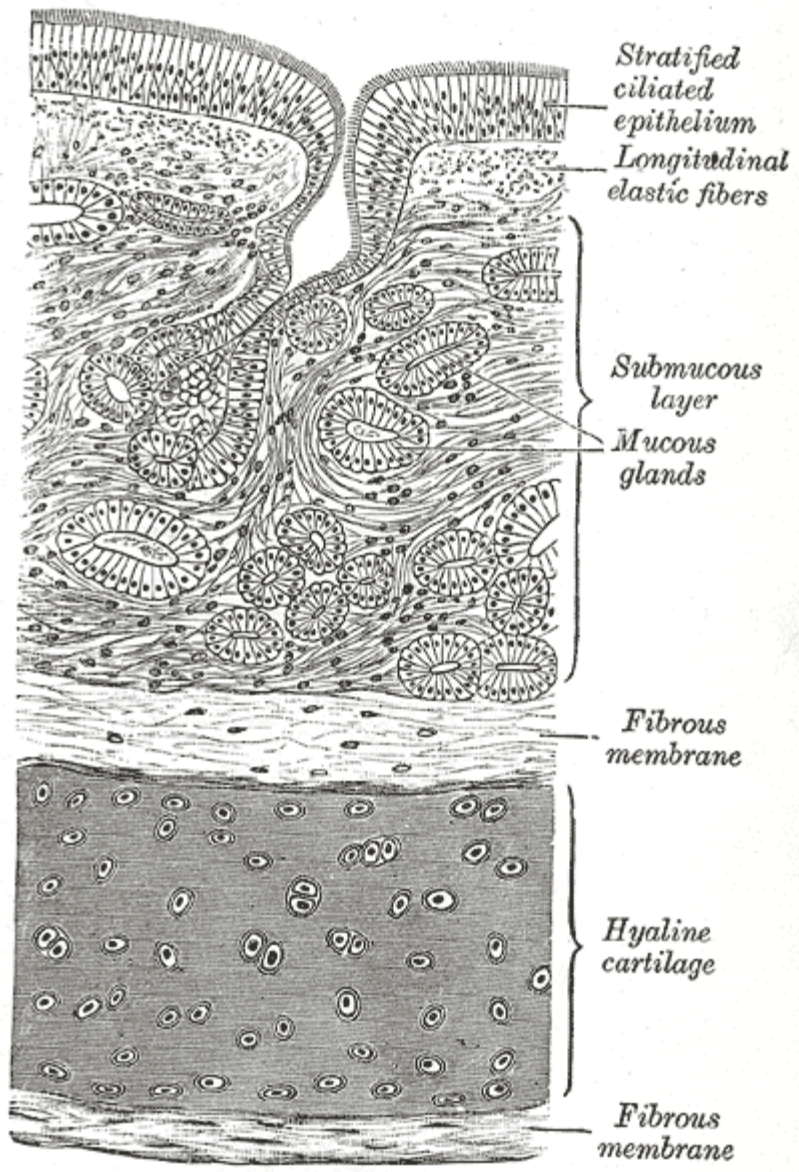
Figure 1.1. Transverse section of trachea wall. [1]

1.1.2 Tracheal obstruction and current treatment options

Airway obstruction treatment presents a significant clinical challenge and is often extremely difficult when multiple morbidity causing factors co-exist. Airway obstruction could be caused by different reasons, mainly airway stenosis and tracheabronchomalacia (TBM). [2]

Figure 1.2. Post-intubation benign tracheal stenosis in a 78-year old patient who was mechanically ventilated for 10 days due to chronic-obstructive lung disease. [3]

Figure 1.3. Patient with locally advanced nonsmall cell lung cancer and impending suffocation from bilateral main stem obstruction. [4]

Tracheal stenosis or laryngotracheal stenosis is the typical form of airway obstruction. In most cases, laryngotracheal stenosis is acquired, but for pediatric patients, tracheal stenosis can also be congenital. The common laryngotracheal stenosis includes postintubation tracheal stenosis (PITS) (as shown in Figure 1.2), post-tracheostomy tracheal stenosis (PTTS), post-TB infection, and transplant-related and idiopathic stenosis. Trachea epithelium is highly sensitive to lesions and may induce proliferation of the underlying cells to initiate wound healing. Airway stenosis happens when the wound healing process fails to stop in time or scar formation occurs, and thus the airway lumen is narrowed. Malignant tracheal stenosis usually happens in patients with locally advanced cancer as shown in Figure 1.3. Patients with malignant airway obstruction are frequently within hours or days of dying due to suffocation. Immediate airway management

is often required. In the case of lung cancer, the goal of airway obstruction management is to restore and maintain airway patency. Most common treatments of tracheal stenosis include surgical resection and reconstruction, laser based bronchoscopy, contact electrocautery, argon plasma coagulation, cryotherapy, photodynamic therapy, brachytherapy, and airway stenting. [5] Surgical resection and reconstruction is the most common approach. [6] In some cases, open surgery is impossible due to the patient's condition, anesthetic risk, or existing situation causing simultaneous morbidity. It also should be noted that these surgical procedures might also lead to restenosis due to trauma caused by the procedure itself. [6, 7] Other interventional bronchoscopic treatments including laser, mechanical dilation and stenting, could only be effective in benign laryngotracheal stenosis cases. For example, bronchoscopic laser and stenting approach only yield 17.6% success rate in complex laryngotracheal stenosis. [8]

Tracheobronchomalacia (TBM) (Figure 1.4) are the most common cases of expiratory central airway collapse. [9] The term malacia, in medical terminology, generally means the softness of cartilage or bone. TBM usually refers to a weakness of tracheal wall with symptoms varying from recurrent wheeze and recurrent lower airways infections to severe dyspnea and respiratory insufficiency. [10, 11] In pediatric patients, TBM occurs in approximately 1 in 2100 births and often lead to life-threatening cardiopulmonary arrests. [10, 11] Current gold standard treatment therapies of TBM include surgical resection and reconstruction, tracheal intubation with prolonged mechanical ventilation, cardiovascular procedures to relieve compression from abnormal anatomy, and intraluminal airway stents. [12, 13] However, all the current treatment options are associated with high complications and failure rates because of the high risk surgical procedures and formation of granulation tissue. [14] About 43% of the pediatric patients who received tracheal intubation experienced serious complications involving tube occlusion or

accidental decannulation. [15] Prolonged mechanical ventilation after tracheal intubation is associated with developmental delay and secondary airway stenosis that frequently requires surgical intervention and correction [16]. Surgical correction of secondary lesions causing TBM carries a complication rate of 36%. [17] Even though airway stents, including silicone tube and metallic stent provide immediate relief and reduced morbidity and risk, none of the stents provide satisfactory long-term effectiveness. [18, 19]
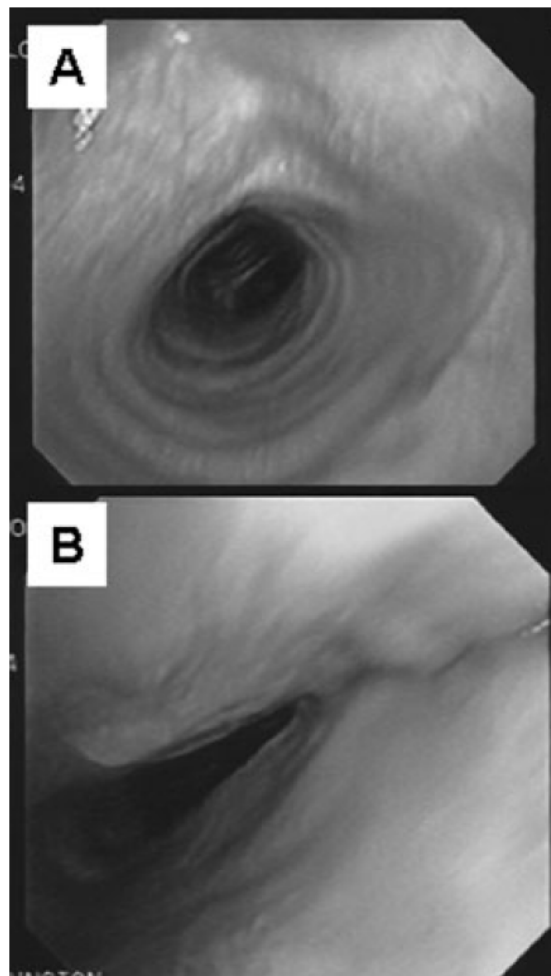
Figure 1.4. Image of trachea with tracheobronchomalacia (TBM) during inspiration (A) and expiration (B)[9].

1.2   TRACHEAL STENTS

1.2.1   Commercial tracheal stents

Current treatment of airway obstruction is still very challenging with various factors involved that can impact the ultimate prognosis. In recent years, bronchoscopy based interventional pulmonology has raised great interest by providing immediate relief and reduced morbidity and risk. In the palliative setting of alleviating airway obstruction, laser resection, electro-cautery, argon plasma coagulation and stenting are techniques that can typically provide effective clinical outcome and improve patients' quality of life [18]. Airway stenting is a valuable adjunct to the other therapeutic bronchoscopic techniques as stenting provides mechanical support to maintain the patency of airway lumen and therefore secures long-term effectiveness.

The medical term "stent" was introduced by Charles R. Stent, a British dentist who developed a device to support the healing of gingival grafts. Since then, this term has been used to refer to any device designed to maintain the integrity of a hollow tubular structure. One of the earliest clinical application of tracheal stent is reported in 1965 by Montogomery, who designed a T-shaped endotracheal silicone tube and suggested that the stent could be used following reconstruction of the cervical trachea or tracheotomy. [20] The design was further optimized by Duvall and Bauer and Coop *et al.* and enable the stents to be delivered bronchoscopically. [21, 22] Metallic stents was firstly introduced in the late 1980s by Gianturco *et al.* and Rosch *et al.* and was widely adopted since then. [23, 24]

Various types of tracheal stents are available for airway stenting ranging from silicone tubes and metallic stents (bare or coated with polymer matrix) as well as hybrid silicone tubes strengthened by metallic cores. Most of the commercially available tracheal stents fall into two

major categories: tube stents made of silicone, and expandable metallic stents. Silicone stents are usually placed with the aid of a rigid bronchoscope while the patient is under general anesthesia. Unlike silicone stents, metal stents can be placed with a flexible bronchoscope. The decision to select a certain type of stent is made based on individual clinical symptoms.

Table 1.1. Advantages and disadvantages of silicone and expandable metallic stents.

Silicone Stents	Metallic Stents (SS 316L, Nitinol)
Advantages:	**Advantages:**
• Removable	• Ease of delivery
• Adjustable	• Minimal migration
• No ingrowth	• Epithelialization & mucociliar clearance
	• High internal/external diameter ratio
Disadvantages:	**Disadvantages:**
• Difficult placement	• Difficult adjustment
• Dislodgment	• Difficult to remove
• Thick stents wall	• Granulation, tumor ingrowth
• Disturb mucus secretion	• Tracheal perforation
Comments:	**Comments:**
• Better long-term clinical outcome, first choice	• FDA Notification: Not to use unless it's the only option for benign airway disorder

Since the introduction of Montgomery T-tube in 1965, several other silicone tube designs have been introduced for different clinical settings. For example, Dumon stent has external studs outside the silicone tube which can significantly reduce the stent migration after implantation.

Since its introduction, the Dumon stent has quickly become the most widely used tracheal stents. The major advantages and disadvantages of the silicone tubes are listed in Table 1.1. Most silicone tubes are easily collapsible, therefore can be removed or adjust after implantation. In addition, since the stent structure is a solid tube, so there is impermeable to tissue or tumor ingrowth. In the meanwhile, silicone tube is relative harder to implant due to larger profile and is more subject to migrate after implantation. The solid tube structure will also interfere with the mucocilliary clearance. [25] In spite of these disadvantages, the silicone tubes are still the first choice in most airway obstruction cases.

Metallic stent was first introduced for the treatment of cardiovascular diseases. The success of this concept led to the expansion of the use of stent in airway obstruction. [26-30] The first generation of metallic tracheal stent was made of 316L stainless steel (ss). [31-33] The 316L ss stent does not exhibit intrinsic radial force and is delivered through a catheter system. The diameter of the stent after expansion is determined by the expanded balloon which, in theory, will eliminate hyperexpansion and stent perforation. However, the first-generation stent is uncommon now due to the inflexibility and complications. The second-generation tracheal stent is self-expandable tubular metal mesh made of nitinol. Nitinol, as known as nickel titanium, is an alloy with close atomic percentage of nickel and titanium. The most unique properties of this alloy are shape memory effect and superelasticity due to a reversible solid-state phase transformation called martensitic transformation. Nitinol self-expandable stents could be compressed and packed onto catheter with extremely small profile. Once the cover outside the stents is released, the stent will expand to a preset diameter. Metallic stents have several advantages over silicone tubes. The insertion and fixation of metallic stents is much easy to handle due to their low profile. The mesh tubular structure significantly reduces the movement of

the stent after implantation and is capable of epithelialization and mucociliar clearance. However, the mesh tubular structure also allows the ingrowth of the tissue, hence the stent is hard to adjust or remove after certain period of implantation and is not capable of preventing the in-stent restenosis caused by granulation and tumor ingrowth. A summary of the advantages and disadvantages of metallic tracheal stents is listed in Table 1.1.

In conclusion, even though all these stents exhibit efficient short-term palliation, none of the stents provide satisfactory long-term effectiveness. Especially for metallic tracheal stents, U.S. Food and Drug Administration (FDA) public health advisory recommends avoiding use of metallic tracheal stents in patients with benign airway obstructions due to the long-term complications caused by metallic stents.

1.2.2 Biodegradable tracheal stents

Due to the obvious deficiencies of currently available treatment options, there is a significant clinical need for the generation and use of a biodegradable medical device which maintains airway patency while totally degrade overtime a predetermined period. Most previous preclinical and clinical study have been focusing on designing polymeric scaffolds as extraluminal splint [34, 35] or intraluminal stents [36-52].

External tracheal stenting is placed through open neck surgery and the stent is sutured outside the airway. In this way, the implant is not directly contact the epithelium of the trachea and therefore won't blocking the airway or causing foreign body reaction. It also allows mucociliary clearance to proceed unimpeded. Weatherly *et al.* firstly reported an *in vivo* study of polyglycolic acid and poly(D,L-lactide-co-glycolide) (85:15) based extraluminal tracheal stents in rabbit model. [53] The results indicated that the polymer stents degraded in a predication

fashion and might provide a new method to augment narrowed trachea. In recent years, several groups have been focusing on fabricating external tracheal splint using 3D printing technology. [35, 54-56] Green *et al.* 3D printed a tracheobronchial splint polycaprolactone (PCL). Three customized splints were fabricated and implanted into three pediatric patients with TBM. The 3D printed external tracheal splint alleviated the TBM symptoms without inhibiting the growth of primary airway. [56]

Despite the early stage promising clinical results of the external tracheal splint, open surgery is always required to place this device. The idea of placing a biodegradable stent through minimal invasive method is much more appealing. A summary of previous animal study of biodegradable stents is listed in Table 1.2. Rabbits model are the most common models for tracheal stent study, this is in line with the review written by Verkerke *et al.* on the choice on animal models in tracheal research. [57] Most polymeric stents reported in these studies were made of polyester based biodegradable materials, such as PLGA, PLLA and PCL. PCL based tracheal stents demonstrated the longest degradation time of more than 33 weeks. [49] All these studies reported excellent biocompatibility of the stent material.

Several studies of biodegradable stents in humans have also been reported. [38-40, 58] Unlike the various selection of biodegradable materials in the reported animal studies, polydioxanone is chosen in most of these human studies. Two human studies were reported in 2011, where polydioxanone stents were implanted both in adults [52] and children [38]. These studies demonstrated the feasibility of the biodegradable tracheal stent for the treatment of airway obstruction with immediate relief of the symptoms. However, repeat stenting happened to more than of the patients in both studies. Vasakova1 *el al.* reported another four cases of human trial with polydioxanone stents later in 2015. [39] In three of total four adult patients, external

fixation was conducted by a thoracic surgeon. A suture was passed through the stent, tracheal wall, and skin in order to prevent the stent from migration. The polydioxanone stents lasted 90 days on average, and again half of the patients received repeated stenting. In one case, the patients started to cough up small bit of the stents struts after 3 months of implantation. The clinical outcome in pediatric patients is controversial. A more recent clinical study in infants reported the potential life-threatening pitfalls of the polydioxanone stents. [59] Two out the three cases indicated the remnants from the degraded stents presented as "foreign body" and cause life-threatening dyspnea.

Table 1.2. Summary of animal studies of biodegradable intraluminal stents. [60]

Stented animals (n)	Material	Stent design	Technique of insertion	ref.
Rabbits (15)	PCL coated with PLLA-PLGA	Mesh-type stent made of interconnected ring-ellipse-ring units	Surgery	[50]
Rabbits (25)	PDS	Tubular and hollowed braided stent	Endoscopy + fluoroscopic guidance	[51]
Rabbits (15)	PLLA-PCL	Helical stent	Surgery	[47]
Rabbits (6)	PCL	Mesh-type stent made of interconnected ring-ellipse-ring units	Surgery	[49]
Dogs (6)	PLLA	Knitted and hollowed tubular stent	Endoscopy	[48]
Rabbits (15)	PLLA	Knitted and hollowed tubular stent	Surgery	[46]
Rabbits (25)	PLGA	Helical stent	Surgery	[45]
Rabbits (11)	PLLA	Helical stent	Surgery	[44]
Rabbits (9)	PLLA	Helical stent	Surgery	[43]
Rats (35)	Vicryl	Homogeneous knitted stent	Surgery	[42]

1.3   MAGNESIUM ALLOY BASED BIODEGRADABLE METALLIC STENTS

1.3.1   Magnesium alloy as biodegradable metallic materials

Magnesium was firstly identified by British chemist Sir Humphrey Davy back in 1808 and isolated by French scientist Antoine-Alexander Bussy in 1828. In the early days of the magnesium commercial production, the magnesium metal was produced by using potassium to reduce $MgCl_2$ and was almost entirely in form of wire and powder for photographic usage. Modern production process of magnesium followed today has changed significantly. Majority of magnesium is now produced by electrolysis of fused anhydrous $MgCl_2$ and the rest are produced by thermal reduction of MgO. Even though the earliest application of magnesium as a biomaterial dates back to 1878 when physician Edward C. Huse tried to use Mg wires as ligatures stop the vessels from bleeding [61], magnesium were mostly used as industrial/structural materials in the past two hundred years. As the focus of biomaterials research shifted from inert materials to bioactive and biodegradable materials, the hype of magnesium alloys as a novel biodegradable metallic material started since early 2000s. Magnesium alloy is unique as a biodegradable material because as metals, magnesium-based alloys provide better mechanical support when compared to conventional polymer and ceramic materials. On the other hand, due to the degradable nature, magnesium alloy-based implants will dissolve overtime obviating secondary surgeries to retrieve them or being implanted permanently in patients. Mg being the second most abundant intracellular cation and the fourth most abundant cation in body, the alloy itself as well as its degradation products are well tolerated by human body.

The typical crystal structure of pure magnesium and most magnesium alloys is hexagonal close packed (HCP). The inherent anisotropy of HCP structure determined the limited absolute strength and ductility of pure magnesium and magnesium alloys compared to other metallic biomaterials, such as stainless steel, nitinol and cobalt-chromium (CoCr) alloys. At body temperature, magnesium predominantly undergoes plastic deformation via slipping of the crystal planes. The lowest critical resolved shear stress (CRSS) for magnesium is the (0001)<11$\bar{2}$1> basal slip system. [62] The pyramidal slip and the prism slip are much unlikely to be activated due to tremendous higher CRSS. Therefore, magnesium only possesses three independent slip systems. According to the Von Mises Criterion, at least five independent systems are required for plastic deformation. This explains the low plastic deformability of magnesium and magnesium alloy. The ductility of magnesium alloys could be improved by alloying with other element, heat treatment and other advanced processing techniques.

Another attribute of magnesium alloy is that magnesium will corrode in aqueous environment. Once implanted in vivo, magnesium alloys will react with water by a series of electrochemical reactions as depicted in the reaction below:

Mg (s) $\leftrightarrow$ Mg^{2+}(aq) + $2e^-$ (anodic reaction)

$2H_2O$ (aq) + $2e^-$ $\leftrightarrow$ H_2 (gas) + $2OH^-$ (aq) (cathodic reaction)

Mg^{2+}(aq) + $2OH^-$(aq) $\leftrightarrow$ $Mg(OH)_2$ (s) (product formation)
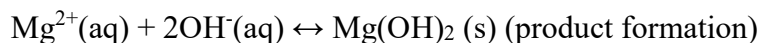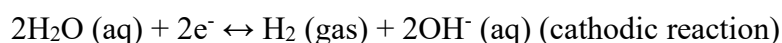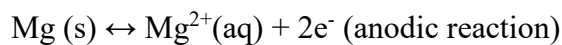
As shown in Figure 1.5, the reactions will be initiated immediately after magnesium alloy contact the body fluid. Magnesium and other alloying elements are oxidized into metal cations, while the electrons generated are transferred to H_2O which leads to the formation of H_2 gas bubbles on the metal surface. The whole reactions occur arbitrarily over the metal surface where galvanic coupling forms. As the reactions continue, a degradation layer, mainly consist of

Mg(OH)$_2$, forms on the metal surface and significantly reduce the degradation rate. However, chloride ions are destructive to the Mg(OH)$_2$ layer, and magnesium alloys will continue degrading as chloride ions penetrate through the degradation layers, and the whole implant will be eventually converted to degradation product and absorbed by the surrounding tissues. In the meantime, hydroxyapatite (HA) will also deposit in the degradation layer by consuming calcium and phosphate ions from the surrounding fluid.
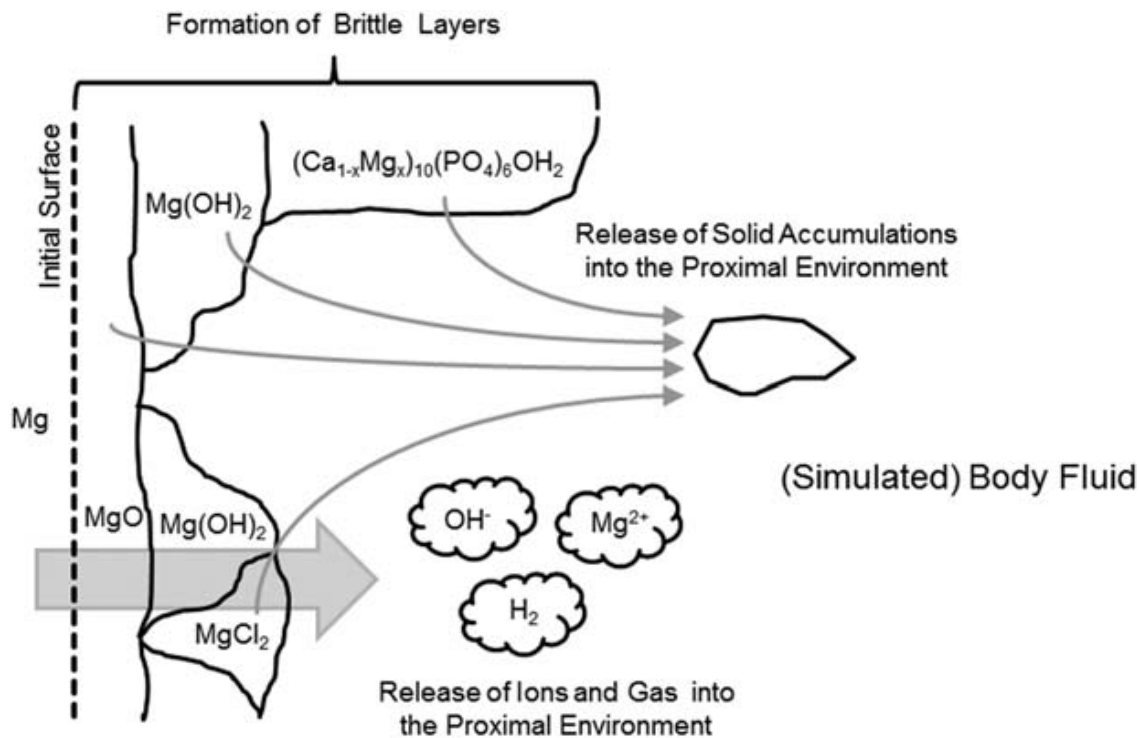
Figure 1.5. Schematic diagram of the magnesium alloy degradation process: (1) electrochemical chemical corrosion happens at the initial surface of the magnesium/media interface; (2) OH$^-$, Mg^{2+} and H$_2$ created by the corrosion process are released into the surrounding environment, and MgO and Mg(OH)$_2$ degradation layer partially covers the surface of the magnesium alloy, (4) Cl$^-$ ions penetrate into the degradation layer, and transfer Mg(OH)$_2$ into MgCl$_2$, (5) the hydroxyapatite forms on the surface of the degradation layer by the consumption of Ca^{2+} and PO$_4^3$, (6) the disintegrated particle-shape residues falls out of the bulk substrate.[63]

17

As for biocompatibility, Mg exhibits multiple essential physiological functions in the human body. [64] Therefore, the release of Mg ions with the degradation of Mg alloy-based implants has shown various bioactive effects on specific cell and tissues. [65-67] Particularly, magnesium alloys have shown osteo-induction function in myriad studies for orthopedic application. [68]

Due to these unique attributes, magnesium alloys will potentially provide a paradigm shift in the current medical device market. Several applications have been explored in the field of biodegradable magnesium alloy research such as orthopedic implants [69, 70], vascular stent [71-75], and sutures [76, 77].

1.3.2 Magnesium alloy based biodegradable metallic stents

The research of biodegradable stents started with polymeric materials date back to 1980s at Duke Medical Center. [78] The Igaki-Tamai (Igaki Medical Planning Company, Kyoto, Japan) stent is the first biodegradable stent that received CE Mark approval for human use in peripheral vascular applications in 2007. The Absorb GT1 Bioresorbable Vascular Scaffold (BVS) from Abbott, which was approved by FDA to treat coronary disease in 2016, was another major advance forward in biodegradable stent technology. However, even though the ABSORB III Trial results of BVS showed performance statistically as good as the market-leading Xience everolimus-eluting metallic stent, all the key parameters are poorer than Xience stents. [79] Another 3-year follow-up study also indicated the clinical outcome of BVS were strongly associated with vessel size and operator technique. [80] These results slowed down the adoption of the BVS, and Abbott eventually stopped selling the first-generation bioresorbable Absorb coronary stent in September 2017.

The difficulty witnessed by the polymeric biodegradable stents opens the opportunities for metallic biodegradable stents. Iron-based stent was the first metallic biodegradable stent proposed, but the pilot animal study showed extremely slow degradation of pure iron *in vivo*. [81, 82] Several groups had reported the idea of alloying with other elements to improve the degradation rate of iron, but none of these showed significantly higher degradation rate *in vivo* or *in vitro*. [83-85] In recent years, Zn-based stents were proposed as another metallic biodegradable stent. [86-89] Despite the promising preliminary *in vivo* data, a lot more work needs to be done in order to address the issues with this new biodegradable metal system. For example, designing a better Zinc basic alloy that can balance the degradation and mechanical properties, more in-depth analysis of cytocompatibility and biocompatibility of these Zinc alloys, long-term *in vivo* study of prototype Zinc alloy stents. Magnesium alloy is the only biodegradable metal that has been extensively studied and demonstrated compelling clinical data.

Magmaris bioresorbable scaffold, which is the first magnesium vascular stent that received CE mark in 2016, has shown promising clinical outcome in a series of clinical trials.[73-75] That being said, there is still long way to go for Biotronik, the company behind Magnaris stent, before the widely adoption of magmaris stents. A recent study had reported the case where restenosis happened after significant degradation and collapse of magmaris stents. [90]

A variety of magnesium-based alloy systems have been developed to meet the design requirement of stent applications. The main principles in the core design of biodegradable magnesium based alloys are: (1) achieve appropriate biodegradation rate in aqueous environment; (2) good ductility to achieve high plastic deformation to endure the stent crimping and expansion processes during stent deployment; (3) display adequate strength to maintain the mechanical

support against the vascular wall during degradation of the device; and (4) exhibit no significant short-term and long-term toxicity of the alloying elements as well as the related degradation products.

Mg-Al [91-93] and Mg-Re [94-97] are the major magnesium alloy systems that have been studied for stent application to date, and both alloy systems have showed good corrosion resistance and biocompatibility. However, due to the hexagonal close packed (HCP) crystal structure of magnesium, the ductility of these magnesium-based alloys is severely limited. Most of the alloys reported exhibit an elongation around 10-30% at fracture posing difficulties in the stent design and manufacture of magnesium stents. [98, 99] For currently used non-degradable stents, the materials usually possess an excellent balance of strength and ductility. 316L stainless steel, for example, exhibits an elongation of 55% at fracture. [100] Difficulties of fine magnesium tube drawing and the fracture of magnesium stents after balloon expansion has been reported in previous studies. [101-103]

In addition, magnesium stent is known for fast degradation *in vivo*. Even for Mg-Al and Mg-Re alloy, the degradation is significantly accelerated when the alloy matrix is exposed to flow [104, 105] or cyclic stress [106, 107]. Therefore, the development of magnesium alloy with excellent corrosion resistance under flow environment and cyclic stress would be considered a great benefit for the next generation magnesium stents.

To conclude, extensive studies have proved the feasibility and safety of using magnesium alloy for stent application. The development of new magnesium alloys specifically for stent applications is of paramount importance and studies are sorely needed to address the critical gaps in the current material offerings. The new magnesium alloy systems developed in this thesis is expected to: (1) provide strong mechanical support with much improved ductility; (2) offer

resistance to corrosion under flow and cyclic stress; (3) ensure safety due to the judicious selection of non-toxic elements.

1.4   SPECIFIC AIMS

Airway obstruction is relative rare but could be life-threatening condition. The current gold standard for treating airway obstruction is open surgery including resection and anastomosis, slide tracheoplasty, and tracheal grafting [12, 13]. However, these reconstructive surgical procedures are usually associated with serious complications. Unavoidable anastomotic tension, ischemia and lesions after open surgery lead to a recurrence of airway stenosis. In some cases, open surgery is impossible due to the patient's condition, anesthetic risk, or existing situation causing simultaneous morbidity.

Bronchoscopy based interventional pulmonology has become popular due to the immediate relief and reduced morbidity and risk. Airway stenting is a valuable adjunct to the other therapeutic bronchoscopic techniques. Even though all these stents exhibit efficient short-term palliation, none of the stents provide satisfactory long-term effectiveness. Silicone tubes interfere with the mucocilliary clearance [25] while metallic stents provide better mechanical support and mucocilliary clearance but unfortunately cause tissue ingrowth and granulation formation [108]. Because of these severe complications, explantation of the stents is often required, which may be difficult to perform and moreover, subjects the patient to additional risks.

Magnesium stent has emerged as another biodegradable stent candidate in the past 10 years. Extensively studies have been reported to explore different magnesium alloys as novel

biodegradable metallic material for stent application. However, there are two major issues with current existing biodegradable magnesium systems. First, the ductility limitation of magnesium alloy has been a key issue for biodegradable stents applications. Currently, no magnesium alloy-based stents have demonstrated similar expansion capability to currently used permanent stents. Second, the degradation rate of magnesium stent is too fast to meet the clinical needs. A more robust alloy matrix that is corrosion resistant especially under flow and cyclic stress condition is necessary for developing the next generation magnesium stents. The ***goal of the proposed work*** thus is to develop a new magnesium alloy system which addresses the limited ductility and fast degrading rate issues of current magnesium systems and to evaluate the feasibility of the proposed magnesium alloy system in form of prototype tracheal stent in clinically relevant animal models.

The ***central hypothesis*** of the proposed work is that Mg-Li-Zn-(Al) alloys with 5-10 wt. % of Li will be suitable materials for biodegradable metallic stent application due to the superior ductility, moderate strength, improved corrosion resistance and negligible cytotoxicity. To test this central hypothesis, four specific aims are proposed here and discussed below.

1.4.1   Specific Aim 1. Synthesize novel Mg-Li-Zn-(Al) alloys and evaluate their structure, microstructure, mechanical properties and in vitro corrosion behavior

Previous publications have demonstrated that adding more than 5.7% of Li will introduce β phases (BCC structure) into magnesium alloys and significantly improve ductility. We hypothesized that the novel Mg-Li-Zn-(Al) alloys we proposed in this work would exhibit comparable ductility to current alloys of commercial permanent stent and appropriate degradation rate in vitro. In this specific aim, six dual-phase Mg-Li-Zn-(Al) alloys were

synthesized. All the alloys were melted, casted and extruded into 2 cm diameter rods. The chemical composition and phase composition were verified by ICP-OES and XRD. Systematic materials characterization for each alloy will be performed to evaluate the mechanical properties and *in vitro* degradation rate. The results were used to understand the correlation between microstructure/chemical composition and materials performance and single out the Mg-Li-Zn-(Al) alloys that were most suitable for stents application.

1.4.2 Specific Aim 2. Identify the potential use of the selected Mg-Li-Zn-(Al) alloys as biodegradable materials by conducting in vitro cytotoxicity tests

In vitro cytotoxicity of selected Mg-Li-Zn-(Al) alloys was further evaluated with respect to the application of the material. We hypothesized that the novel Mg-Li-Zn-(Al) alloys would demonstrate comparable cytotoxicity to pure magnesium and AZ31 alloy for tracheal stent application. In this aim, human bronchial epithelial cells (BEAS-2B cells) was used to evaluate the cytotoxicity of the selected Mg-Li-Zn-(Al) alloys for tracheal stent application. MTT assay, live/dead imaging, DAPI&F-actin staining, cell apoptosis assay and cell cycle assay were performed to evaluate the *in vitro* cytotoxicity of the selected Mg-Li-Zn-(Al) alloys.

1.4.3 Specific Aim 3. Evaluate the biocompatibility and *in vivo* degradation of the Mg-Li-Zn-(Al) alloys in mouse subcutaneous model

Due to the difference between *in* vitro and *in vivo* test setting. All the six Mg-Li-Zn-(Al) alloys were implanted in mouse subcutaneous model to evaluate the *in vivo* degradation and biocompatibility. We **hypothesized** that the novel Mg-Li-Zn-(Al) alloys would demonstrate

excellent *in vivo* biocompatibility and biosafety. In this aim, Mg-Li-Zn-(Al) alloys samples were implanted in mouse subcutaneously. The *in vivo* degradation, hydrogen evolution and tissue/organ response were calculated. Histology staining of implanted site and key organs of be performed to evaluate the local toxicity and systematic toxicity.

1.4.4   Specific Aim 4. Fabricate of Mg-Li alloy stents and validate the feasibility of prototype Mg-Li alloy tracheal stents in bioreactor and rabbit airway model

With the data obtained from previous aims, we selected the best alloy for stent fabrication and testing. We hypothesized that the Mg-Li alloy tracheal stent would be more corrosion resistant under flow environment and will safely degrade in the rabbit airway without inhibiting further growth of the airway. In this aim, bench tests were performed to evaluate the *in vitro* degradation of the stents. These stents were then implanted into rabbit trachea to evaluate the feasibility of Mg-Li alloy stent for the treatment of airway obstruction.

2.0 SPECIFIC AIM 1. SYNTHESIZE NOVEL MG-LI-ZN-(AL) ALLOYS AND EVALUATE THEIR STRUCTURE, MICROSTRUCTURE, MECHANICAL PROPERTIES AND IN VITRO CORROSION BEHAVIOR

2.1 INTRODUCTION

Mg-Li alloys were first developed by NASA as an ultra-light alloy for aerospace applications in 1960s [109]. The microstructure of the Mg-Li alloys depends on the Li content. With less than 5.7 wt. % of Li, the binary alloy is comprised of single phase α, exhibiting the HCP structure; with more than 10.3 wt. % of Li, the Mg-Li alloy exhibits single-phase β belonging to the BCC structure. Both α phase and β phases co-exist when the Li content is between 5.7% and 10.3%. Several studies have been conducted on single phase, α Mg-Li alloys for biomedical application. For example, LAE442 alloy has been extensively studied as an orthopedic implant [110-112]. Mg-Li-Ca alloys were also investigated for biomedical applications [113, 114]. Compared to the α phase, Mg-Li alloy, the β phase Mg-Li alloy is more attractive because of the unique BCC structure especially for biodegradable stents and other applications requiring high ductility material. However, due to the inferior mechanical properties of single β phase Mg-Li alloy, no study has been reported on the biomedical applications of single phase β Mg-Li alloy. With a mixture of α and β phases, the multi-phase Mg-Li alloys exhibit ultra-high ductility while also maintaining relatively high strength, and therefore, would

be more amenable for load-bearing biomedical applications. Zhou *et al.* first reported the long-term *in vitro* hydrogen evolution of multi-phase Mg-Li-Al-(Re) alloys, and demonstrated the stable degradation of the LA92 alloy and higher corrosion of Mg-Li-Al-Re alloys. [115] A more detailed study was later published demonstrating the superior mechanical property, stable degradation and acceptable biocompatibility of Mg-Li-Al-(Re) alloys [116]. Zeng *et al.* also investigated the corrosion mechanism of multi-phase Mg-Li-Ca alloy in Hank's solution [117]. To the best of the authors' knowledge, however, there is no study reported to date investigating the mechanical properties, degradation and biocompatibility of multi-phase Mg-Li alloys containing Zn and Al. In this context, Mg-Li-Zn-(Al) alloy has been proposed as an ultra-light metal for industrial aerospace and automobile applications. The study has extensively focused on mechanical properties and plastic deformation of Mg-Li-Zn alloys [118-121]. A recent publication has studied the three single α phase Mg-Li-Zn alloy and three multi-phase Mg-Li-Zn alloys for stent application, mechanical properties and *in vitro* degradation were discussed demonstrating the potential of Mg-Li-Zn alloy for stent application. [122]

In specific aim 1, six multi-phase Mg-Li-Zn ternary alloys were accordingly designed and evaluated. The alloying elements were selected based on the design principle mentioned above. Besides alloying with Li, as one of the human essential elements, Zn is also chosen to further improve the strength of the Mg-Li system via solid solution strengthening mechanism. Furthermore, our previous first principles study executed also demonstrated that the addition of Zn into the magnesium alloy will lead to enhancement of the ductility of these alloys [123]. Al is added to further strength the alloy and improve the corrosion resistance. The goal of this study is thus, to demonstrate the following: (1) the multi-phase Mg-Li alloy will likely exhibit superior mechanical properties suitable for stent application when compared to the currently used

common Mg alloy systems; (2) the co-existence of the α and β dual phases will not alter the *in vitro* degradation rates significantly.

2.2   MATERIALS AND METHODS

2.2.1   Materials design and fabrication

Six multi-phase Mg-Li-Zn-(Al) alloys with different percentage of Li and Al elements were proposed and synthesized in this study. Among the six alloys, three alloys, namely Mg-6Li-1Zn (LZ61), Mg-6Li-1Al-1Zn (LAZ611) and Mg-6Li-3Al-1Zn (LAZ631) alloys, have higher percentage of the α phase (HCP structure) and the rest three alloys, namely Mg-9Li-1Zn (LZ91), Mg-9Li-1Al-1Zn (LAZ911) and Mg-9Li-3Al-1Zn (LAZ931) alloys, have higher percentage of the β phase (BCC structure). All the alloys will be melted, casted and extruded into 2 cm diameter rods with the assistance from Xi'an SiFang EM CO., LTD (Xi'an, China).

2.2.2   Chemical composition analysis

The actual chemical composition of the fabricated Mg-Li-Zn-(Al) alloys were then verified by inductively coupled plasma optical emission spectroscopy (ICP-OES, iCAP duo 6500 Thermo Fisher, Waltham, MA). Two standard solutions with known different concentrations of Mg, Li, Al, Zn, Mn, Fe, Cu, and Ni elements was prepared using certified single element standard solutions suitable for ICP (Sigma-Aldrich, St. Louis, MO). Deionized water was used as blank standard. Small pieces of the six alloys were cut from the extruded rod and dissolved in

27

1% nitric acid. The solutions were then diluted to analyze the concentration of elements mentioned above.

2.2.3 Metallic phase characterization

The formation and presence of the individual phases was identified by X-ray diffraction using the X-ray diffractometer (Philips X'Pert PRO diffractometer), employing Cu Kα (λ = 1.54056 Å) radiation with a Si detector (X'celerator). The X-ray generator was operated at 45 kV employing 40 mA current in the 2θ range from 10-90°. Mg-Li-Zn-(Al) alloy disks with 10 mm in diameter and 2 mm in thickness were used for the analysis, and the results were analyzed using X'Pert HighScore Plus version 3.5 software. The peaks identified in the XRD patterns were compared with the standard XRD spectra in the Inorganic Crystal Structure Database (ICSD) database to confirm the major phases and intermetallic compounds. 99.9% pure Mg as drawn rod, and AZ31 extruded rod were purchased from Goodfellow (Coraopolis, PA) and used as control.

2.2.4 Microstructure characterization

To observe the microstructure of the Mg-Li-Zn-(Al) alloys, round plate samples (ϕ=10mm×2mm) were sliced by lathe from the center of the extruded rods. All the samples were ground with SiC abrasive sandpapers up to 1200 grit and polished initially with monocrystalline diamond suspension spray (1 μm, Buehler) and finally with Masterprep® Alumina Suspension (0.05 μm, Buehler). Samples were etched using a solution of 5 ml acetic acid, 6 g picric acid, 10

ml water and 100 ml ethanol (picral). Microstructures of the polished and etched samples were then observed under a Nikon Optiphot microscope (Nikon, Tokyo, Japan).

2.2.5 Mechanical property characterization

Tensile testing was performed using the extruded Mg-Li-Zn-(Al) alloys employing commercially obtained AZ31 plate (Alfa Aesar, Tewksbury, MA) as the control. Tensile bars were machined along the axis direction of the extruded rods by CNS machine. The size of the tensile bars was determined as per ASTM E8/E8M-11 standard with 12.7 mm gauge length and 3 mm × 3mm gauge area. For each sample, the stress-strain curve was generated by Instron 5969 testing system (Instron, Norwood, MA) equipped with an extensometer (Instron 2630 series, Norwood, MA) measuring the elongation. Three typical stress-train curves obtained from each group were used to calculate the yield strength (YS) and ultimate strength (UTS) and elongation at fracture (EL) using the Bluehill® 3 Testing Software for Mechanical Testing Systems (Instron, Norwood, MA).

2.2.6 Electrochemical analysis

Mg-Li-Zn-(Al) alloy samples in the shape of disks (10 mm in diameter and 2 mm in thickness) were mounted in epoxy with only one side of the flat surface exposed. The edge of the sample was then sealed using nail polish. The alloy surface was ground using SiC abrasive sand papers up to 1200 grit. A three-electrode cell setup was employed for electrochemical corrosion testing utilizing platinum wire as the auxiliary electrode, Ag/AgCl as the reference electrode and the epoxy-mounted sample as the working electrode. Each sample was subsequently immersed in

Hank's Balanced Salt Solution (HBSS) for at least 10 min to reach a stable open circuit potential. Potentiodynamic polarization (PDP) plots were obtained in 37°C HBSS with an electrochemical workstation (CHI 604A, CH Instruments, Inc., Austin, TX). All the samples were tested employing a scan rate of 1 mV/s within a potential window of ~500 mV above and below the open circuit potential. The corrosion potential, E_{corr}, the corrosion current density, i_{corr}, and corrosion rate, CR_{corr}, were then calculated following the method described in ASTM-G102-89.

2.2.7 Immersion corrosion measurement

Immersion test was conducted to evaluate the *in vitro* degradation of Mg-Li-Zn-(Al) alloys based on ASTM standard G31-12a. Round plate samples (ϕ=10mm×2mm) were ground with SiC abrasive sand papers up to 1200 grit. All the samples were then sonicated in ethanol, weighed and sterilized under UV. Each sample was immersed in HBSS in a 50 mL conical centrifuge tubes. The ratio of HBSS volume to sample surface area is 0.20 mL/mm². All the samples were kept in 37°C. After immersion for 1, 3, and 5 weeks, the samples were retrieved from the buffer media, washed in DI water, ethanol and dried in air. The corrosion products were removed by immersion in solution of 200 g chromium trioxide, 10 g silver nitrate and 1000 ml water for 10 min. The samples were then washed in DI water, ethanol, dried in air and weighed. The corrosion rate was calculated based on the mass loss utilizing the equation given below[97]:

$$\text{Corrosion Rate } (mm/year) = K \times \frac{W}{A \times T \times D} \quad (1)$$

Where, the constant K is 3.65×10^3, W is mass loss (g), A is the surface area of each sample (cm²), T is the immersion time (day), and D is the density of each alloy (g/cm³). The sample

surface after removing the corrosion product was observed by scanning electron microscopy (SEM; JSM6610LV, JEOL).

2.2.8 Statistical analysis

The obtained results were expressed as the mean ± standard deviation. One-way ANOVA was conducted to determine the differences between different groups of samples with Bonferroni Procedure as post hoc test. Statistical significance was defined as $p < 0.05$. Statistical analysis was performed utilizing the IBM SPSS Statistics 23 package for Windows.

2.3   RESULTS

2.3.1   Chemical composition and microstructure of Mg-Li-Zn-(Al) alloy

Mg-Li-Zn-(Al) alloys were firstly verified by measuring the chemical composition and observing the microstructure. Table 2.1 shows the ICP results of the actual chemical composition of each Mg-Li-Zn-(Al) alloy. The elemental compositions of most elements are close to the nominal composition, and the impurities level of each alloy was low, this is partially due to the usage of high vacuum furnace. Less impurities will contribute to better mechanical properties and corrosion resistance. The optical images (Figure 2.1) of the microstructure clearly show the presence of a mixture of α ($Li_{0.92}Mg_{4.08}$) and β (Li_3Mg_7) phases with the lighter colored area representing the α phase and the darker colored area representing the β phase. In Figure 2.1 (a-f), both the cross-section and longitudinal sections of LZ61, LAZ611 and LAZ631 microstructure

images show a higher percentage of the lighter colored area (α phase), whereas in Figure 2.1 (g-l), the microstructure images of LZ91, LAZ911 and LAZ93 show a much higher percentage of the darker colored area (β phase). The cross-section of all the six alloys showed a typical fibrous extrusion texture and the grains were extremely elongated in the longitudinal direction. The X-ray diffraction analysis result (Figure 2.2) further confirms the co-existence of both phases. The peaks representing the β phase were significantly more intense in the LZ91 pattern than in the LZ61 diffraction pattern indicating the presence of a higher percentage of the β phase. The X-ray diffraction trace also exhibited the diffraction peak of the MgZn intermetallic in all alloys except LAZ631 and LAZ931. $Al_{12}Mg_{17}$ phase was also identified in all Al containing alloys.

Table 2.1. Chemical composition of Mg-Li-Zn-(Al) alloy.

Alloy	Chemical composition (wt. %)			
	Li	Al	Zn	Mg
Mg-6Li-1Zn	6.11±0.13	0.04±0.06	0.92±0.08	Bal.
Mg-6Li-1Al-1Zn	5.87±0.12	1.10±0.02	0.74±0.05	Bal.
Mg-6Li-3Al-1Zn	5.90±0.15	3.32±0.13	0.89±0.05	Bal.
Mg-9Li-1Zn	9.00±0.14	0.01±0.01	0.96±0.04	Bal.
Mg-9Li-1Al-1Zn	8.99±0.13	1.07±0.02	0.87±0.06	Bal.
Mg-9Li-3Al-1Zn	9.37±0.07	3.30±0.10	0.87±0.06	Bal.
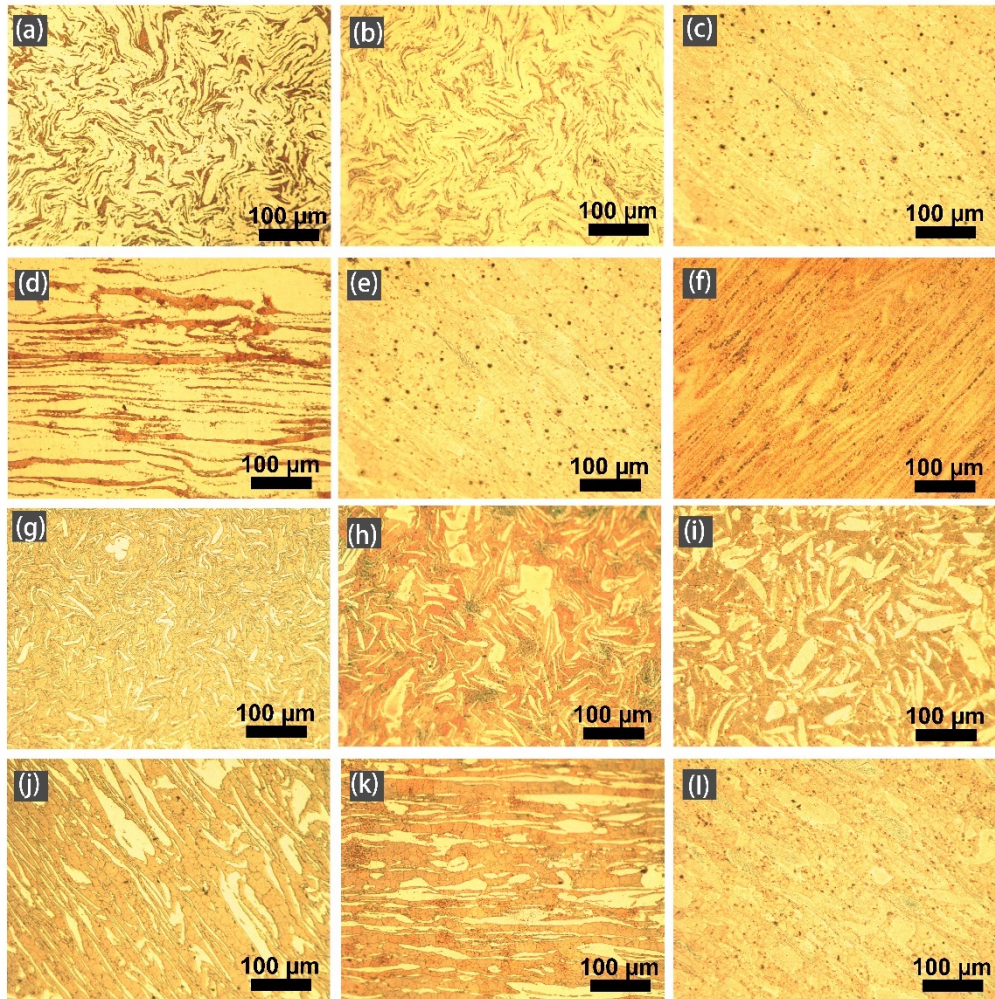
Figure 2.1. Microstructure of the Mg-Li-Zn-(Al) alloys. LZ61 alloy (a) cross-section, (b) longitudinal section, LAZ611 alloy (c) cross-section, (d) longitudinal section, LAZ631 alloy (e) cross-section, (f) longitudinal section, LZ91 alloy (g) cross-section, (h) longitudinal section, LAZ911 alloy (i) cross-section, (j) longitudinal section, LAZ931 alloy (k) cross-section, (l) longitudinal section.
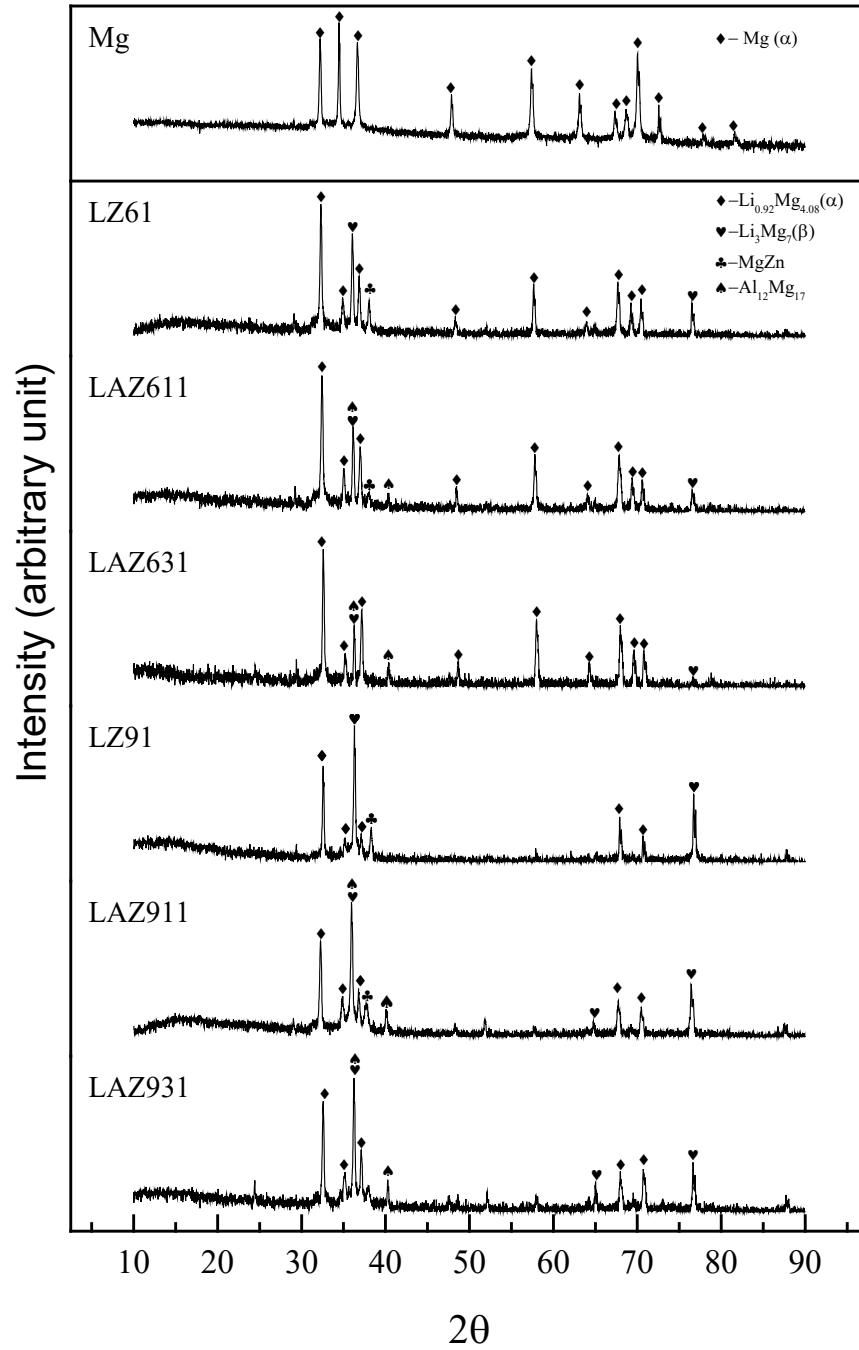
Figure 2.2. XRD pattern of Mg-Li-Zn-(Al) alloys compare with pure Mg and AZ31 alloy.

2.3.2   Mechanical properties of Mg-Li-Zn-(Al) alloy

It is well known that for balloon expandable stents, the routine stent delivery method requires the system to exhibit and demonstrate the capability to undergo plastic deformation. At the same time, higher strength is preferred for the system to maintain the mechanical support against the vessel wall after stent delivery. To screen the candidate material, tensile test is usually selected to evaluate both, the strength and the ductility of the selected material [116, 124, 125] . Figure 2.3 shows the mechanical properties of the Mg-Li-Zn-(Al) alloys compared with commercial AZ31 alloy used as the control. The strength and elongation at fracture of the tested groups were plotted in Figure 2.3(a) and Figure 2.3(b). Typical stress-strain curves obtained from the tensile test are plotted in Figure 2.3(c). All the Mg-Li-Zn-(Al) alloys except LAZ631 showed much higher strain before fracture when compared to the AZ31 control alloy which exhibited a steep increase in the strength. Our results clearly demonstrate that, with the addition of Li, the ductility of the Mg-Li-Zn-(Al) alloys is significantly improved (P < 0.05) as shown in Figure 2.3(b). The average elongation at fracture of all the Mg-Li-Zn-(Al) alloys are 2-3 times of the elongation at fracture of AZ31 alloy (17±2%). However, increasing the Li content to 9 wt.% only marginally increased the ductility of Mg-Li-Zn-(Al) alloys. Meanwhile, adding more Al into the alloy system steadily increased the strength of the alloys at the sacrifice of ductility. Moreover, it should be noted that the significant increase in ductility resulted in compromising the strength of the Mg-Li-Zn-(Al) alloys likely due to Li being a softer metal. For example, the yield strength (YS) of the LZ61 and LZ91 decreased to 119±11 MPa and 115±3 MPa, respectively, while the AZ31 alloy displays a YS of 158±20 MPa. Similar trend is observed for the ultimate tensile strength (UTS). The AZ31 alloy exhibits the highest UTS (260±7 MPa), followed by LZ61 (179±3 MPa), and LZ91 (146±8 MPa), respectively.

Figure 2.4 shows the fracture surface of the tensile bars. All the Mg-Li-Zn-(Al) alloys samples experienced a similar cup-and-cone facture during the tensile test. The AZ31 alloy exhibited a mixture of both, ductile and brittle fracture. The major portion of the fracture surface shows an irregular and fibrous appearance, accompanied with several sharp and smooth cleavage planes which is indicative of a brittle fracture. The Mg-Li-Zn-(Al) alloys on the other hand, show much more necking before facture. Hence, only ductile fracture pattern could be observed in the central interior region of the fracture surface. At higher magnification as shown in Figure 2.4, the fracture surface of Mg-Li-Zn-(Al) alloys is consisted of numerous spherical dimples. The dimpled feature is a typical structure that results from uniaxial tensile failure, and each dimple represents half of a micro-void that is formed which then separates during the fracture process.
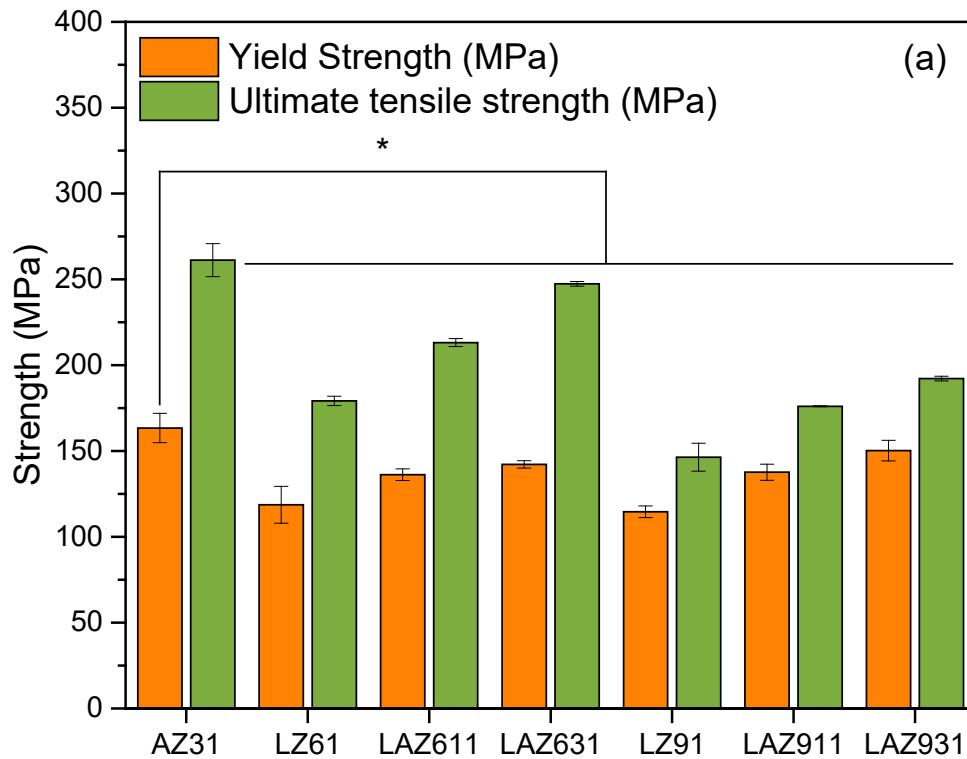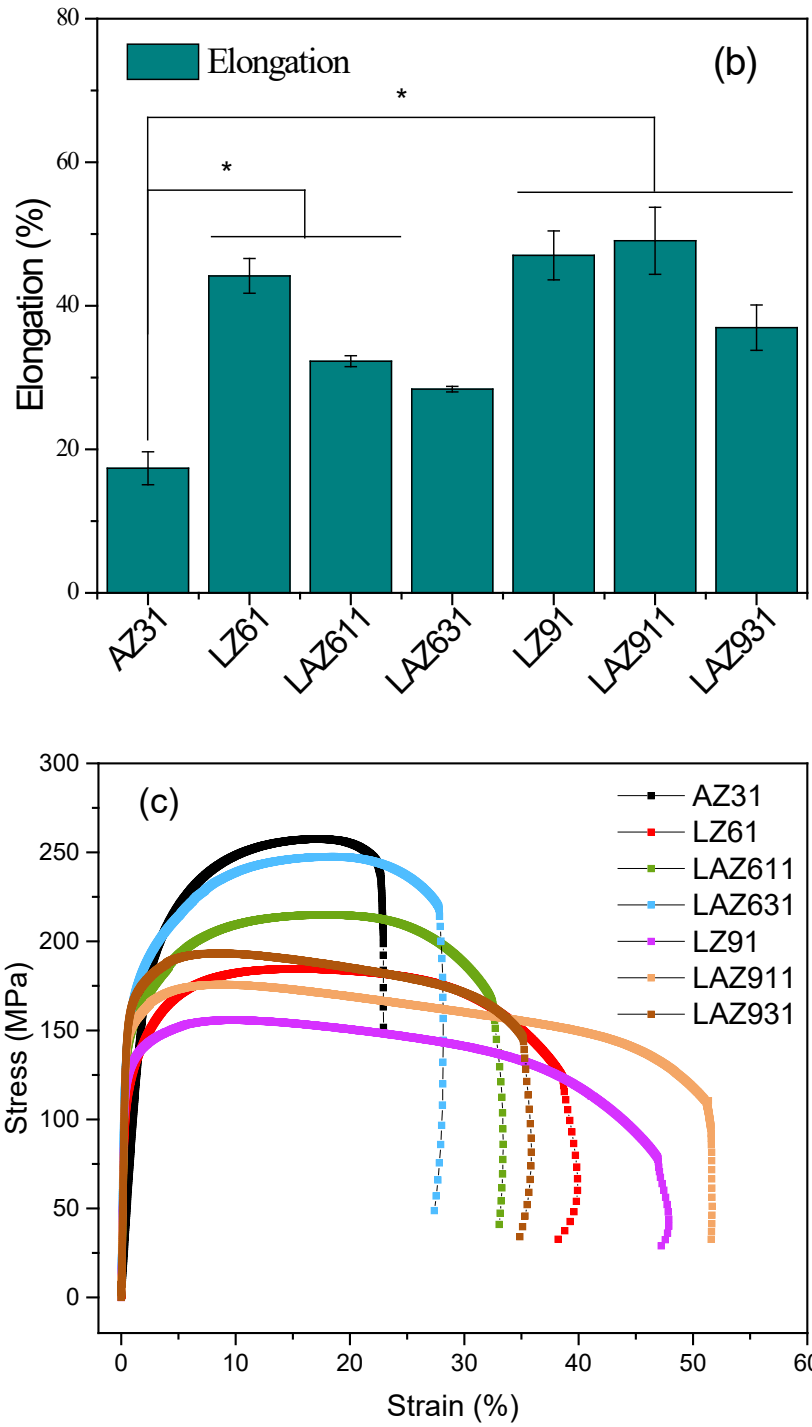
Figure 2.3. Mechanical properties of Mg-Li-Zn-(Al) alloys. (a) Tensile strength and (b) elongation at fracture of Mg-Li-Zn-(Al) alloys. (c) Typical stress-strain curves. *denotes a significant difference between Mg-Li-Zn-(Al) alloys and AZ31 alloy ($p < 0.05$, n=3).
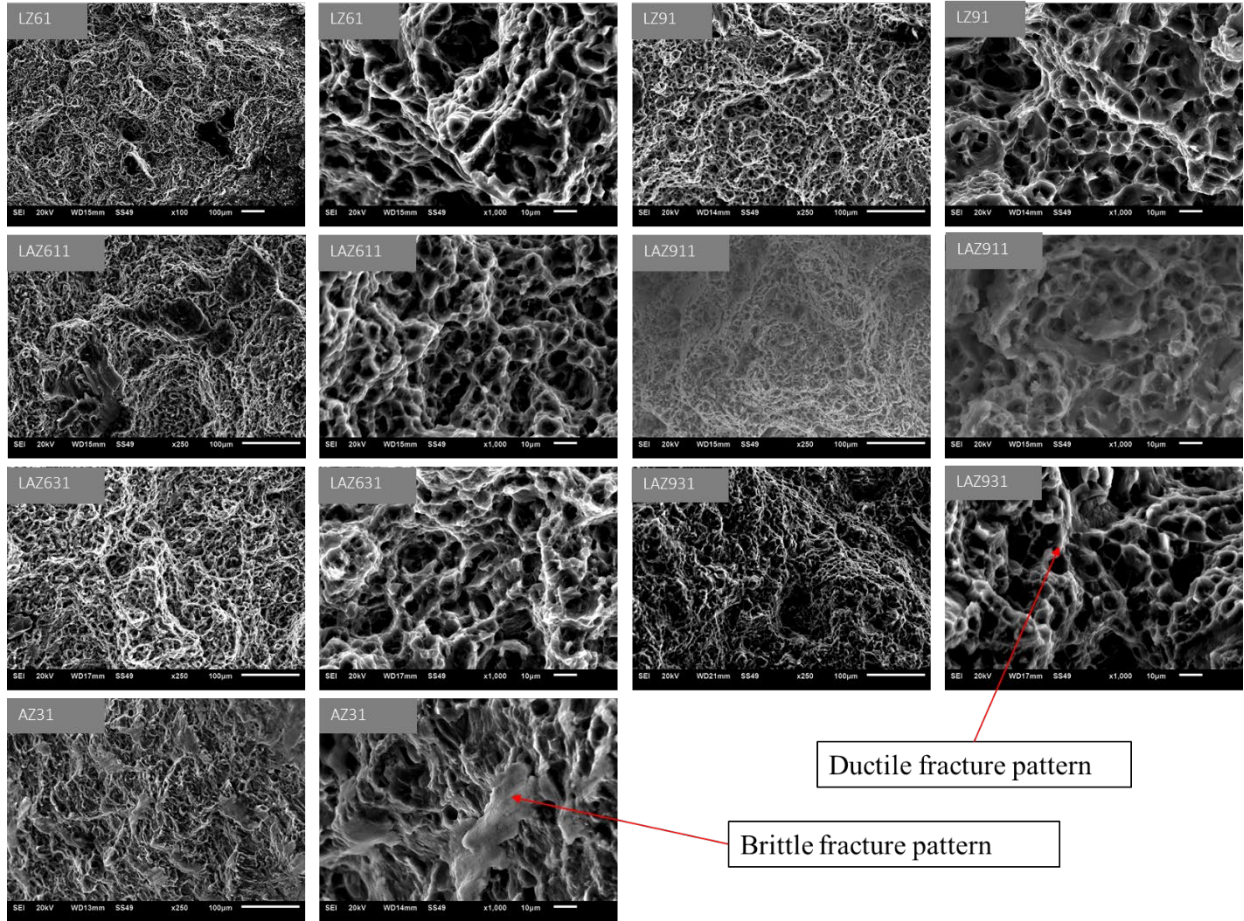
Figure 2.4. Scanning electron fractography of the tensile bar fracture surface.

2.3.3 In vitro degradation of Mg-Li-Zn alloy

Several techniques are commonly used to evaluate the degradation of magnesium alloys, such as electrochemical analysis, hydrogen evolution, and immersion tests. In this study, electrochemical and static immersion tests were conducted to study the degradation behavior of the Mg-Li-Zn-(Al) alloys. Figure 2.5 shows the potentiodynamic polarization (PDP) curves collected for the six Mg-Li-Zn-(Al) alloys as well as control groups: pure Mg and AZ31 alloy. E_{corr}, i_{corr}, and CR_{corr} calculated based on the tafel plots are listed in Table 2.2. All the groups showed dramatic increase in corrosion current 200-300 mV above the E_{corr} indicating the film breakdown characteristic. The anodic processes of all the Mg-Li-Zn-(Al) alloys were altered when compared to pure Mg and AZ31 alloy which implies that the corrosion was largely controlled by the anodic reaction. The corrosion current representing the dissolution reaction of the alloy is noticeably higher, which increased the overall corrosion current density.

Immersion test was further conducted to evaluate the long-term in vitro degradation of Mg-Li-Zn-(Al) alloys in HBSS. The weight loss of samples at the end of each time point was converted into the corrosion rate and plotted in Figuer 2.5(b). The slowest corrosion rate was observed for the AZ31 group at all 1, 3 and 5 weeks' time point. LAZ631 alloy exhibited the highest corrosion rate throughout the 5-week long immersion test. Three other alloys, namely LZ61, LAZ611 and LAZ911, on the other hand, showed a moderate corrosion resistance which was close to the corrosion resistance of pure Mg. The statistical analysis result revealed that there is no statistical difference between the 5-week corrosion rates of pure Mg, AZ31, LZ61, LAZ611 and LAZ911 groups, and LAZ631, LZ91 and LAZ931 groups corroded at significantly higher rate ($p < 0.05$) than all the other groups.

39

Table 2.2. Corrosion rates of pure Mg, AZ31, and Mg-Li-Zn-(Al) alloys determined by potentiodynamic polarization.

	E_{corr} (V)	i_{corr} ($\mu A/cm^2$)	CR_{corr} (mm/year)
Pure Mg	-1.46 ± 0.03	1.094 ± 0.373	0.025 ± 0.008
AZ31	-1.52 ± 0.01	2.144 ± 0.139	0.035 ± 0.002
LZ61	-1.54 ± 0.03	1.725 ± 0.888	0.042 ± 0.020
LAZ611	-1.51 ± 0.01	0.640 ± 0.071	0.015 ± 0.001
LAZ631	-1.56 ± 0.01	65.627 ± 4.804	1.565 ± 0.114
LZ91	-1.57 ± 0.01	6.367 ±0.511	0.158 ± 0.013
LAZ911	-1.54 ± 0.02	0.643 ± 0.148	0.016 ± 0.004
LAZ931	-1.53 ± 0.01	12.296 ± 4.794	0.300 ± 0.117

E_{corr}: corrosion potential; i_{corr}: corrosion current density; CR_{corr}: corrosion rate calculated based on i_{corr}

Except for LAZ611 group, the average corrosion rate determined following immersion tests showed a similar trend among all the groups studied suggesting that the corrosion rates expectedly increase over the period of immersion, and the 5-week *corrosion* rate was the highest compared to the corrosion rate after 1 week and 3 weeks of immersion. The average corrosion rate of LAZ611 was constantly decrease over the 5 weeks of immersion. The corrosion rate after 3 weeks of immersion was the slowest for pure Mg and AZ31 alloy while the slowest corrosion rate for Mg-Li-Zn-(Al) alloys was observed after 1 week of immersion except for LAZ611, of which the slowest corrosion rate was observed at week 5. Figure 2.6 shows the SEM image of the sample surface without the corrosion product after 5 weeks of immersion. The sample surface of LZ61, LAZ611, pure Mg and AZ31 showed only partially corroded region, but the LAZ631, LZ91 and LAZ931 alloy surfaces showed much higher roughness indicating a higher corrosion rate. Despite the low corrosion rate of LAZ911 alloy, the sample surface was more homogeneously corroded. Localized corrosion was however, observed on the surface of all the

samples studied reflective of the higher reactivity of both Li and Mg. Localized corrosion would potentially lead to the fracture of the stents, and coating will be needed to protect the stents from losing the mechanical integrity too fast.
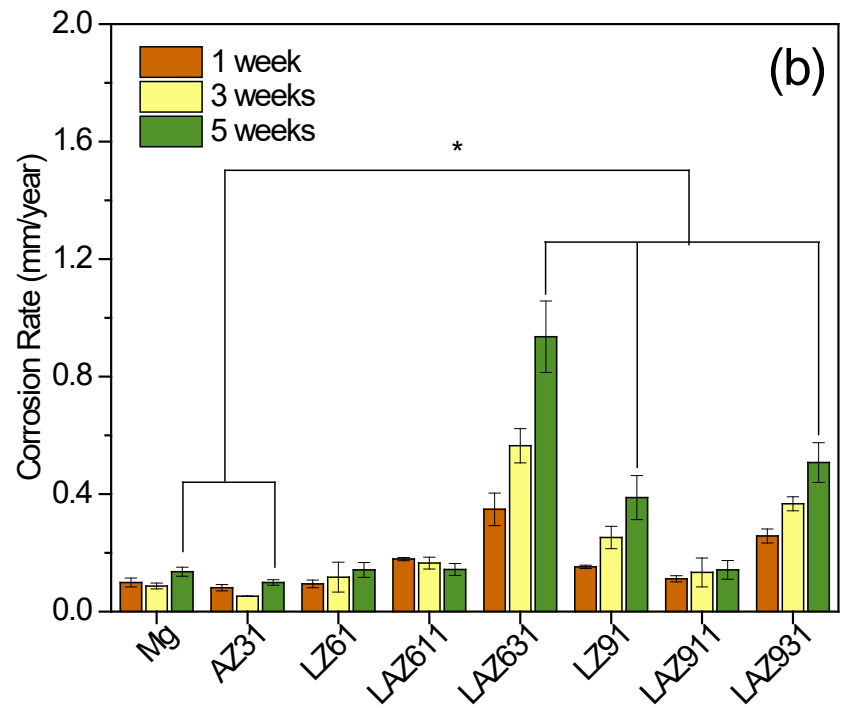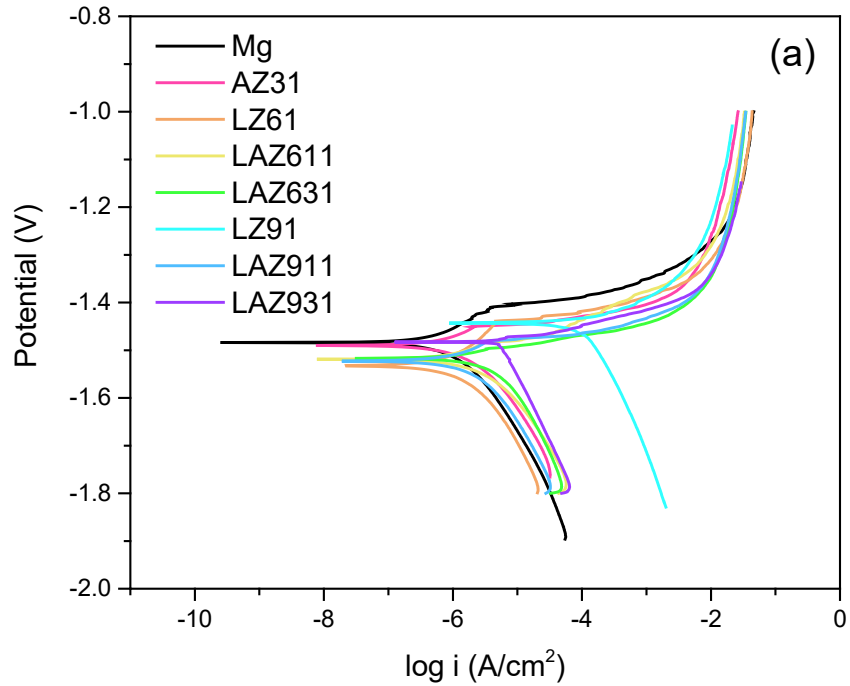
Figure 2.5. (a) Potentiodynamic polarization curves of LZ61, LZ91, pure Mg and AZ31 alloy in HBSS. (b) In vitro degradation rate of Mg-Li alloys in Hank's solution by immersion test. *denotes a significant difference between LZ91 and other groups ($p < 0.05$, n=3).
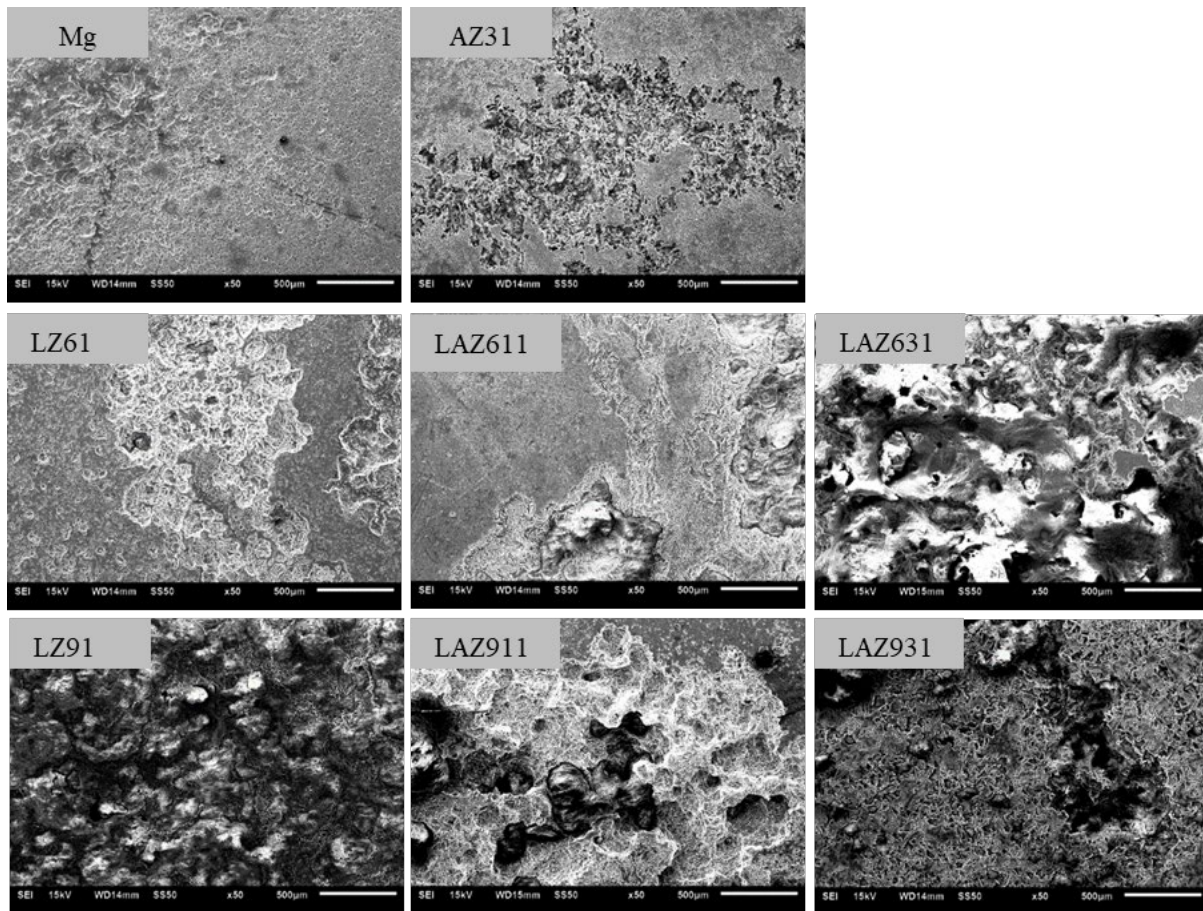
Figure 2.6. SEM of alloy sample surface after 5 weeks of immersion in HBSS.

2.4   DISCUSSION

In the present study, we have demonstrated the promising potential of Mg-Li-Zn-(Al) alloys for possible application as biodegradable stents. By alloying with Li and Zn, we successfully produced six Mg-Li-Zn-(Al) alloys. The co-existence of both α ($Li_{0.92}Mg_{4.08}$) and β

(Li₃Mg₇) phases were verified by the optical micrographs of the corresponding dual phase microstructure as well as the XRD patterns discussed earlier.

For stent application, ductility of the alloy is one of the critical determining factors for evaluation of the alloy proficiency for use as stents. It is well-known that polycrystalline magnesium alloy which exhibits the hexagonal close packed (HCP) structure, the room temperature ductility is limited due to the lack of allowable slip systems. The dominant slip mode for magnesium has the burger victor $1/3<11\bar{2}1>$ with the basal plane serving as the primary slip plane [126]. However, by creating the alloys considered in the present study, the tensile test successfully demonstrates that the ductility of magnesium alloy is significantly improved by introducing the body centered cubic (BCC) phase into the Mg-Li alloy by effectively alloying with Li. However, a decrease in the tensile strength is also overserved due to the softer nature of Li. Lee *et al.* reported that adding 1.2 wt. % of Li would increase the strength of the Mg alloys because of solid solution strengthening. However, with more Li additions (> 4.2 wt.%), the strength and strain hardening rate decreased [127]. These results are clearly in line with the current study. This phenomenon could be explained to be attributable to the following: (1) In the α phase, the critical resolved shear stress (CRSS) is decreased with the presence of Li which leads to the activation of the non-basal slip [128]. Lower critical resolved shear stress enables plastic deformation of Mg-Li-Zn alloy to occur at lower applied force which thus results in lower yield strengths (YS) and ultimate tensile strengths (UTS). The activation of the non-basal slip however, further enhances the ductility of the Mg-Li-Zn alloy. (2) With the presence of the BCC structure, the β phase of Mg-Li-Zn alloy provides more slip systems than the α phase, which as mentioned above exhibits the HCP structure. The β phase is relative softer than the α phase, which leads to decrease in the strength and improves ductility of Mg-Li-Zn-(Al) alloy. (3)

Alloying of Li also alters the lattice parameter of magnesium crystal. Hardie and Parkins studied the lattice distortion of a series of binary magnesium alloy solutions and discovered that the addition of Li decreases both **a** and **c** lattice parameter spacing, particularly, the **c** lattice parameter spacing [129]. This lattice distortion caused by Li is believed to ease the cross gliding of the non-basal slip contributing to enhanced ductility. Al, on the other hand, consistently improve the strength of the Mg-Li-Zn-(Al) alloys. This is caused by solid-solution strengthening of Al in Mg-Li alloy matrix, as well as precipitation hardening from $Al_{12}Mg_{17}$ phase. It should be mentioned that it is possible that control of the second phase precipitates and microstructure control could lead to improvements in the strength without compromising the ductility. These aspects were however, not considered in the present study as the primary aim was to demonstrate the higher ductility by alloying with Li, Zn and Al.

The alloy system of Mg-Li-Zn-(Al) is expected to be more susceptible to corrosion since Li is a very active and reactive element. Albeit, however, it is surprising to see that the LZ61, LAZ611 and LAZ911 alloy exhibited no significant difference when compared to pure Mg and AZ31 after 5 weeks of immersion in HBSS. The corrosion resistance of Mg alloys is known to be mainly influenced by the presence of a protective oxide film on the alloy surface. It is also observed in the immersion study that Mg-Li-Zn-(Al) alloys generated more fine hydrogen bubbles right after the samples were immersed into HBSS. The bubbles then grow larger and more stable as the sample surface loses its metallic sheen and lustre. The CR_{corr} depicted in Table 2.2 represents the corrosion tendency of the fresh alloy surface, while the 5-week corrosion rate calculated from the immersion test is the average corrosion rate determined over a long period of immersion. The abstract value of the degradation rate calculated using different methods was different, but the trends of the degradation was similar, LAZ631, LZ91 and LAZ931 exhibited

higher CR_{corr}. The corrosion continues, the top of the sample would form an increasingly thick corrosion layer of $Mg(OH)_2$, $MgCO_3$ and $Mg_3(PO_4)_2$ products that coat the implant surface. [130] Song *et al.* reported that, for the dual phase Mg-Li alloys, the initial corrosion commenced at the interface of the α phase and the β phase and then spread across the entire sample surface. [131]

As the corrosion continued, the oxide film on the surface of the Mg-Li-Zn-(Al) alloys became thicker, consequently, providing more corrosion protection. However, the thicker the protective film, the brittle nature of the ceramic oxide would lead to a higher propensity of crack formation. The integrity of the protective film is however, determined by two major factors: pH value of the medium and the Cl^- ion concentration. Higher pH value will help stabilize the protective film while higher a Cl^- concentration is detrimental to the integrity of the film. Due to the large volume of the HBSS solution and its buffering capacity, the pH value of the medium remained neutral over the duration of immersion. The Cl^- in HBSS penetrated the protective film thus resulting in crack formation. Further subsequent corrosion of Mg-Li-Zn-(Al) alloys is localized in the area wherein the alloy is unprotected. When compare the degradation rate of LZ91 and LZ61, the LZ91 alloy corrodes the faster than the LZ61 alloy. Since there is a higher percentage of the β phase with a higher amount of Li in LZ91, and the β phase is more active than the α phase in aqueous environment, it is possible that the protective film on the surface of β phase is less stable and provides less corrosion protection which causes the difference in the measured and observed corrosion resistance between the LZ61 alloy and LZ91 alloys. Also, with more Al in the alloys, the degradation is increased. Indicating that $Al_{12}Mg_{17}$ phase detrimental to the corrosion resistance of the Mg-Li-Zn-(Al) alloys. Figure 2.7 also summarizes the degradation rate in simulated physiological buffer and the elongation to fracture of current Mg-Li alloys that

has been reported for biomedical application. In comparison, it can be seen that LZ61 alloy shows an excellent balance of corrosion rate and ductility. Even though, Mg-8.5Li-1Al as reported in the literature and LAZ911 showed similar low corrosion rate and ductility, LZ61 it should be noted is free of Al, an element that has been extensively reported to be related to cause damage to the nervous systems. [132-134]
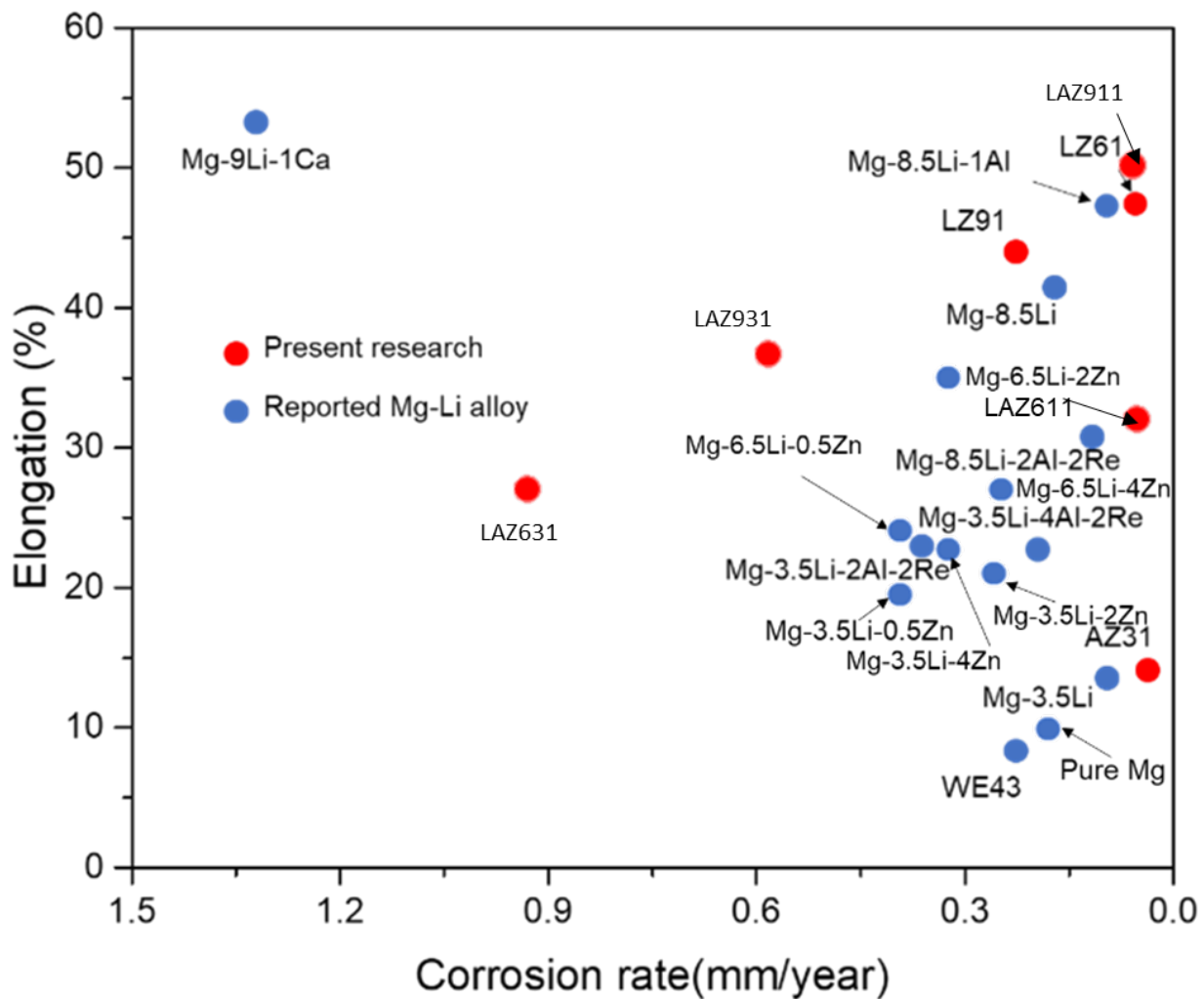
Figure 2.7. Summary of elongation and corrosion rate of reported Mg-Li alloys [116, 117, 122, 135].

3.0   SPECIFIC AIM 2. IDENTIFY THE POTENTIAL USE OF THE SELECTED MG-LI-ZN-(AL) ALLOYS AS BIODEGRADABLE MATERIALS BY CONDUCTING IN VITRO CYTOTOXICITY TESTS

3.1   INTRODUCTION

The characterization of chemical composition, mechanical properties and degradation rate is only the first step of screening materials. As biomaterials, the biocompatiblity evaluation of the Mg-Li-Zn-(Al) alloys and the degradation products of them is as equally important as material characterization. In the age of bioinert materials, the evaluation of biocompatibility is much straightforward since the interaction between the biological system and the material only happens at the interphase. As for biodegradable materials, this evaluation is much more challenging for two reasons. First, the interaction between the biological system and the material has switched from 2D, the interface, to 3D, the space that the material itself possesses as well as surrounding space where degradation products reach. Cells and tissues are consistently exposed the new surface as the material degrades and are even guided to grow inside the material when porosity is intentionally created. As the degradation products move in the body, more tissues and cells are exposed to the material at different level. Second, the interaction is now time sensitive. For traditional inert materials, such as stainless steel, the materials almost remain the same for decades. However, for biodegradable materials, the chemical composition, the geometry, and the

mechanical properties are changing over time. In certain cases, the materials are even programmed to change in order to serve different functions at different stage.

The biosafety of the materials could be evaluated *in vitro* or *in vivo*. Due to the complexity of the biological environment, the results from *in vitro* tests and *in vivo* tests are often not in line with each other. But in most cases, materials are subject to *in vitro* test first especially when there is large quantity of candidate materials.

In vitro biocompatibility evaluation of Mg alloy is challenging since current ISO and ASTM standards are not applied to biodegradable metals due to the reasons we mentioned above. Efforts have been made to standardize the *in vitro* cytotoxicity protocol for Mg alloys [136], however no standard protocol has been established yet. In this aim, four tests were designed to: (1) measure the specific aspects of cellular metabolism (MTT assay); (2) assess the cell damage by imaging the cell morphology (live/dead imaging, DAPI&F-actin staining); (3) evaluate cell damage (cell apoptosis assay) and finally (4) measure the cell growth (cell cycle assay).

All these tests were conducted in an indirect fashion using the alloy extracts. The rationale is that duplicating the *in vivo* direct contact between the cells/tissues and the magnesium alloy is very complicated and costly. As we discussed in previous chapter, the degradation of magnesium gives rise to the ions of magnesium and other alloying elements, as well as pH value, H_2 gas. The goal of the aim was to gain a full understand of the potential toxicity of the Mg-Li-Zn-(Al) alloys and their degradation products. Also, the individual contribution of each element in the alloys was also evaluated.

3.2   MATERIALS AND METHODS

3.2.1   BEAS-2B Cell culture

Human bronchial epithelial cells, BEAS-2B (ATCC® CRL-9609™), were purchased from ATCC to evaluate the toxicity of the alloys. Before seeding cells, coating solution was prepared with mixture of 0.01 mg/mL fibronectin, 0.03 mg/mL bovine collagen type I and 0.01 mg/mL bovine serum albumin (BSA) dissolved in cell culture medium, BEGM medium (Lonza/Clonetics, Walkersville, MD). All T75 tissue culture flasks were coated with 4.5 ml coating solution which covered the entire surface and incubated in a 37°C incubator overnight. BEAS-2B cells were then seeded in the flask in culture in cell incubator with an environment of 95% relative humidity with 5% CO_2. Cells were subcultured before reaching confluence to avoid squamous terminal differentiation. BEAS-2B cells beyond passage 4 and within passage 10 were used in all experiments.

3.2.2   Magnesium extract preparation

Alloy samples were machined into round disks using lathe, high temperature caused by heating during machining was minimalized using coolant. Samples were ground utilizing SiC abrasive sand papers up to 1200 grit, sonicated in acetone and sterilized for 30 min by exposure to UV radiation for each side. After sterilization, the sample disks were placed in 12-well plate and immersed in cell culture medium for 72 hours in a standard cell culture incubator. The specimen surface area to extraction medium ratio was maintained at 1.25 cm^2/ml in accordance with EN ISO standard 10993-12:2004. This extraction ratio was designated as 100% extract.

Extracts were sterile filtered using a 0.2 μm syringe filter before being added to the cells. Low concentration extracts were prepared by diluting the 100% extract into 75%, 50%, 25% and 10% with cell culture medium.

3.2.3 Indirect MTT assay

Indirect MTT assay were conducted following the same procedure described in previous publications from our group [97, 137]. BEAS-2B cells were seeded in 96-well plate at a cell density of 8,000/well and incubated for 12 hours to allow all the cells fully attached to the 96-well plate. Following this, 100 μl 75%, 50%, 25% and 10% extracts were added with normal BEGM cell culture medium serving as the negative control while 10% DMSO cell culture medium served as the positive control. The well plates were incubated for 1 day and 3 days respectively.

The MTT solution was prepared by dissolving 3-(4,5-Dimethylthiazol-2-yl)-2,5-diphenyltetrazolium bromide (MTT) (Invitrogen, Thermo Fisher Scientific) in phosphate buffer solution (PBS) at the concentration of 5mg/ml. Then the MTT solution were mixed with BEGM at the ratio of 1:10. In the meantime. SDS solution was prepared by dissolving 1g SDS (Sodium dodecyl sulfate, Sigma-Aldrich) in 10 ml of 0.01 M HCl. After 1 or 3 days of incubating, the media in 96-well plated were removed and replaced with 100 μl diluted MTT solution and incubated for 4 hours. Following that, 100 μl SDS solution was added, and the plates were incubated for 16 hours and analyzed by Synergy 2 Multi-Mode Microplate Reader (Bio-Tek Instruments, Winooski, VT).

3.2.4 Live/dead staining

Live/dead staining was performed to investigate the cell viability. BEAS-2B Cells with a cell density of 50,000 cell/well were seeded in a 24-well plate and incubated for 12 hours. The media were then replaced with incubated in 25% extract and cultured for 1 day and 3 days. LIVE/DEAD viability/cytotoxicity kit (Invitrogen Inc., Karlsruhe, Germany) was used to stain the live and dead cells to glow green (ethidium homodimer-1) and red (calcein-AM), respectively. Staining solution was prepared by diluting ethidium homodimer-1and calcein-AM in Dulbecco's phosphate-buffered saline (DPBS) (Lonza, Walkersville, MD) at ratio of 1:1000. After removing 25% extract, the cells were then incubated in the staining solution for 15-30 mins, depends on the strength of the signal. The live/dead images were captured using fluorescence microscopy.

3.2.5 DAPI&F-actin staining

DAPI&F-actin staining was performed to image the cell morphology. BEAS-2B Cells with a cell density of 50,000 cell/well were seeded in a 24-well plate and incubated for 12 hours. The media were then replaced with incubated in 25% extract and cultured for 1 day and 3 days. For DAPI&F-actin staining, DAPI (AppliChem, Darmstadt, Germany) served as the fluorescent probe for DNA (blue), and rhodamine phalloidin served as the fluorescent probe to label the F-actin (red). After 3 days culturing, the extract was removed, and the cells were fixed with 4% paraformaldehyde for 10 min. and then washed with PBS. The fixed BEAS-2B cells were permeabilized with 0.1% Tween 20 solution for 10 min. and washed in PBS 3 times. Cells were stained with Rhodamine phalloidin/PBS solution (1:500) for 40 min first, washed in PBS and

then stained in DAPI/PBS solution (1:2000) for 15 min. Cell morphology images were captured using fluorescence microscopy.

3.2.6 Cell apoptosis assay

BEAS-2B Cells with a cell density of 100,000 cell/well were seeded into a 6-well plate and incubated for 12 hours. The media were then replaced with incubated in 25% extract and cultured for 1 day. FITC Annexin V Apoptosis Detection Kit I (BD Biosciences, USA) was used to detect the early apoptosis and late apoptosis. Cells were labelled following the instructions of the Kit and then sorted through BD Accuri™ C6 Plus personal flow cytometer.

3.2.7 Cell cycle assay

BEAS-2B Cells with a cell density of 100,000 cell/well were seeded into a 6-well plate and incubated for 12 hours. For the cell cycle study, the cells were culture in serum-free medium for 24 hours for synchronization. The media were then replaced with incubated in 25% extract and cultured for 1 day. Then the cells were preserved and permeabilized in 70% ethanol for at least 24 hours. Cells were stained by Propidium Iodide (PI) (PI/RNase Staining Buffer, BD Biosciences, USA) for 15 min following the instruction and then sorted by BD Accuri™ C6 Plus personal flow cytometer based on DNA content.

3.2.8 MTT test of Mg and Li ion

To test the effect of Mg^{2+} and Li^+, $MgCl_2$ and LiCl were dissolved in BEBM media individually or together to form a series of media with different concentrations between 2.5mM to 180mM were made. Two sets of MTT tests were performed. In the first set, the BEAS-2B cells were cultured in BEBM media with only $MgCl_2$ or LiCl. In the second set, the BEAS-2B cells were cultured in BEBM media with only $MgCl_2$ and LiCl. The concentration ratio of $MgCl_2$ and LiCl was 1:1.

3.2.9 Statistical analysis

The obtained results were expressed as the mean ± standard deviation. One-way ANOVA was conducted to determine the differences between different groups of samples with Bonferroni Procedure as post hoc test. Two-way ANOVA was performed for MTT test with Bonferroni procedure as post hoc test. Statistical significance was defined as $p < 0.05$. Statistical analysis was performed utilizing the IBM SPSS Statistics 23 package for Windows.

3.3   RESULTS

3.3.1 Cytotoxicity of Mg-Li-Zn-(Al) alloys

The ICP result (Figure 3.1) indicates a burst release of Mg and Li ions collected from pure Mg and Mg alloys after incubation for 72 hours in the BEGM cell culture medium. The

concentration of Zn was below the detection limits and hence, was not plotted. It can be seen that the Mg ion concentration increases more than 600 times compared to normal BEBM cell culture medium. There was no significant difference in Mg ion concentration among LZ61, LAZ611 and LAZ911 alloy extract ($p>0.05$). But the Mg concentration in of all these three alloy groups are significantly lower than Mg concentration in AZ31 alloy extract. Li ion concentration was also significantly higher in LAZ911 alloy extract than LAZ611 alloy extract ($p<0.05$).

MTT results were plot in Figure 3.2. BEAS-2B cell viability was negatively correlated to extract concentration with higher cell viability in lower extract concentration. The cell viability in 75% extract after culturing for both 1 day and 3 days was less than 20% for Mg-Li-Zn-(Al) alloys. At day 1, only groups with extract concentration below 10% showed close to or more than 100% cell viability. At day 3, only the even 10% extract group showed more than 100% cell viability. Two-way ANOVA was performed to analyze the statistical difference between the different alloy groups. Magnesium alloy group and extract dilution ratio served as the two independent variables and cell viability served as the dependent variables in the two-way ANOVA analysis. Cell viability of each magnesium alloy group is discussed as an independent variable in general regardless of the extract dilution ratio. At day 1, there is no significant difference observed between the LZ61, LAZ611 and LAZ911 alloy groups ($p>0.05$). Both pure Mg and AZ31 groups showed higher cell viability than Mg-Li-Zn-(Al) alloy groups ($p<0.05$). At day 3, the gap between pure Mg/AZ31 and Mg-Li-Zn-(Al) alloy groups are way smaller. However, the cell viability in pure Mg and AZ31 groups are still higher than the other and Mg-Li-Zn-(Al) alloy groups. Only cell viability of LAZ611showed no significant difference to Pure Mg group ($p>0.05$).
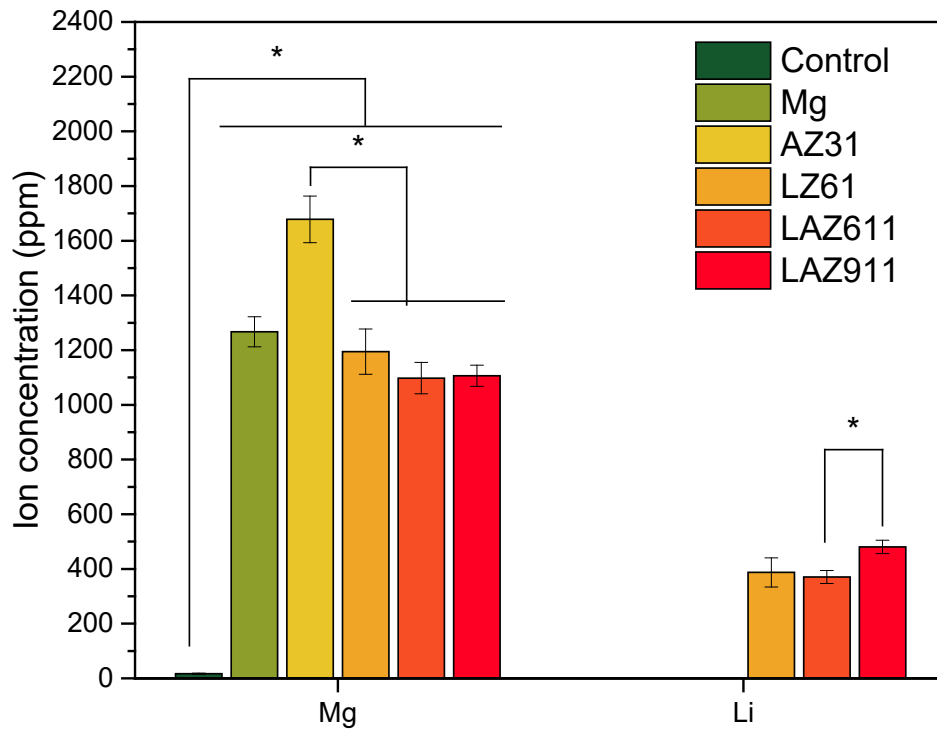
Figure 3.1. Concentration of Mg and Li ion in BEBM media extract after 3 days of incubation.
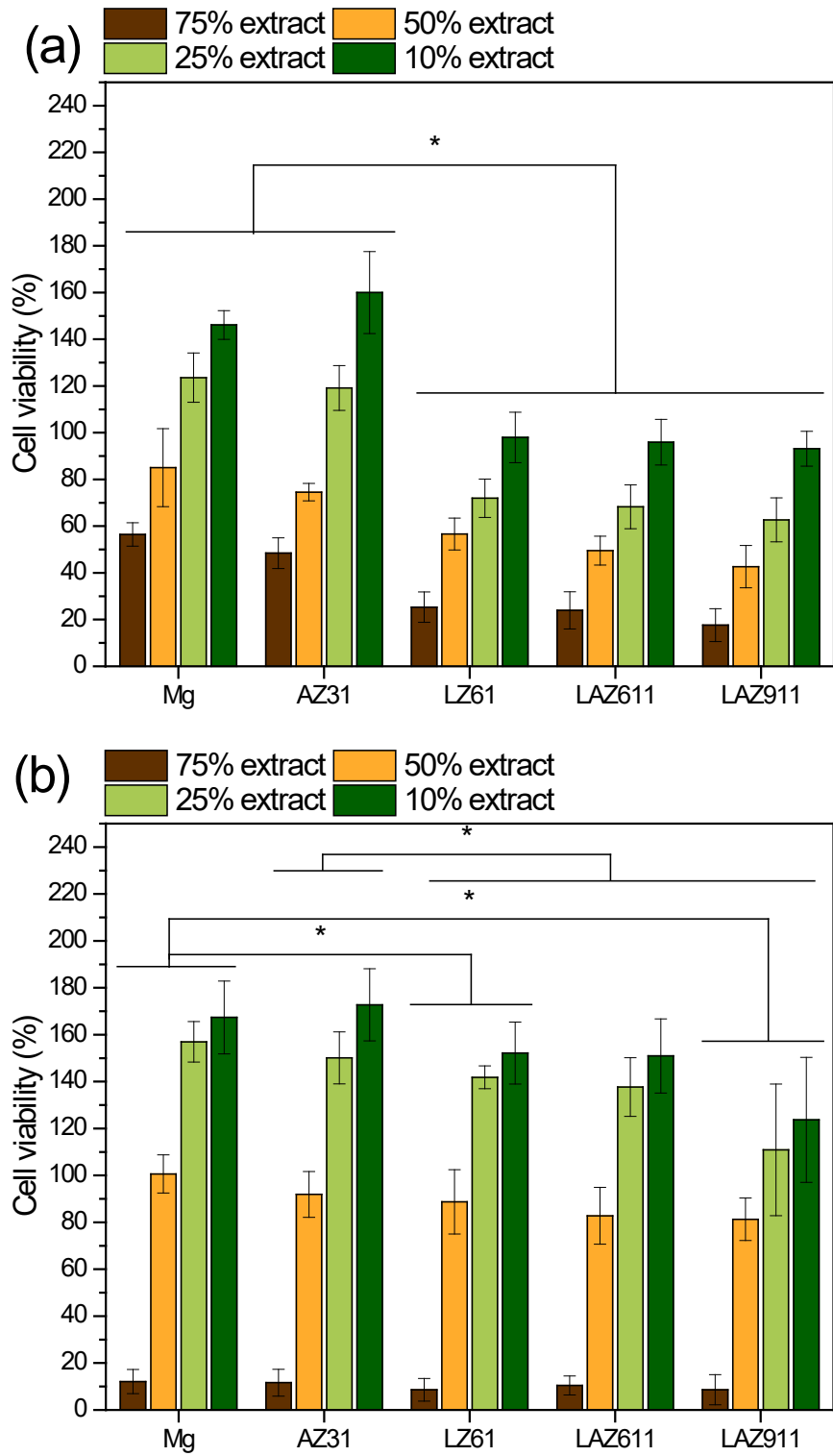
Figure 3.2. BEAS-2B cell viability after culturing in different concentration extract for (a) 1 day; (b) 3 days; *denotes a significant difference between alloy groups (p <0.05, n=3).

Based on MTT results, 25% extract was the only group that showed the impact of degradation products on different cells while still supporting limited cell proliferation. Therefore, 25% extract was used for live/dead staining and DAPI/F-actin staining to visualize the impact of degradation product on cells. Despite the differences observed in the MTT assay discussed above, the live/dead staining of BEAS-2B cell after culturing in 25% extract showed similar results (Figure 3.3). Compared the cell intensity in day 1 and day 3, the higher cell density indeed indicates a healthy BEAS-2B cell proliferation in the extract. Between groups, the difference is unnoticeable in day 1, but a day 3 the Mg-Li-Zn-(Al) alloy groups seems to be slightly lower cell. All the groups demonstrated comparable live cell density with very few apoptotic cells observed under microscope.

Regardless of the lower cell density, all cells in the pure Mg and Mg alloy groups showed same individual cell morphology as the BEAS-2B cells cultured in normal cell culture medium (Figure 3.4). We also notice that cells congregated in control groups, where cells were cultured in normal cell culture media.
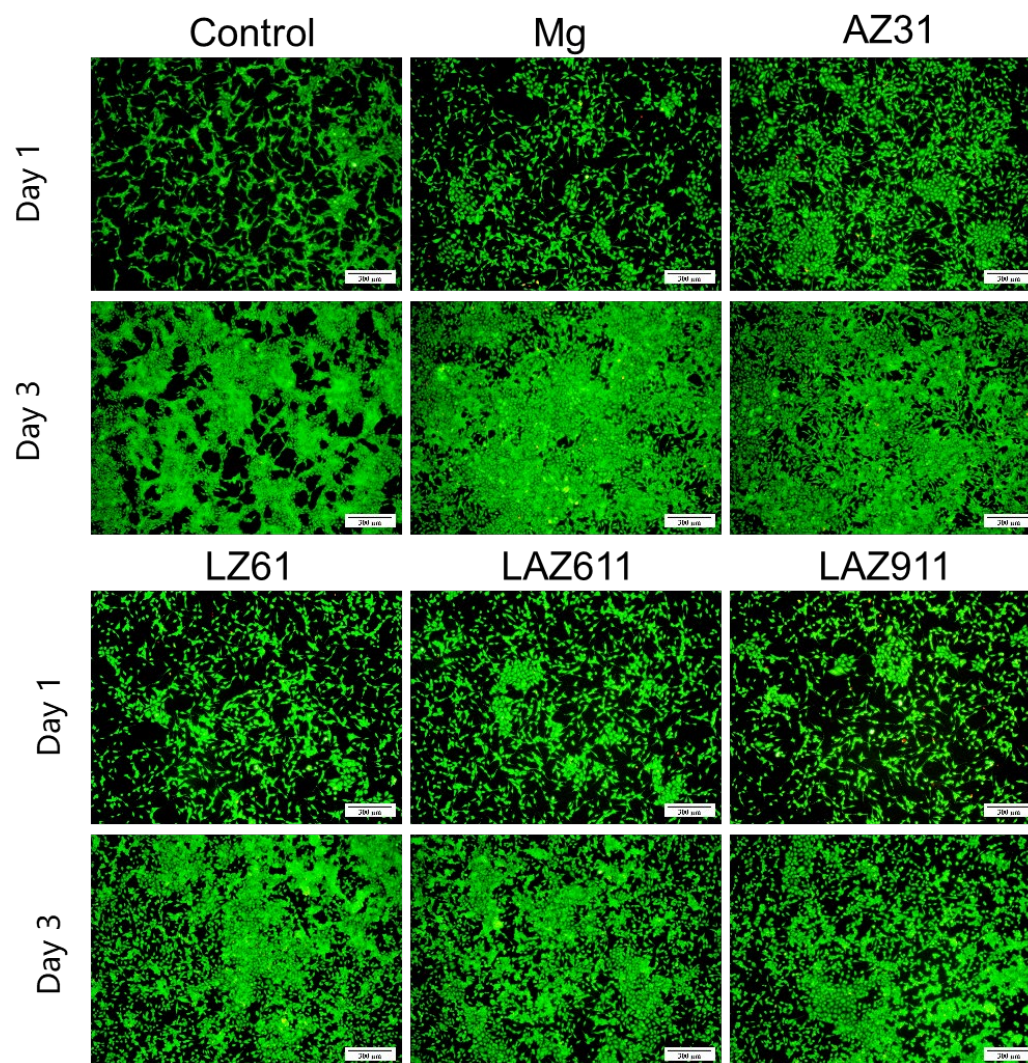
Figure 3.3. Live/dead staining of BEAS-2B cells after 3 days of culture in 25% extract or normal cell culture medium (control), scale bar = 300 µm.
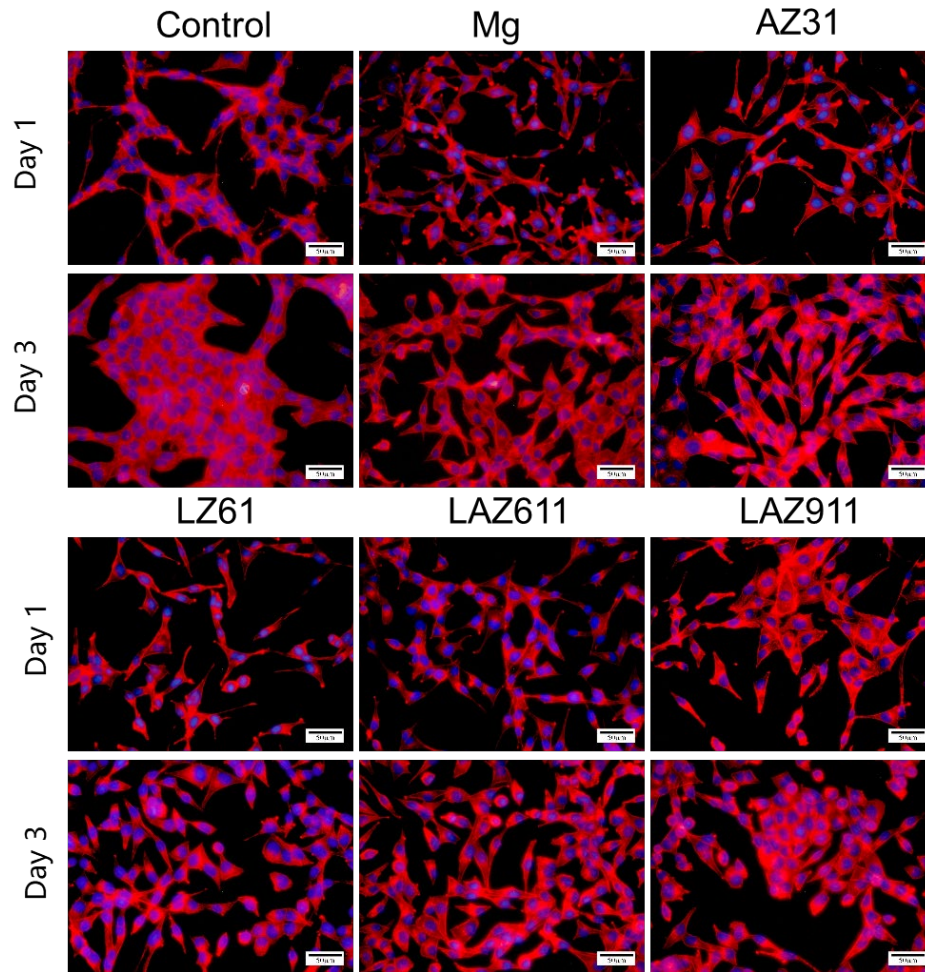
Figure 3.4. DAPI&F-actin staining of BEAS-2B cells after 3 days of culture in 25% extract or normal cell culture medium (control), scale bar = 50 μm.

The effect of degradation products on cell apoptosis and cell cycle were further investigated by culturing the cells in 25% extract for 24 hours. Results of the apoptosis assay were plotted in Figure 3.5. Despite the relatively large error, late stenosis rate showed no significantly difference among all groups ($p > 0.05$). As for early apoptosis rate, only LAZ911 showed lower rate than AZ31 alloy group. ($p < 0.05$) There is no statistically difference among all other groups. ($p > 0.05$). As depicted in Figure 3.6, the Mg-Li-Zn-(Al) alloy groups showed

dramatic difference when compared to control, pure Mg and AZ31 alloy groups. Significantly less BEAS-2B cells (p<0.05) were in G0/G1 phase for LZ61, LAZ611 and LAZ911 groups, while more BEAS-2B cells (p<0.05) were in G2/M phases. The difference in S phase were not as dramatic. Only LZ61 alloy group showed high percentage of cell than pure Mg and AZ31 alloy groups (p<0.05).
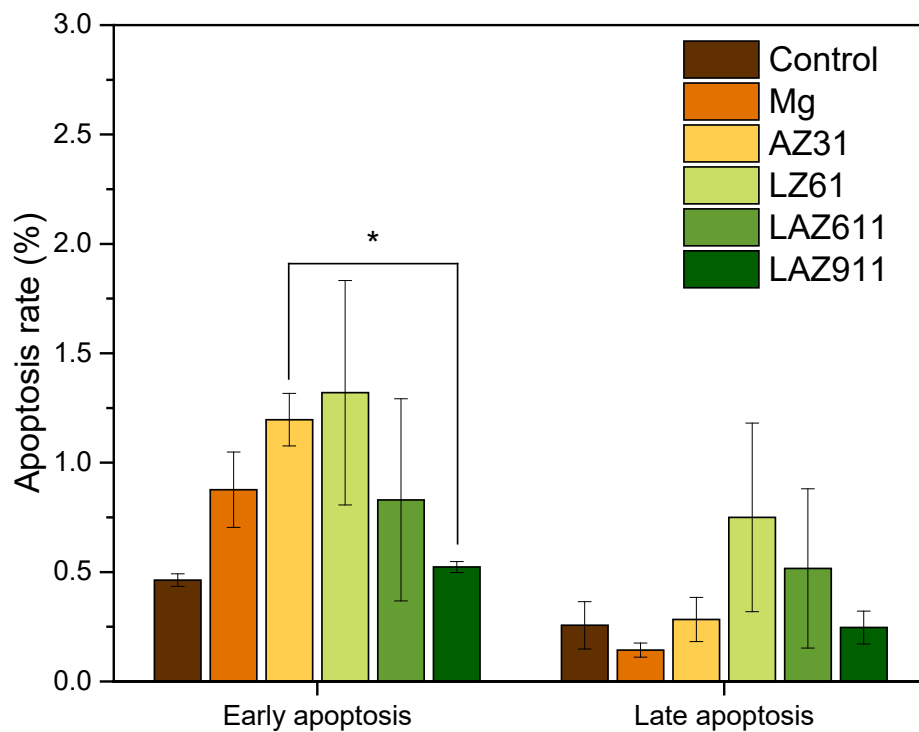
Figure 3.5. Early apoptosis and later apoptosis rate of BEAS-2B cells after culturing in 25% extract for 24 hours.

*denotes a significant difference between alloy groups (p < 0.05, n=3).
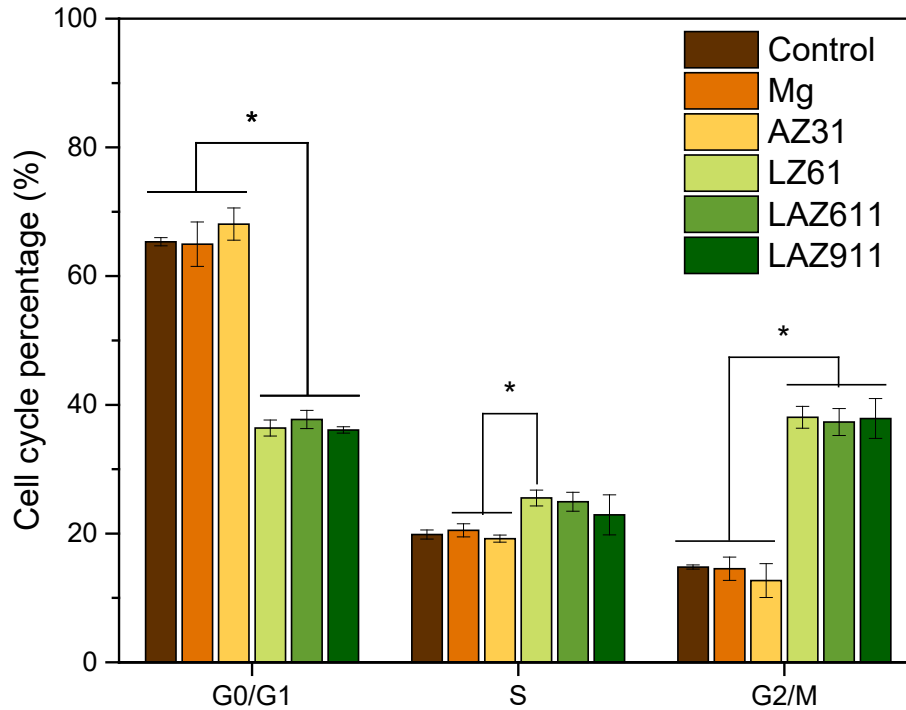
Figure 3.6. Percentage of BEAS-2B cells in at different cell cycle phase after culturing in 25% extract for 24 hours. *denotes a significant difference between alloy groups ($p < 0.05$, n=3).

3.3.2 Cytotoxicity of Mg^{2+} and Li^+

To further investigate if the impact of extract is caused by all the alloying element together or by certain single alloying elements, a series of MTT tests were performed using $MgCl_2$ and LiCl salts. Only Mg^{2+} and Li^+ were considered because the ICP results in Figure 3.1 showed that other elements such as Zn and Al were extremely low in the extract.

As shown in Figure 3.7, when BEAS-2B cell were cultured in BEGM dissolved with different concentration of $MgCl_2$. The darker region in the figure represent the concentration range of Mg^{2+} in the 100% extract based on Figure 3.1. When the Mg^{2+} concentration was lower

than the dark region, the BEAS-2B cell viability between day 1 and day 3 was very close. Cell viability rate was high reaching more than 100% when Mg^{2+} concentration is lower than 40mM. At the Mg^{2+} concentration higher than the dark region, cell viability at day 3 was lower than day 1. The cell viability at day 3 decreased to almost 0% when the Mg^{2+} concentration is higher than 80mM.

The BEAS-2B cell viability after culturing in different concentration of LiCl for 1 day and 3 days were plotted in Figure 3.8. Similar to Figure 3.7 the darker region in the figure represents the concentration range of Li^+ in the 100% extract based on Figure 3.1. Identical cell viability trend was observed again. However, the cell viability decreased sharply with increase in LiCl concentration especially for cell viability at day 3. Even at lower LiCl concentration, the cell viability was not able to reach 100%.
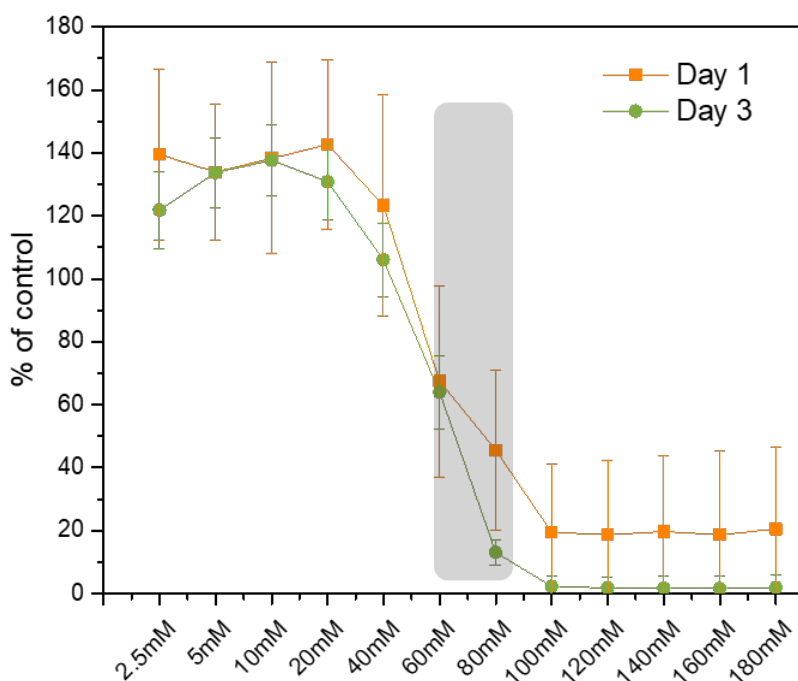
Figure 3.7. BEAS-2B cell viability after culturing in different concentration of MgCl$_2$ for 1 day and 3 days.

63
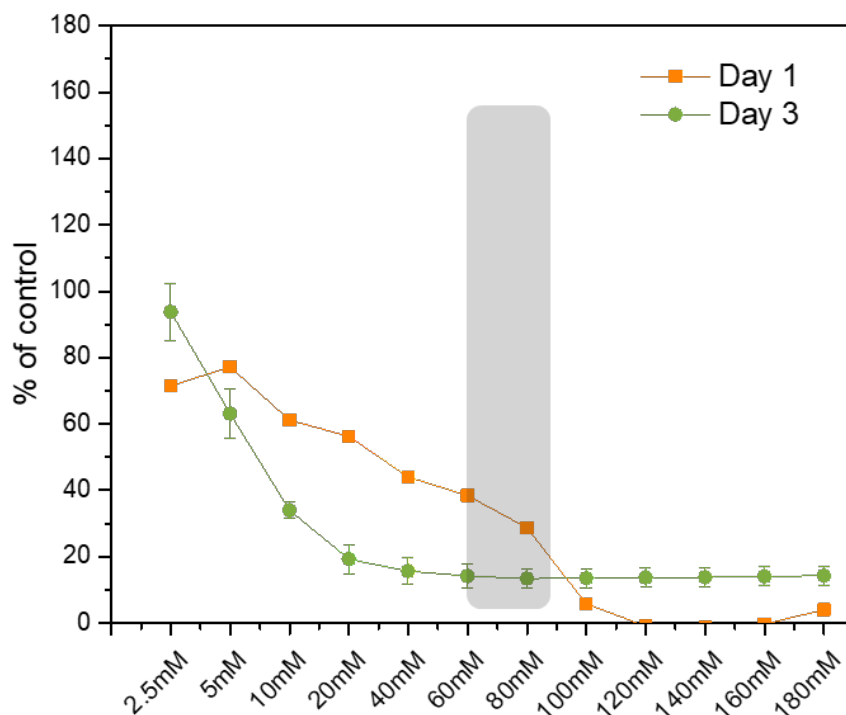
Figure 3.8. BEAS-2B cell viability after culturing in different concentration of LiCl for 1 day and 3 days.

The concentration of Mg and Li ions in Figure 3.1 were weight percentage (ppm), when converted the concentration to molarity, it's surprising to notice that the concentration Mg and Li ions were the very close when measured in molarity. Therefore, a mixture of 1:1 $MgCl_2$ and LiCl solution (molarity concentration) was then prepared and used for cell viability test. The results were plotted in Figure 3.9. The results of $MgCl_2$ and LiCl mixture were similar to LiCl alone (Figure 3.8) rather than $MgCl_2$ alone. Cell viability decreased sharply as the increase of ion concentration especially for day 3. The cell viability at the concentration of 100% extract or higher was close to 0%. At lower concentration (between 5mM and 60mM), the cell viability was acceptable (>50%) at day 1, but the dropped dramatically at day 3.
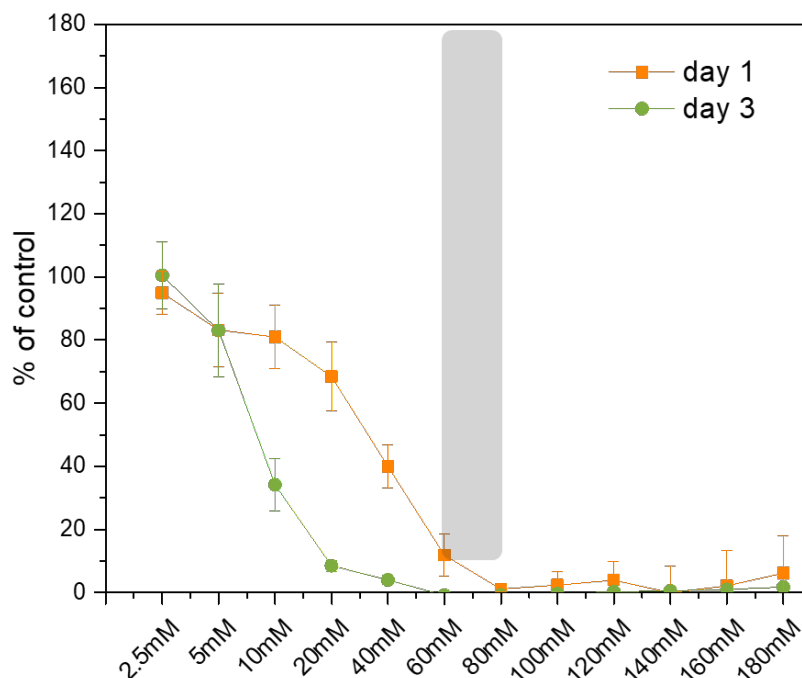
Figure 3.9. BEAS-2B cell viability after culturing in different concentration of $MgCl_2$ and LiCl solution for 1 day and 3 days. The molarity concentration of $MgCl_2$ and LiCl are the same (1:1 ratio).

3.4   DISCUSSION

When tracheal stent was implanted the tracheal epithelial cells were the major cell type that stent will interact with. BEAS-2B cells were selected because it was commonly used to evaluate the cytotoxicity of inhaled nanoparticles. [138-142]

Previous study [143] showed that cells exhibited low viability when directly seeded on Mg alloy surface. Therefore, in this study, all cytotoxicity tests were conducted in an indirect manner using the extract protocol. We first prepared extract following EN ISO standard 10993-

12:2004 and investigated the ion concentrations in the extract, since the ion concentration is positively correlated to the pH value and osmolality [144]. The degradation of Mg alloy indeed led to a burst release of metal ions. However, when the Mg alloy is *implanted in vivo*, the surrounding physiological environment provides a barrier against the dramatic release of ions. To better mimic the *in vivo* environment, the extract was further diluted into four different concentrations in the MTT assay. The MTT test indicated a lower cell viability in Mg-Li-Zn-(Al) alloy groups especially in day 1. Since the Live/Dead imaging result proved that BEAS-2B cells were constantly proliferating. The lower cell viability is could either caused by higher cell death rate or lower cell proliferation. To further investigate this, cell apoptosis and cell cycle assays were performed.

In our study, the accumulation of degradation product in the extract have relatively limited impact on cell apoptosis. When the result was compared to previously reported studies, we believe that the effect of extracts on the cell cycle also depends on the cell types. Some studies reported that Mg alloy extract caused an increase in the cell apoptosis rate when tested with different cell types [143, 145-147].

As for the impact of degradation product in the extract on cell cycle, Zhanhui Wang *et al*. reported that more intestinal epithelial cells were locked in the G1/G0 phase but less cells were present in the S phase. [148] In the present study, more BEAS-2B cells were arrested in G2/M phases different from the referenced study. However, the higher percentage of cells in the G2/M phase did not impact the percentage of cells in S phase. Again, we proved that the response to magnesium extract highly depends on the cell type. With these results, it seems that the low cell viability in the MTT test might have been caused by the slower cell proliferation due to the cells being locked in the G2/M phase.

Despite these effects discussed above, the cell morphology of BEAS-2B remained normal after culturing for 1 day or 3 days in 25% extract which indicates that the surviving cells might still function well.

The MTT results of the $MgCl_2$ and LiCl help us better understand the impact of alloying elements both individually and collectively. BEAS-2B cells exhibited tolerance of high Mg^{2+} concentration. The lower cell viability seems to be caused by Li ions. Wang *et al.* proved that LiCl inhibits vascular smooth muscle cells proliferation and migration [149]. This result implies that lower percentage of Li in Mg-Li-Zn-(Al) alloys could be beneficial to reduce the cytotoxicity of airway epithelium cells.

4.0 SPECIFIC AIM 3. EVALUATE THE BIOCOMPATIBILITY AND IN VIVO DEGRADATION OF THE MG-LI-ZN-(AL) ALLOYS IN MOUSE SUBCUTANEOUS MODEL

4.1 INTRODUCTION

Based on what we discussed in the previous chapter, it is indeed challenging to duplicate the *in vivo* condition or environment to evaluate biocompatibility of biomaterials *in vitro*. Many previous studies have shown the different results between *in vitro* and *in vivo*. [150] Therefore, *in vivo* testing is unavoidable for any biomaterial/device to be approved for clinical application. The ideal animal model for *in vivo* testing is based on the type of the device. For tracheal stents, the best *in vivo* model is to fabricate the tracheal stents and implant it into airway. But, it would be costly to evaluate all the six Mg-Li-Zn-(Al) alloys in that way and hence, a cost-efficient *in vivo* evaluation model is needed in this situation.

Mouse subcutaneous has been used in many previous studies on Mg alloys [97, 137, 151] and coatings[152-154]. This animal is easy to operate and much less expensive but is still capable of revealing many different aspects of magnesium corrosion *in vivo* that *in vitro* tests cannot offer.

The first advantage of mouse subcutaneous model is that it gives us a picture of how Mg-Li-Zn-(Al) alloys degrade *in vivo* when they are implanted as a medical device. This degradation

rate might be different from what we have calculated in specific aim 1. This difference has been noticed in many previous studies discussed elaborated in previous publications. [150, 155] There is obviously a need to develop a model to correlate the *in vitro* and *in vivo* degradation, so we would be able to predict the *in vivo* degradation rate of magnesium alloys based on the results of *in vitro* tests.

The second advantage of mouse subcutaneous model is that it offers us a way to measure the impact of H_2 gas released during the Mg-Li-Zn-(Al) alloys degradation. The effect of H_2 gas is commonly ignored when conducting *in vitro* cytotoxicity tests since the H_2 gas is hardly accumulated in the cell culture media. The mouse subcutaneous model offers us the opportunity to observe if the H_2 gas will be accumulated around the implanted Mg-Li-Zn-(Al) alloys and what's the pathological impact of the gas pocket formed subcutaneously. [156]

Last but not the least, we will be able to exam the tissue response surrounding the Mg-Li-Zn-(Al) alloys implant through histology and pathology analysis. The clearance pathway of magnesium alloy implant is currently unknown. It is generally accepted that the degradation of magnesium implant will follow the same human magnesium metabolism pathway which means that magnesium ions will be converted into soluble species in plasma, and cleared by kidney. [157] Thus the histological analysis of the key organ that might be impacted by the plasma magnesium will enable us to study if the implantation of magnesium alloy and the degradation product will lead to systematic toxicity.

In light of this, mouse subcutaneous model was considered in this specific aim to evaluate the Mg-Li-Zn-(Al) alloys *in vivo*. The goal of this specific aim is to (1) study is the *in vivo* degradation rate of the six Mg-Li-Zn-(Al) alloys, the release of H_2 gas and the formation of

H$_2$ gas pocket; (2) study the local toxicity and systematic toxicity of the Mg-Li-Zn-(Al) alloy implant.

4.2   MATERIALS AND METHODS

4.2.1   Sample preparation

Mg-Li-Zn-(Al) alloys, round plate samples (ϕ=5mm$\times$2mm) were sliced by lathe from the center of the extruded rods. All the samples were ground with SiC abrasive sandpapers up to 1200 grit. All the alloy disks were then sonicated in acetone and air dried. Before implantation, all the pellets were placed in 70% ethanol for 5 min, rinsed with Dulbecco's phosphate buffer saline (DPBS, KCl 2.7 mM, KH$_2$PO$_4$ 1.5 mM, NaCl 138 mM, Na$_2$HPO$_4$ anhydrous 8.1 mM, pH 7.0) and then irradiated under UV light allowing for 20 min exposure on each side of the discs.

4.2.2   Procedures for laboratory mice implantation

The implantation was performed at the University of Cincinnati in collaboration with Dr. Zhonghyun Dong. Specific pathogen-free female athymic nude mice were purchased from Harlan Laboratory (Indianapolis, IN) and used in the study when they were 8 to 10 weeks of age. The mice were maintained in a facility approved by the American Association for Accreditation of Laboratory Animal Care and in accordance with current regulations and standards of the U.S. Department of Agriculture, U.S. Department of Health and Human Services, and NIH. The

animal studies were approved by the Institutional Animal Care and Use Committee (IACUC) and executed according to the specific IACUC guidelines.

The alloy disks (6 sample/mouse type) were placed subcutaneously into the mice. For the surgery procedure, all the mice were anesthetized with isoflurane, sterilized, and a small skin incision was made to create a subcutaneous pocket on the back of the mouse. The Mg alloy disc was then inserted into the pocket, and the incision was closed with surgical staples (Autoclip, Clay Adama) which was subsequently removed following 2 weeks after the surgery. Mice were housed under controlled conditions and maintained with a standard diet and water.

Gas bubble was measured twice a week using calipers and the specific bubble volume (mm^3) was calculated according to the formula: (width^2 x length)/2, a formula that was routinely used in measurement of subcutaneous tumor volumes in mice.[158] Regular X-ray images were taken to confirm the position of the implants. The mice were accordingly weighed twice a week and sacrificed approximately at 4 and 12 weeks, respectively. The implants were weighed before and after implantation following which, the weight loss was calculated and converted to corrosion rate employing the same equation used to determine corrosion in the immersion test. The *in vivo* corrosion rates were then further compared with the *in vitro* corrosion rates.

4.2.3   H$_2$ measurement by amperometric H$_2$ sensor

Amperometric H$_2$ measurements were performed using a H$_2$ microsensor (H$_2$- 50, 50 μm tip diameter from Unisense, Aarhus, Denmark). The calibration and the appropriate conversion from the H$_2$ microsensor current to the specific concentration used was similar to previous work published by our collaborator Dr. William Heineman at the University of Cincinnati. [130, 159, 160]. For *in vivo* measurements, the anesthetized mice were immobilized on a heated swiveling

table. The microsensor was the appropriately positioned with a micromanipulator [130, 160]. Measurements were then taken by touching the sensor tip on the skin above the gas cavity near the implant area. The current obtained from the H_2 sensor was then converted to a regional H_2 concentration using a calibration curve generated from known levels of H_2 in water prepared by diluting the H_2 saturated water.

4.2.4 Histology analysis

For histological evaluation, the skin tissue adjacent to the implants and major organs were sampled, fixed in neutral buffered 4% formalin solution, embedded in paraffin, sectioned (4 µm), and stained accordingly with hemotoxylin and eosin (H&E).

4.2.5 Statistical Analysis

The obtained results were expressed as the mean ± standard deviation. One-way ANOVA was conducted to determine the differences between different groups of samples with Bonferroni Procedure as post hoc test. Statistical significance was defined as $p < 0.05$. Statistical analysis was performed utilizing the IBM SPSS Statistics 23 package for Windows.

4.3 RESULTS

4.3.1 *In vivo* degradation of Mg-Li-Zn alloy in mouse subcutaneous model

As shown in Figure 4.1, the implants were visible up to 12 weeks of implantation for all the alloys indicating a promising low degradation rate for stent application. The weight loss of each sample was measured before and after the implantation (with the remaining tissue on the surface removed), and then converted in to *in vivo* corrosion rate (Figure 4.2). The order of average corrosion rate at week 4 is LZ61 < AZ31 < LAZ631 < pure Mg < LAZ611 < LAZ931 < LAZ911 < LZ91. As we can see, after 4 weeks of implantation, LZ91 alloy showed the highest corrosion rate of 0.70 mm/year. *In vitro* immersion test showed that LAZ631 alloy showed the highest corrosion rate, whereas *in vivo* corrosion rate was relatively low. It is worth mentioning here that LZ61 exhibited the lowest corrosion rate of 0.06 mm/year at week 4, demonstrating promising stability following implantation. One-way ANOVA results showed that LZ91 alloy corroded significantly faster than all the other alloys (P<0.05), while there is not significantly different among the rest of the groups.
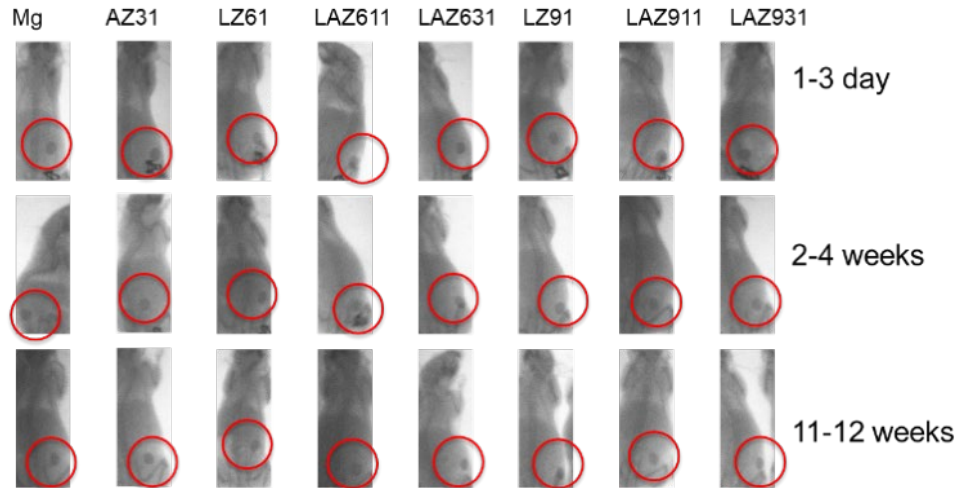
Figure 4.1. X-ray images of the implanted Mg-Li-Zn-(Al) implants in mouse at different time of implantation.

After 12 weeks of immersion, the new order of average corrosion rate is AZ31 < LZ61< pure Mg < LAZ631 < LAZ911 < LAZ611 < LZ91 < LAZ931. Even though the order changed significantly when compared to the order at week 4, the top 4 lowest corroding alloys still remained the same, namely AZ31, LZ61, pure Mg and LAZ631. AZ31 was the most corrosion resistant alloy, but LZ61 alloy still exhibited corrosion rate similar to AZ31. For the other four faster corroding alloys, the corrosion rate of LZ91 alloy decreased considerably compared to the first 4 weeks leaving LAZ931 alloy the fastest corroding alloy. One-way ANOVA results showed that LZ61 and LAZ631 alloy did not show non-significant degradation rate to pure Mg and AZ31 ($P>0.05$). The other four alloys, LAZ611, LZ91, LAZ911 and LAZ931 all corroded significantly faster than AZ31 ($P<0.05$). On the other hand, LZ91and LAZ931 corroded significantly faster than LZ61 alloys ($P<0.05$).
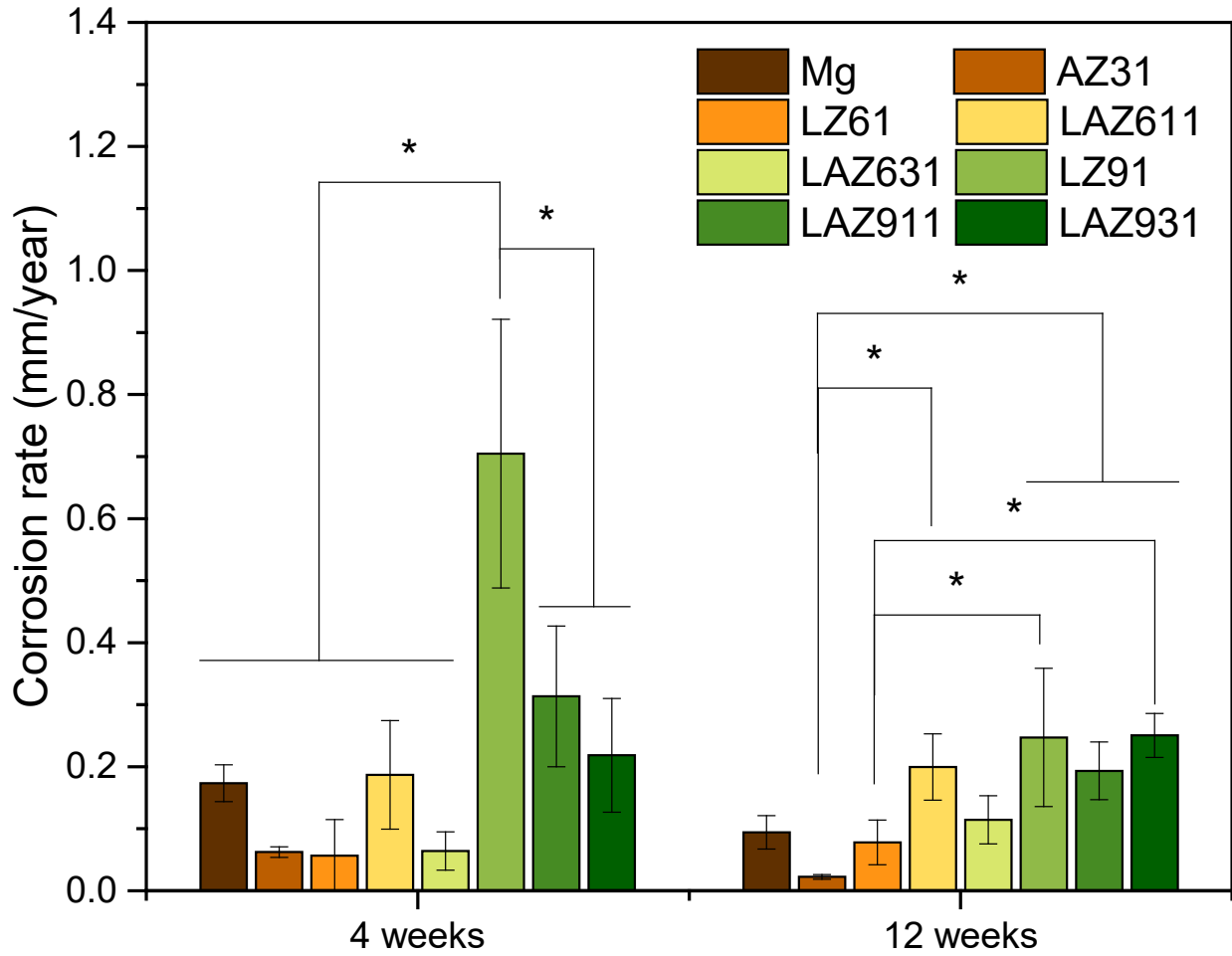
Figure 4.2. *In vivo* corrosion rate of Mg-Li-Zn-(Al) at 4 weeks and 12 weeks calculated based on weight loss.

*denotes a significant difference between alloy groups (p <0.05, n=3).
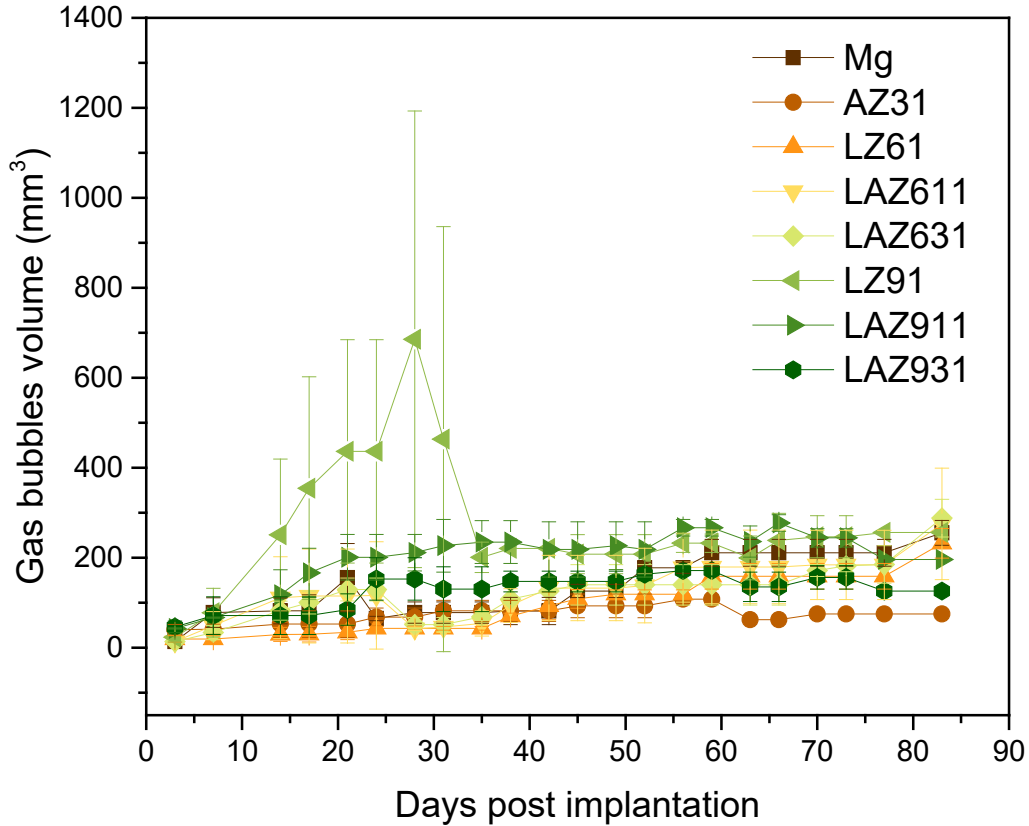
Figure 4.3. The size of H_2 gas bubbles accumulated subcutaneously during the 12-week implantation in mice.

The formation of gas cavities is another concern of magnesium implant. [161] The main source of gas formation in Mg alloys is the degradation process of the magnesium implant depending on the metal composition and surface area. In the subcutaneous model, Heineman and Witte have demonstrated that the gas cavities will slowly be absorbed by diffusing through the skin as well as the capillaries and transported by the vascular system.[162] The sizes of the gas cavities were measured to qualitatively correlate and assess the biodegradation rate of all of these six Mg-Li-Zn-(Al) alloys *in vivo*. As seen in Figure 4.3, there was a burst release of H_2 gas for LZ91 alloys in the first 4 weeks of implantation, and the gas cavity in mice bearing LZ91 increases during the first 4 weeks, reaching a maximum size of 685 ± 507 mm^3 (n=6) by 4 weeks

after implantation. The volume of the gas cavity is much smaller after 4 weeks when the alloy was stabilized. This result is in line with the corrosion rate calculated based on the weight loss. The variation of the volume of the gas cavity was stable for the rest the alloy groups after the initial increase during the first 2-3 weeks of implantation. LZ61 exhibited the smallest size of the gas cavity in the first few weeks, indicating the slowest corrosion rate. The size of the gas cavity for the AZ31 alloy was the smallest during the later stage of the implantation when compared to all the Mg-Li-ZN-(Al) alloys and pure Mg which suggests that the biodegradation rate for AZ31 is the lowest among the groups studied herein. However, the size of gas cavity is not exactly in line with the corrosion rate calculated based on weight loss. For example, LAZ911 and LAZ931 exhibited relatively small gas cavity size compared to the rest of Mg-Li-Zn-(Al) alloys even though the corrosion rates of these two alloys were not the lowest among all the six Mg-Li-Zn-(Al) alloys.

Earlier studies from our collaborator, Dr. William Heineman's lab, showed that measurements of H_2 release from the biodegrading Mg implanted subcutaneously in mice obtained non-invasively by just pressing the tip of an amperometric H_2 sensor against the skin covering the implant were similar to those made invasively by inserting the sensor tip inside the cavity [130]. Subsequent research showed the effectiveness of the transdermal H_2 measurements in studying Mg alloys with different corrosion rates [159, 160, 163, 164]. Herein therefore, we used the transdermal measurement of H_2 from six biodegradable alloys implanted subcutaneously in mice with the electrochemical H_2 sensor. The transdermal H_2 sensing was first explored using LZ91 alloy which corrodes fast enough to create enough H_2 gas to form visible gas cavities. The H_2 microsensor tip was positioned directly on the gas cavity that surrounds the implants to obtain each measurement. As shown in Figure 4.4, pure Mg, AZ31, LZ61 and

LAZ631 were the four alloys showing lower H_2 readings. H_2 concentrations of 70 ± 20 μM, 138 ± 44 μM, 80 ± 18 μM, and 36 ± 18 μM were obtained for LZ61, LAZ631, pure Mg and AZ31 under the same condition, respectively. Similarly, LAZ611, LZ91, LAZ911 and LAZ931 were the four alloys showing higher H_2 readings. H_2 concentration is 368 ± 45 μM for the LZ91 alloy after 1-week implantation the highest reading among all the groups. H_2 concentrations of 289 ± 35 μM, 369 ± 45 μM, 301 ± 40 μM, 323 ± 43 μM were obtained for LAZ611, LZ91, LAZ911 and LAZ931 alloy groups. Error bars are standard deviation for measurement made on three mice (n=3). As expected, the higher corroding alloys produce more H_2. The H_2 concentration at the center of the gas cavity is in the order of LZ91 > LAZ931 > LAZ911 > LAZ611 > LAZ631 > pure Mg > LZ61 > AZ31. One-way ANOVA results showed that H_2 concentrations of pure Mg, AZ31, LZ61 and LAZ631 were significantly lower than the H_2 concentrations of LAZ611, LZ91, LAZ911 and LAZ931 (P<0.05).
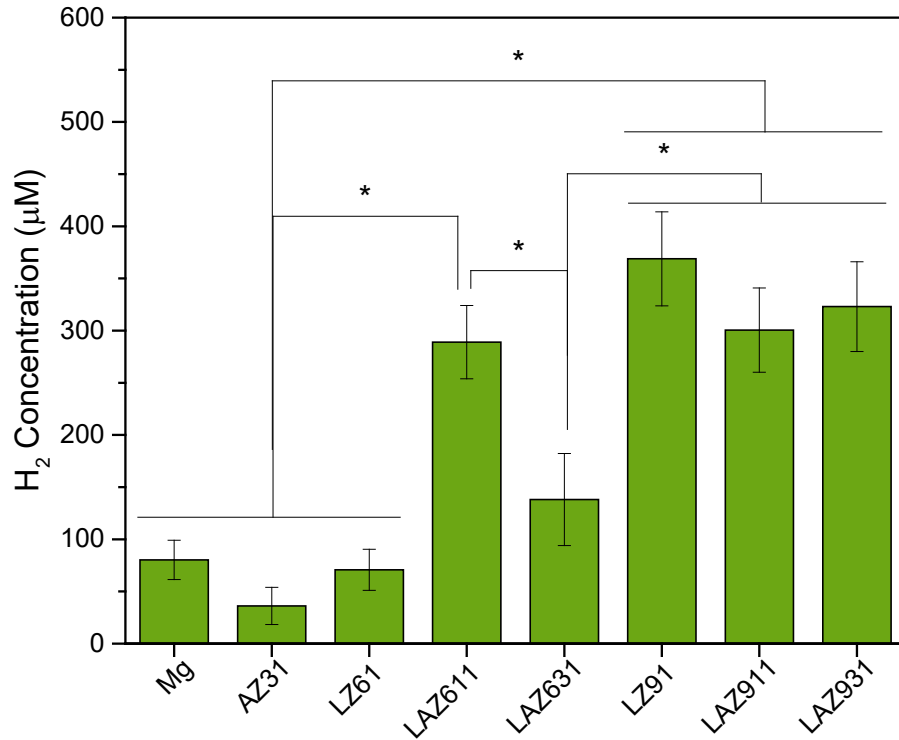
Figure 4.4. H_2 concentration measured on anaesthetized nude mice with AZ31, pure Mg, and six Mg-Li-Zn-(Al) alloy implanted subcutaneously 1 week after implantation; *denotes a significant difference between alloy groups (p <0.05, n=3)).

4.3.2   H&E study of the biodegradation of these alloys

Histology analysis were further conducted to assess the local toxicity and systemic toxicity of the metal itself, the degradation process, and the degradation products. The mice implanted with six Mg-Li-Zn-(Al) alloys, pure Mg and AZ31 alloy were accordingly sacrificed at 12 weeks following surgery. Eight organs (skin, lung, brain, heart, intestine, kidney, liver, and spleen) were prepared into the specific pathological sections and were stained with hematoxylin and eosin. The corresponding histological images obtained are shown in Figure 4.5.

Figure 4.5 shows the histological images of the surrounding tissues of the magnesium alloy implants. No significant macrophage infiltration was observed in the tissue surrounding the implant site indicating no inflammatory response to the Mg-Li-Zn-(Al) alloys as well as pure Mg and AZ31. Other major organs that are involved in the metabolic clearance of Mg^{2+} also did not exhibit any noticeable abnormality. The H&E staining image of the kidney tissue (Figure 4.6) obtained in all the experimental groups show clear and healthy epithelial cell structure without any signs of distortion or congestion as well as particle degeneration and necrosis. No infiltration of inflammatory cells is also observed. Liver sections (Figure 4.7) clearly show healthy hepatic lobule as well as uniform cytoplasm which are arranged in a normal pattern. Spleen sections (Figure 4.8) also show clear red and white pulp without any capsule thickening and signs of possible inflammatory response. Other organs, namely lung (Figure 4.9), heart (Figure 4.10), brain (Figure 4.11), and intestine (Figure 4.12) were also studied with H&E staining. The stained tissue samples clearly indicate no abnormality or any noticeable biocompatibility issues in all of the above organs analyzed. The H&E stains shows that there is no apparent pathological alteration in any of the tissue obtained from the experimental animals.
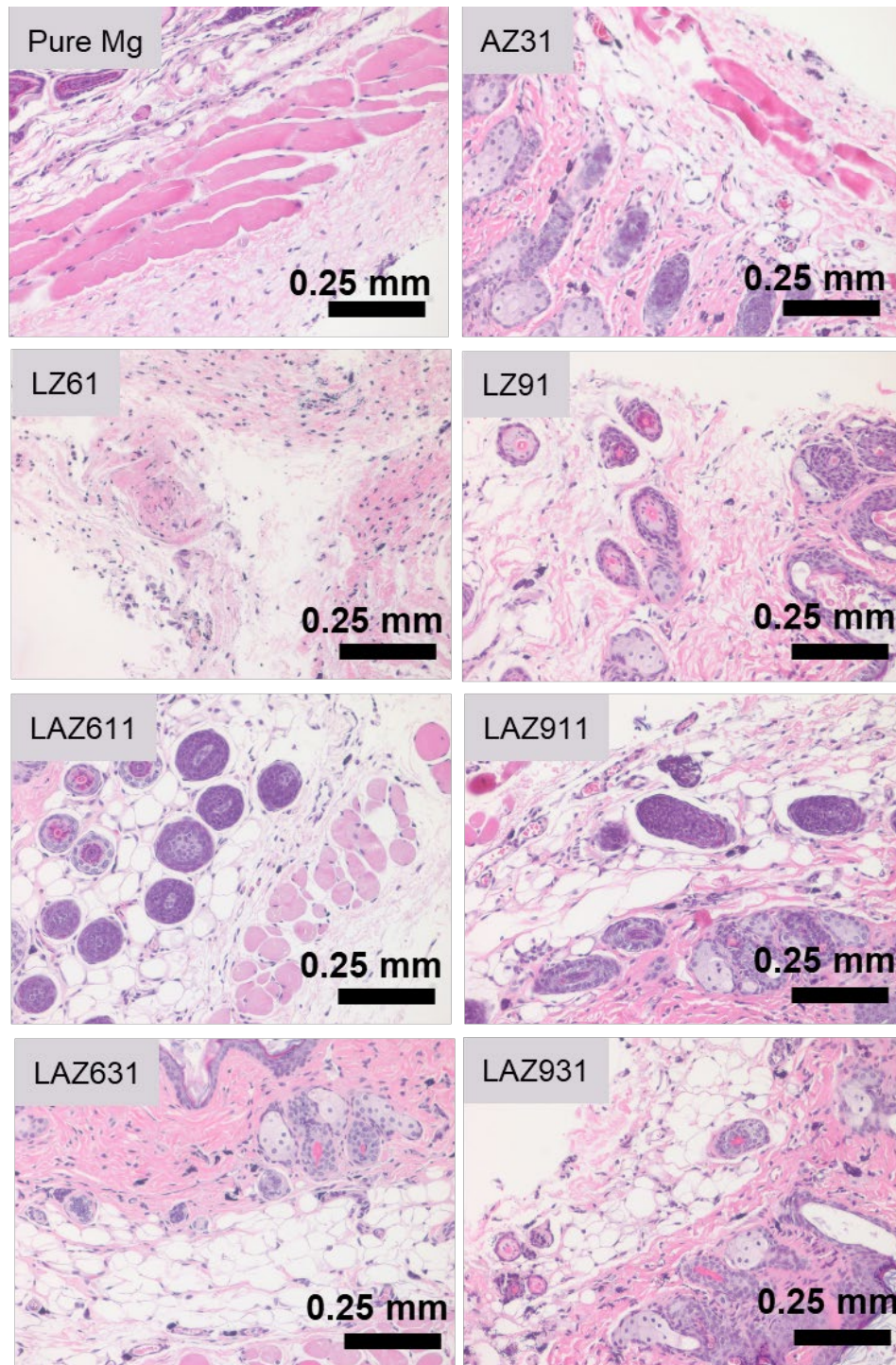
Figure 4.5. H&E staining of the issue surrounding the Mg-Li-Zn-(Al) implants 12 weeks of implantation (scale bar

= 0.25 mm).
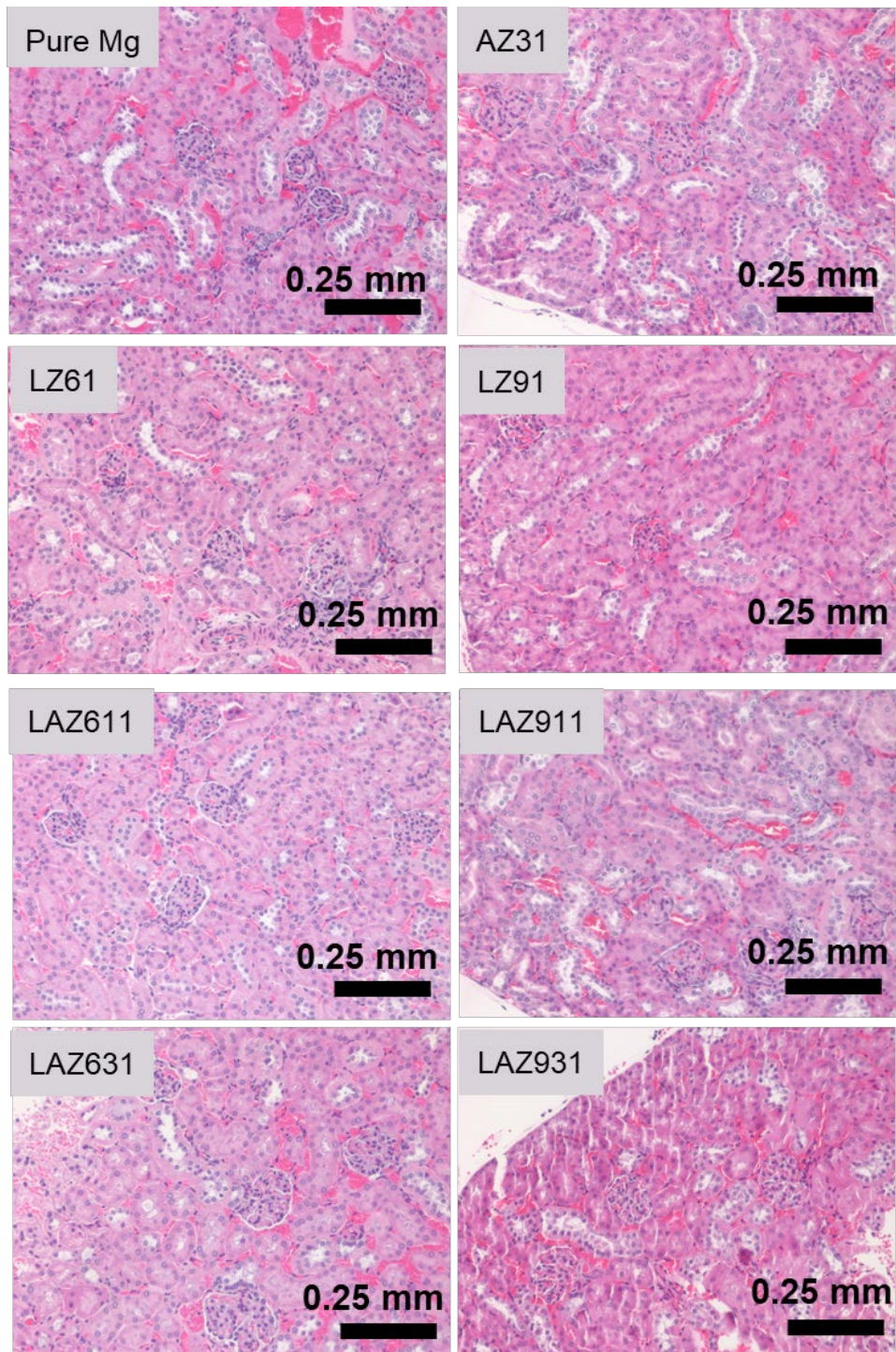
Figure 4.6. H&E staining of the kidney tissue of the mice implanted with the Mg-Li-Zn-(Al) alloy for 12 weeks
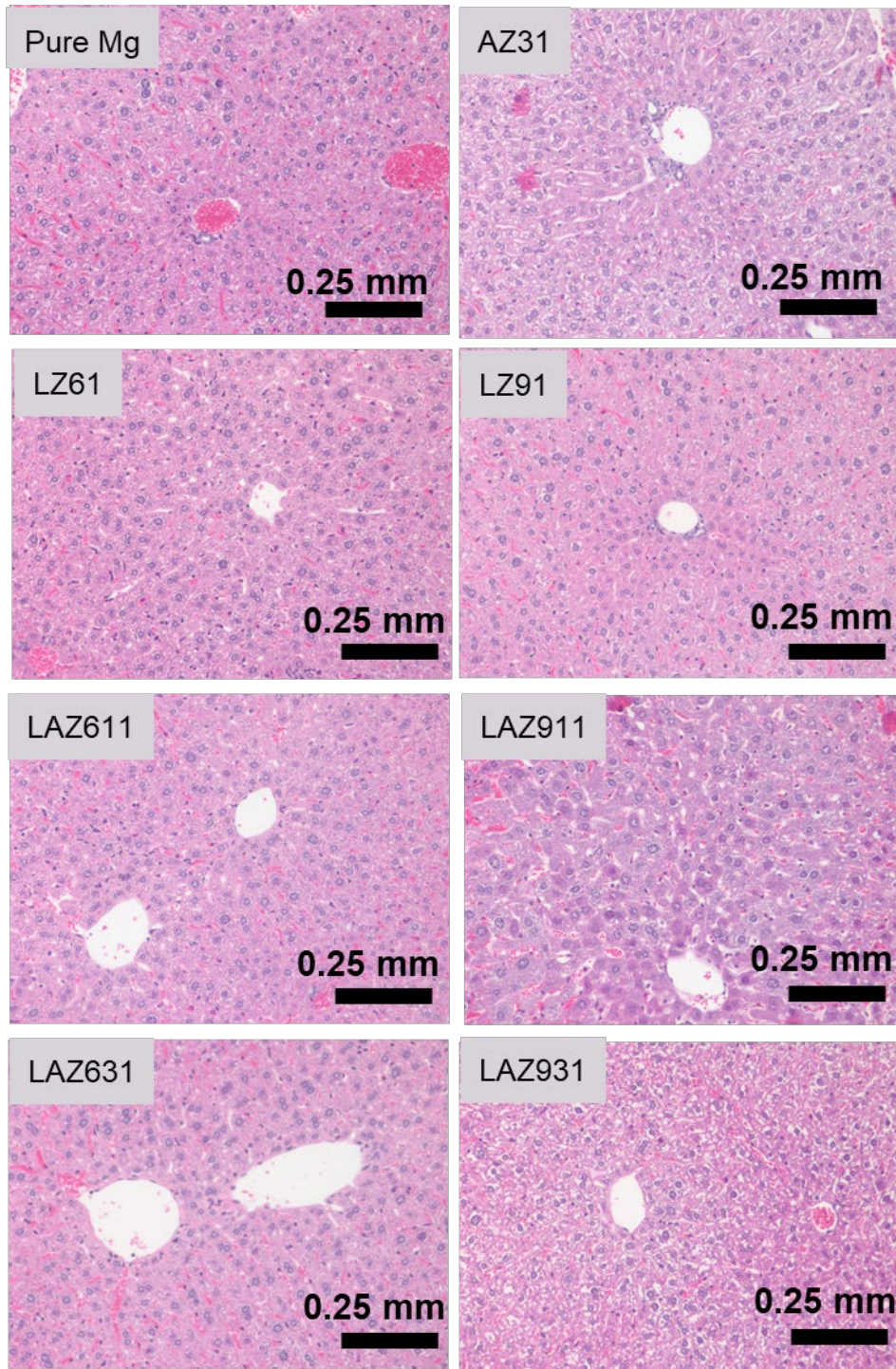
(scale bar = 0.25 mm).

Figure 4.7. H&E staining of the liver tissue of the mice implanted with the Mg-Li-Zn-(Al) alloy for 12 weeks (scale bar = 0.25 mm).
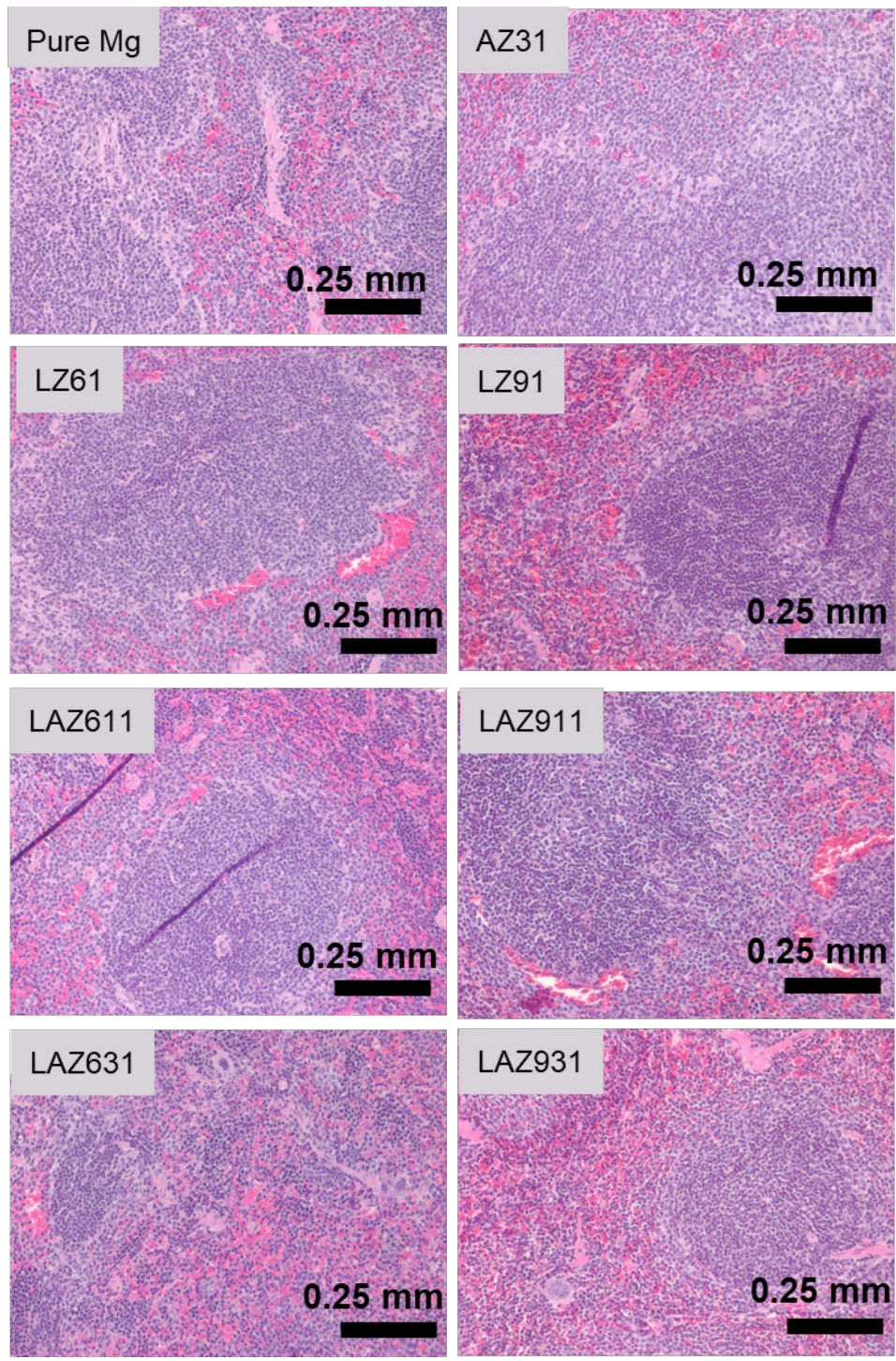
Figure 4.8. H&E staining of the spleen tissue of the mice implanted with the Mg-Li-Zn-(Al) alloy for 12 weeks
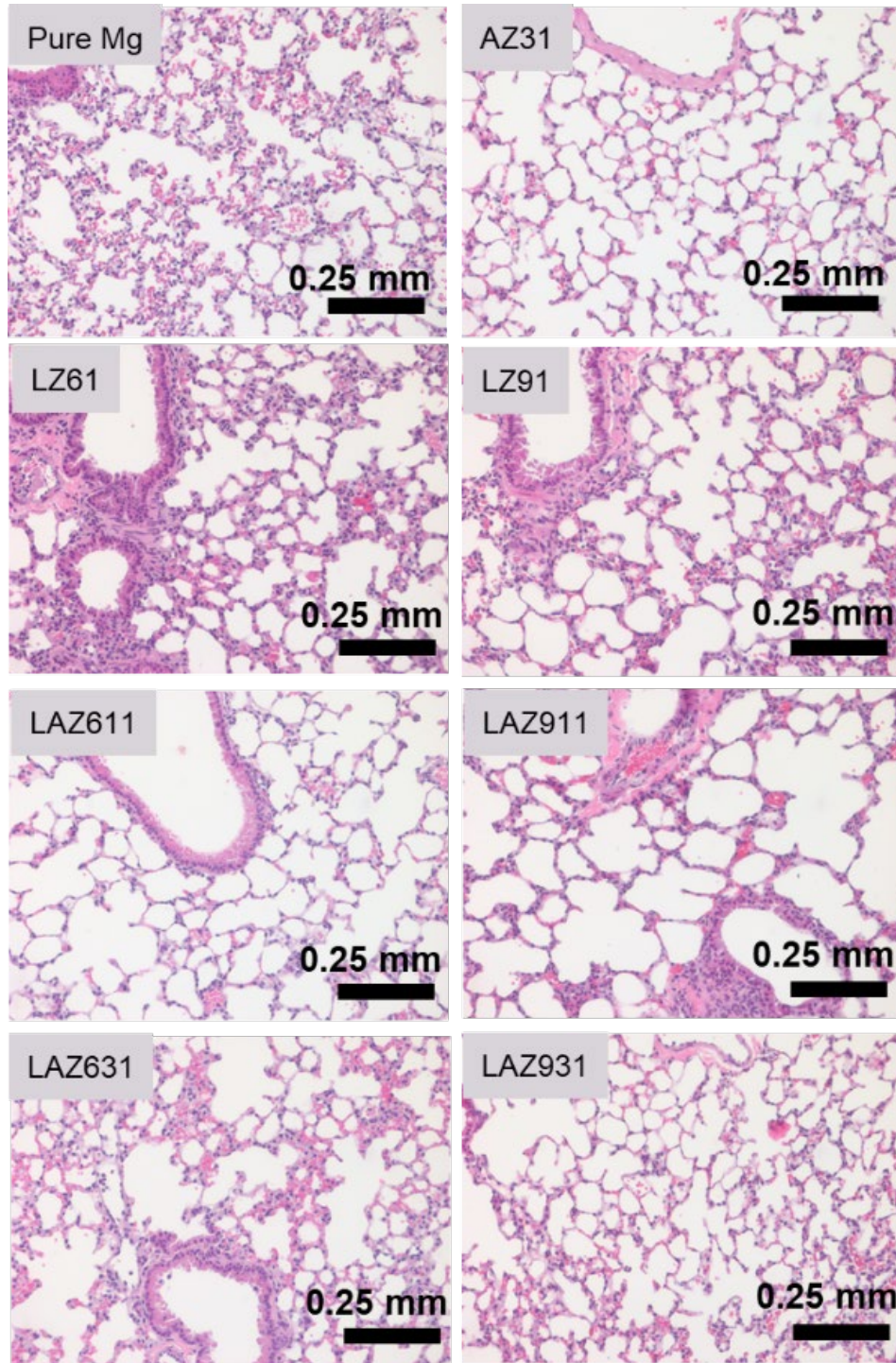
(scale bar = 0.25 mm).

Figure 4.9. H&E staining of the lung tissue of the mice implanted with the Mg-Li-Zn-(Al) alloy for 12 weeks (scale bar = 0.25 mm).
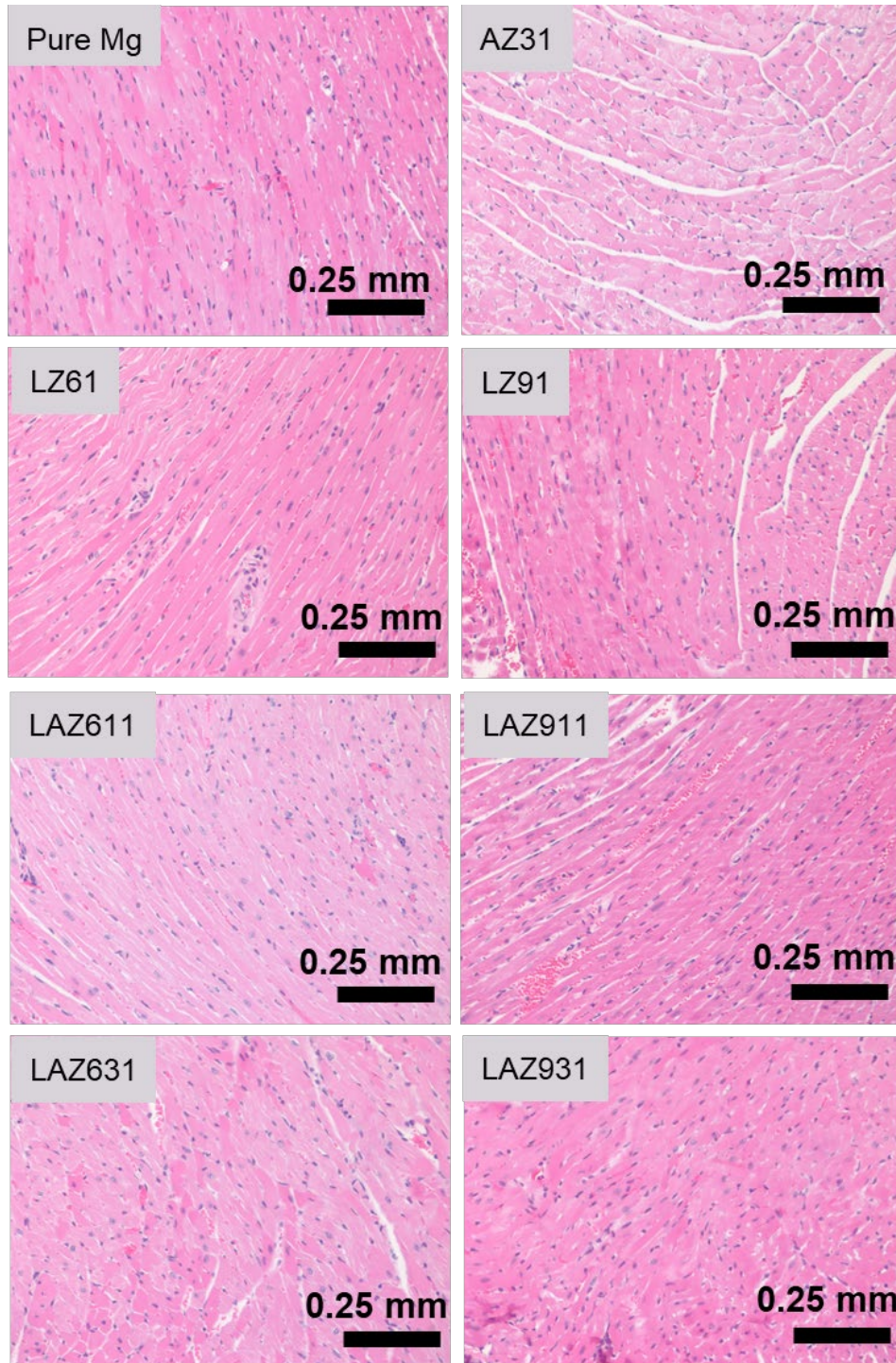
Figure 4.10. H&E staining of the heart tissue of the mice implanted with the Mg-Li-Zn-(Al) alloy for 12 weeks
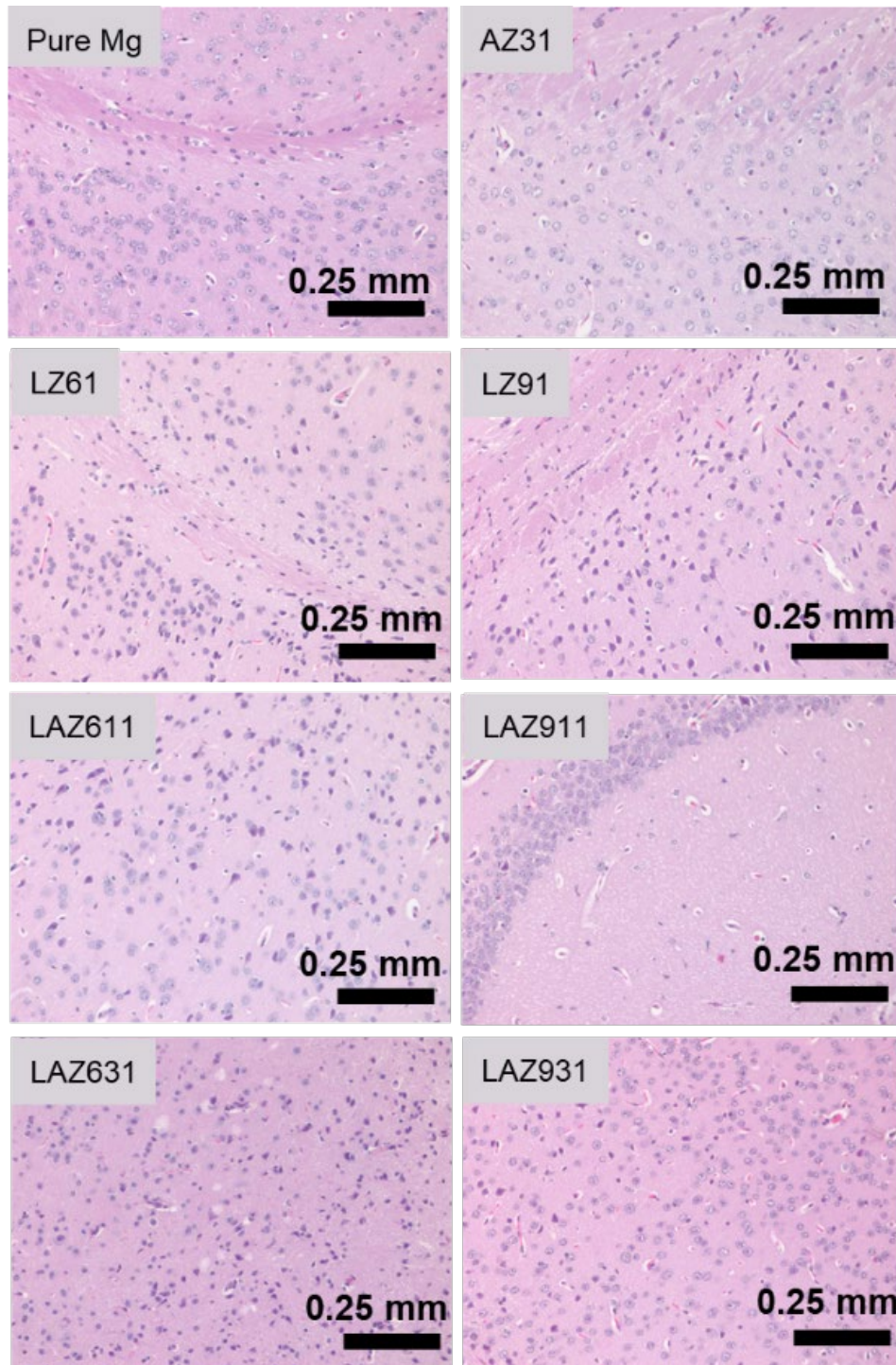
(scale bar = 0.25 mm).

Figure 4.11. H&E staining of the brain tissue of the mice implanted with the Mg-Li-Zn-(Al) alloy for 12 weeks
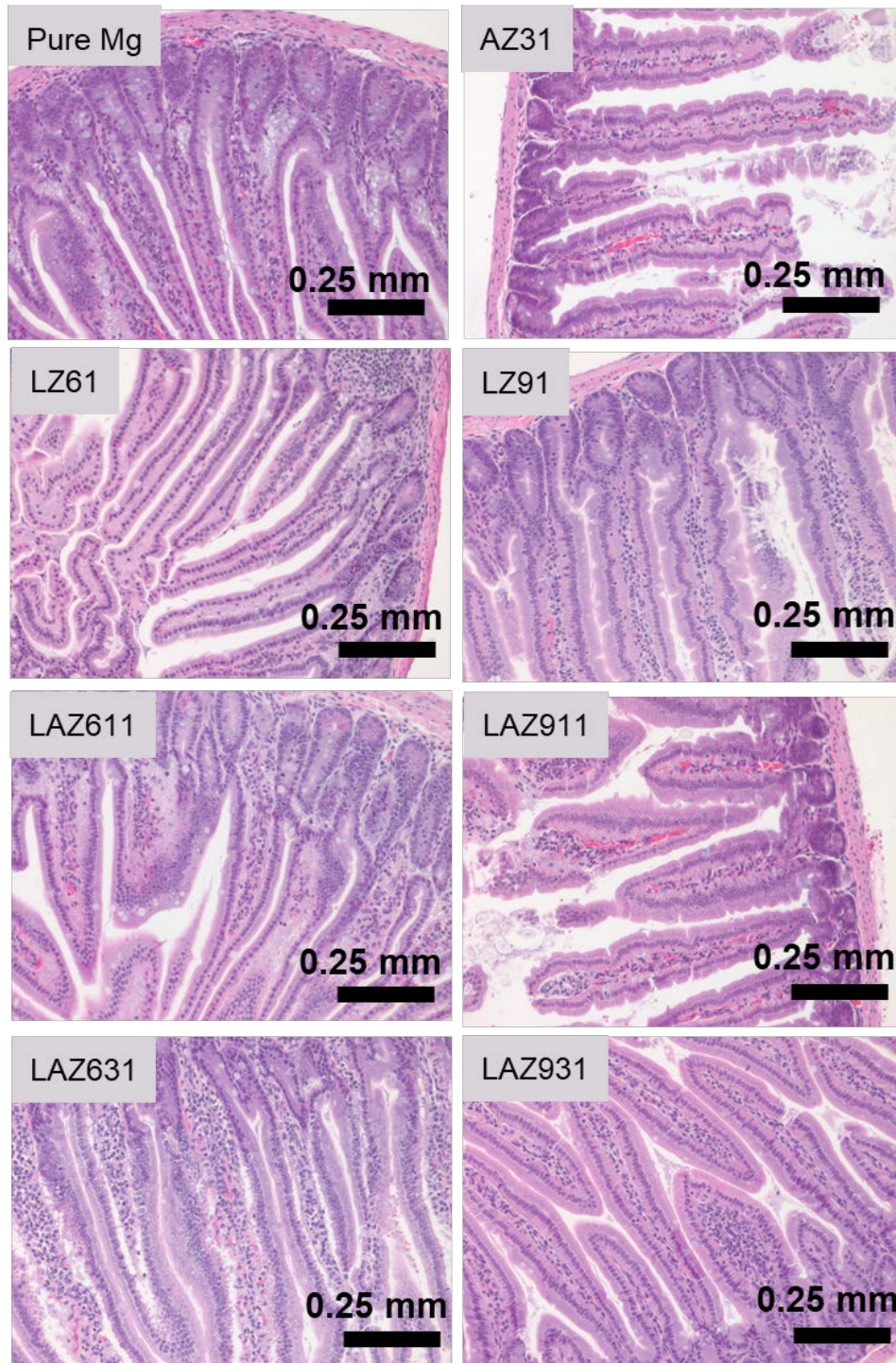
(scale bar = 0.25 mm).

Figure 4.12. H&E staining of the intestine tissue of the mice implanted with the Mg-Li-Zn-(Al) alloy for 12 weeks (scale bar = 0.25 mm).

4.4 DISCUSSION

Thus far, to the best of our knowledge, there is no *in vivo* study of magnesium alloy based tracheal stent reported in the literature. Most of the previous research has been focusing on magnesium alloy based vascular stents. The most clinically relevant animal model for studying the biodegradation of magnesium in a vascular environment is the porcine animal model [165-167]. Some study also reported using the rabbit abdominal aorta model [143]. Pierson *et al.* on the other hand, proposed a simplified *in vivo* model by implanting magnesium alloy wire into the rat abdominal aorta wall or lumen to mimic the conditions of stent implantation [168]. However, these animal models are relatively complicated and less cost-efficient for early stage *in vivo* evaluation. Therefore, to obtain an initial *in vivo* assessment, the *in vivo* degradation behavior and biocompatibility of the Mg-Li-Zn-(Al) alloys was studied herein in a simple mouse subcutaneous model.

In this specific aim, the *in vivo* corrosion rates of Mg-Li-Zn-(Al) alloys were measured through three different methods: weight loss, H_2 gas cavity size and H_2 measurement by amperometric H_2 sensor. It is expected that different measurement will exhibit different corrosion rate of the Mg-Li-Zn-(Al) alloys, but we still see similar trends among these three different measurement methods. In general, pure Mg, AZ31, LZ61 and LAZ631 were the four alloys that degraded slower than the rest of the four alloys, LAZ611, LZ91, LAZ911 and LAZ931. H_2 measurement by amperometric H_2 sensor also clearly showed the statistical difference between these two groups (pure Mg, AZ31, LZ61 and LAZ631 vs. LAZ611, LZ91, LAZ911 and LAZ931). This result was however, different from what was observed in the *in vitro* immersion test in HBSS solution. The *in vitro* test indicated that pure Mg, AZ31, LZ61, LAZ611 and LAZ911 were the alloys that exhibited non-significant difference in degradation

rate after 5 weeks of immersion in HBSS and were also much slower than the rest of Mg-Li-Zn-(Al) alloys, namely LAZ631, LZ91 and LAZ931. LAZ611, LAZ631 and LAZ911 are the three alloys that showed dramatically different corrosion rates *in vivo* compared to *in vitro* tests. Thus, either the alloys corroded faster *in vitro* (LZ611, LAZ631) or corroded faster *in vivo* (LAZ911). At the current stage, there is no mathematical model that can be used to correlate the corrosion rate *in vivo* and *in vitro*. [155] The degradation rate is largely dependent on the testing method, time and external environments. In general, the corrosion rate is slower *in vivo* than *in vitro* based on the published review. [155] This is the case for most of the Mg-Li-Zn-(Al) alloys except for LAZ611 and LAZ911 alloys. Previous studies reported have also shown that the *in vivo* and *in vitro* corrosion rates of Mg alloys tend to be conflicted with the results sometimes being totally different or even opposite [150, 169]

Table 4.1. Summary of corrosion rates of pure Mg, AZ31, and Mg-Li-Zn-(Al)1alloys determined by immersion test, electrochemical test and *in vivo* study.

	In vitro (mm/year)		*In vivo* (mm/year)	
	Immersion test (5 weeks)	Electrochemical test	4 weeks	12 weeks
Pure Mg	0.117±0.035	0.025 ± 0.008	0.173±0.030	0.094±0.027
AZ31	0.099±0.009	0.035 ± 0.002	0.062±0.009	0.022±0.004
LZ61	0.142±0.025	0.042 ± 0.020	0.057±0.058	0.078±0.036
LAZ611	0.143±0.020	0.015 ± 0.001	0.187±0.088	0.199±0.053
LAZ631	0.936±0.122	1.565 ± 0.114	0.064±0.031	0.114±0.039
LZ91	0.388±0.075	0.158 ± 0.013	0.705±0.216	0.247±0.111
LAZ911	0.142±0.032	0.016 ± 0.004	0.313±0.113	0.193±0.047
LAZ931	0.507±0.068	0.300 ± 0.117	0.218±0.092	0.250±0.035

Table 4.1 summaries all the corrosion rates obtained by different methods, LZ61 alloy was the only alloy that demonstrated low corrosion rate both *in vivo* and *in vitro*. The consistent corrosion rates of LZ61 obtained and observed in the present study conducted herein might imply that the corrosion mechanism is less prone to be susceptible to the surrounding environment, and the alloy probably goes through similar corrosion mechanisms under both *in vitro* and *in vivo* conditions.

Our H&E analysis also showed that there were no substantial signs of necrosis, expansion, inflammation, swelling, encapsulation, hemorrhage, or any perceived discoloration of the key organs nor at the implant site. The histological analyses also indicate that addition of Li element into these alloys and their varying corrosion rate did not introduce any semblance of encapsulation, toxicity, necrosis, hemorrhage, discoloration or excessive inflammatory response to the surrounding tissue. These results taken in total indicate that the Mg-Li-Zn-(Al) alloys all showed good biocompatibility when assessed in the 8 animal organs harvested at the end of the 3 months. It can be safely inferred based on the results reported herein that the alloys implanted in the animals at the early stage can be indeed considered to be biologically safe and the experimental animals tolerated the degradation products generated by these alloys. Similarly, previous study also demonstrated that no biocompatibility issue was caused by AZ31 after 2 months implantation under similar conditions [170].

The current assessment thus, elucidates the potential of the new ultra-high ductility Mg-Li-Zn-(Al) alloys for possible tracheal stent application applications, especially for LZ61 alloy which demonstrated the consistent low corrosion rate both *in vitro* and *in vivo*.

5.0 SPECIFIC AIM 4. VALIDATE THE FEASIBILITY OF PROTOTYPE MG-LI ALLOY STENTS IN RABBIT AIRWAY MODEL

5.1 INTRODUCTION

Based on the results from specific aim 1 to specific aim 3, Mg-Li-Zn-(Al) alloys demonstrated the potential for the application of tracheal stent. Figure 5.1 showed how alloys performed in each of the past specific aims. The *in vitro* characterization (specific aim 1) showed LZ61, LAZ611 and LAZ911 were the overall best alloys due to low corrosion rate and significantly higher ductility. The cytotoxicity tests in specific aim 2 indicating acceptable cell viability for all the Mg-Li-Zn-(Al) alloy tested. However, the cell proliferation was inhibited due to the G2/M phase arrest. The study of Mg and Li salts indicating that this effect was caused by the Li^+. Thus, a lower Li percentage in the alloy will improve the cell viability. The result of the *in vivo* tests in specific aim 3 indicates that pure Mg, AZ31, LZ61 and LAZ631 alloys corroded slower and were biocompatible. LZ61 was the only alloy that performed among the best in all the tests. Thus, LZ61 alloy was selected for the stent prototyping and evaluation.

The first step of this specific aim was to fabricate LZ61 tracheal stents. Since LZ61 tracheal stent was designed as a balloon expandable stents rather than self-expandable stents, the manufacture steps of traditional 316L stainless steel stent was followed to fabricate LZ61 stents.

The first step of stent manufacturing is mini-tube fabrication. The traditional way is tube extrusion and drawing, many previous studies have shown this process of producing the mini-tubes. [101-103, 171-174] However, due the limitation of available resource and equipment, we decided to fabricate LZ61 mini-tube by wire electrical discharge machining (wire EDM). Wire EDM is capable of producing the mini-tube is in the case of tracheal stent because the dimension of the tracheal stent is larger than vascular stents, especially the thickness of the stent is much thicker than coronary vascular stents. By wire EDM, the microstructure of the LZ61 alloy was preserved, and therefore the LZ61 tube possessed similar mechanical properties and degradation behavior as the LZ61 buck alloy. If the tube was manufactured through tube extrusion and drawing, the microstructure of the alloy would be altered, and the properties of the alloy would be different. [172]
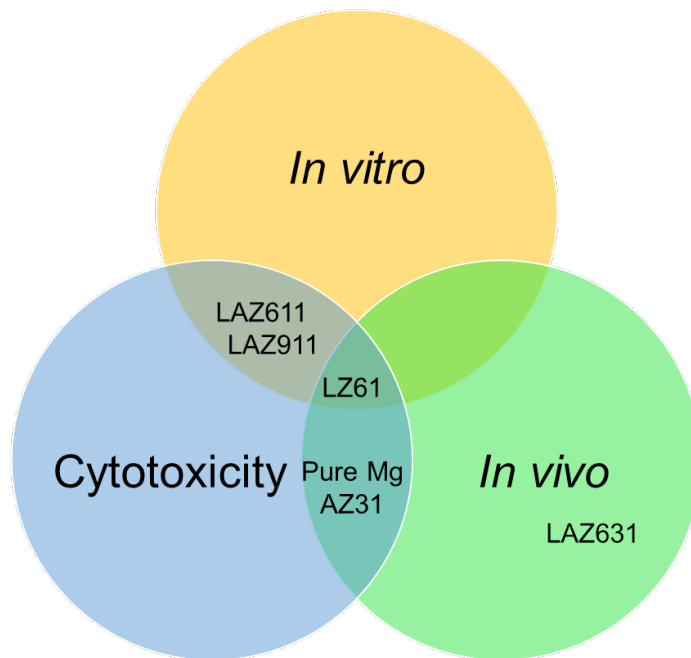
Figure 5.1. The rationale of selecting the LZ61 alloy for tracheal stent fabrication and evaluation.

The second step in the stent fabrication is laser cutting. We followed the same procedure as traditional manufacturing process used for 316L stainless steel stents. A 2D CAD file of the stent pattern was generated. Following this 2D stent pattern, a high-powered beam of light was fired at the tube surface which melts the material until a cut was made. The final step is electrochemical polishing of stents to achieve a smooth mirror-like surface of the stents. The electrolyte solution, current, voltage and duration of time is adjusted based on the stent materials.

After the LZ61 tracheal stents were ready, these stents were firstly evaluated in a bioreactor system using AZ31 stents as the control. This step was key to ensure that LZ61 would perform well before implantation. The failure of the stent implantation could be fatal due to dyspnea. After *in vitro* evaluation, the LZ61 was implanted into healthy rabbit airway to evaluate the feasibly of LZ61 tracheal stent. In this study, 316L stainless steel stent were used as control.

5.2   MATERIALS AND METHODS

5.2.1   LZ61 tracheal stent fabrication

LZ61 extruded rods were cut into mini-tubes with 4.2 mm in diameter, 0.3 mm in wall thickness and 60 mm in length using wire EDM with the help from with the technique support from Advanced Manufacturing Techniques, Inc (Clifton Park, NY). AZ31 extruded rod was purchased from Goodfellow (Coraopolis, PA) and machined into same dimension tube as well. Same dimension 316L stainless steel mini-tube is commercially available and was purchase from Goodfellow (Coraopolis, PA).

Stent geometry was designed based on the mechanical properties of LZ61 alloy with the support from our collaborator, Dr. Ke Yang's lab from the Institute of Metal Research, Chinese Academy of Sciences (Shenyang, China) as shown in Figure 5.2. The stent design was saved in form of a 2D geometry pattern as an CAD file. The mini-tubes were later laser cut into stents based on this pattern with the technique support from Inotech Laser, Inc (San Jose, CA).
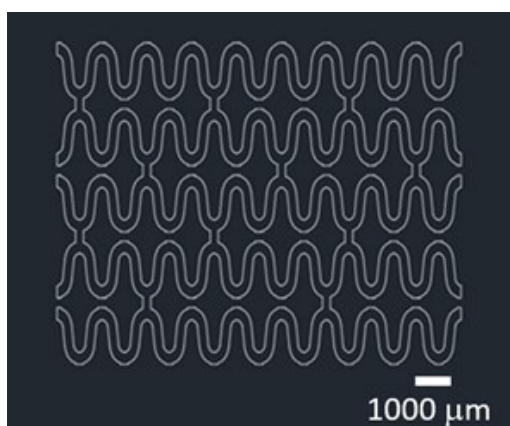
Figure 5.2. 2D pattern of tracheal stent design used in this study.

5.2.2   Electrochemical polishing

Electrochemical polishing of the stents was conducted using a self-designed setup. A DC power supply (Genesys™ Programmable AC/DC Power 2400W, TDK-Lambda Americas, Neptune, NJ) was used as power supply. A 250 ml glass beaker was used as the container of the electrolyte. Platinum wire were connected to negative terminal of the DC power supply acting as cathode. The LZ61 or AZ31 stents were hooked on pure Mg wire while 316L stainless steel (ss)

stents were hooked on 316L ss wire. The Mg wire or 316L ss wire was then connected to the positive terminal of the DC power supply acting as anode. Both anode and cathode were immersed in electrolyte throughout the electrochemical polishing process. The composition of the different electrolytes used for the different stent materials are listed in Table 5.1.

Table 5.1. The composition of electrolyte for electrochemical polishing of different tracheal stents.

	Component	Amount
Mg stent	H_3PO_4 (85 wt. %)	37.5% v/v
	EtOH	62.5% v/v
316L ss stent	H_3PO_4 (85 wt. %)	42 wt. %
	Glycerol	47 wt. %
	H_2O	11 wt. %

Table 5.2. Parameters of the electrochemical polishing process for different tracheal stents.

	Anodic current (A)	Applied voltage (V)	Time (min)	Temperature (°C)
LZ61 stent	0.6	20-30	4	Dry ice cooling
AZ31 stent	0.6	20-30	5	Dry ice cooling
316L ss stent	1.2	25-30	3	Tap water cooling

The parameters of the electrochemical polishing process were listed in Table 5.2. The current was fixed throughout the process; the total time of polishing process were optimized experimentally. Due to the heat generated during the electrochemical chemical polishing process, dry ice was used to cool down the electrolyte for LZ61 stent and AZ31 stent. Tap water was used to cool down the electrolyte for 316L ss stent. After electrochemical polishing, the stents were cleaned using distilled water in an ultrasonic agitation bath for 15 min, then rinsed in Acetone and dried in air.

5.2.3 Micro-computed tomography (μ-CT) imaging

Micro-CT were primary used to analyze the volume of the stents to reflect the degradation profile and degradation rate of the stent. Stents were placed in sample holder to prevent movement and scanned with continuous rotation μCT at 10.5 μm voxel size. The files were converted into digital imaging and communications in medicine (DICOM) format and analyzed using mimics software (Materialise, Belgium). A threshold was set to isolate the implant from the surrounding tissues and the region growth function were used to identify the remaining structure of the stent which was then reconstructed into 3D images of the stents. The volume of the stents was calculated based on the reconstructed 3D images.

5.2.4 Bioreactor setup

TA ElectroForce 3D CulturePro™ bioreactor setup (TA Instruments, New Castle, DE) was used to mimic the dynamic environment *in vivo*. Silicone tubes (Nalgene™ Pharma-Grade Platinum-Cured Silicone Tubing, Thermo Scientific) with 3/16 inches (4.76 mm) inner diameter, 1/16 inch (1.59 mm) wall thickness were used to mimic the tracheal tissue. Stents were mounted on a 5mm × 2cm balloon catheter (Mustang, Boston scientific), inserted into the silicon tube, and expanded using an inflation device (Acclarent®, Irvine, CA) which continually pushed saline into the balloon until reaching a pressure of 12 atm. The silicone tube with the stent inside was then hooked into the bioreactor chamber. In total, 3 LZ61 stents and 3 AZ31 stents were used, and each chamber only hosted one stent. Once the chamber was sealed with stent insides, HBSS was pumped into the circulation system at the flow rate of 80 ml/min. All the stents were scanned at 1 week, 3 weeks and 5 weeks using micro-CT. After 5 weeks of immersion, the

remaining stents were dried in ethanol and scanned under SEM (SEM; JSM6610LV, JEOL) and EDAX (EDAX Genesis, Mahwah, NJ).

5.2.5 Procedures for implantation

All animal experiments were approved by the University of Pittsburgh's Institutional Animal Case and Use Committee (IACUC). 12 weeks old female New Zealand white rabbits (3.5-4lbs) was purchased from Covance Research (Denver, PA). All the rabbits were acclimated for 5 days before undergoing any invasive procedure and received a standard rabbit diet and water ad libitum. Before the surgery, animals were anesthetized by IM (intramuscular) injection of ketamine/xylazine, 35mg/kg and 5mg/kg, respectively. The skin was prepared for surgery by clipping the hair and scrubbing the skin with betadine solution. For airway stenting, a vertical midline incision was made in the neck to expose the airway. The subglottis was entered via a midline cricoidotomy extending through the first and second tracheal rings, analogous to a laryngo-fissure procedure in a patient. The tracheal stent was mounted on the balloon of the catheter (Mustang™, Boston Scientific). The catheter was then placed through the incision along with the stent. When reached the target site, saline was injected into the balloon to expand the stent until 12 atmospheric pressure was reached within the balloon for 30 seconds. To further fix the stents from moving, the stents were fixed with 4/0 Vicryl (polyglactin 910) interrupted sutures by suturing the stent to the tracheal wall. At the end of the procedure, skin and subcutaneous layer together closed with 4/0 Vicryl (polyglactin 910) interrupted sutures allowing air passage to prevent subcutaneous emphysema. Right after completion of the surgery, X-ray images was captured for all the animals to confirm the success of the surgical procedure.

Groups of 5 animals for LZ61 stents and 316L ss stents were used for each time point of 4, 8, and 12 weeks. Animals were sacrificed at the end of each time point by injecting with euthanasia drug sodium pentobarbitol at the dosage of 50 mg/kg administered IC. Stented airway section, lung, liver, and kidney were collected and fixed in 10% neutral buffered formalin for 3 days and then preserved in 70% ethanol.

5.2.6 Endoscope

A Parsons laryngoscope, Hopkins II 0º telescope (4 mm x 18 cm) and endoscopy tower (1288 HH definition camera and X8000 light source with fiber optic light cable, Stryker) were used to capture the stented airway of each rabbit right after the implantation and after 4 weeks, 8 weeks and 12 weeks of implantation depend on the end time point.

5.2.7 Optical coherence tomography (OCT)

The fixe stented airway was scanned by OCT (Ilumien™ system, St Jude Medical) to examine the tracheal wall. The fixed trachea was immersion in PBS solution, and an image catheter (Dragonfly™ Imaging Catheter, St Jude Medical) were inserted from the distal end of the trachea all the way to the proximal end of the trachea. The catheter was then pulled back to scan the inner wall of the stented trachea which were controlled by the program.

5.2.8   Histology analysis

Fixed trachea and organs were dehydrated, infiltrated and embedded in paraffin. The paraffin blocks with tissues inside were then sectioned with a rotary microtome (Leica RM 2255, Leica Biosystems, Buffalo Grove, IL). These tissue sections were transferred to histology slides for histological staining. H&E staining was performed to examine the tissue morphology of the trachea and organs. Alcian blue staining was performed to examine the mucus and goblet cells within the mucosa.

5.2.9   Statistical analysis

The obtained results were expressed as the mean ± standard deviation. One-way ANOVA was conducted to determine the differences between different groups of samples with Bonferroni Procedure as post hoc test. Statistical significance was defined as $p < 0.05$. Statistical analysis was performed utilizing the IBM SPSS Statistics 23 package for Windows.

5.3   RESULTS

5.3.1   Stent fabrication

Balloon expandable prototype stents for a pilot *in vitro* and *in vivo* study following traditional fabrication method and electrochemically polished the stents to reach a smooth mirror-like surface before testing. As shown in Figure 5.3 and Figure 5.4, both wire-EDM

machining and laser cutting left a rough surface on the stent with the laser cut surface slightly more fined. Electrochemical polishing effectively improved the surface finishing by removing the sharp tips on the surface. As show in Figure 5.3-5.5, more Rounded edges and smoother surface can be observed on LZ61 stent (Figure 5.3c-d), AZ31 stent (Figure 5.4c-d) and 316L ss stent (Figure 5.5c-d). It should be noted that, due to the simple setup, the electrochemical polishing is not very homogeneous. Part of the stents that was contacting the pure magnesium wire became slightly thinner than the rest part of the stents. A better setup could be designed by offering a more even contact to achieve homogeneous polishing of the stent.
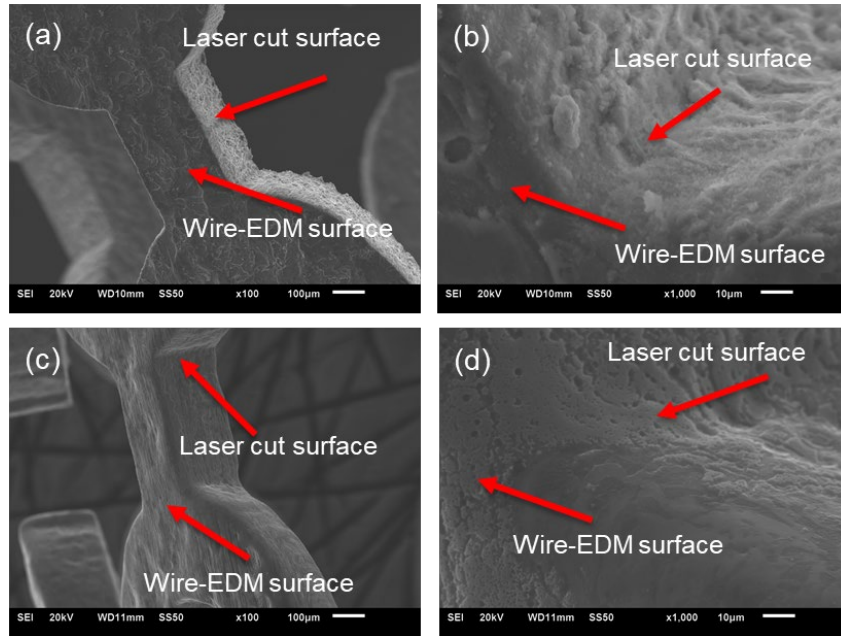
Figure 5.3. Surface morphology of LZ61 stents before (a) 100X (b) 1000X and after (c) 100X (d) 1000X electrochemical polishing.
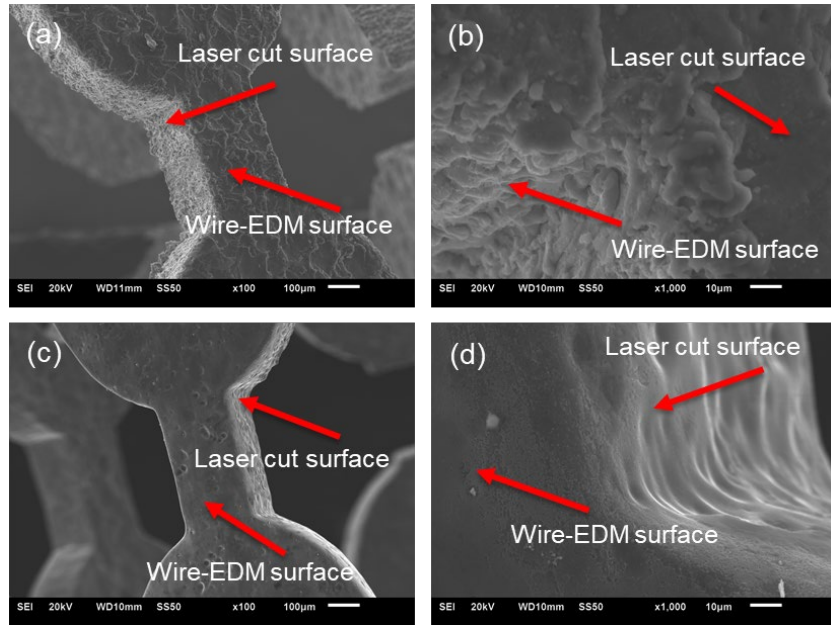
Figure 5.4. Surface morphology of AZ31 stents before (a) 100X (b) 1000X and after (c) 100X (d) 1000X electrochemical polishing.
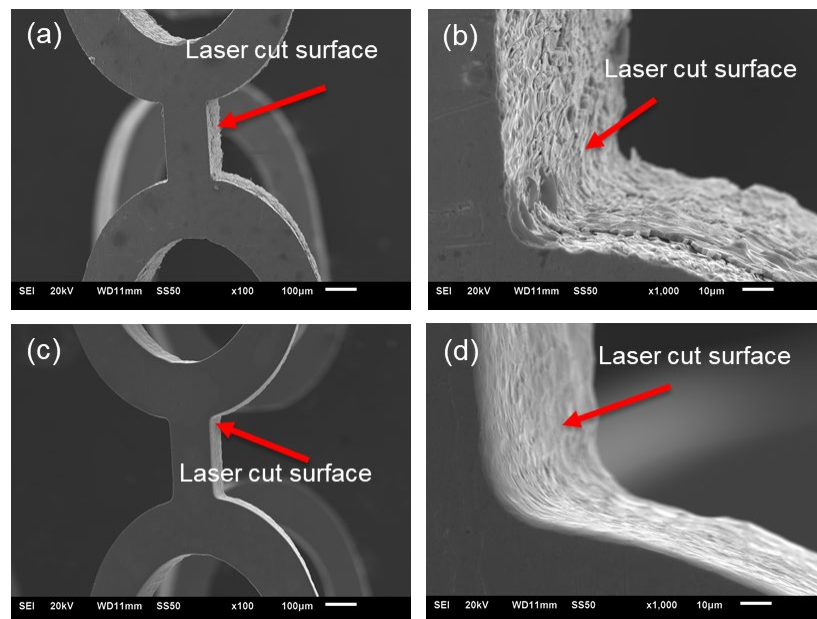
Figure 5.5. Surface morphology of 316L ss stents before (a) 100X (b) 1000X and after (c) 100X (d) 1000X electrochemical polishing.

5.3.2 *In vitro* degradation of LZ61 stents in a bioreactor system

The results in specific aim 1 have demonstrated that LZ61 degraded at a non-significantly different degradation rate compared to AZ31 alloy under static environments. In this specific aim, however, we aimed to test and analyze how the LZ61 stent would degrade compared to AZ31 stent in a bioreactor environment. As shown in Figure 5.6, the µ-CT scan of both LZ61 stent and AZ31 stent at different time point were reconstructed into 3D images. These images clearly show that the LZ61 stents degraded significantly slower than our control group, AZ31 stents, under the dynamic flow environment. Most of the stent structure was maintained up to five weeks of immersion in dynamic flow environment, whereas AZ31 stents almost dissolved completely in the same time period. In addition, the volume of remaining stents was calculated and plotted in Figure 5.7. The results indicate that 47.6% of the LZ61 stents degraded while only 7.8% of the total volume was left for AZ31 stents with 92.2% dissolving.
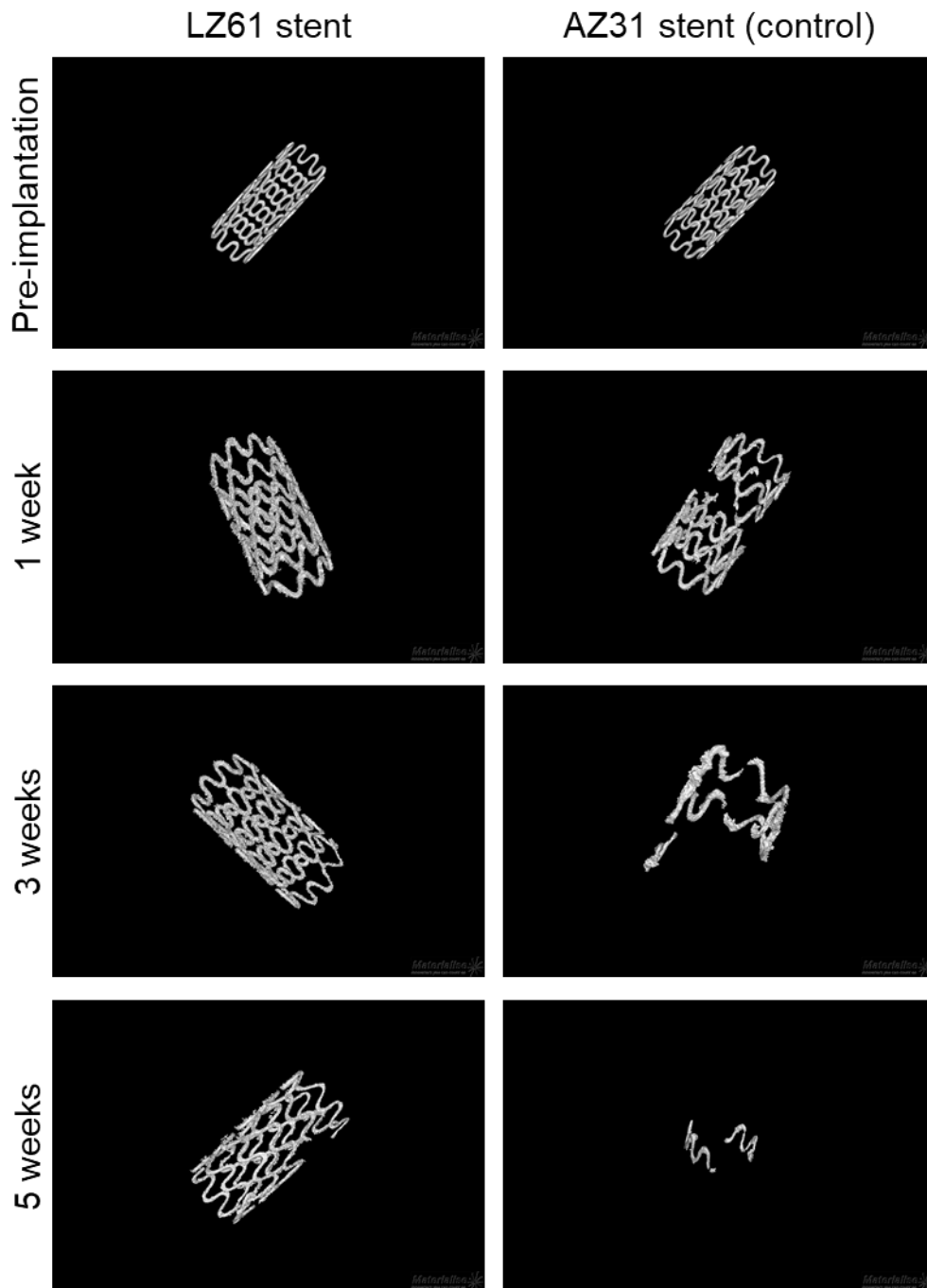
Figure 5.6. The 3D structure of AZ31 stents and LZ61 stents based on micro-CT scan at different time points indicating the remaining stents after immersion in dynamic flow environment.
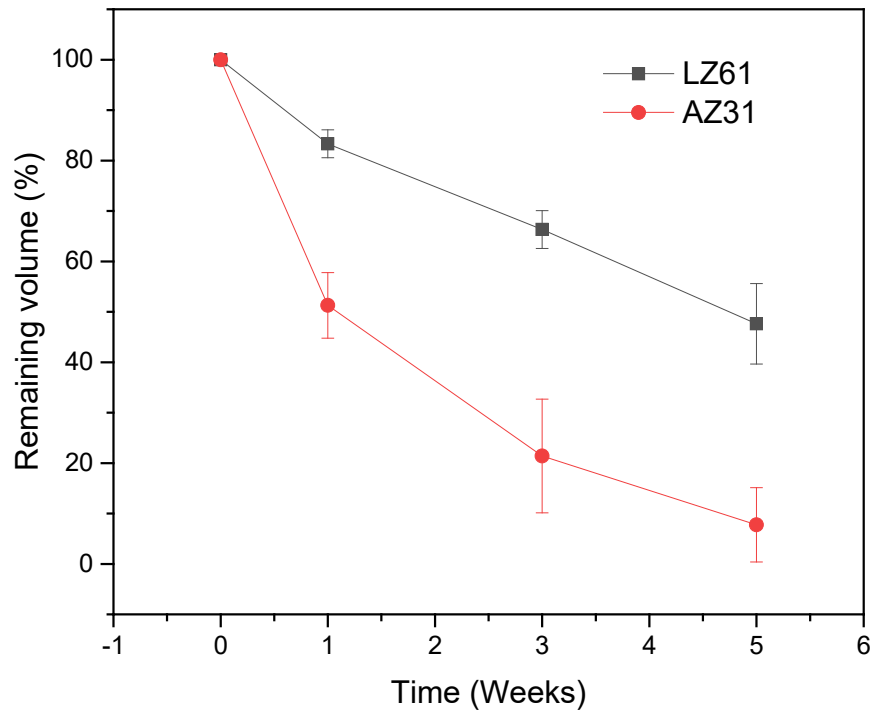
Figure 5.7. The remaining volume of the stents calculated based on the 3D structure of AZ31 stents and LZ61 stents.

(n=3).

The localized corrosion was observed during the degradation of the stent AZ31 stent, as shown in Figure 5.6. The AZ31 stent is fractured into two parts after 1 week of immersion and became even more fragmented afterward. This degradation pattern is detrimental to the durability of tracheal stent since localized corrosion would quickly lead to disassembly of the stent. AZ31 stent therefore will not be able to provide enough mechanical support against the tracheal wall if the structure had disassembled. LZ61 stent on the other hand, was quite robust throughout the study, and no obvious localized corrosion was observed in the first few weeks. At the end of week 5, we did observed part of the stent strut totally degraded, mostly at the locations where more metal was removed during the electrochemical polishing process.

Our results therefore demonstrate that LA61 alloy was much more resistant to the increased corrosion caused by the flow-induced shear stress. This result is indeed very encouraging since stents are exposed to dynamic environment where the mucus is consistently moving to clean the airway. In fact, the speed of mucus movement is much slower than the flow rate used in this study, and the part of the magnesium stent would be exposed at the air-liquid interface, so the degradation might be slower than what was shown in the aqueous bioreactor environment. One of the missing factors in the system is that we did not apply cyclic mechanic force mimicking the stress caused by the respiratory cycle. The cyclic stress might impact and increase the degradation of LZ61 stent as well.

After 5 weeks of immersion, the stent surface was covered with degradation layer and precipitate from the Hank's Balanced Salt Solution (Figure 5.8(a, b)), especially at the locations where massive degradation occurred. To examine the composition of the degradation product, EDAX mapping was performed at the spots marked with + sign in Figure 5.8(a, b). The results were plotted in Figure 5.8(c), indicating that there was significantly more Ca and P deposited on the surface of the LZ61 stents than the AZ31 stent. For AZ31 stent, the major composition of the degradation layer is MgO and $Mg(OH)_2$. More Ca and P tends to deposit on the surface of the slower degrading magnesium alloy. Conceivably therefore, the presence of a stable Ca and P degradation layer would provide better corrosion protection to the alloy matrix and therefore, improve the corrosion resistance. [175, 176]
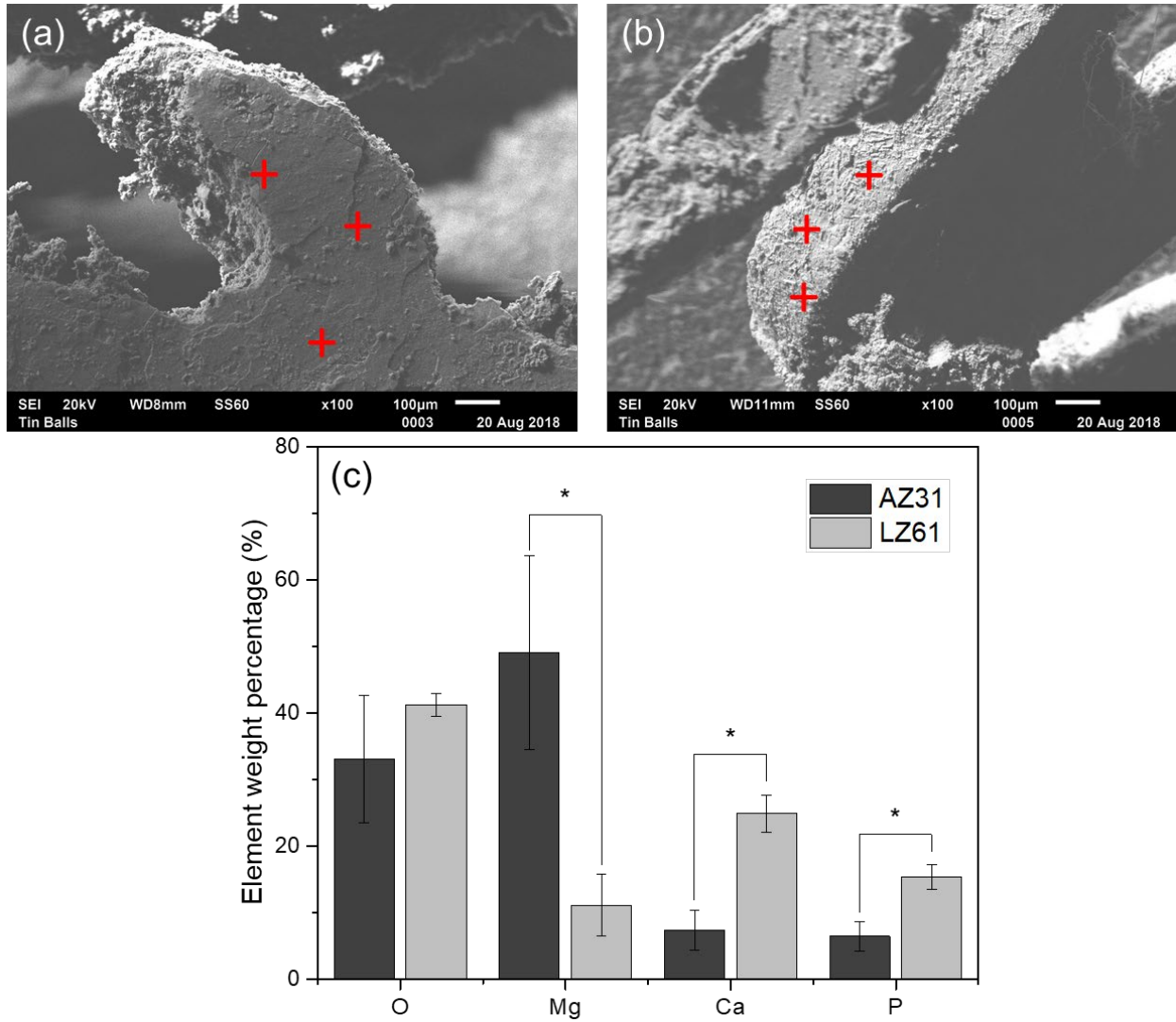
Figure 5.8. The surface condition of (a) LZ61 stent and (b) AZ31 stent after 5 weeks of immersion in dynamic flow environment under SEM. (b) The O, Mg, Ca and P composition on the surface of stents after 5 weeks of immersion using EDAS. *denotes a significant difference between alloy groups ($p < 0.05$, n=3).

5.3.3 *In vivo* implantation of LZ61 stent in health rabbit airway model

To understand how LZ61 tracheal stent will perform *in vivo*, same LZ61 stents were implanted into normal trachea of New Zealand rabbits. A rabbit model was chosen based on the previous review of animals models for tracheal research.[57] In the meantime, 316L stainless steel, a typical metallic material for commercial non-degradable balloon expandable stents[13, 177-179], were selected to serve as control in this animal study. The procedure of the surgery was shown in Figure 5.9, tracheal stent was mounted on the balloon and was then inserted into rabbit trachea. After reaching the first airway cartilage ring, the balloon was injected with saline and expanded the tracheal stent against the tracheal wall. After expansion, the balloon was deflated and pulled out of the trachea leaving the stent inside the tracheal lumen. The position of the stent was verified by X-ray images, as shown in Figure 5.10. The density of LZ61 is much smaller than bone, thus the LZ61 was hard to identify under the X-ray. In Figure 5.10(b), the dark shadow of the LZ61 stent was still visible while 316L ss stent was bright in the X-ray images as show in Figure 5.10(a).

The endoscopic images of the stented tracheal with LZ61 stents or 316L ss stent at different time point were shown in Figure 5.11. The stents looked similar right after implantation for both groups. The strut of the stent was exposed in the airway and partially covered by the blood which as caused by the incision. At week 4, the airway was clean for both groups, no blood was seen in the tracheal lumen. Stents in both groups were partially encapsulated in the tissue as show in Figure 5.11, shining metal surface could still be seen in the endoscope images. After 8 weeks of immersion, a fully healed healthy tracheal lumen could be seen in LZ61 stent group. LZ61 stent was invisible in all the rabbits. At the current stage, it is unclear if the stent has fully degraded or is encapsulated by the tracheal tissue. On the contrary, a whitish stenosis tissue

begins to build up on top of the 316L ss stent. At week 12, the LZ61 stent group showed a clean and larger size trachea due to the growth of the rabbit. There was no stenosis tissue building up during the 12 weeks of implantation and the trachea lumen looks very healthy. However, for 316L ss stent group, a thick whitish stenosis tissue formed along the tracheal wall and the trachea lumen was significantly narrowed due to the steady growth of the stenosis tissue on 316L ss stent. No rabbit in 316L ss steel group exhibited dyspnea throughout the study until the end of the study. The endoscope image of a normal rabbit trachea is also shown in Figure 5.11 for comparison.

Figure 5.9. The surgical procedure of the stent placement. (a) Tracheal stent was mounted on the balloon. (b) The balloon was injected with saline and expanded the tracheal stent against the tracheal wall. (c) The balloon was deflated and pulled out of the trachea leaving the stent inside the tracheal lumen.
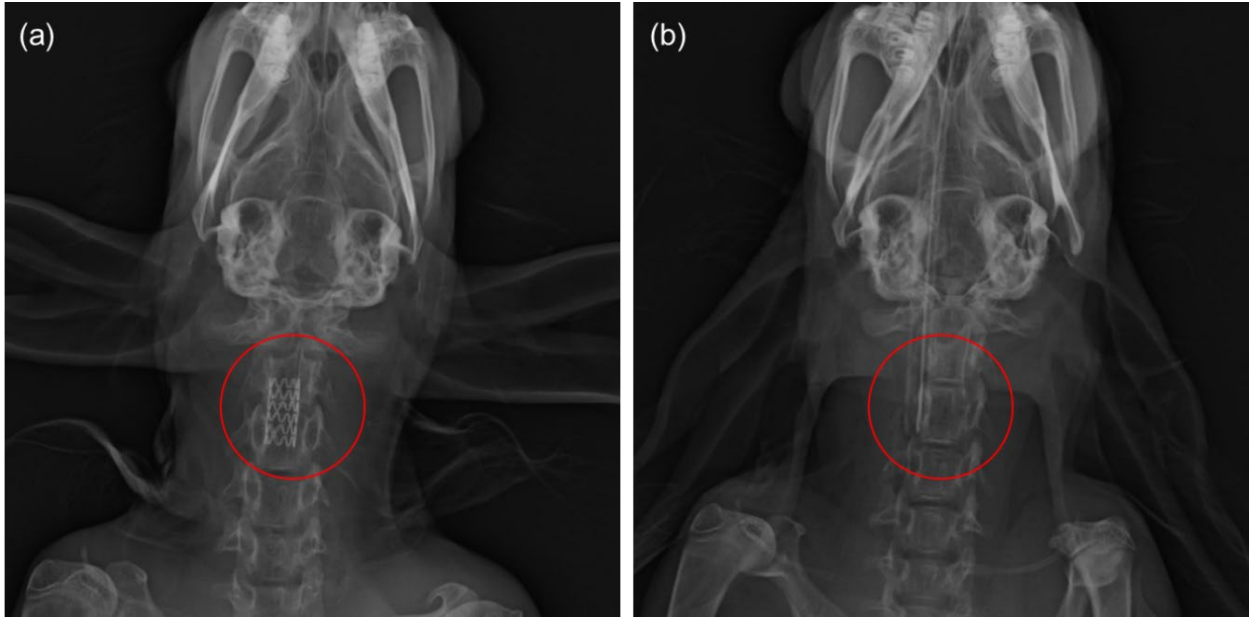
Figure 5.10. X-ray image of the implantation site of the (a) 316L ss stent and (b) LZ61 alloys after the tracheal stent implantation. The positions of the stents are circled in the images. LZ61 stent is hard to identify here under x-ray due to the lower density, only a dark shadow is visible here.
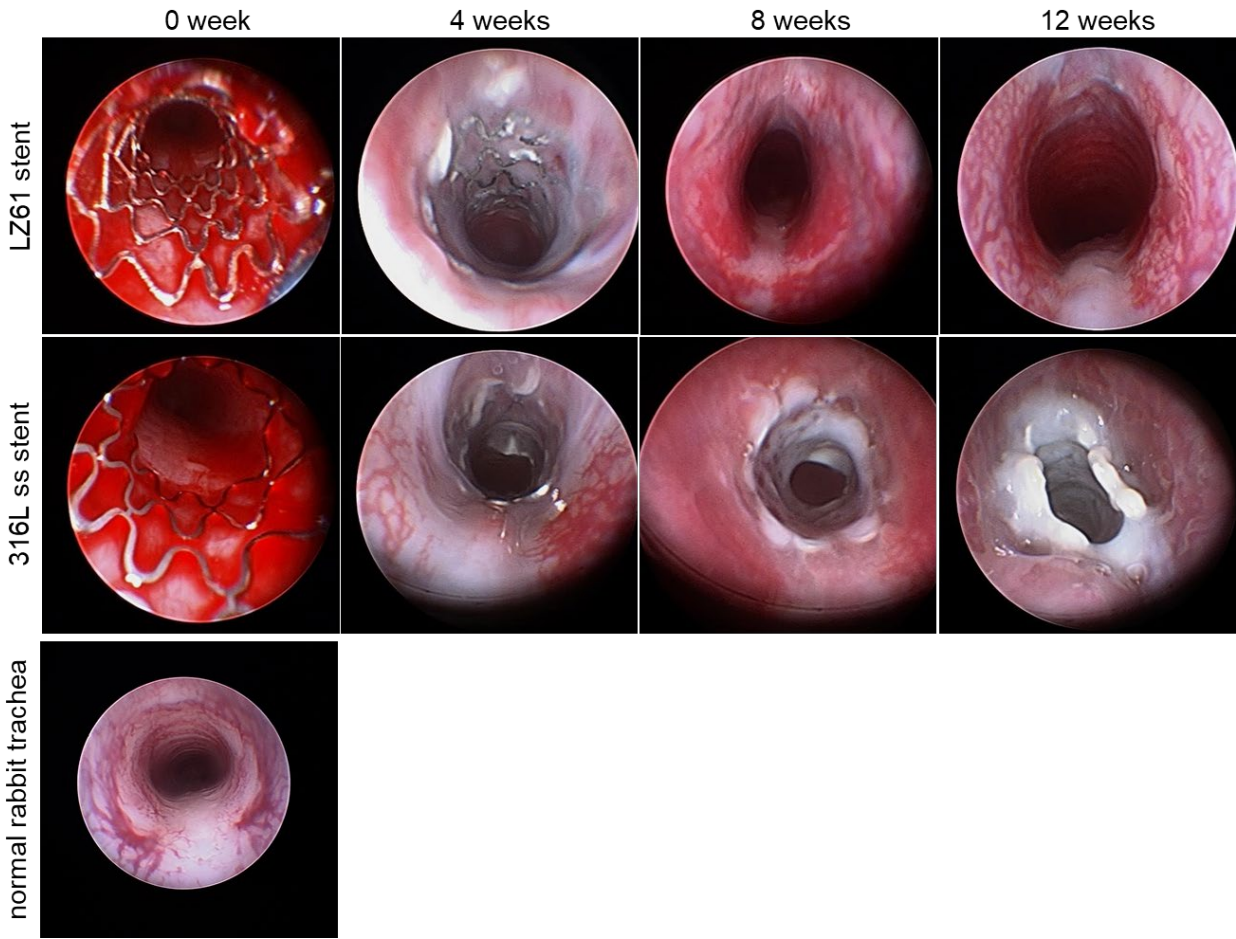
Figure 5.11. Endoscopic images of the stented airway right after implantation, and after 4 weeks, 8 weeks and 12 weeks.
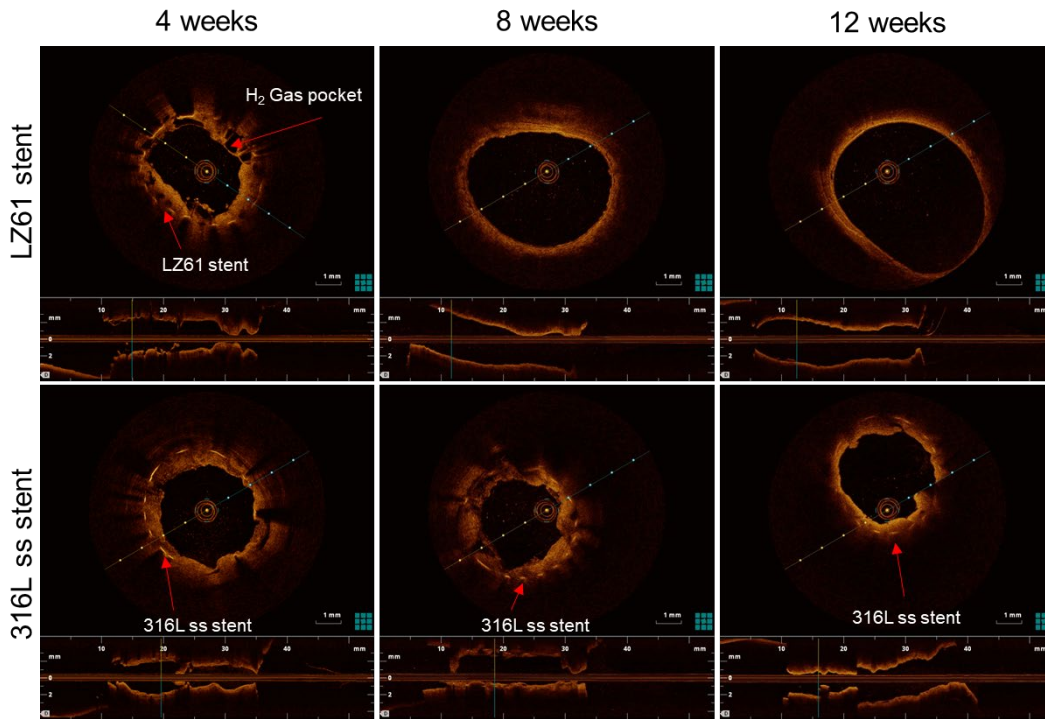
Figure 5.12. OCT images of the transverse section and longitudinal section of the stents airway after 4 weeks, 8 weeks and 12 weeks of implantation.

Optical coherence tomography (OCT) is a powerful tool to observe the intralumenal surface of the stented tracheal. The scanning results were show in Figure 5.12. For each image, the top part shows the transverse section of the trachea, and the bottom part of the images showed the longitudinal section of the stented trachea. At week 4, both groups showed the presence of stents. Since the density of the stent is much higher than the soft tissue, the stent strut was much brighter than the soft tissue and the metal stents posed a shadow along the radial direction. For LZ61, the tissue around the stents was porous indicating the formation of H_2 gas pockets as shown in Figure 5.12. The effect of these gas pocket on airway tissue is unknown. The results after 8 weeks and 12 weeks were however, similar. For LZ61 stent group, no

112

remaining stents were observed. The stent fully degraded, and the airway lumen fully restored to normal smooth surface after 8 weeks post the stent implantation. For 316L ss stent group, it should be noted that at week 8 and week 12, the stenosis tissue was continually building up on top of the 316L ss stents which further narrowed the airway. This observation is in line with what was observed in the endoscope images (Figure 5.11).
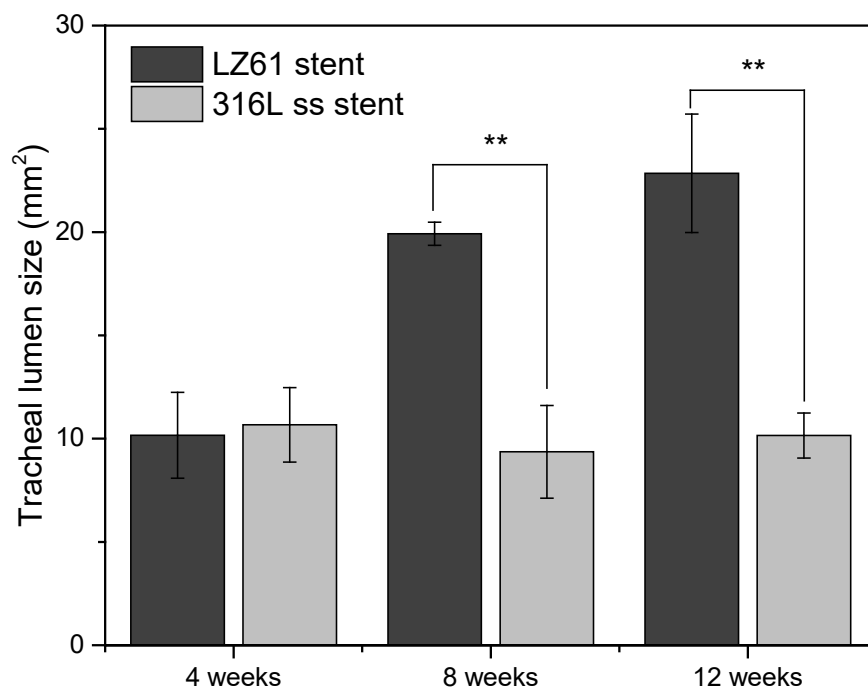
Figure 5.13. Tracheal lumen area calculated based on the cross-section of OCT images at 4 weeks, 8 weeks and 12 weeks. **denotes a significant difference between alloy groups (p <0.01, n=3).

It is critical to understand how the implantation of the stents impact the tracheal lumen size, since this is the key indicator deciding if the patient will be able to breathe normally after receiving the tracheal stent implantation. Therefore, we calculated the tracheal lumen size with

the stents implanted insides based on OCT images using ImageJ software and plotted it Figure 5.13. The results demonstrated that, with the implantation and degradation of LZ61 stents, the lumen size of the tracheal increased steadily leaving no impact on the further growth of the rabbit airway as the rabbit grew bigger. This is very promising sign for the potential application especially among pediatric patients. On the contrary, the airway lumen size decreased while the whole airway was growing for the 316L ss steel group, the airway lumen size of the control group was also significantly smaller than the airway lumen size of LZ61 stent group at week 8 and week 12, respectively.

The 3D structure of the remaining stents was reconstructed based on the μ-CT scan. 316L ss stents were stable throughout the 12 weeks' implantation due to its inert nature. For LZ61 stent group, ~30% of the initial volume degraded after 4 weeks of implantation on average. The major structure was still maintained at week 4, which was same as what was observed in the bioreactor study. No localized corrosion was observed that could disassemble the stent. However, no stent was observed at week 8 and week 12 which means that the stent fully degraded after week 8. This observation echoes what we have seen in the endoscopic imaging and OCT imaging results. It is encouraging to see that the LZ61 was able to fully degrade without impacting further growth of the airway, however, we do notice that there was a steep increase in the degradation after the initial stage (~ 4 weeks) considering almost half of the LZ61 stents remained after 5 weeks under the flow environment *in vitro*.
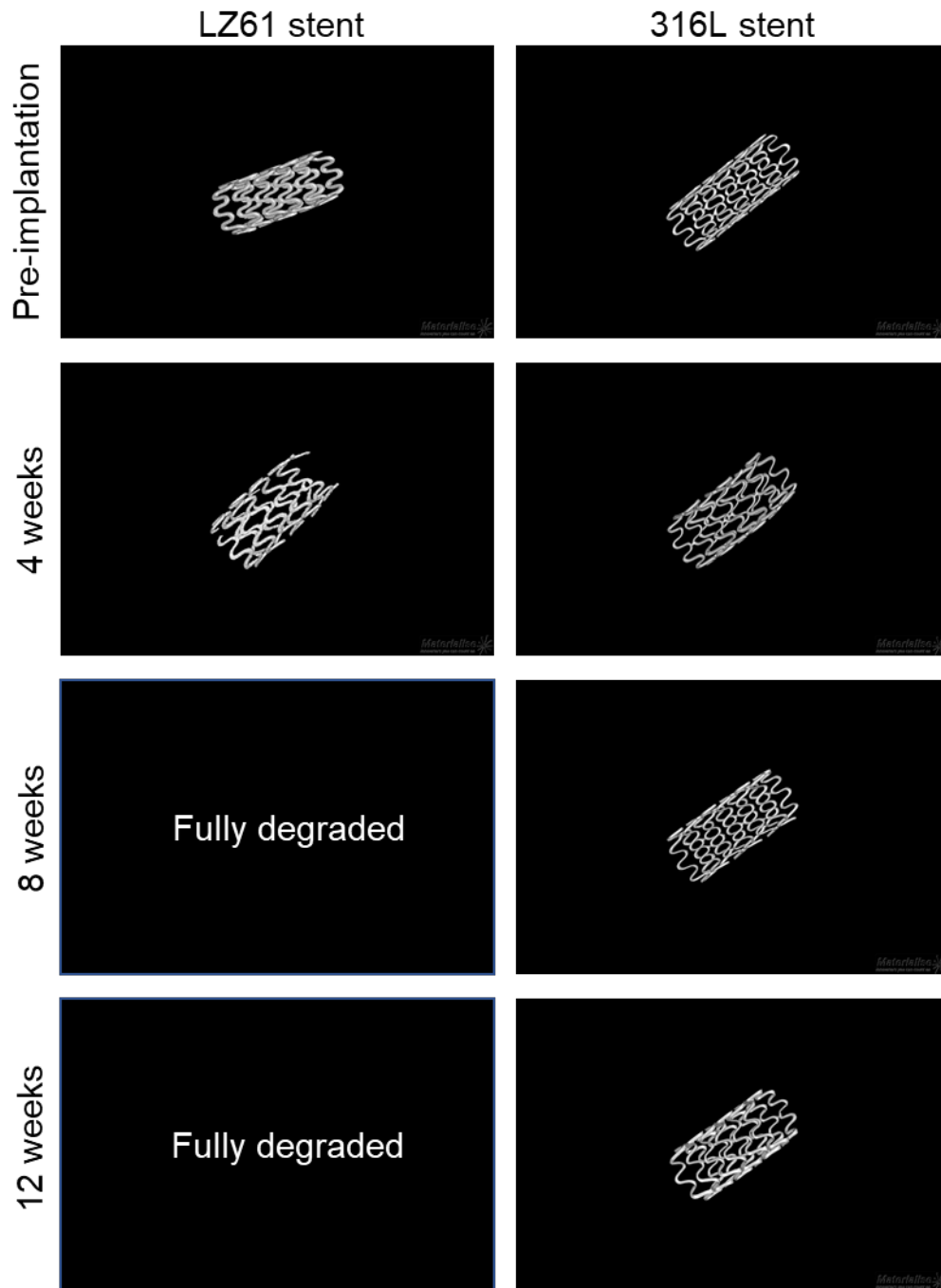
Figure 5.14. The 3D structure of 316L ss stents and LZ61 stents based on micro-CT scan at different time point indicating the remaining stents after implantation *in vivo*.

5.3.4 Histology analysis

Figure 5.15 showed the H&E staining of the LZ61 stent stented trachea at different time points. At week 4, the cross-section of the trachea (Figure 5.15(a)) showed that half of the stent was encapsulated in the tracheal submucosa. Higher magnification images of the trachea (Figure 5.15(d)) showed that a thin layer of epithelium had covered the LZ61 stent after 4 weeks of implantation. The dark hematoxylin staining surrounding the LZ61 stent strut showed a higher density of the cells indicating potential inflammatory response at the early stage of the implantation. This result demonstrated LZ61 alloy was well tolerated by airway tissues. The shape of the trachea lumen was close to circle rather than the normal elliptic shape due the expansion of the stent indicating that the LZ61 stent was still providing sufficient mechanical support against the tracheal wall. The H&E staining at week 8 (Figure 5.15(b, e)) and week 12 (Figure 5.15(c, f) shows the fully restored normal tracheal cross-section of the airway. Compared to the normal tracheal (Figure 5.17(a, b)), the rabbit trachea of LZ61 stent group at week 8 and 12 exhibited same complete epithelium layer. However, larger vessels in submucosa were observed at both week 8 and week 12. Vascularization was also observed in normal rabbit trachea (5.17 (b)), but the vessel size was much smaller than the LZ61 stent group. The shape of the trachea restored to normal elliptic shape after the stent was dissolved.
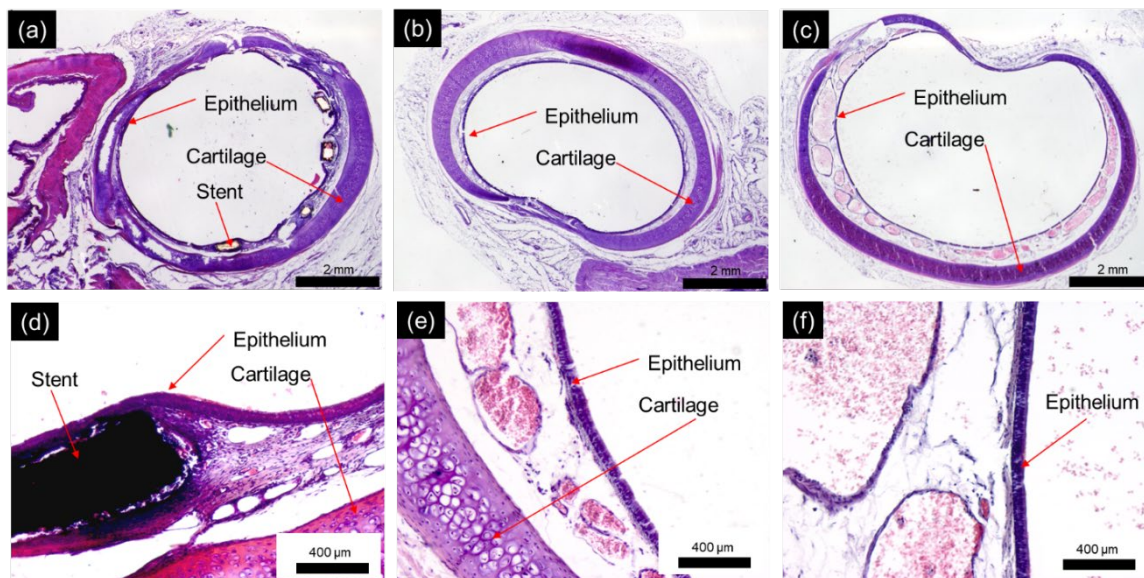
Figure 5.15. H&E staining of LZ61 stent stented trachea 4 weeks post implantation(a) 2X, (d) 20X; 8 weeks post implantation (b) 2X, (e) 20X and 12 weeks post implantation (c) 2X, (f) 20X.
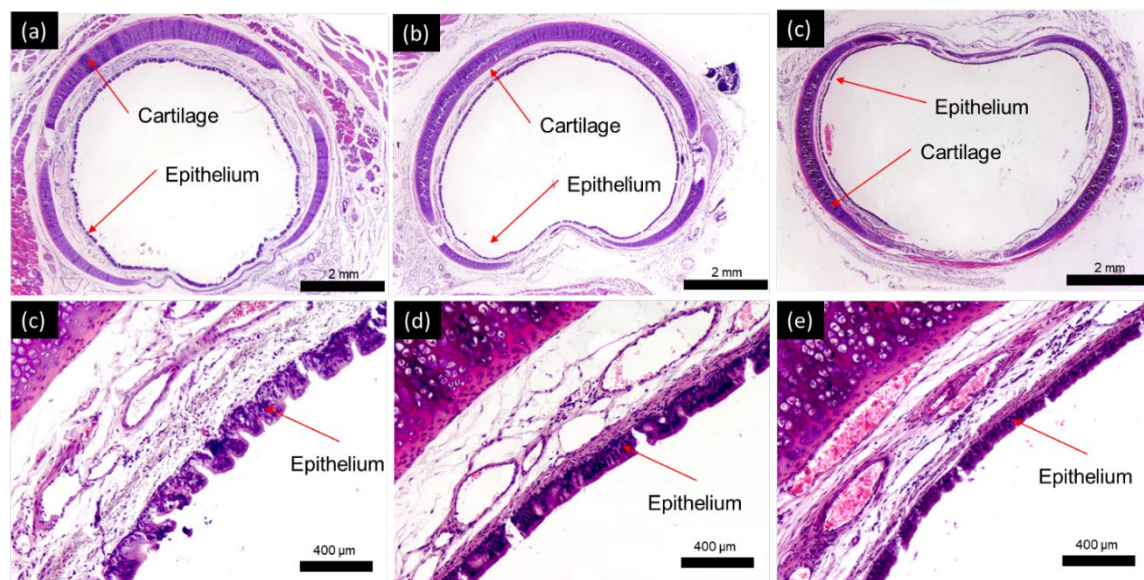
Figure 5.16. H&E staining of 316L ss stent stented trachea 4 weeks post implantation(a) 2X, (d) 20X; 8 weeks post implantation (b) 2X, (e) 20X and 12 weeks post implantation (c) 2X, (f) 20X.
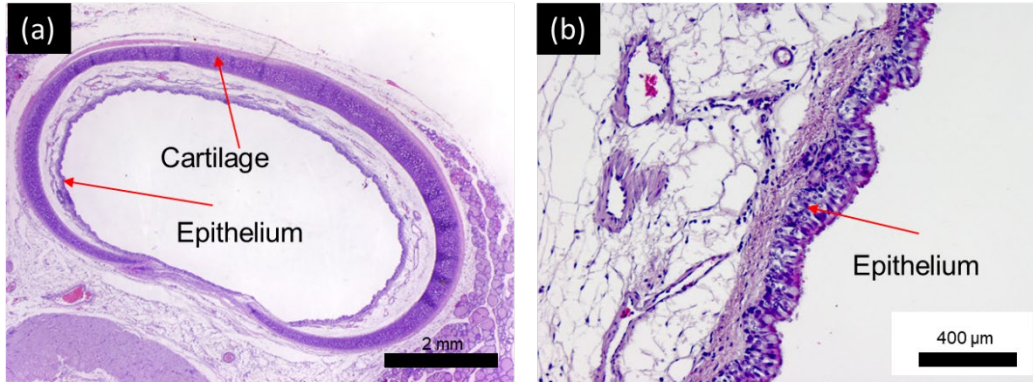
Figure 5.17. H&E staining of healthy rabbit trachea (a) 2X (b)20X.
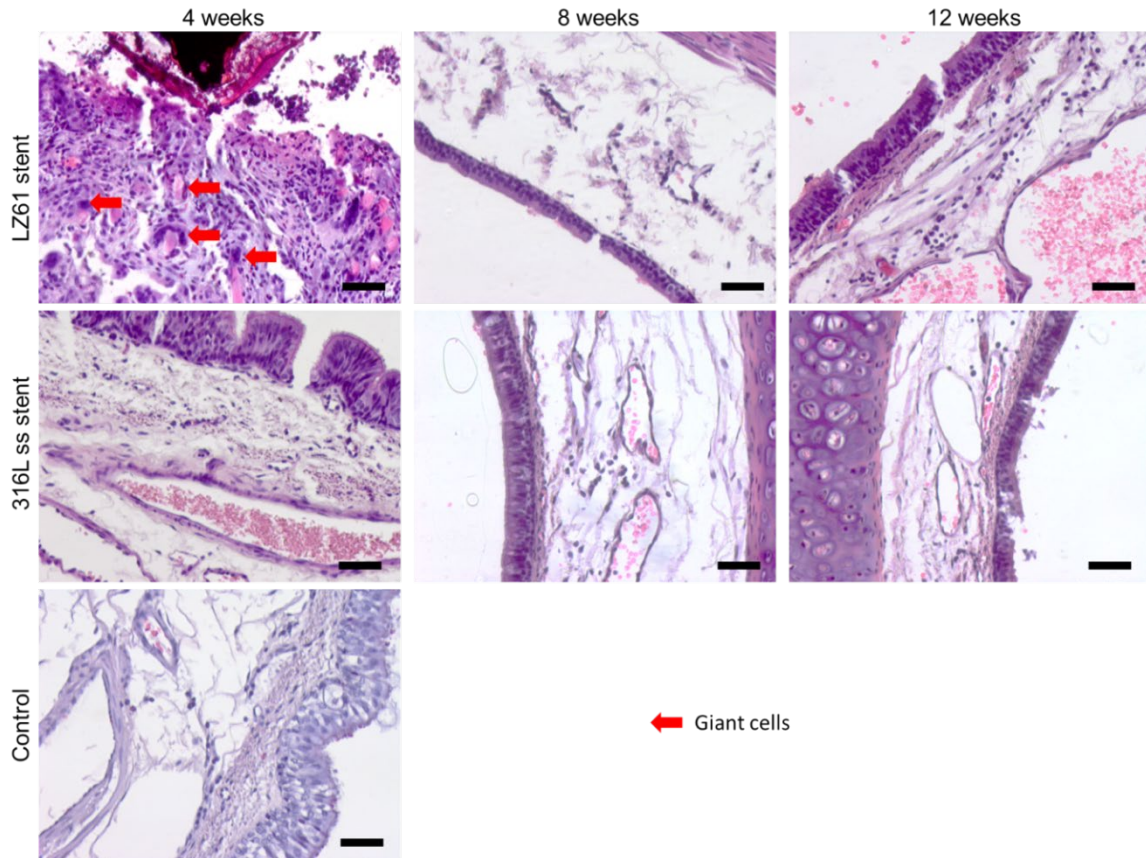
Figure 5.18. Giant cells in stented rabbit trachea in higher magnification H&E staining images, the red arrow indicates the position of the giant cells. (scale bar = 50μm)

Figure 5.16 showed the H&E staining of the 316L ss stent stented trachea at week 4, week 8 and week 12. Due to the hardness of the 316L stainless steel, it was extremely difficult to cut the paraffin block without breaking the tissue around the stent. Therefore, all the 316L ss stents were removed from the trachea before the paraffin imbedding. Similar to LZ61 stent group, at week 4, the tracheal lumen was closer to a circle due to the mechanical force provided by the expanded 316L ss stent. As the rabbit trachea had grown larger due to the advancing rabbit age, the trachea lumen was restored to the elliptic shape. Integrated epithelium layer was clearly observed at all the time points except at week 12. Part of the epithelium layer was gone due to the removal of the stent at week 12. Large vessels were also shown in the trachea submucosa at week 8 and week 12.

As shown in Figure 5.18, giant cells are only observed in few spots of the LZ61 stented trachea submucosa at week 4. No giant cells could be observed at week 8 and week 12 when the stents were fully degraded. For 316L ss stented trachea and the normal healthy trachea, giant cells were hardly noticeable to be identified.

The presence of glycosaminoglycans was identified by Alcian blue staining as shown in Figure 5.19. For LZ61 stent group, a layer of mucus which was in blue color was observed at week 4 (Figure 5.19(a)), indicating more mucus was secreted due the existence of LZ61 stents. In the submucosa where the stent strut existed, there was also higher density of blue color, indicating fibrosis tissue formed around the LZ61 stents. At week 8 (Figure 5.19(b)) and week 12 (Figure 5.19(c)), the epithelium and mucus secretion was normal for LZ61 group when compared to normal trachea (Figure 5.19(g)). Since the stent were removed for the 316L ss stent group, we were not able to identify the location of the stent strut, however, the epithelium and mucus secretion was normal. Goblet cells were evenly distributed in all the groups at different

119

time point same as normal trachea. The number of goblet cells were counted along the epithelium in random selected regions and plotted in Figure 5.19(h). There was no statistically noticeable difference observed among all the groups studied.

H&E staining of key organs (lung (Figure 5.20), kidney (Figure 5.21) and liver (Figure 5.22) that related to the metabolism of the degradation also demonstrated good biocompatibility of the LZ61 stent and its degradation products. No noticeable abnormality was observed when compared to the corresponding organs of the healthy rabbit.
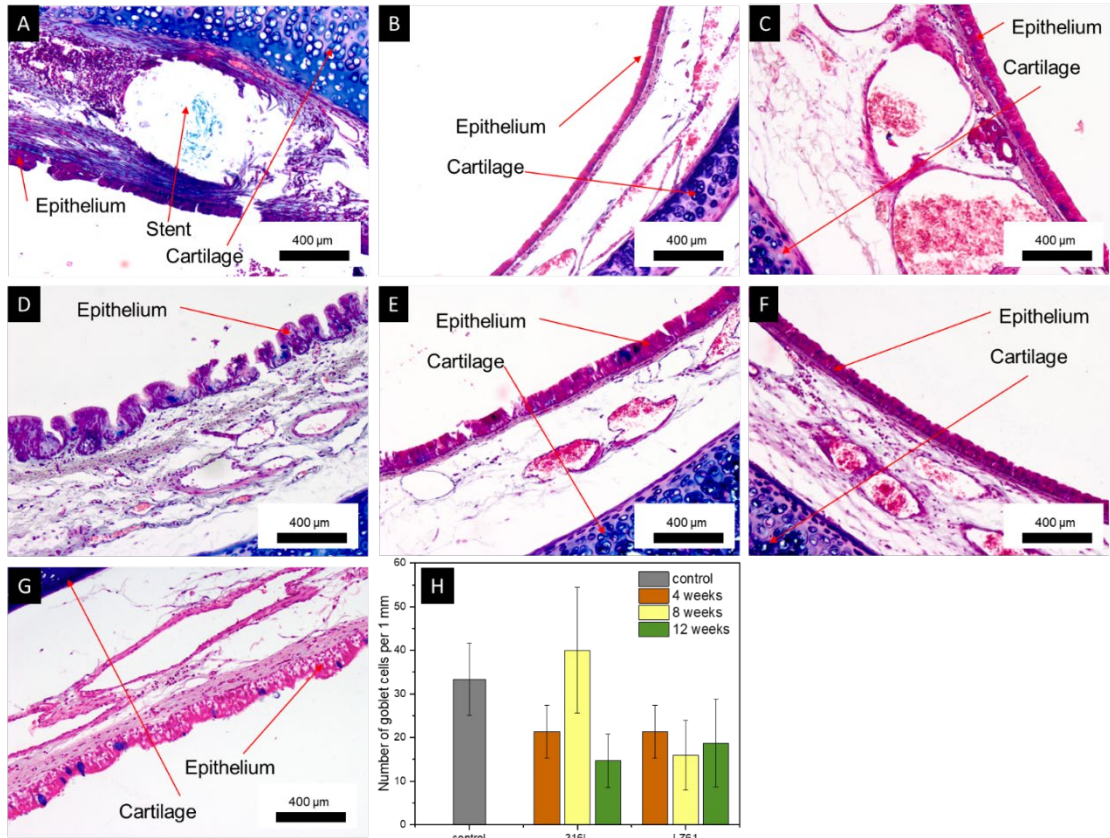
Figure 5.19. Alcian blue staining of the LZ61 stent stented trachea (a) 4 weeks, (b) 8 weeks and (c) 12 weeks post implantation; Alcian blue staining of the 316L ss stent stented trachea (d) 4 weeks, (e) 8 weeks and (f) 12 weeks post implantation; (g) Alcian blue staining of normal trachea; (h) number of goblet cells per 1 mm along the epithelium. No statistically noticeable difference is identified among the different groups.
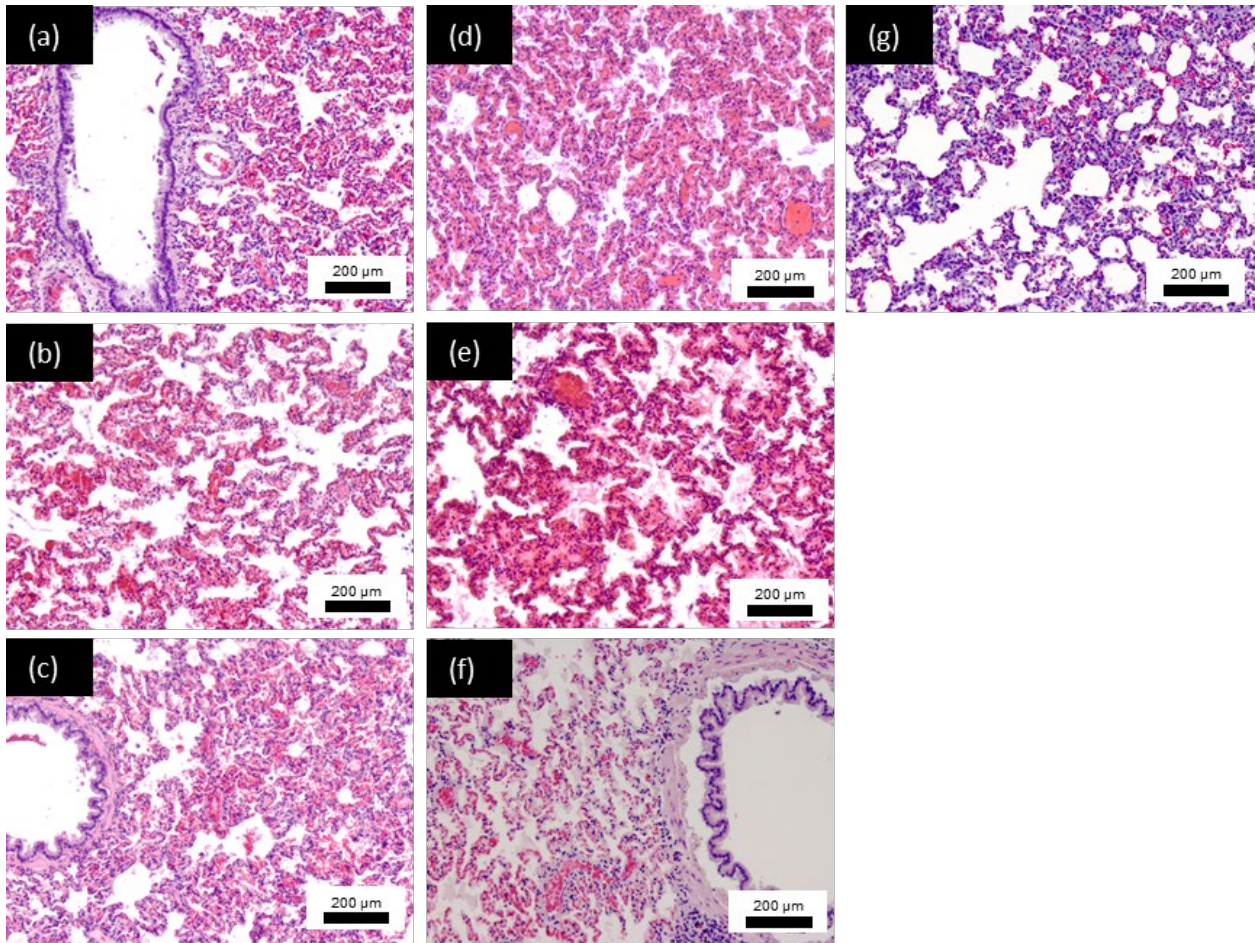
Figure 5.20. H&E staining of the lung tissue. LZ61 stent group at (a) 4 weeks, (b) 8 weeks and (c) 12 weeks post implantation; 316L ss stent group at (d) 4 weeks, (e) 8 weeks and (f) 12 weeks post implantation; (g) normal rabbit lung tissue.
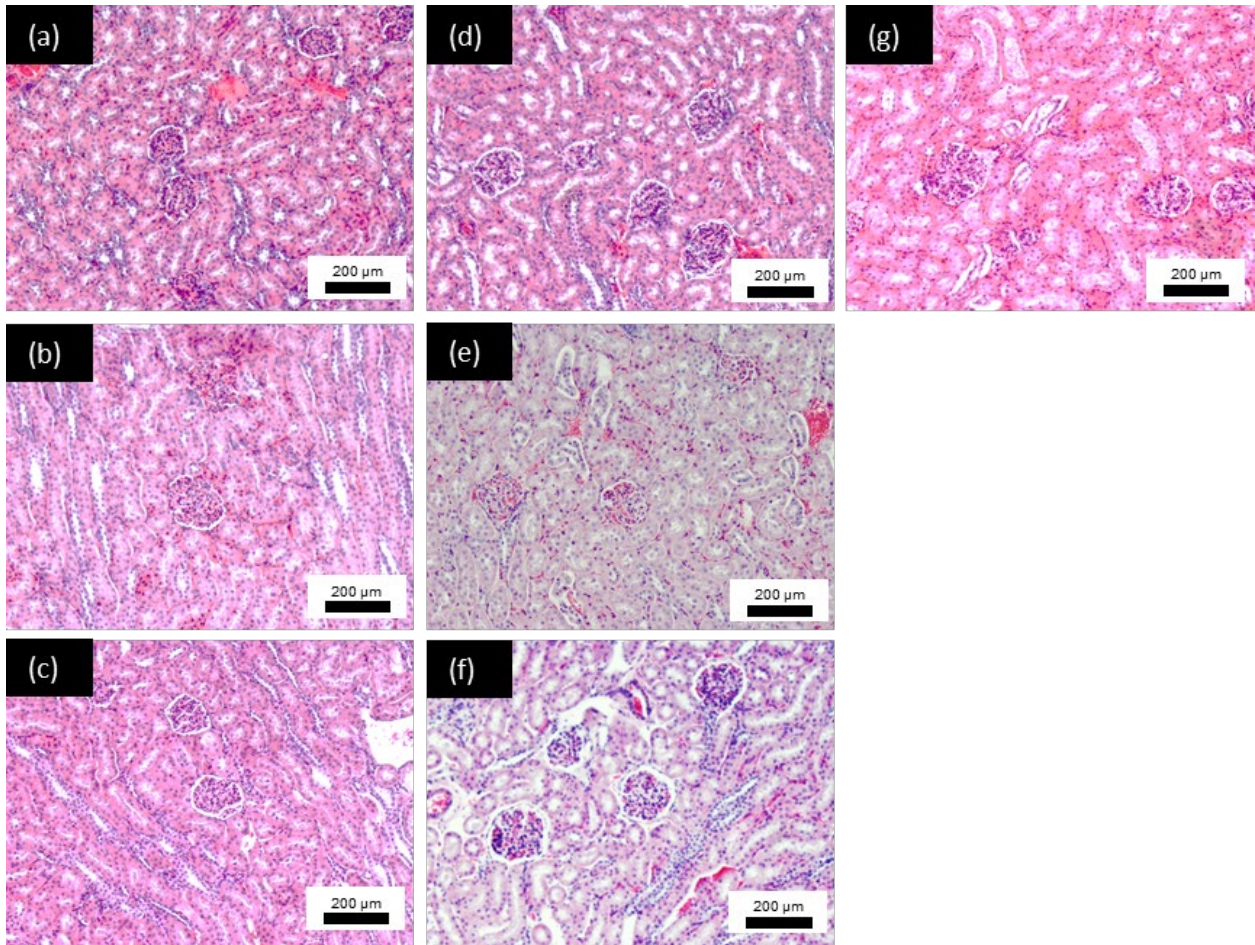
Figure 5.21. H&E staining of the kidney tissue. LZ61 stent group at (a) 4 weeks, (b) 8 weeks and (c) 12 weeks post implantation; 316L ss stent group at (d) 4 weeks, (e) 8 weeks and (f) 12 weeks post implantation; (g) normal rabbit kidney tissue.
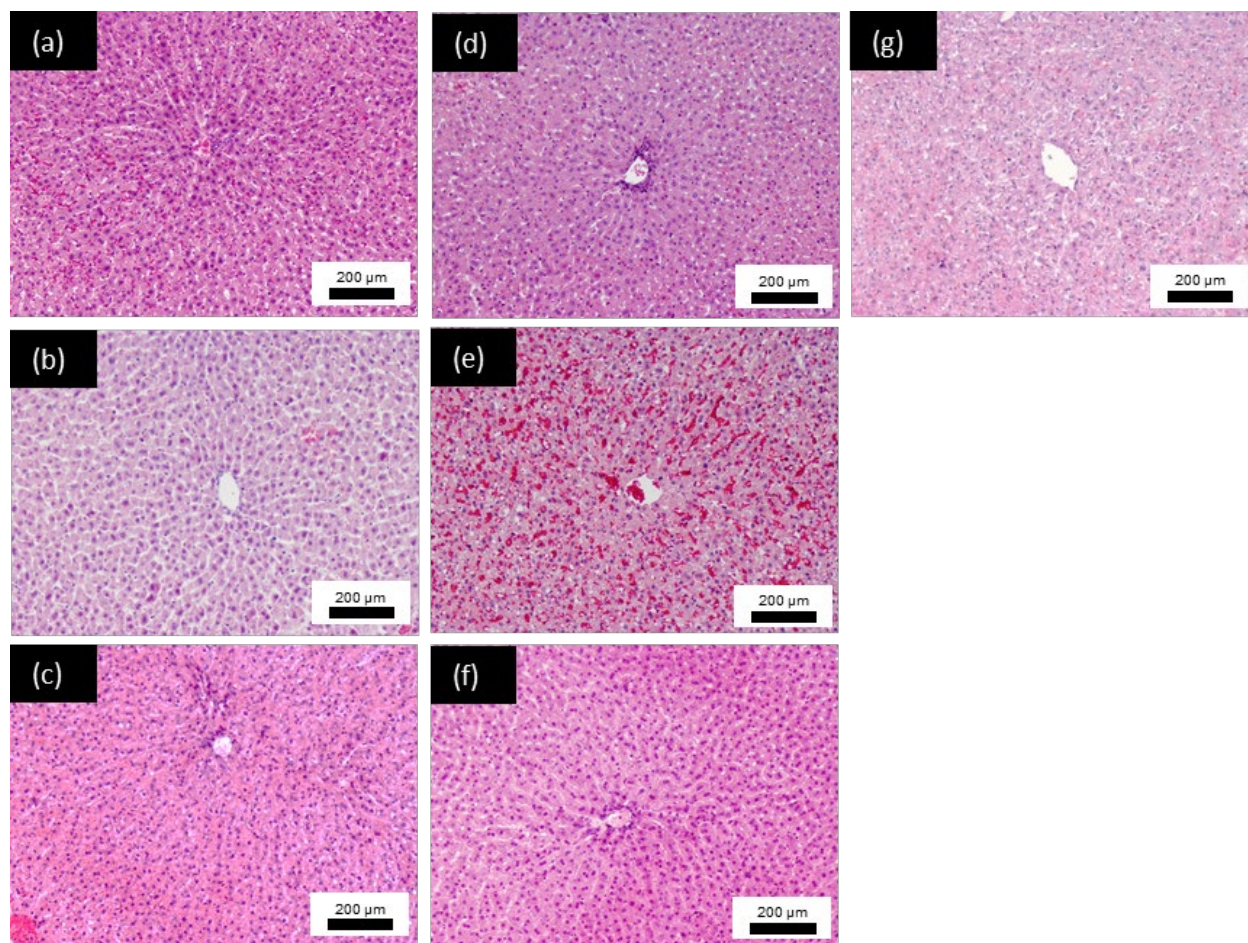
Figure 5.22. H&E staining of the liver tissue. LZ61 stent group at (a) 4 weeks, (b) 8 weeks and (c) 12 weeks post implantation; 316L ss stent group at (d) 4 weeks, (e) 8 weeks and (f) 12 weeks post implantation; (g) normal rabbit liver tissue.

5.4   DISCUSSION

All the commercial balloon stents were manufactured using mini-tubes fabricated by tube extrusion and tube drawing. However, in this study, we chose to produce Mg alloy tubes using

wire EDM considering the ease of processing. Another advantage of using wire EDM is that the microstructure of the Mg alloy was preserved and therefore the mechanical properties and corrosion resistance will not be altered. The impact of tube extrusion and tube drawing on LZ61 alloy is still worthy to be studied in the future since this is a routinely used standard process for industrial grade manufacturing of stent.

This bioreactor study demonstrated much better corrosion resistance of LZ61 alloy when compared to AZ31 alloy. Yun *et al.* proved that the flow-induced shear stress plays an important role in the degradation of Mg alloys. [104] McHugh *et al.* also reported that flow conditions significantly increased the corrosion rate of AZ31 alloys relative to static tests.[105] Three mechanisms were proposed to explain the increase corrosion rate: (1) the flow induced sheer stress prevents the formation of uniform corrosion layer; (2) the flow induced sheer stress leads to more localized corrosion; (3) the flow induced sheer stress causes the detachment of the corrosion layer. For LZ61 stent, more Ca and P was deposited into the degradation layers, and the degradation layer was therefore, much stable than the degradation layer of AZ31 stent. Therefore, LZ61 stents was better protected under flow environment, and exhibited much slower corrosion rate.

Different animal models have been used in tracheal study research, such as rabbit [180, 181], pig [182-184], sheep [185-187] and dog [188]. In general, the trachea of larger animals, such as pig and sheep, are closer to the human trachea in terms of dimension, wall thickness. Rabbits were chosen as the animal model in this study because the major targeting patient group of the LZ61 tracheal stent is pediatric patient. Smaller trachea size of rabbits is closer to the situation of pediatric patients, especially newborns justifying its selection.

After 12 weeks of implantation, there was clear narrowing of the airway due to stenosis formation in 316L ss stent group. Building up of stenosis tissue is typical for metallic non-degradable stents. [25] This is problematic because (1) it is impossible to remove or adjust the metallic stents without causing trauma; (2) the airway will be blocked again due to the ingrowth of stenosis tissue; (3) for pediatric patients, the metallic stent will act as metal cage and inhibit the growth of trachea. LZ61 stents showed advantages over 316L ss stent due the nature of degradable. Rabbit airway fully restored to normal and continued to grow after LZ61 stent was degraded. We also noticed the formation of gas pocket around the LZ61 stents, which were common for magnesium alloy-based implants. [161, 162, 189] For tracheal stent application, the formation of H_2 gas pocket is not issue, all the H_2 gas could be easily removed during respiration.

Despite the encouraging result, LZ61 stent experienced a steep increase of degradation after 4 weeks of implantation. The major difference between the bioreactor system we used here, and the *in vivo* condition is that stents experience cyclic stress after implantation. It is known that the cyclic stress leads to stress corrosion cracking (SCC) [106, 107], which eventually break down the structure of the stents. In addition, the mechanical strength of the stent decreases as the degradation of the magnesium matrix. The stent might crash due the stress from the trachea movement, this will further speed up the degradation/failure of the stent. Further study is clearly necessary to understand how external stress lead to the different degradation pattern of LZ61 stents. At the current stage, there is no standard guidance indicating how long the tracheal stent should last, however, further optimization could be achieved to improve the durability of the stents, such as design optimization, coating technology etc.

As shown in Figure 5.23, the corrosion rates of LZ61 alloy and AZ31 alloy under different tests are summarized. Since AZ31 stents were not implanted *in vivo*, therefore no AZ31

in-vivo stent degradation rate was plotted in Figure 5.23. However, when the LZ61 alloy and AZ31 alloys were fabricated into stents, the degradation rate was observed to significantly increase compared to the corrosion rate measured from the alloys tested in-vitro and in mice sub-cutaneous studies outlined in specific aim 1 in chapter 2 and specific aim 3 in chapter 4, respectively. This could be attributed to two reasons: First, the surface area to weight ratio is much larger for the stents, therefore, a larger area of the metal matrix is exposed to the corrosive environment; Second, the surface condition resulting from electrochemical polishing is different from the surface condition of the disk sample polished by sand paper. It should also be noted that there is no significant difference in the average corrosion rate of LZ61 stent observed in the bioreactor setup after 5 weeks and that determined from the stent implanted in the rabbit trachea model after 4 weeks. These results indicate that the conditions in the bioreactor set up indeed reflects the dynamic nature of the fluid flow across the stent as opposed to the static conditions prevalent in the in-vitro tests of the same alloys tested in the form of discs. At the same time, as discussed in chapter 4, when both alloys were tested as disks implanted in the mice sub-cutaneous model, the corrosion rates exhibited no statistical difference. It therefore appears that the bioreactor conditions are more representative of the actual in-vivo conditions seen in the trachea. More studies are however, clearly warranted to validate and establish a more scientific correlation between the dynamic in-vitro and in-vivo corrosion rates. These studies are planned to be executed in the future and will be tested using the next generation of fabricated tracheal stents.
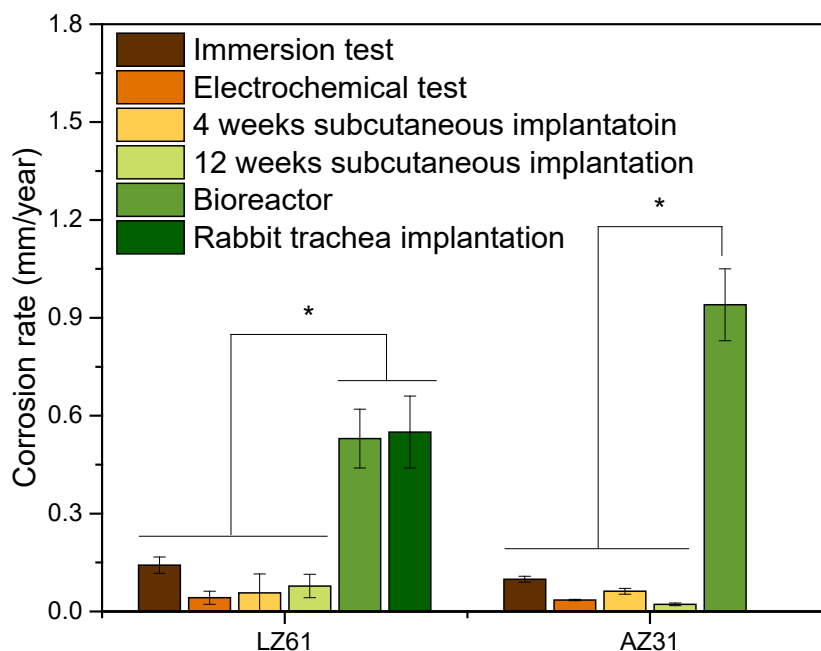
Figure 5.23. A summary of corrosion rate of LZ61 and AZ31 alloy under different test. Immersion test: 5-week corrosion rates calculated based on the immersion test; Electrochemical test: corrosion rates calculated based on tafel plot; 4 weeks subcutaneous implantation: corrosion rates calculated based on the weight loss after 4 weeks of implantation; 12 weeks subcutaneous implantation: corrosion rates calculated based on the weight loss after 12 weeks of implantation; Bioreactor: corrosion rate calculated based on the stent volume loss after 5 weeks of immersion in bioreactor; Rabbit trachea implantation: corrosion rate calculated based on the stent volume loss after 4 weeks of implantation in rabbit trachea. *denotes a significant difference between alloy groups (p <0.05, n=3).

LZ61 stents demonstrated comparable biocompatibility as 316L ss stents based on the H&E staining and alcian blue staining. This is encouraging since 316L ss stents are widely used as biomaterials for implants and demonstrate excellent biocompatibility. Giant cells were noticeable only in few spots of the LZ61 stent stented airway at week 4. This implies the likelihood of potential inflammation observed in the early stages of implantation when the LZ61 stent was undergoing degradation and the corresponding degradation products were released into

the surrounding tissues, mainly the submucosa. For 316L ss stent, since there is no evidence of degradation observed, and the part of the tissue connecting to the stent was removed, no giant cells were identified at the 4 week time point. After the LZ61 stent was fully degraded, the tracheal tissue was observed to be normal when compared to the tracheal tissue of healthy rabbit. No giant cells were identified in the LZ61 stent stented airway at week 8 and 12 which is same for the 316L ss stent group as well, Trachea mucosa layer was fully restored at 8 weeks for LZ61 stent. This is critical, since the scarring of the mucosa layer was the major reason of the stenosis tissue formation. There was no statistically relevant change in regards to the goblets cells observed throughout this study, indicating that the mucus secretion was not impacted by the presence of the 316L ss stent or LZ61 stent. One of the biggest pitfalls raised by previously reported study is that these remnants of the degraded stents might migrate to the bronchi leading to progressing dyspnea.[59] In our study, all the rabbits however, survived the implantation surgery and also endured the stents well. Histology of the lung also did not show any abnormality caused by the debris of the degraded stents. We believe that this is a major advantage of our newly developed Mg-Li ultra-high ductility (UHD) alloy stents compared to biodegradable polymeric stents reported in the literature.

6.0 CONCLUSIONS AND FUTURE WORK

The dissertation herein has presented a comprehensive study utilizing ultra-high ductility (UHD) multi-phase Mg-Li based alloys for biodegradable tracheal stent application. The study began with Mg-Li based alloy design, fabrication and characterization of the generated alloys. This was then followed by further exploring the *in vitro* cytotoxicity using BEAS-2B cells and the *in vivo* degradation and toxicity in mouse subcutaneous model. Finally, prototype stents were fabricated using the overall best alloy, LZ61 alloy, and then assessed for the feasibility of this newly fabricated stent device in a bioreactor system and rabbit airway model. Six Mg-Li based alloys were studied in this study comprising various chemical compositions. Three alloys, namely Mg-6Li-1Zn (LZ61), Mg-6Li-1Al-1Zn (LAZ611) and Mg-6Li-3Al-1Zn (LAZ631) alloys, have higher percentage of the α phase (HCP structure). The other three alloys, namely Mg-9Li-1Zn (LZ91), Mg-9Li-1Al-1Zn (LAZ911) and Mg-9Li-3Al-1Zn (LAZ931) alloys, exhibit higher percentage of the β phase (BCC structure). LZ61 alloy demonstrated the best overall performance and was eventually used for stent fabrication and evaluation. In addition, the work presented here showcased a systematic method of materials design, fabrication, screening and device prototyping, bench testing, and finally, *in vivo* evaluation of the biodegradable tracheal stent. This process could be applied to the study of other materials targeting biodegradable tracheal stent application or the study of novel magnesium alloys for other biodegradable medical device applications.

In specific aim 1, we demonstrated that all the six Mg-Li-Zn-(Al) alloys exhibited chemical composition close to the nominal composition. Both α phase and β phase co-existed in all the six Mg-Li-Zn-(Al) alloys as verified by the X-ray diffraction analysis. With the correct chemical composition and microstructure, all the six alloys exhibited significantly better ductility due to the introduction of the β phase. The strength of the alloy however, expectedly decreased with the presence of a high percentage of the softer metallic Li in the alloy. The alloying element Al contributed to the strength of the materials. With high content of Al in the alloy, the tensile strength and ultimate tensile strength of the Mg-Li-Zn-(Al) alloys also increased. However, the ductility also reduced. In terms of degradation, it appears that alloying with Li and Al both increased the degradation of the alloys. LZ61, LAZ611 and LAZ911 exhibited the lowest corrosion rate after 5 weeks of immersion in HBSS.

In specific aim 2, three Mg-Li-Zn-(Al) alloys, LZ61, LAZ611 and LAZ911, were selected for *in vitro* cytotoxicity test. All the alloys showed acceptable *in vitro* cytotoxicity compared to pure Mg and AZ31. The cell viability of Mg-Li-Zn-(Al) alloys was lower based on the MTT test result, even though Live/Dead imaging showed that cells were still proliferating, and the cell morphology was normal. Further, cell apoptosis assay and cell cycle assay showed that the lower cell viability was not caused by cell apoptosis but due to the inhibition of BEAS-2B cell proliferation. Significantly more cells were locked in the G2/M phases. Further study was performed using $MgCl_2$ and LiCl salts, the results indicating that the lower cell viability was the result of Li ions released into the cell culture media. This implies that, Mg-Li-Zn-(Al) alloys with lower Li content might be beneficial to improve the *in vitro* cytotoxicity.

In specific aim 3, *in vivo* degradation and toxicity of Mg-Li-Zn-(Al) alloys were evaluated in a mouse subcutaneous model. The results clearly showed that the corrosion of Mg-

Li-Zn-(Al) alloys largely depended on the testing method employed, the time of implantation, and the external environment. Weight loss, H_2 gas cavity size and H_2 measurement all resulted in slightly different results. In general, the degradation rate was slower at longer time points due to the protection induced by the stabilized degradation layer. The *in vivo* degradation rate was quite different from the *in vitro* degradation rate calculated by the immersion test. Only LZ61 alloy showed consistently low corrosion rate both, in the *in vivo* and *in vitro* studies. In terms of local toxicity and systematic toxicity, all the six Mg-Li-Zn-(Al) alloys demonstrated excellent biosafety of the alloy and the degradation products.

In the final specific aim, LZ61 alloy were used for stent fabrication. Prototype tracheal stents were successfully manufactured following the procedure we developed. LZ61 stent was first evaluated in a bioreactor system using AZ31 stent as the control. LZ61 stent demonstrated significantly higher corrosion resistance in a dynamic flow environment. This is due to a more stable degradation layer formed with the significant presence of more Ca and P. LZ61 stent was finally implanted in rabbit trachea with 316L ss stent as control. The LZ61 stent fully degraded at week 8 post implantation without displaying any inhibition of growth of the trachea. However, in contrast, the trachea was significantly narrowed after 12 weeks of implantation with the 316L ss stent. The histology analysis also showed excellent biocompatibility of LZ61 stents. However, there was a steep increase in degradation after 4 weeks of implantation. This might likely be due to the prevalence of cyclic stresses continuously applied on the LZ61 stent during the dynamic respiratory process endured by the rabbit.

In conclusion, we have demonstrated the feasibility of using LZ61 alloy based biodegradable magnesium alloy for tracheal stent application. With this new technology, clinicians will be able to apply tracheal stents without the concern of long-term existence of the

stent or combat the difficulty associated with removing these stents. Future studies should be directed to further improve the performance of the proposed magnesium alloy based biodegradable tracheal stent. These studies will focus on: (1) studying the impact of mini-tube fabrication on the mechanical properties and corrosion resistance of LZ61 alloys; (2) optimizing the LZ61 stent design to offer better deliverability and mechanical support: (3) incorporating advanced coating and drug eluting strategies to improve the durability of LZ61 stent and add therapeutic benefits. Execution of research in these directions in the future will likely further improve the performance of LZ61 tracheal stent, and eventually pave the way for a new treatment method for airway obstruction.

APPENDIX A

IDENTIFY THE POTENTIAL USE OF THE SELECTED MG-LI-ZN-(AL) ALLOYS AS BIODEGRADABLE VASCULAR STENT MATERIALS BY CONDUCTING IN VITRO STUDIES

A.1   INTRODUCTION

Cardiovascular disease is the number one killer all over the globe accounting for one out of every three deaths. Since first introduced in 1989, vascular stents have become the default medical device for percutaneous coronary intervention (PCI). [190] Drug-eluting stent (DES) are the current golden standard of vascular stents, which significantly reduce the restenosis rate compared to bare metal stent (BMS). However, concerns have been raised about the use of DES, such as late arterial healing, late stent thrombosis and abnormal vessel remodeling.[73] Bioresorbable Vascular Scaffolds (BVS) are considered as the 4th revolution in PCI technology. The scaffolds will provide temporary support to the vessel wall after angioplasty and are subsequently absorbed upon fulfilling the objectives. However, polymer stents are associated with issues such as stent fracture, inferior deliverability, and malapposition. In addition to tracheal stent application, in the present study, we evaluated the *in vitro* cytotoxicity of Mg-Li-Zn-(Al) alloy for vascular stent application.

A.2   MATERIALS AND METHODS

A.2.1 Cell culture and extract preparation

Human aorta smooth muscle cells (HASMC) (ScienCell Research Labratories #6110) and human vascular endothelial cells (HUVEC) (ATCC #PCS-100-010) were cultured in smooth muscle cell medium (SMCM) (ScienCell Research Labratories) and endothelial cell growth medium (EGM-2) (EGM™-2 BulletKit™, Lonza Biosciences), respectively. Samples were ground utilizing SiC abrasive sand papers up to 1200 grit, sterilized for 30 min by exposure to UV radiation for each side and then immersed in cell culture medium for 72 hours in a standard cell culture incubator. The specimen surface area to extraction medium ratio was maintained at 1.25 cm^2/ml in accordance with EN ISO standard 10993-12:2004. This extraction ratio was designated as 100% extract. Extracts were sterile filtered using a 0.2 µm syringe filter before being added to the cells. Low concentration extracts were prepared by diluting the 100% extract into 75%, 50%, 25% and 10% with cell culture medium.

A.2.2 Indirect MTT assay

Indirect MTT assay were conducted following the same procedure described in previous publications from our group [97, 137]. Briefly, the cells were seeded in 96-well plate at a cell density of 2, 000/well for HASMC and 4,000/well for HUVEC and incubated for 12 hours. Following this, 75%, 50%, 25% and 10% extracts were added with normal cell culture medium serving as the negative control while 10% DMSO cell culture medium served as the positive

control. The well plates were incubated for 1 day and 3 days respectively, and analyzed by Synergy 2 Multi-Mode Microplate Reader (Bio-Tek Instruments, Winooski, VT).

A.2.3   Live/dead staining and DAPI&F-actin staining

In addition to the tests above, live/dead staining was performed to investigate the cell viability while DAPI&F-actin staining was performed to image the cell morphology. Cells with a cell density of 2, 000/well for HASMC and 4,000/well for HUVEC were seeded in 48-well plates and accordingly incubated in 25% extract for 3 days. LIVE/DEAD viability/cytotoxicity kit (Invitrogen Inc., Karlsruhe, Germany) was used to stain the live and dead cells to glow green (ethidium homodimer-1) and red (calcein-AM), respectively. For DAPI&F-actin staining, DAPI (AppliChem, Darmstadt, Germany) served as the fluorescent probe for DNA (blue), and rhodamine phalloidin served as the fluorescent probe to label the F-actin (red).

A.2.4   Cell apoptosis and cell cycle assay

The effect of degradation product on cell apoptosis and cell cycle was evaluated by culturing 50,000 HASMC/well or 100,000 HUVEC/well in 6-well plates in 25% extract for 24 hours. For the cell cycle study, the cells were culture in serum-free medium for 24 hours for synchronization. FITC Annexin V Apoptosis Detection Kit I (BD Biosciences, USA) was used to detect the early apoptosis and late apoptosis. Propidium Iodide (PI) (PI/RNase Staining Buffer, BD Biosciences, USA) was used to measure the DNA content and evaluate the percentage of cells in each cell cycle phase.

A.3   RESULTS AND DISCUSSION

The ICP result (Figure A.1 and Figure A.3) indicates a burst release of Mg and Li ions collected from pure Mg and Mg alloys after incubation for 72 hours in the appropriate cell culture medium. The concentration of Zn was below the detection limits and hence, was not plotted. It can be seen that the Mg ion concentration increases more than 10 folds compared to normal cell culture medium for both SMCM and EBM-2 culture media. For SMCM, The Mg concentration in both pure Mg and AZ31 alloy extracts were significantly higher than LZ61, LAZ611 and LAZ911 alloy extract ($p<0.05$). Li ion concentration was also significantly higher in LAZ911 alloy extract than LZ61 alloy and LAZ611 extract ($p<0.05$). Similar trends applied to EBM-2, the only difference being that there was no significant difference in Mg ion concentration between pure Mg and LZ61 and LAZ611 alloy extract ($p>0.05$).
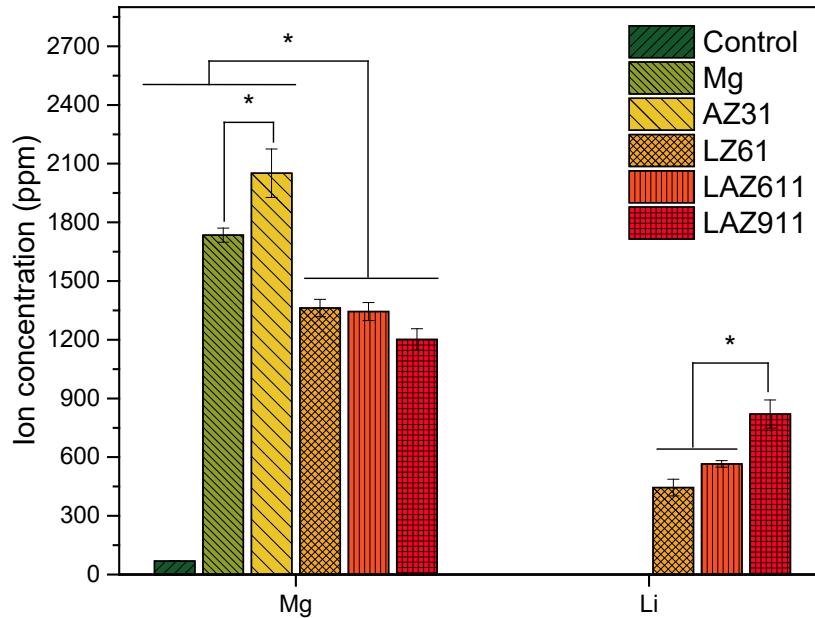
Figure A.1. Concentration of Mg and Li ion in SMCM media extract after 3 days of incubation.

As shown in Figure A.2, HASMC viability was negatively correlated to extract concentration with higher cell viability in lower extract concentration. The cell viability in 75% extract after culturing for 1 day was less than 40%, and even close to 0% for after 3 days of culturing. At day 1 and day 3, only groups with extract concentration of 10% showed close to or more than 100% cell viability. Two-way ANOVA was performed to analyze the statistical difference between the different alloy groups. Magnesium alloy group and extract dilution ratio served as the two independent variables and cell viability served as the dependent variables in the two-way ANOVA analysis. Cell viability of each magnesium alloy group is discussed as an independent variable in general regardless of the extract dilution ratio. At day 1, LZ61 alloy, LAZ611 and LAZ911 groups showed higher cell viability than Mg and AZ31 group ($p < 0.05$), which is because of the high cell viability at 75% extract dilution ratio. At day 3, no significant difference was observed between LAZ611 alloy group and LAZ911 alloy group ($p > 0.05$). LZ61 alloy groups however, showed higher cell viability than all the other groups ($p < 0.05$).
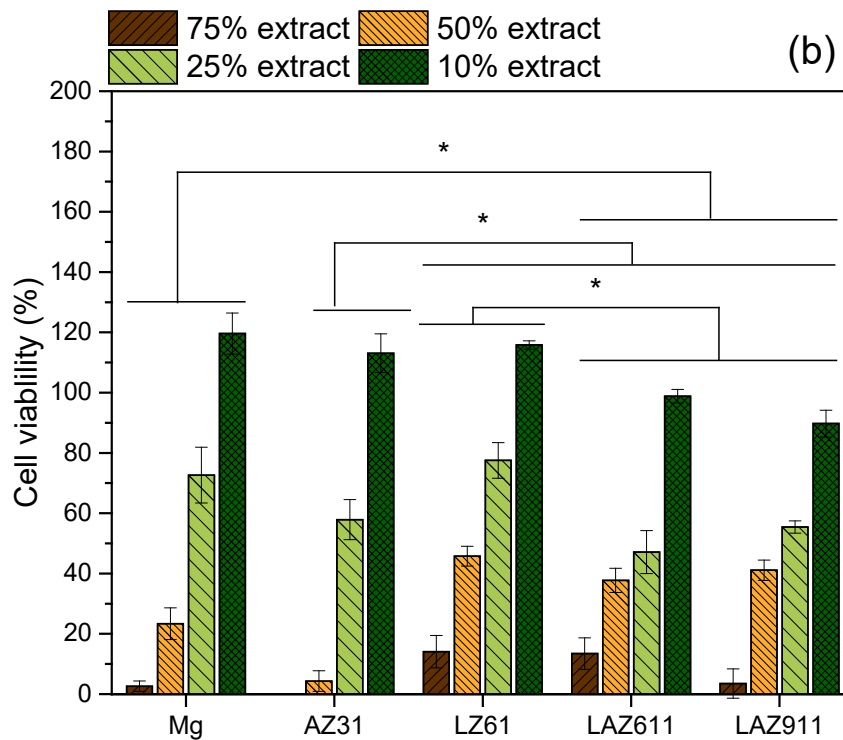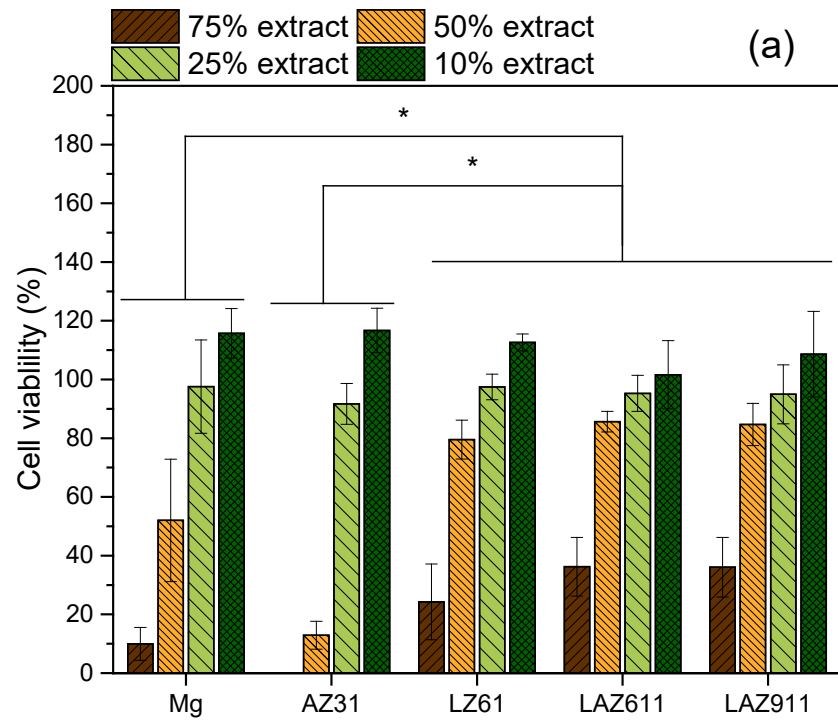
Figure A.2. HASMC cell viability after culturing in different concentration extract for (a) 1 day; (b) 3 days;

*denotes a significant difference between alloy groups (p <0.05, n=3).
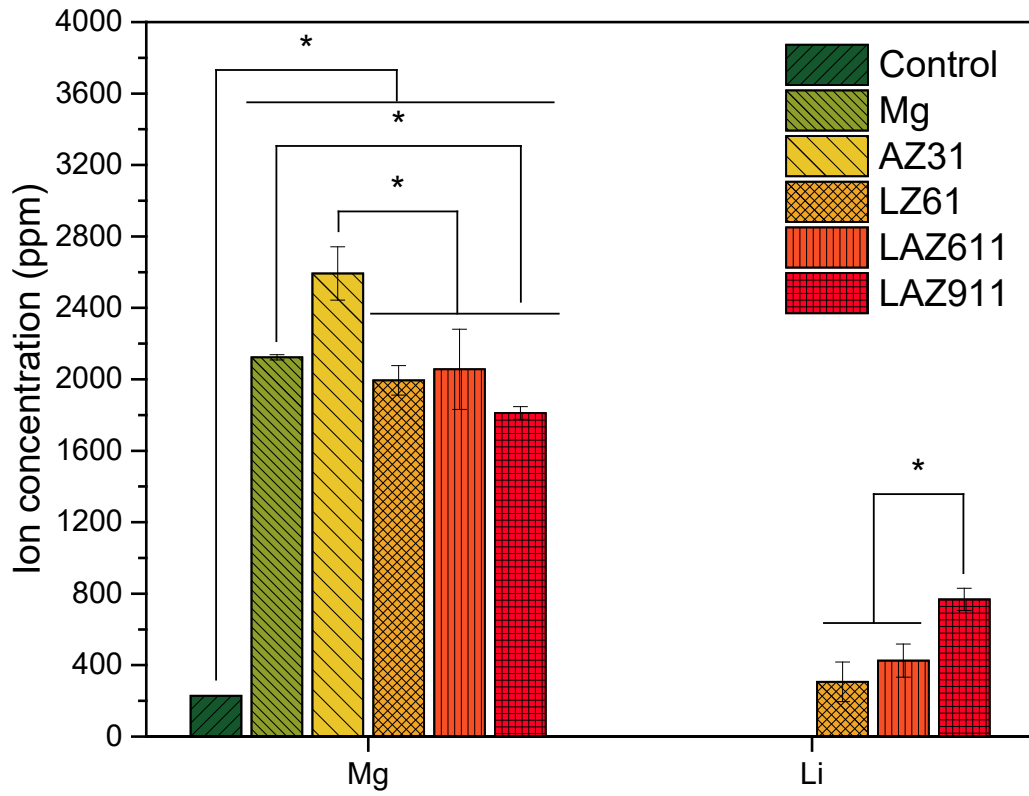
Figure A.3. Concentration of Mg and Li ion in EGM-2 media extract after 3 days of incubation.
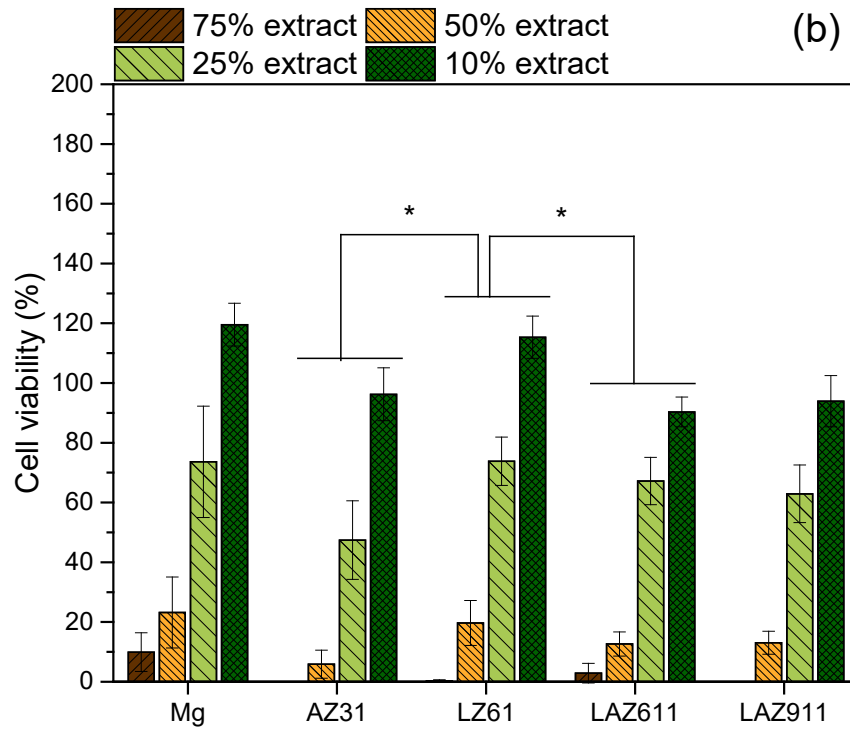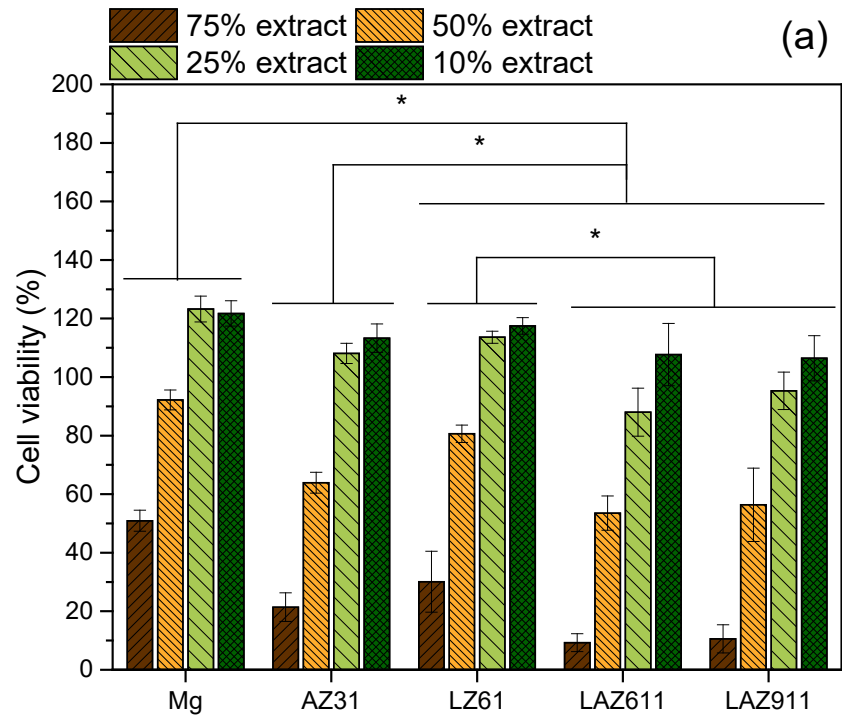
Figure A.4. HUVEC cell viability after culturing in different concentration extract for (a) 1 day; (b) 3 days;

*denotes a significant difference between alloy groups (p <0.05, n=3).

Similar results were observed for the HUVEC cells. Higher HUVEC viability was observed in lower extract concentrations. At day 1, there is no statistically significant difference observed between LAZ611 alloy group and LAZ911 alloy group ($p>0.05$). LZ61 alloy showed lower cell viability than Mg group ($p<0.05$) but higher cell viability than AZ31, LZ61 and LZ91 alloy groups ($p<0.05$). There is also no statistical difference observed between the Mg and AZ31 alloy group ($P>0.05$). At day 3 however, LZ61 alloy group showed higher cell viability than AZ31 and LAZ611 alloy group ($p<0.05$).

Based on MTT results, 25% extract was the only group that showed the impact of degradation products on different cells while still supporting limited cell proliferation. Therefore, 25% extract was used for live/dead staining and DAPI/F-actin staining to visualize the impact of degradation product on cells. Despite the differences observed in the MTT assay discussed above, the live/dead staining of HASMC and HUVEC after culturing in 25% extract showed similar results (**Figure A. 5**, **Figure A.6**). All pure Mg and Mg alloy groups showed lower cell density when compared to the control group, wherein cells were cultured in normal cell culture medium. The Mg-Li-Zn-(Al) alloy groups demonstrated comparable live cell density with very few apoptotic cells. Regardless of the lower cell density, all the pure Mg and Mg alloy groups showed same cell morphology as the cells cultured in normal cell culture medium (**Figure A. 5**, **Figure A.6**). The HASMCs demonstrated a spindle shaped cell morphology while the HUVECs exhibited a rather rounded shaped cell morphology.
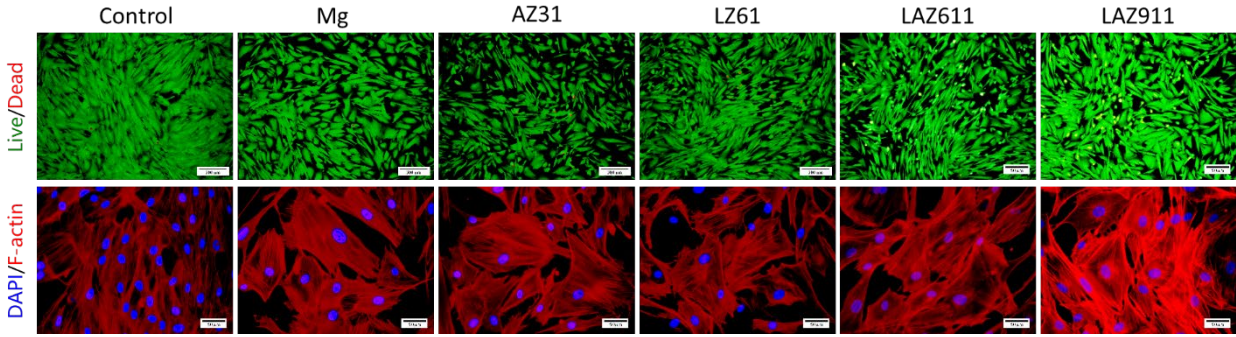
Figure A. 5. (a) Live/dead staining (b) DAPI/F-actin staining of HASMC after 3 days culture in 25% extract or normal cell culture medium (control), scale bar = 300 μm (upper), scale bar = 50 μm (bottom).
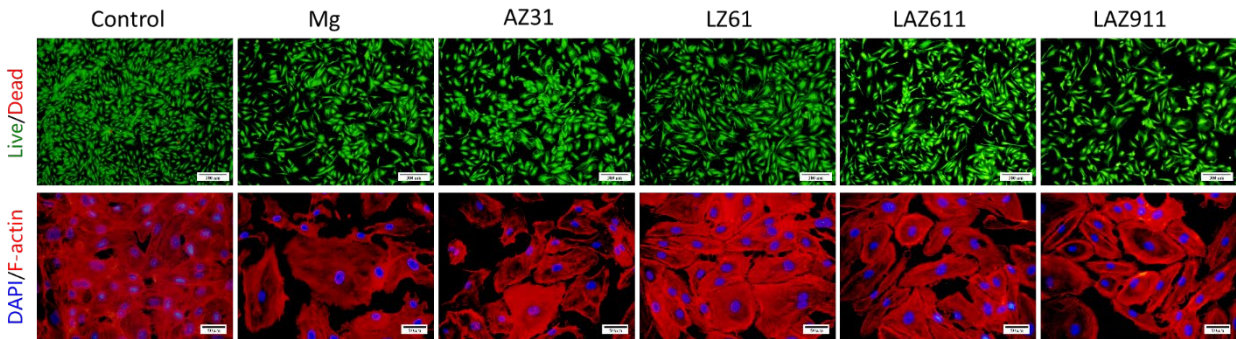
Figure A.6. (a) Live/dead staining (b) DAPI/F-actin staining of HUVEC after 3 days culture in 25% extract or normal cell culture medium (control), scale bar = 300 μm (upper), scale bar = 50 μm (bottom).

The effect of degradation products on cell apoptosis and cell cycle were further investigated by culturing the cells in 25% extract for 24 hours. The apoptosis assay demonstrated a significantly higher early apoptosis and late apoptosis of HASMC cells in the LAZ611 and LAZ911 alloy groups when compared to the other alloy groups (p<0.05) (Figure A.7). As depicted in Figure A.8, pure Mg, AZ31 and Mg-Li-Zn-(Al) alloys extract exhibit similar distribution of HASMC in each of the cell cycle phases to the control groups, where the cells

were cultured in normal cell culture medium. For the HUVECs, the LAZ611 alloy group exhibit significantly higher early stage apoptosis rate (p<0.05) compared to the other groups (Figure A.9). As show in Figure A.10, for HUVEC, no significantly difference was observed among the percentage of cells in G0/G1 and S phases. Slightly more cells were in G2/M phases for LAZ611 and LAZ911 alloys compare to AZ31 and Control (P<0.05).
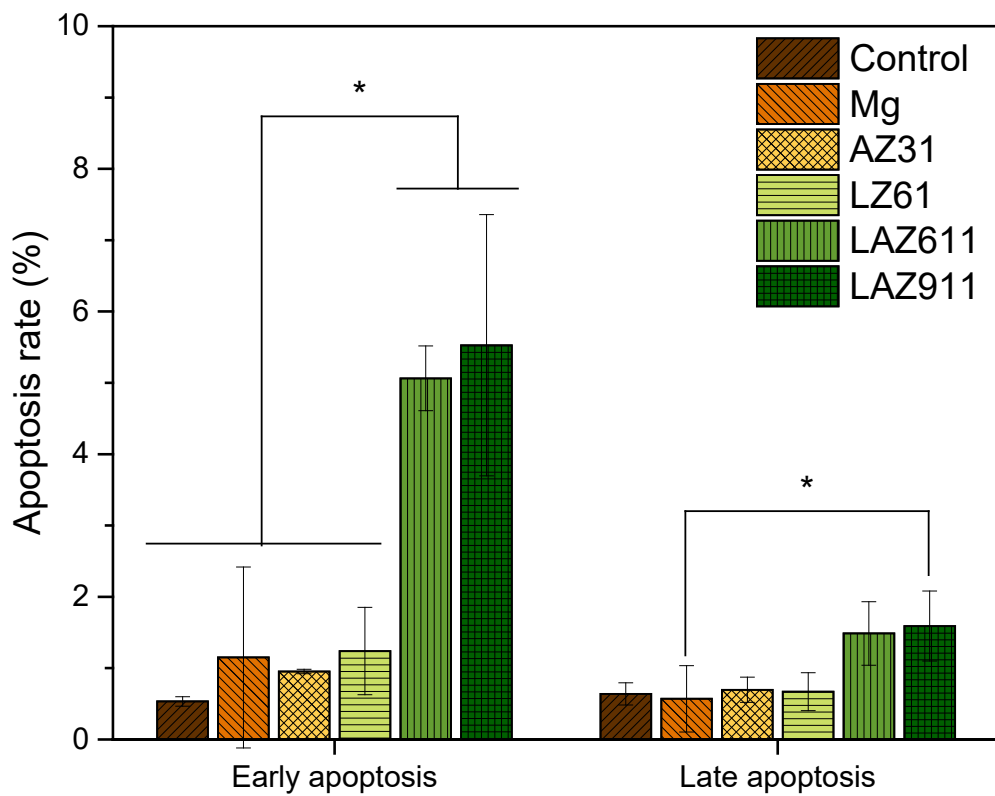
Figure A.7. Early apoptosis and later apoptosis rate of HASMC cells after culturing in 25% extract for 24 hours.

*denotes a significant difference between alloy groups (p < 0.05, n=3).
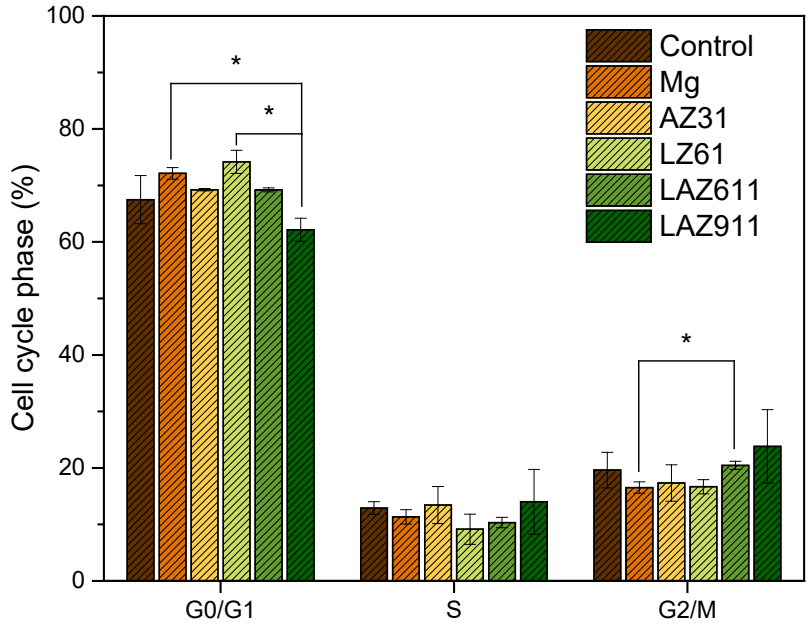
Figure A.8. Percentage of HASMC cells in at different cell cycle phase after culturing in 25% extract for 24 hours.

*denotes a significant difference between alloy groups (p < 0.05, n=3).
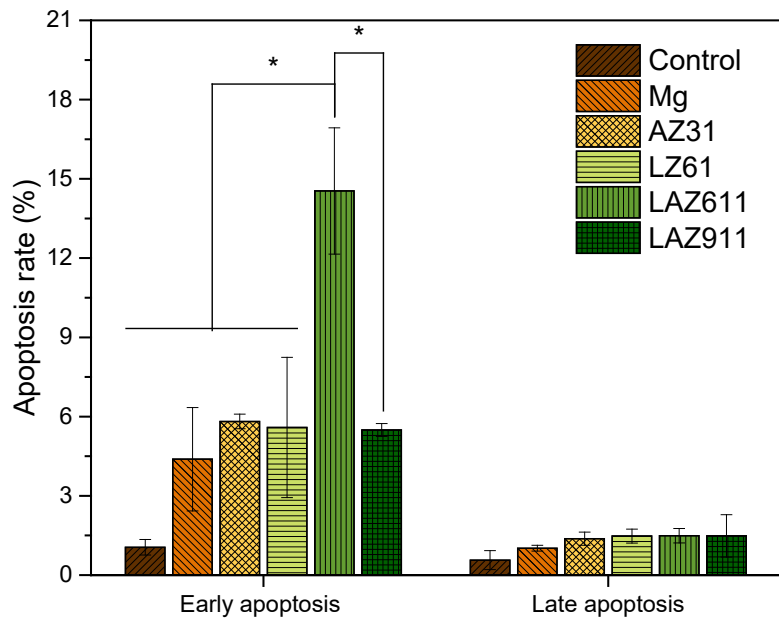
Figure A.9. Early apoptosis and later apoptosis rate of HUVEC cells after culturing in 25% extract for 24 hours.

*denotes a significant difference between alloy groups (p < 0.05, n=3).
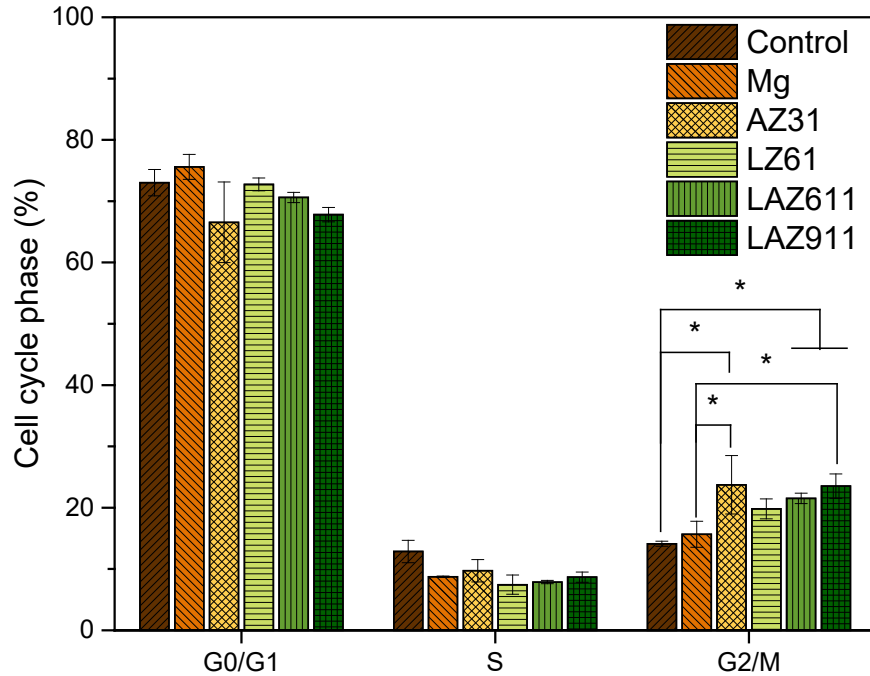
Figure A.10. Percentage of HUVEC cells in at different cell cycle phase after culturing in 25% extract for 24 hours. *denotes a significant difference between alloy groups (p < 0.05, n=3).

Smooth muscle cells and endothelial cells are the two reverent cells that will interact with the magnesium stents following implantation. Therefore, the two human prime cells, HASMC and HUVEC, were selected for evaluating the *in vitro* cytotoxicity of the two selected Mg-Li-Zn alloys of LZ61 and LZ91. Previous study [143] showed that vascular cells exhibited low viability when directly seeded on Mg alloy surface. Therefore, in this study, all cytotoxicity tests were conducted in an indirect manner using the extract protocol. The indirect MTT assay results indicated that 75% and 50% extract concentration resulted in relatively lower cell viability especially after 3 days, while the 10% extract promoted the cell viability. Therefore, the 25% extracts were selected as the extract concentration for all the other *in vitro* cyto-compatibility tests.

The accumulation of degradation product in the extract led to an increase in the apoptosis rate in both HASCMs and HUVECs. Even though Mg-Li-Zn-(Al) alloy groups showed significant increase in the apoptosis rate, we do notice that the average apoptosis rate is higher for all pure Mg group and Mg alloy groups than the negative control group. This result is in agreement with previous studies, where Mg alloy extract caused an increase in the cell apoptosis rate [143, 145, 146]. Zhanhui Wang *et al*. believe that the elevated pH value, and Mg ion concentration are the determining factors that contribute to the observed cell apoptosis [145]. The increase in apoptosis rate also explains why the cell viability is lower at day 3 in the MTT assay for all the extract concentrations studied except for the 10% extract. The effect of extract on the cell cycle also depends on the cell types.

In this study, the cell cycle phase distribution of HASMC and HUVEC cells were by and large observed to be similar, with certain groups exhibiting slightly higher than other groups. Based on the results from this study and previous studies, it could be concluded that the degradation product might affect the occurrence and progression of all three phases of cell proliferation and the effect will depend on alloy composition and corrosion rate. Despite these effects discussed above, the cell morphology of HASMC and HUVEC remained normal after culturing for 3 days in 25% extract which indicates that the surviving cells might still function well. The effect of Li ion on the HASMC and HUVEC is not clear, since the effect of the extract is indeed a combination of all alloying elements. Wang *et al.* proved that LiCl inhibits vascular smooth muscle cells proliferation and migration [149]. However, in the present study, the extract of Mg-Li-Zn-(Al) alloys did not reduce the cell viability of HASMC and HUVEC as well as the cell apoptosis rate and the cell cycle stages. Further study is however, required to clearly understand the effect of Li ion on both the HASMC and HUVEC cell response and eventual fate.

A.4 CONCLUSIONS

All Mg-Li-Zn-(Al) alloys showed comparable *in vitro* cytotoxicity. Particularly, for the LZ61 alloy, similar results of cell viability, cell apoptosis and proliferation to pure Mg and AZ31 alloy were observed. This study clearly indicates that the multi-phase ultra-high ductility Mg-Li-Zn-(Al) alloys displays the potential to be used as stents in cardiovascular disease treatment. Further studies will focus on vascular stent prototyping and evaluating these stents in a clinically relevant animal model.

APPENDIX B

A FEASIBILITY STUDY OF USING BIODEGRADABLE AZXM ALLOY FOR TRACHEAL STENTS APPLICATION

B.1 INTRODUCTION

We evaluated the feasibility of using new developed AZXM alloy for airway stenting application. AZXM alloy was fabricated using conventional casting facility and extruded into rods. The mechanical properties, *in vitro* degradation behavior and cyto-biocompatibility of AZXM alloys were evaluated. In addition, a pilot short-term implantation of prototype stents was conducted to evaluation the airway tissue response to AZXM alloys.

B.2 MATERIALS AND METHODS

B.2.1 Materials fabrication and characterization

AZXM alloy was prepared by conventional casting. Pure metal ingots or pellets were added in the sequence of Mg, Mn, Al, Ca and Zn based on the nominal composition, and were

melted in a mild steel crucible heated to 720°C using an electrical resistance furnace (Wenesco Inc., Chicago, IL). Ar + 0.1% SF_6 was used to create a protective environment. After adding Zn, the melt were kept at 720°C for 10min, mixed by appropriate stirring and poured into a mild steel mold pre-heated at 500°C. The as-cast ingots were solution treated (T4 treated) at 385°C for 10h under the protection of continuous ultra-high pure Argon in a tubular furnace and then quenched in water. After T4 treatment, the ingots were machined into cylinders (ϕ=38mm×60mm) and extruded into rods (ϕ=12mm) at 300°C with an extrusion speed of 1 mm/s followed by quenching in water. The extrusion ratio is 10 for all ingots. The actual chemical composition of AZXM alloy was verified by inductively coupled plasma optical emission spectroscopy (ICP-OES, iCAP duo 6500 Thermo Fisher, Waltham, MA). The formation of phases was tested by XRD (Philips X'Pert PRO diffractometer), employing Cu Kα (λ = 1.54056 Å) radiation with a Si detector (X'celerator). The X-ray generator operated at 45 kV and 40 mA at a 2θ range of 10–80°.

B.2.2 Microstructure characterization

To observe the microstructure of AZXM alloys, round plate samples (ϕ=10mm×2mm) were sliced by lathe from the center of the as-cast/T4 treated ingots and extruded rods. All samples were grinded with SiC abrasive sandpapers up to 1200 grit and polished with monocrystalline diamond suspension spray (1 μm, Buehler) and finally with Masterprep® Alumina Suspension (0.05 μm, Buehler). Samples were etched in a solution of 5 ml acetic acid, 6 g picric acid, 10 ml water and 100 ml ethanol. Microstructures of samples were observed under a Nikon Optiphot microscope (Nikon, Tokyo, Japan) and scanning electron microscopy (SEM;

JSM6610LV, JEOL) coupled to an energy dispersive x-ray (EDX) (Oxford Instruments, Abingdon, Oxfordshire, UK).

B.2.3   Mechanical property characterization

Tensile testing was performed for as-cast, T4 treated and extruded AZXM alloys, as well as AZ31 alloys as control. Tensile bars were machined along the axis direction of the ingots or extruded rods by CNS machine. The size of the tensile bars was determined as per ASTM E8/E8M-11 standard with a half inch gauge length and 3 mm × 3mm gauge area. For each sample, a stress-strain curve was generated by Instron 5969 testing system (Instron, Norwood, MA) equipped with an extensometer (Instron 2630 series, Norwood, MA) measuring the elongation. Three typical stress-train curves from each group were used to calculate the yield strength (YS) and ultimate strength (UTS) and elongation at fracture (EL) using Bluehill® 3 Testing Software for Mechanical Testing Systems (Instron, Norwood, MA). Average and standard deviation of the three samples were calculated for each group.

B.2.4   *In vitro* degradation evaluation

Immersion test was conducted to evaluate the *in vitro* degradation of AZXM alloys based on ASTM standard G31-12a. Round plate samples (ϕ=10mm×2mm) were sliced by lathe from the center of the as-cast/T4 treated ingots or extruded rods along the axis direction. All samples were grinded with SiC abrasive sandpapers up to 1200 grit. All samples were then sonicated in ethanol, weighed and sterilized under UV. Each sample was immersed in Hanks' solution in a 50mL Bio-Reaction centrifuge tube with a 0.22μm hydrophobic membrane in the vent cap. The

ratio of Hank's solution volume to sample surface area is 0.20 mL/mm^2. All samples were stored in CO_2 incubator and kept in 37°C and 5% CO_2 humidified atmosphere. After immersion for 1, 2, and 3 weeks, samples were retrieved from buffer media, washed in DI water, ethanol and dried in air. Corrosion products were removed by immersion in solution of 200g chromium trioxide, 10g silver nitrate and 100ml water for 10min. The samples were then washed in DI water, ehanol, dried in air and weighed. Corrosion rate was calculated based on mass loss; the equation used for calculation is list below:

$$Corrosion\ Rate(mm/year) = (K \times W)/(A \times T \times D) \quad (1)$$

Where the constant K is 3.65×10^3, W is mass loss (g), A is the surface area of each sample (cm^2), T is the immersion time (Day), and D is the density of each alloy (g/cm^3). One sample from each group at each time point will be mounted in epoxy to obtain the cross-section profile of degradation layer and degradation morphology.

B.2.5 Extract preparation

Round plate samples (ϕ=10mm×2mm) were sliced and grinded with SiC abrasive sandpapers up to 1200 grit. All samples were then ultrasonically cleaned in ethanol, dried in air, sterilized under UV for 30 min each side. The extract was obtained based on the IOS 10993-12-2012 standard. All the samples were pre-incubated in Bronchial Epithelial Cell Growth Medium (BEGM™; Lonza, Walkersville, MD, USA) for 72 hours at 37°C in a humidified atmosphere with 5% CO_2. The ratio of sample surface area to medium volume is 1.25 cm^2/ml. After pre-incubation, the extract was filtered with 0.22μm syringe-driven filter and kept in 4°C freezer.

Totally 3 samples were used for each group at each time point in following tests. The concentrations of different elements in extract were measured by ICP-OES.

B.2.6 Cell viability test

Normal human bronchial epithelial cells (BEAS-2B, American Type Culture Collection, Rockville, MD) were cultured in BEGM medium at 37ºC in a humidified atmosphere with 5% CO_2 before seeded into 96-well plates at the density of $8 \times 10^3/100$ μl in each well. After incubation for 24 hours to allow the cells to attach the 96-well plates, the media were replaced by extract diluted by BEGM at different diluting ratio (10%, 25%, 50% and 75%). Same volume of BEGM medium was added as control. BEAS-2B cells were incubated in extract for another 1 or 3 days. CyQUANT® NF Cell Proliferation Assay Kit (Life Technologies, Grand Island, NY) were used based on its protocol. Briefly, before the test, a standard curve was generated by measuring the fluorescence intensities of $4 \times 10^3, 8 \times 10^3, 1.2 \times 10^4$ and 1.6×10^4 BEAS-2B cells. After each time point, BEAS-2B cells in 96-well plates were washed with PBS and then incubate with 50μL dye binding solution. Plates were incubated at 37ºC and measured using fluorescence microplate reader with excitation at ~485 nm and emission detection at ~530nm. The highest fluorescence intensity value was picked and converted to cell number using standard curve.

B.2.7 Live & Dead and DAPI/α-actin staining

1.6×10^4 BEAS-2B cells were seeded in each well of 48-well plates and incubated for 24 hours for cell attachment. Cell culture medium was then replaced by a mixture of 50% alloy extract and 50% BEGM. After 3 days of incubation, BEAS-2B cells were staining with calcein and ethidium homodimer-1 using commercial available LIVE/DEAD® Viability/Cytotoxicity Kit (Invitrogen Inc., Karlsruhe, Germany). The cells were then imaged under fluorescence with ex/em ~495 nm/~515 nm (live cells) and ex/em ~495 nm/~635 nm (dead cells) respectively. To image the cell morphology, BEAS-2B cells were stained by DAPI (AppliChem, Darmstadt, Germany) and Phalloidin (Sigma-Aldrich, St. Louis, MO) to visualize the nucleus and F-actin.

B.2.8 *In vivo* evaluation of AZXM prototype stents

To further evaluate the biocompatibility of the AZXM alloys, prototype stents were machined from extruded AZXM rods using CNC machining. The stents were designed as a non-expandable tube structure with an outer diameter of 5mm, inner diameter of 4mm and length of 15mm. All stents were sonicated in isopropanol for 5 minutes and dried in air, and then terminally sterilized with γ-irradiation (J.L. Shepherd, San Fernando, CA) before implantation. The dose rate is 2425cGy/min, and total dosage is 2,000,000 cGy.

This animal study was conducted under a protocol approved by Institutional Animal Care and Use Committee (IACUC) at University of Pittsburgh. One rabbits was anesthetized by intramuscular injection of ketamine/xylazine, 35mg/kg and 5mg/kg respectively, before surgery. A vertical midline incision was made to expose the airway. The prototype stent was delivered

through the incision and placed inside the lumen of tracheal. The anterior vertical airway incision was closed using 4/0 Vicryl (polyglactin 910) and skin and subcutaneous layer were together closed with 4/0 Vicryl (polyglactin 910) interrupted sutures allowing air.

After 4 weeks of implantation, endoscopy imaging was performed before the rabbit was anesthetized. Laryngo-tracheal region of the airways was harvested with prototype stent inside and fixed in formalin. The tissue was trimmed and embedded in paraffin. The embedded paraffin blocks were fixed on a microtone and cut into thin slices and stained with hematoxylin-eosin.

B.2.9 Statistics

The obtained results were expressed as the mean ± standard deviation. Two-way ANOVA was conducted to determine differences between different groups of samples. Statistical significance was defined as $p < 0.05$. Statistical analysis was performed with IBM SPSS Statistics 24 for Windows.

B.3   RESULTS AND DISCUSSION

B.3.1 Microstructure and mechanical properties of AZXM alloy

AZ31 alloy has been tested as a biodegradable magnesium alloy in numerous studies because of the high corrosion resistance and mechanical properties.[92, 93, 102] Al is the most common alloying element which improves the mechanical properties and corrosion resistance of magnesium alloys.[191] However, the neurotoxicity of aluminum of Al has been reported in

previous publications.[132-134] The release of Al ions as magnesium alloy degrades might lead to similar neurotoxicity as reported. Therefore, it would be beneficial to reduce the content of Al and maintain the mechanical properties and corrosion resistance of AZ31 alloys. In this study, a novel AZXM alloy was developed by modifying AZ31 alloy where Al is partially replaced by Ca.

Table B.1 **Chemical Composition of AZXM alloys** listed the actual chemical composition of AZXM alloy. The actual content of each alloys were close to nominal composition of AZXM alloy except Mn. The reasons could be: (1) Mn has much higher melting temperature compared to other elements in AZXM alloys, it's likely that Mn is not fully melted; (2) In Mg-Al alloys, Mn reacts with detrimental impurity iron and form $Al_5(Fe, Mn)_2$ which precipitate to the bottom of the melt. [192]

Table B.1. Chemical Composition of AZXM alloys.

	Al	Zn	Ca	Mn	Mg
Nominal Composition (wt. %)	2%	1%	0.6%	0.2%	Bal.
Chemical Composition (wt. %)	1.92%	1.05%	0.56%	0.02%	Bal.

As shown in Figure B.1(a), as-cast AZXM alloy consists of fine equiaxed grains with secondary phase precipitation homogenously distributed within the grains. After T4 treatment, AZXM alloy exhibited no significant change but the partially dissolve of second phase precipitation (Figure B.1(b)). Extruded AZXM alloys (Figure B.1(c, d)) exhibited typical fibrous extrusion texture. The grains are significantly refined and elongated along the extrusion direction

indicating that dynamic recrystallization happened during the extrusion process. Similar results were observed under SEM/EDX (Figure B.2). The SEM image showed same microstructure to what was observed under optical microscope. The enlarged view of the microstructure of AZXM alloys and spot chemical analysis of the grain and the grain boundaries by SEM and EDX are show in Figure B.2(b, d, f, g). The EDX (Figure B.2(g)) results indicated that the Ca content was rich in both grain boundary and precipitated secondary phases. The content of Ca in AZXM alloy matrix was much lower. This result is in agreement with previous studies that Ca is preferentially precipitates along gran boundaries and second phase of magnesium alloys.[193] [194] The solubility of Ca in Mg matrix is low with a maximal solubility of ~1.35% (wt. %) at 516.5°C. As the ingot cool down, a eutectic structure is formed between Mg_2Ca and Mg. And therefore Ca was preferentially concentrated in intermetallic phases and grain boundaries. However, the XRD spectacular (Figure B.3) of AZXM alloys didn't show any obvious peaks associated with second phases, but only peaks of α-phase. This might due to the low volume percentage of second phases.
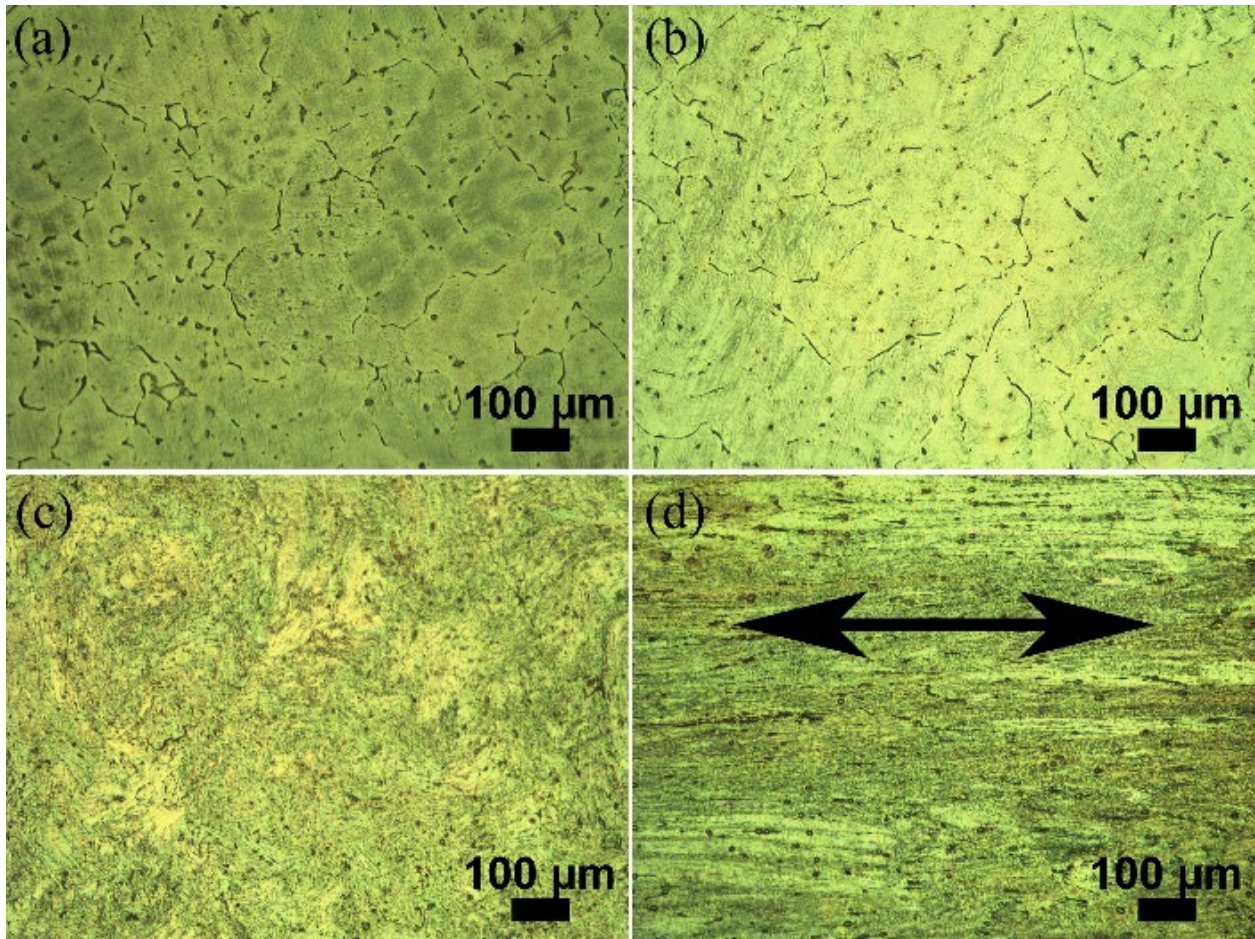
Figure B.1. Optical microstructure of the AZXM alloys a) as cast, b) T4 treated, and extruded c) transverse direction, d) longitudinal direction; the arrow indicates the extrusion direction.
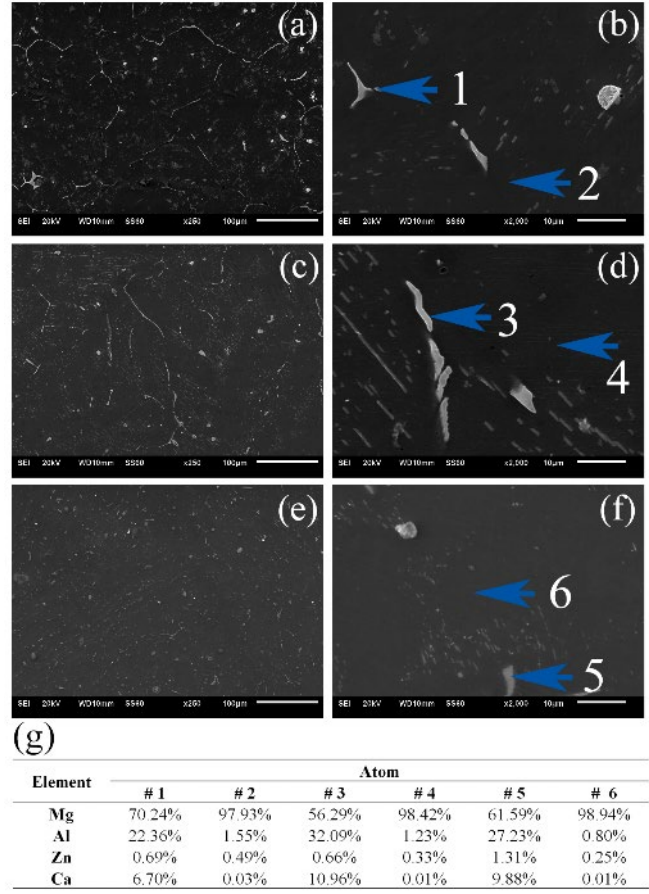
Figure B.2. SEM microstructure of the AZXM alloys as cast (a, b), T4 treated (c, d), as extruded (e, f). (g) The chemical compositions of corresponding spots obtained from EDS analysis.

Element	Atom					
	# 1	# 2	# 3	# 4	# 5	# 6
Mg	70.24%	97.93%	56.29%	98.42%	61.59%	98.94%
Al	22.36%	1.55%	32.09%	1.23%	27.23%	0.80%
Zn	0.69%	0.49%	0.66%	0.33%	1.31%	0.25%
Ca	6.70%	0.03%	10.96%	0.01%	9.88%	0.01%
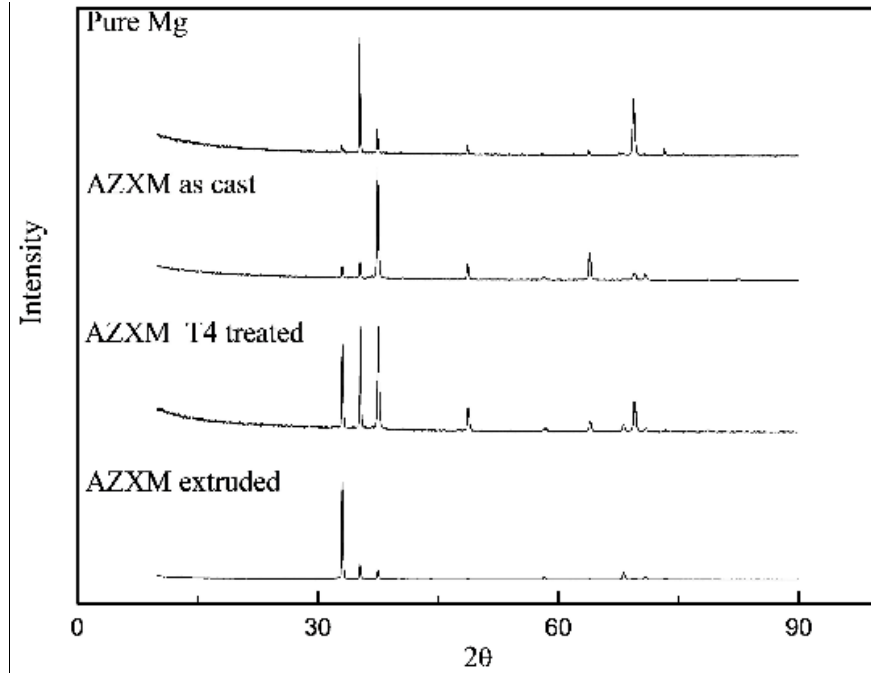
Figure B.3. XRD pattern of AZXM alloys.
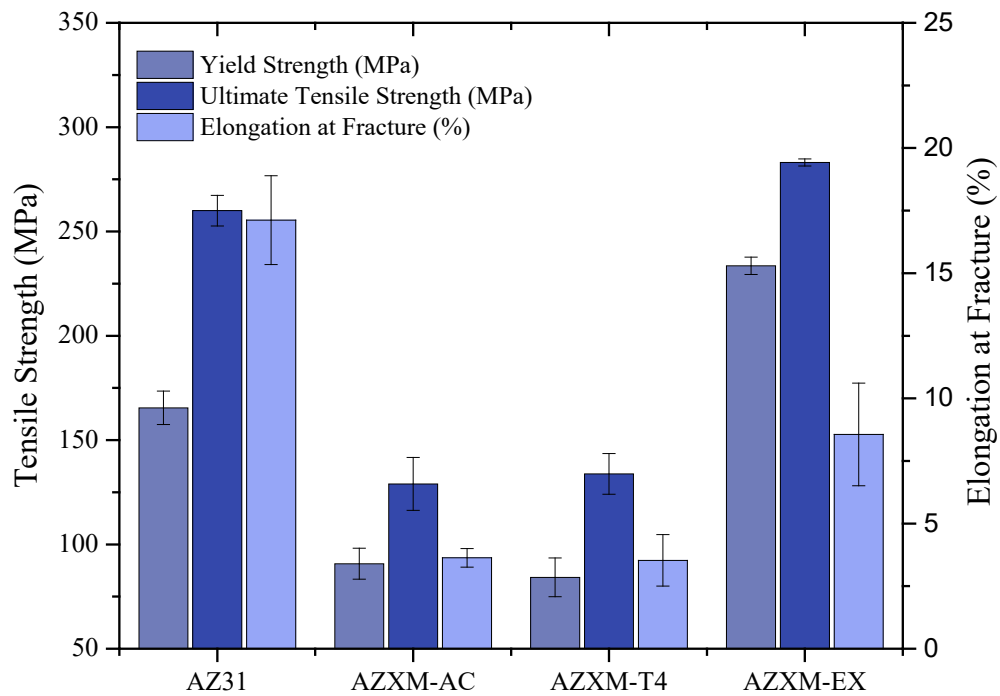
Figure B.4. Mechanical properties of AZXM alloys.

160

For stents application, the tensile properties are of more interest. The tensile properties of AZXM alloy were shown in Figure B.4. As cast AZXM alloys possessed low strength and ductility when compared to AZ31 alloy. T4 treatment resulted in a slightly decrease of YS, however, slightly improvement of UTS. Significant mechanical properties improvement was observed after hot extrusion. Both strength and ductility of AZXM alloy were significantly higher than as-cast and T4 treated AZXM alloys. Compared to AZ31 alloys with YS of 165.45 ± 8.01MPa and UST of 259.97 ± 7.30 MPa, the extruded AZXM alloys exhibited higher strength with YS of 233.53 ± 4.15 MPa and UST of 283.08 ± 1.72 MPa. In this study, AZXM alloy was relatively brittle compared to AZ31 alloys. After extrusion, AZXM alloy possessed elongation of $8.56\pm2.05\%$ at fracture, which is much smaller than $17.12\pm1.77\%$ of AZ31 alloys. This results are in line with previous observations[194, 195].

By adding Ca into Mg-Al-Zn alloy system, the strength of the alloy is improved because of the solid solution strengthening. The reduction of ductility after adding Ca is also found in the study of other Mg alloys[195, 196]. It was reported that the lamellar Mg_2Ca phase had a harmful effect on the ductility of binary Mg-Ca alloy[197]. The Mg_2Ca phase which was concentrated at the grain boundaries acted as the nucleus of cracking. As metallic materials, Mg alloys are easy of hot working, therefore the further material processing could potentially improve the ductility of Mg alloys, such as ECAP.

B.3.2 *In* vitro degradation of AZXM alloy

In vitro degradation profile of AZXM alloy was presented in Figure B.5. As cast AZXM group exhibited poor corrosion resistance and corroded fastest among all groups. The corrosion rate was increasing over 3 weeks of immersion reaching 6.78 ± 0.31mm/year at week 3. T4

treatment significantly improved the corrosion resistance of AZXM alloy and the average corrosion rate peaked after 2 weeks of immersion (1.46±0.07mm/year), and started to decrease thereafter with a corrosion rate of 0.77±0.32mm/year at the end of 3 weeks. Slowest corrosion rate of AZXM alloy was observed after extrusion. The 3-week average corrosion rate of AZXM alloy is 0.19±0.06mm/year, slightly higher than the 3-week average corrosion rate of AZ31 alloy (0.13±0.07mm/year). To investigate the corrosion mode of the AZXM alloys, the cross-sections of samples after 3 weeks of immersion were observed under SEM (Figure B.6). Even though pure Mg corroded relative slow, pit corrosion is the primary corrosion mode. The corrosion of AZ31 is much uniform compared to pure Mg, but corrosion is not homogeneous, pit corrosion is the major corrosion mode. As cast AZXM and T4 treated AZXM corrode much faster, and hence after 3 weeks of immersion, a thick degradation layer formed on the surface of the samples. Compared to AZ31, even though the corrosion rate of extruded AZXM is slightly higher, the overall corrosion appears to be more uniform (Figure B.6). The EDX element mapping of as cast AZXM degradation layer is shown in Figure B.7, the result shows that the degradation layer is made of MgO and $Mg(OH)_2$ with Ca and P deposited on the surface of corrosion layer.
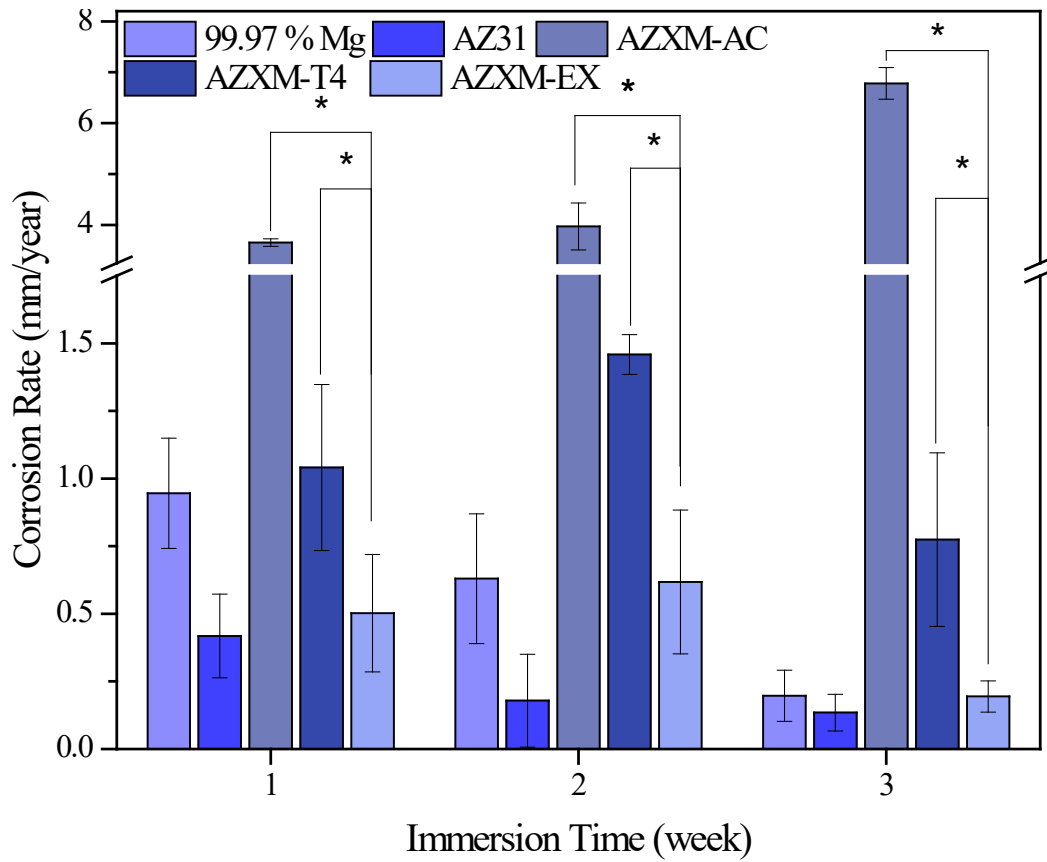
Figure B.5. In vitro degradation rate of AZXM alloy in Hank's solution.
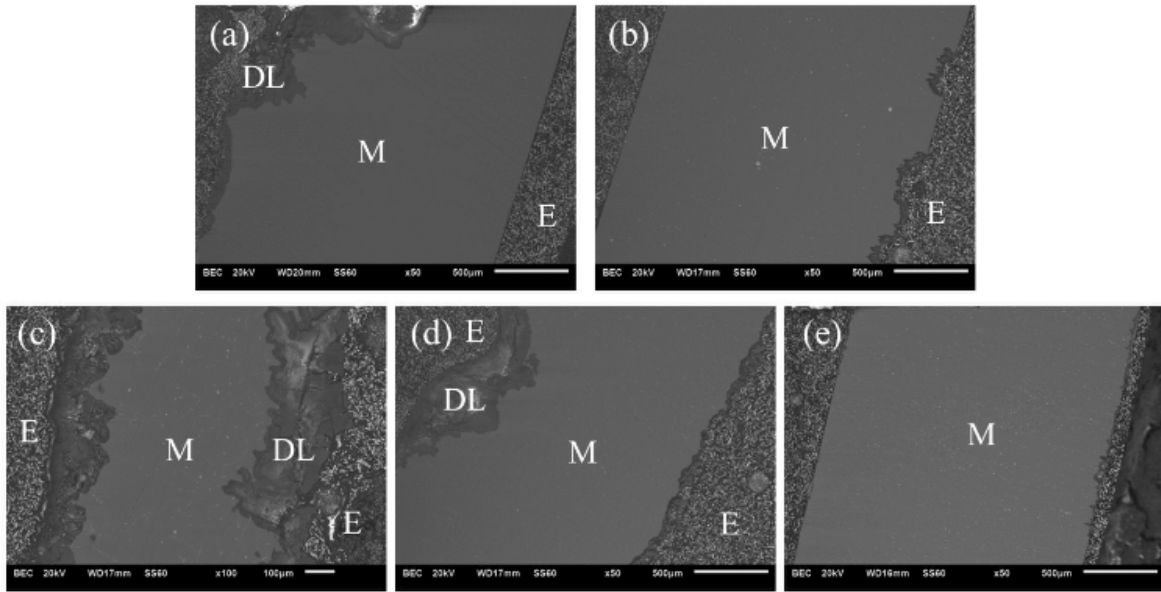
Figure B.6. SEM micrographs of the corrosion profile after immersion for 3 weeks. (a) 99.97% pure Mg, (b) AZ31, (c) AZXM as cast. (d) AZXM T4 treated. (e) AZXM as extruded. (E=epoxy, DL=Degradation layer, M=Mg or Mg alloys.) The bar equals 500 μm for (a), (b), (d), (e) and 500 μm for (c).
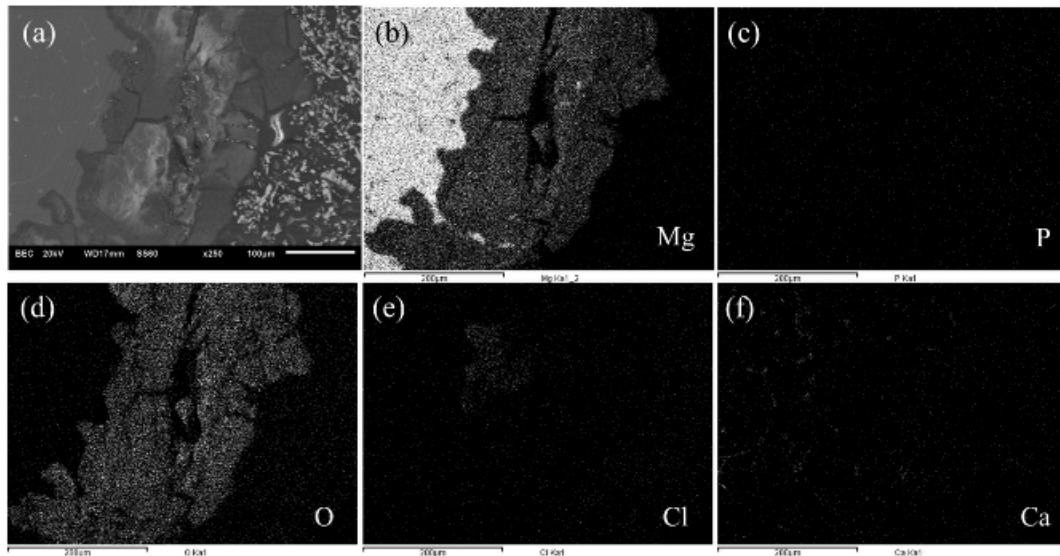
Figure B.7. EDS mapping of the corrosion pit of as cast AZXM sample (a) SEM image corrosion pit; EDS mapping of (b) Mg, (c) P, (d) O, (e) Cl, (f) Ca.

According to previous publications, the corrosion resistance of Mg alloy could be enhanced by increasing the Ca content, but became worse after the amount of Ca reaching certain limitation. Wan *et al.* demonstrated that Mg–0.6Ca showed highest polarization resistance indicating the highest corrosion resistance and the polarization resistance decreased when more calcium is added.[198] The increased corrosion rate could be explained by the higher amount of second phase that causes micro-glavanic corrosion. The enhancement of corrosion resistance after adding small amount of Ca (< 1%) generally could cause by the reduction of oxidation in the molten condition and lower Ca containing α-Mg activity.[195] Grain refinement also significantly improved the corrosion resistance of AZXM alloys in this study. Ca is believed to server as a grain refinement additives, [199] and the extrusion further reduced the grain size resulting in higher corrosion resistance, similar results were also shown in previous study on Mg-Ca alloy [194]. In this study, AZ31 showed the slowest corrosion rate indicating that replacing Al with Ca led to the increase of the corrosion rate.

The corrosion of AZXM alloy is also governed by the oxide film formed on the surface of magnesium alloy. The protective film on magnesium formed in Hank's solution was composed mainly of $Mg(OH)_2$. However, of $Mg(OH)_2$ layer is soluble in most aqueous environments, and incompletely cover the metal surface, localized corrosion usually happens at unprotected spot of the surface. The *in vitro* corrosion showed that, after extrusion, AZXM alloys exhibited much more uniform corrosion when compared to AZ31. The reason could be the addition of Ca stabilized the degradation layer of AZXM alloys, and further inhibit the pit corrosion. For stent application, less pit corrosion could prevent stent from facture.

B.3.3 *In vitro* and *in vivo* evaluation of AZXM alloy

Figure B.8(a) shows the ion concentrations of Mg, Al, Zn, and Ca in the extract. Compared to the cell culture medium, the concentration of Mg increased from ~12 ppm in BEGM to 1000-1300 ppm in extract. The concentration of Al increased slightly, implying that most Al incorporated into oxide film on the magnesium alloy surface. Zn concentration increased in all groups except pure Mg which means that the increase of Mg concentration induce the deposition of Zn on the samples. For Ca, the pure Mg and AZ31 groups both showed a dramatic drop of the Ca concentration indicating the reduced solubility of Ca in high magnesium concentration medium. However, because of the corrosion of AZXM, the amount of Ca released compensated the deposition of Ca, hence the concentration of Ca in AZXM groups remain similar level as the cell culture medium.
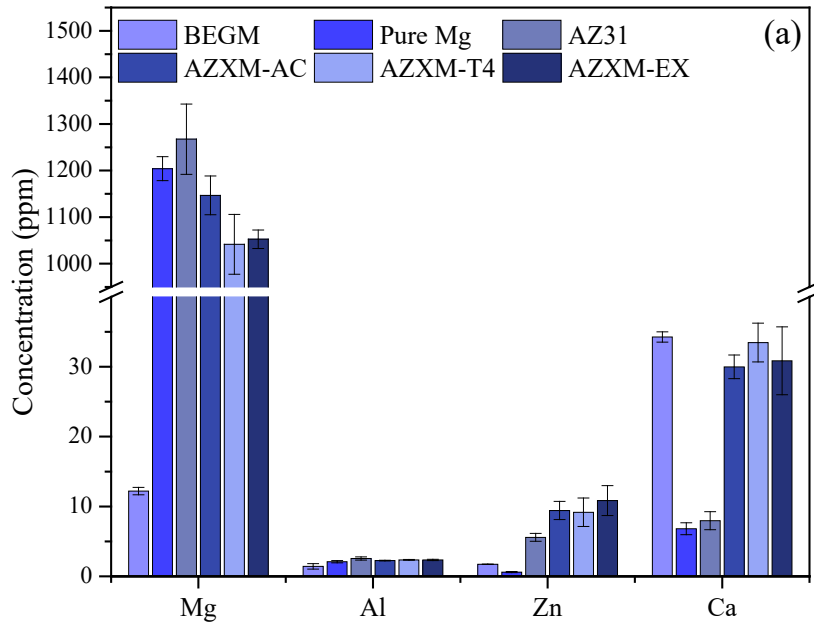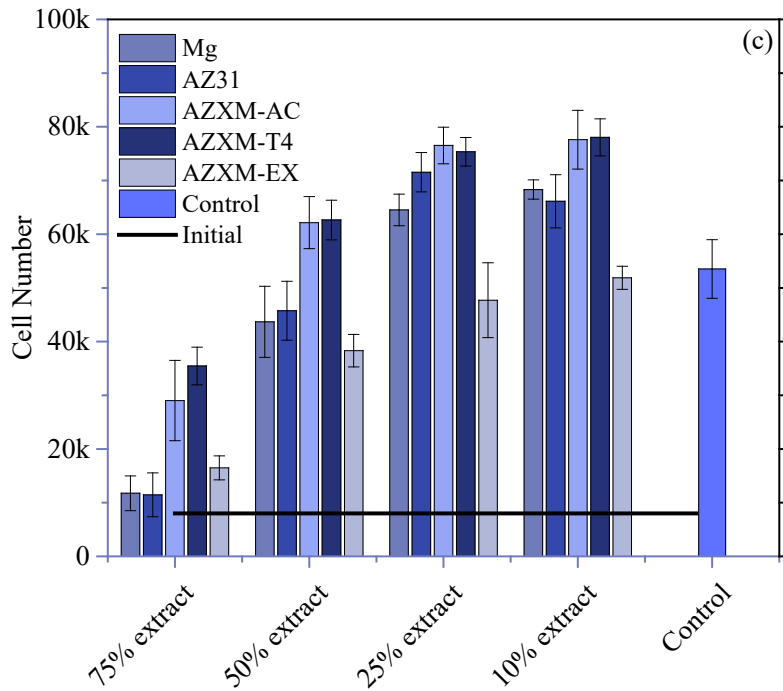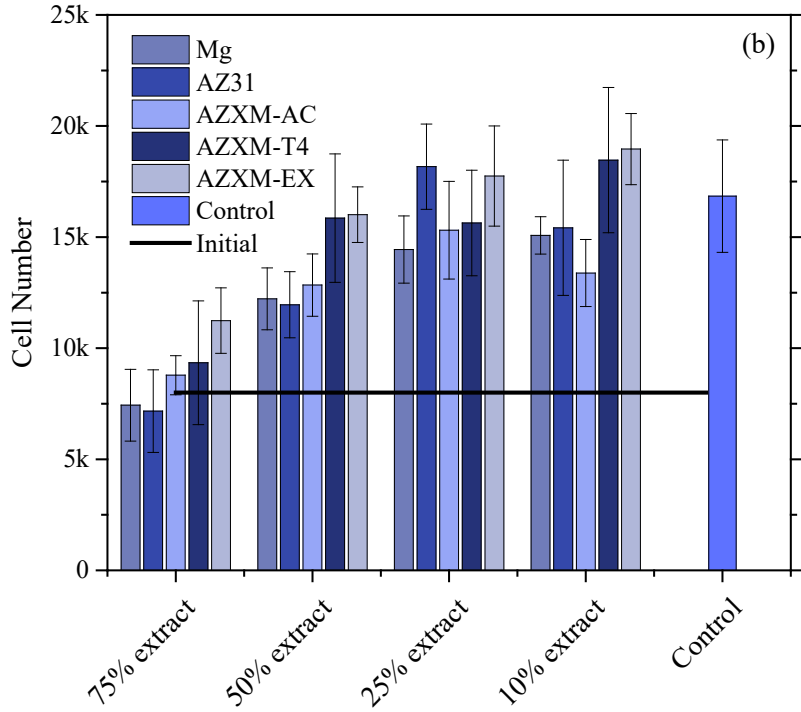
Figure B.8. (a) The concentration of metal ions in extract; cell viability of BEAS-2B cultured in extracts with different dilution ratios. (b) day 1, (c) day 3. (Initial: number of cells initially seeded; control: number of cells after culture in normal BEGM).
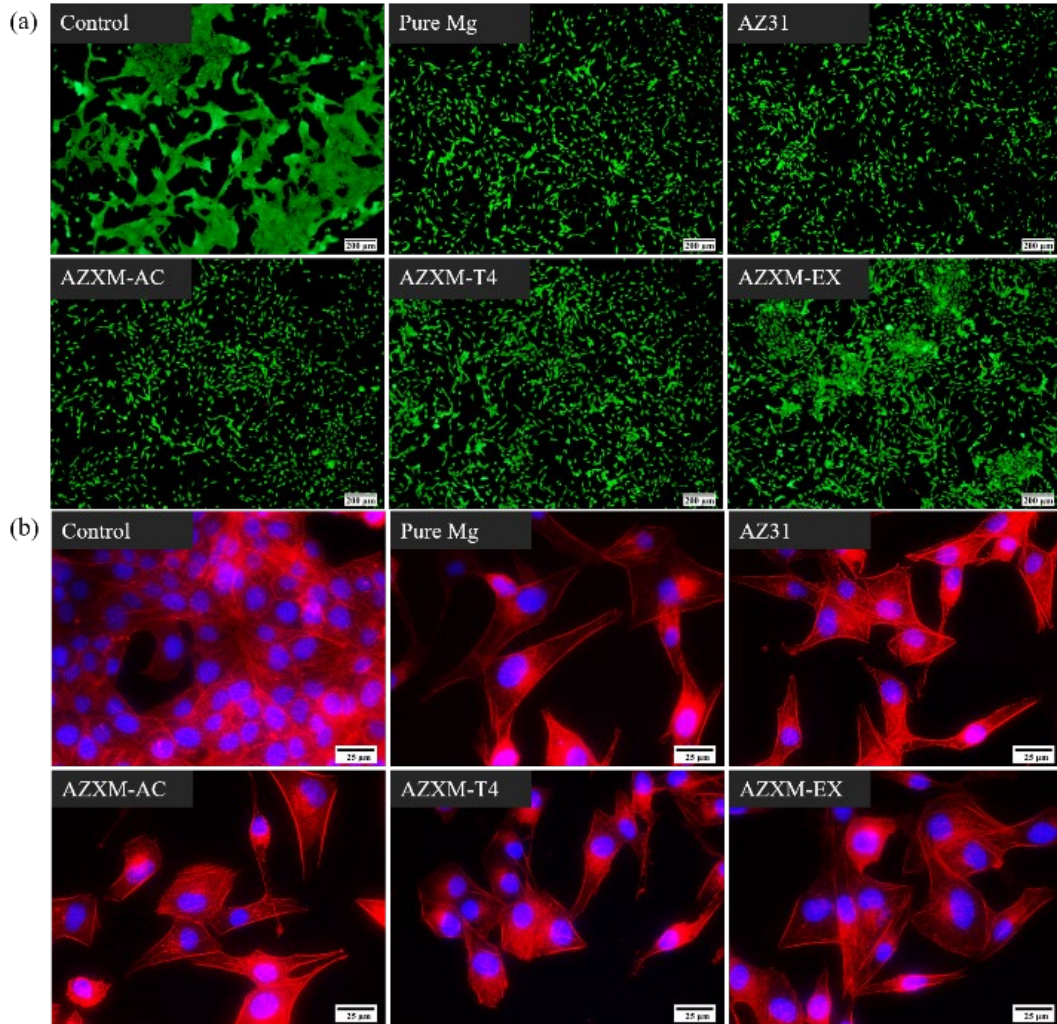
Figure B.9. (a) Live & dead and (b) DAPI/F-actin staining of BEAS-2B cells after 3 days of culture in 50% extract of pure Mg, AZ31 and AZXM alloys.

Figure B.8(b, c) showed the cytotoxicity results of AZXM alloys performed using BEAS-2B cells, and the CyQuant assay. The level of cytotoxicity level is evaluated by calculating the numbers of BEAS-2B cells after culture in different concentration of extracts for 1 day and 3 days. After 1 day of culture, all groups showed higher cell numbers compared to initial cell numbers seeded (8,000 cells) except for pure Mg and AZ31 75% extract groups. As the extract

the diluted from 75% to 10%, the cell number increased for most groups. After 3 days of culture, cell numbers increased to 10 folds of the cell numbers initially seeded for 50% and 25% extract groups. It should be noted that, for 75% extract groups, even though the number of BEAS-2B cells was much lower compare to 10% extract groups, the number of cells still significantly increased reaching ~11,000 cells for pure Mg and AZ31 groups compared to initial 8,000 cells seeded. For AZXM alloy groups, much more cells were observed in as-cast and T4 treated AZXM alloy groups compare to extruded AZXM alloy group, even though the composition of the extract didn't show much difference.

Similar trend was observed in indirect live & dead test (Figure B.9(a)). After culture in 50% extract for 3 days, BEAS-2B cells in the control group started to aggregated and showed the highest cell density. AZXM alloys groups demonstrated comparable live cell density compared to pure Mg and AZ31 with only few apoptotic cells observed. Figure 9 showed the morphology of BEAS-2B cells are normal in all groups. Cytoskeletons of BEAS-2B cells after immersion for 3 days in 50% extract is shown in Figure B.9(b). BEAS-2B cells in control groups aggregated and therefore individual cell morphology is hard to distinguish. BEAS-2B cells in experimental groups exhibited similar spreading and filopodia extension.

As-cast and T4 treated AZXM alloys showed excellent cytocompatibiliy with human trachea epithelial cells. Even cultured in high concentration of extract (75%), the cell numbers still increased after 3 days of cell culture. The more the extract was diluted, the higher cell proliferated. It worth noticing that for extruded AZXM alloys, the cell proliferation was similar to control group and lower than as-cast and T4 treated groups. However, the ICP data of key element of extract showed non-significant difference between different groups, implying that the concentration of metal ions might not be the only reason affect the cell viability and proliferation,

other reasons such as the change of the protein in the cell culture medium could also affect the *in vitro* cytotoxicity result.
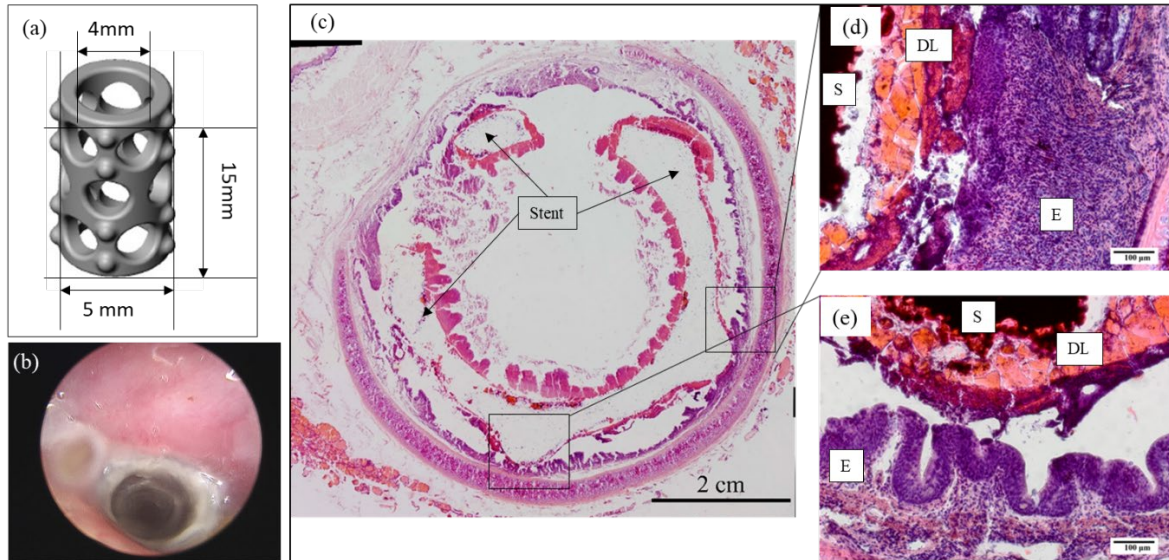
Figure B.10. (a) Design of prototype AZXM stent, (b) Endoscopy images of stented airway after 4 weeks of implantation. (c, d, e) H&E staining of stented tracheal of 4 weeks of implantation. (S: stent, E: Epithelium and DL: Degradation layer)

Due to the lack of previous *in vivo* study on magnesium stent for tracheal stent application, we only implanted one AZXM prototype stent to evaluate the feasibility of the concept. The stent was machined based on the design in Figure B.10(a). The endoscopy images indicated that a whitish gel was formed inside of the trachea as shown in Figure B.10(b). However, the patency of the airway was maintained throughout the 4 weeks study, and the rabbits didn't exhibit any respiratory issues. H&E staining was performed to investigate the airway tissue response. As shown in Figure B.10(c-e), the integrity of epithelium was maintained

along the airway lumen indicating that the existence of AZXM prototype stents didn't interfere with the normal function of the tracheal epithelial layer. A thin degradation layer was formed between the epithelium and the remaining AZXM metal substrate. The normal morphology of the epithelium layers in the H&E staining images (Figure B.10(d, e)) shows that the degradation layer was well tolerated by the airway tissue.

B.4   CONCLUSIONS

After partially replacing Al with Ca, AZXM exhibited higher strength compared to AZ31 alloys. Ca is preferentially concentrated in intermetallic phases and grain boundaries forming second phase that was homogeneously distributed in the magnesium matrix. However, the corrosion rate of AZXM was not affected by the second phase after extrusion. The extruded AZXM alloy showed less pitting, higher corrosion resistance and optimized mechanical properties. *In vitro* cytotoxicity evaluation using human trachea epithelial cells demonstrated the excellent cytocompatibility of AZXM alloys compared to pure Mg and AZ31. As-cast and T4 treated AZXM alloys showed the highest cell numbers after 3 days of cell culture. The pilot implantation of AZXM prototype stents showed the feasibility of the concept. The 4 weeks study indicated that the AZXM alloy and its degradation product were well tolerated by the airway tissue. The existence of AZXM stent won't interfere with the epithelium, the morphology of the epithelium was normal. Further study should focus on processing AZXM to increase the ductility and evaluating the prototype device in animal models at longer time point. It can be concluded that the newly developed AZXM alloy is a strong candidate for biodegradable trachea stent application.

BIBLIOGRAPHY

[1] H. Gray, W.H. Lewis, Anatomy of the Human Body, Lea & Febiger1918.

[2] A. Ernst, D. Feller-Kopman, H.D. Becker, A.C. Mehta, Central airway obstruction, Am. J. Respir. Crit. Care Med. 169(12) (2004) 1278-1297.

[3] N.A. Rahman, O. Fruchter, D. Shitrit, B.D. Fox, M.R. Kramer, Flexible bronchoscopic management of benign tracheal stenosis: long term follow-up of 115 patients, J. Cardiothorac. Surg. 5 (2010) 2.

[4] D.E. Wood, Y.-H. Liu, E. Vallières, R. Karmy-Jones, M.S. Mulligan, Airway stenting for malignant and benign tracheobronchial stenosis, The Annals of Thoracic Surgery 76(1) (2003) 167-174.

[5] J.A. Gorden, A. Ernst, Endoscopic Management of Central Airway Obstruction, Semin. Thorac. Cardiovasc. Surg. 21(3) (2009) 263-273.

[6] M.A. Bitar, R. Al Barazi, R. Barakeh, Airway reconstruction: review of an approach to the advanced-stage laryngotracheal stenosis, Braz. J. Otorhinolaryngol. 83(3) (2017) 299-312.

[7] S. Lewis, M. Earley, R. Rosenfeld, J. Silverman, Systematic review for surgical treatment of adult and adolescent laryngotracheal stenosis, Laryngoscope 127(1) (2017) 191-198.

[8] A. Brichet, C. Verkindre, J. Dupont, M.L. Carlier, J. Darras, A. Wurtz, P. Ramon, C.H. Marquette, Multidisciplinary approach to management of postintubation tracheal stenoses, Eur. Respir. J. 13(4) (1999) 888-93.

[9] S.D. MURGU, H.G. COLT, Tracheobronchomalacia and excessive dynamic airway collapse, Respirology 11(4) (2006) 388-406.

[10] J. Austin, T. Ali, Tracheomalacia and bronchomalacia in children: pathophysiology, assessment, treatment and anaesthesia management, Pediatric Anesthesia 13(1) (2003) 3-11.

[11] R. Boogaard, S.H. Huijsmans, M.W.H. Pijnenburg, H.A.W.M. Tiddens, J.C. de Jongste, P.J.F.M. Merkus, Tracheomalacia and Bronchomalacia in Children*Incidence and Patient Characteristics, CHEST Journal 128(5) (2005) 3391-3397.

[12] A.S. Ho, P.J. Koltai, Pediatric Tracheal Stenosis, Otolaryngol. Clin. North Am. 41(5) (2008) 999-1021.

[13] X. Xu, D. Li, S. Zhao, X. Liu, Z. Feng, H. Ding, Treatment of congenital tracheal stenosis by balloon-expandable metallic stents in paediatric intensive care unit, Interact. Cardiovasc. Thorac. Surg. 14(5) (2012) 548-50.

[14] T. Nicolai, Airway stents in children, Pediatr. Pulmonol. 43(4) (2008) 330-44.

[15] M.M. Carr, C.P. Poje, L. Kingston, D. Kielma, C. Heard, Complications in Pediatric Tracheostomies, The Laryngoscope 111(11) (2001) 1925-1928.

[16] A.E. Overman, M. Liu, S.C. Kurachek, M.R. Shreve, R.C. Maynard, M.C. Mammel, B.M. Moore, Tracheostomy for Infants Requiring Prolonged Mechanical Ventilation: 10 Years' Experience, Pediatrics 131(5) (2013) e1491-e1496.

[17] V. Goyal, I.B. Masters, A.B. Chang, Interventions for primary (intrinsic) tracheomalacia in children, Cochrane Database Syst Rev 10 (2012) Cd005304.

[18] C.T. Bolliger, T.G. Sutedja, J. Strausz, L. Freitag, Therapeutic bronchoscopy with immediate effect: laser, electrocautery, argon plasma coagulation and stents, Eur. Respir. J. 27(6) (2006) 1258-71.

[19] E.P. Valerie, A.C. Durrant, V. Forte, P. Wales, P. Chait, P.C.W. Kim, A decade of using intraluminal tracheal/bronchial stents in the management of tracheomalacia and/or bronchomalacia: is it better than aortopexy?, J. Pediatr. Surg. 40(6) (2005) 904-907.

[20] W.W. Montgomery, T-tube tracheal stent, Arch. Otolaryngol. 82(3) (1965) 320-321.

[21] J.D. Cooper, T.R. Todd, R. Ilves, F.G. Pearson, Use of the silicone tracheal T-tube for the management of complex tracheal injuries, J. Thorac. Cardiovasc. Surg. 82(4) (1981) 559-68.

[22] A.J. Duvall, W. Bauer, An endoscopically-introducible T-tube for tracheal stenosis, Laryngoscope 87(12) (1977) 2031-7.

[23] B.T. Uchida, J.S. Putnam, J. Rosch, Modifications of Gianturco expandable wire stents, AJR Am. J. Roentgenol. 150(5) (1988) 1185-7.

[24] M.J. Wallace, C. Charnsangavej, K. Ogawa, C.H. Carrasco, K.C. Wright, R. McKenna, M. McMurtrey, C. Gianturco, Tracheobronchial tree: expandable metallic stents used in experimental and clinical applications. Work in progress, Radiology 158(2) (1986) 309-12.

[25] C.S. Chin, V. Litle, J. Yun, T. Weiser, S.J. Swanson, Airway stents, Ann. Thorac. Surg. 85(2) (2008) S792-6.

[26] H.G. Coons, Self-expanding stainless steel biliary stents, Radiology 170(3 Pt 2) (1989) 979-83.

[27] W. Domschke, E.C. Foerster, W. Matek, W. Rodl, Self-expanding mesh stent for esophageal cancer stenosis, Endoscopy 22(3) (1990) 134-6.

[28] J.A. Dunne, S. Sabanathan, Use of metallic stents in relapsing polychondritis, Chest 105(3) (1994) 864-7.

[29] A.K. Simonds, J.D. Irving, S.W. Clarke, R. Dick, Use of expandable metal stents in the treatment of bronchial obstruction, Thorax 44(8) (1989) 680-681.

[30] A. Varela, M. Maynar, D. Irving, R. Dick, R. Reyes, H. Rousseau, L. Lopez, J.M. Pulido-Duque, J.G. Letourneau, W.R. Castaneda-Zuniga, Use of Gianturco self-expandable stents in the tracheobronchial tree, Ann. Thorac. Surg. 49(5) (1990) 806-9.

[31] R.M. Filler, V. Forte, J.C. Fraga, J. Matute, The use of expandable metallic airway stents for tracheobronchial obstruction in children, J. Pediatr. Surg. 30(7) (1995) 1050-5; discussion 1055-6.

[32] J.P. Shaffer, J.N. Allen, The use of expandable metal stents to facilitate extubation in patients with large airway obstruction, Chest 114(5) (1998) 1378-82.

[33] I. Susanto, J.I. Peters, S.M. Levine, E.Y. Sako, A. Anzueto, C.L. Bryan, Use of balloon-expandable metallic stents in the management of bronchial stenosis and bronchomalacia after lung transplantation, Chest 114(5) (1998) 1330-5.

[34] F. Gorostidi, C. Courbon, M. Burki, A. Reinhard, K. Sandu, Extraluminal biodegradable splint to treat upper airway anterior malacia: A preclinical proof of principle, The Laryngoscope (2017) n/a-n/a.

[35] R.J. Morrison, S.J. Hollister, M.F. Niedner, M.G. Mahani, A.H. Park, D.K. Mehta, R.G. Ohye, G.E. Green, Mitigation of tracheobronchomalacia with 3D-printed personalized medical devices in pediatric patients, Sci. Transl. Med. 7(285) (2015) 285ra64.

[36] G. Di Dedda, C. Mirabile, Use of a biodegradable, oversized stent in a child with tracheomalacia secondary to vascular external compression, Cardiol. Young 27(1) (2017) 196-198.

[37] J. Wang, K.G. Boutin, O. Abdulhadi, L.D. Personnat, T. Shazly, R. Langer, C.L. Channick, J.T. Borenstein, Fully Biodegradable Airway Stents Using Amino Alcohol-Based Poly(ester amide) Elastomers, Adv Healthc Mater (2013).

[38] D. Vondrys, M.J. Elliott, C.A. McLaren, C. Noctor, D.J. Roebuck, First experience with biodegradable airway stents in children, Ann. Thorac. Surg. 92(5) (2011) 1870-4.

[39] L. Stehlik, V. Hytych, J. Letackova, P. Kubena, M. Vasakova, Biodegradable polydioxanone stents in the treatment of adult patients with tracheal narrowing, BMC Pulm. Med. 15(1) (2015) 164.

[40] L. Stehlik, V. Hytych, S. Lefnerova, M. Vasakova, Biodegradable polydioxanone stents: Preliminary results in adult patients with tracheal narrowing, Eur. Respir. J. 46(suppl 59) (2015).

[41] L.F. Schopf, J.C. Fraga, R. Porto, L.A. Santos, D.R. Marques, P.R. Sanchez, F.S. Meyer, J.M. Ulbrich, Experimental use of new absorbable tracheal stent, J. Pediatr. Surg. (2017).

[42] H. Lochbihler, J. Hoelzl, H.G. Dietz, Tissue compatility and biodegradation of new absorbable stents for tracheal stabilization: an experimental study, J. Pediatr. Surg. 32(5) (1997) 717-20.

[43] A. Korpela, P. Aarnio, H. Sariola, P. Tormala, A. Harjula, Comparison of tissue reactions in the tracheal mucosa surrounding a bioabsorbable and silicone airway stents, Ann. Thorac. Surg. 66(5) (1998) 1772-6.

[44] A. Korpela, P. Aarnio, H. Sariola, P. Tormala, A. Harjula, Bioabsorbable self-reinforced poly-L-lactide, metallic, and silicone stents in the management of experimental tracheal stenosis, Chest 115(2) (1999) 490-5.

[45] T.C. Robey, T. Valimaa, H.S. Murphy, P. Tormala, D.J. Mooney, R.A. Weatherly, Use of internal bioabsorbable PLGA "finger-type" stents in a rabbit tracheal reconstruction model, Arch. Otolaryngol. Head Neck Surg. 126(8) (2000) 985-91.

[46] Y. Saito, K. Minami, M. Kobayashi, Y. Nakao, H. Omiya, H. Imamura, N. Sakaida, A. Okamura, New tubular bioabsorbable knitted airway stent: biocompatibility and mechanical strength, J. Thorac. Cardiovasc. Surg. 123(1) (2002) 161-7.

[47] G.H. Zhu, A.H. Ng, S.S. Venkatraman, F.Y. Boey, A.L. Wee, S.L. Trasti, L.H. Yee Lim, A novel bioabsorbable drug-eluting tracheal stent, Laryngoscope 121(10) (2011) 2234-9.

[48] Y. Saito, K. Minami, H. Kaneda, T. Okada, T. Maniwa, Y. Araki, H. Imamura, H. Yamada, K. Igaki, H. Tamai, New tubular bioabsorbable knitted airway stent: feasibility assessment for delivery and deployment in a dog model, Ann. Thorac. Surg. 78(4) (2004) 1438-40.

[49] K.S. Liu, Y.H. Liu, Y.J. Peng, S.J. Liu, Experimental absorbable stent permits airway remodeling, J. Thorac. Cardiovasc. Surg. 141(2) (2011) 463-8.

[50] Y.K. Chao, K.S. Liu, Y.C. Wang, Y.L. Huang, S.J. Liu, Biodegradable cisplatin-eluting tracheal stent for malignant airway obstruction: in vivo and in vitro studies, Chest 144(1) (2013) 193-199.

[51] L. Novotny, M. Crha, P. Rauser, A. Hep, J. Misik, A. Necas, D. Vondrys, Novel biodegradable polydioxanone stents in a rabbit airway model, J. Thorac. Cardiovasc. Surg. 143(2) (2012) 437-44.

[52] R. Lischke, J. Pozniak, D. Vondrys, M.J. Elliott, Novel biodegradable stents in the treatment of bronchial stenosis after lung transplantation, Eur. J. Cardiothorac. Surg. 40(3) (2011) 619-24.

[53] T.C. Robey, P.M. Eiselt, H.S. Murphy, D.J. Mooney, R.A. Weatherly, Biodegradable external tracheal stents and their use in a rabbit tracheal reconstruction model, Laryngoscope 110(11) (2000) 1936-42.

[54] S.V. Murphy, A. Atala, 3D bioprinting of tissues and organs, Nat. Biotechnol. 32 (2014) 773.

[55] S.K. Misra, F. Ostadhossein, R. Babu, J. Kus, D. Tankasala, A. Sutrisno, K.A. Walsh, C.R. Bromfield, D. Pan, 3D-Printed Multidrug-Eluting Stent from Graphene-Nanoplatelet-Doped Biodegradable Polymer Composite, Advanced Healthcare Materials (2017) 1700008-n/a.

[56] R. Kaye, T. Goldstein, D. Aronowitz, D.A. Grande, D. Zeltsman, L.P. Smith, Ex vivo tracheomalacia model with 3D-printed external tracheal splint, Laryngoscope (2016).

[57] E.J. ten Hallers, G. Rakhorst, H.A. Marres, J.A. Jansen, T.G. van Kooten, H.K. Schutte, J.P. van Loon, E.B. van der Houwen, G.J. Verkerke, Animal models for tracheal research, Biomaterials 25(9) (2004) 1533-43.

[58] J.L. Antón-Pacheco, C. Luna, E. García, M. López, R. Morante, C. Tordable, A. Palacios, M. de Miguel, I. Benavent, A. Gómez, Initial experience with a new biodegradable airway stent in children: Is this the stent we were waiting for?, Pediatr. Pulmonol. (2015) n/a-n/a.

[59] B. Sztano, G. Kiss, K. Marai, G. Racz, I. Szegesdi, K. Racz, G. Katona, L. Rovo, Biodegradable airway stents in infants - Potential life-threatening pitfalls, Int. J. Pediatr. Otorhinolaryngol. 91 (2016) 86-89.

[60] H. Dutau, A.I. Musani, S. Laroumagne, K. Darwiche, L. Freitag, P. Astoul, Biodegradable Airway Stents - Bench to Bedside: A Comprehensive Review, Respiration 0(0) (2015) 512-521.

[61] H. EC., A new ligature?, Chicago Med J Exam (1878) 172-2.

[62] M.M. Avedesian, H. Baker, A.S.M.I.H. Committee, ASM Specialty Handbook: Magnesium and Magnesium Alloys, ASM International1999.

[63] J.M. Seitz, R. Eifler, F.W. Bach, H.J. Maier, Magnesium degradation products: Effects on tissue and human metabolism, Journal of Biomedical Materials Research Part A 102(10) (2014) 3744-3753.

[64] R. Swaminathan, Magnesium metabolism and its disorders, Clin. Biochem. Rev. 24(2) (2003) 47-66.

[65] F. Feyerabend, F. Witte, M. Kammal, R. Willumeit, Unphysiologically high magnesium concentrations support chondrocyte proliferation and redifferentiation, Tissue Eng. 12(12) (2006) 3545-56.

[66] Z. Zhai, X. Qu, H. Li, K. Yang, P. Wan, L. Tan, Z. Ouyang, X. Liu, B. Tian, F. Xiao, W. Wang, C. Jiang, T. Tang, Q. Fan, A. Qin, K. Dai, The effect of metallic magnesium degradation products on osteoclast-induced osteolysis and attenuation of NF-κB and NFATc1 signaling, Biomaterials 35(0) (2014) 6299-310.

[67] Y. Dou, N. Li, Y. Zheng, Z. Ge, Effects of fluctuant magnesium concentration on phenotype of the primary chondrocytes, Journal of Biomedical Materials Research Part A 102(12) (2014) 4455-4463.

[68] F. Witte, H. Ulrich, C. Palm, E. Willbold, Biodegradable magnesium scaffolds: Part II: Peri-implant bone remodeling, Journal of Biomedical Materials Research Part A 81A(3) (2007) 757-765.

[69] D. Zhao, F. Witte, F. Lu, J. Wang, J. Li, L. Qin, Current status on clinical applications of magnesium-based orthopaedic implants: A review from clinical translational perspective, Biomaterials 112 (2017) 287-302.

[70] D. Zhao, S. Huang, F. Lu, B. Wang, L. Yang, L. Qin, K. Yang, Y. Li, W. Li, W. Wang, S. Tian, X. Zhang, W. Gao, Z. Wang, Y. Zhang, X. Xie, J. Wang, J. Li, Vascularized bone grafting fixed by biodegradable magnesium screw for treating osteonecrosis of the femoral head, Biomaterials 81 (2016) 84-92.

[71] Y. Shi, L. Zhang, J. Chen, J. Zhang, F. Yuan, L. Shen, C. Chen, J. Pei, Z. Li, J. Tan, G. Yuan, In vitro and in vivo degradation of rapamycin-eluting Mg-Nd-Zn-Zr alloy stents in porcine coronary arteries, Materials Science and Engineering: C 80 (2017) 1-6.

[72] J. Liu, P. Wang, C.C. Chu, T. Xi, Arginine-leucine based poly (ester urea urethane) coating for Mg-Zn-Y-Nd alloy in cardiovascular stent applications, Colloids Surf. B. Biointerfaces 159 (2017) 78-88.

[73] M. Haude, H. Ince, A. Abizaid, R. Toelg, P.A. Lemos, C. von Birgelen, E.H. Christiansen, W. Wijns, F.J. Neumann, C. Kaiser, E. Eeckhout, S.T. Lim, J. Escaned, H.M. Garcia-Garcia, R. Waksman, Safety and performance of the second-generation drug-eluting absorbable metal scaffold in patients with de-novo coronary artery lesions (BIOSOLVE-II): 6 month results of a prospective, multicentre, non-randomised, first-in-man trial, Lancet 387(10013) (2016) 31-39.

[74] M. Haude, R. Erbel, P. Erne, S. Verheye, H. Degen, D. Bose, P. Vermeersch, I. Wijnbergen, N. Weissman, F. Prati, R. Waksman, J. Koolen, Safety and performance of the drug-eluting absorbable metal scaffold (DREAMS) in patients with de-novo coronary lesions: 12 month results of the prospective, multicentre, first-in-man BIOSOLVE-I trial, Lancet 381(9869) (2013) 836-844.

[75] R. Erbel, C. Di Mario, J. Bartunek, J. Bonnier, B. de Bruyne, F.R. Eberli, P. Erne, M. Haude, B. Heublein, M. Horrigan, C. Ilsley, D. Bose, J. Koolen, T.F. Luscher, N. Weissman, R. Waksman, P.-A. Investigators, Temporary scaffolding of coronary arteries with bioabsorbable magnesium stents: a prospective, non-randomised multicentre trial, Lancet 369(9576) (2007) 1869-1875.

[76] J.-M. Seitz, M. Durisin, J. Goldman, J.W. Drelich, Recent Advances in Biodegradable Metals for Medical Sutures: A Critical Review, Advanced Healthcare Materials (2015) n/a-n/a.

[77] J.-M. Seitz, D. Utermöhlen, E. Wulf, C. Klose, F.-W. Bach, The Manufacture of Resorbable Suture Material from Magnesium – Drawing and Stranding of Thin Wires, Adv. Eng. Mater. 13(12) (2011) 1087-1095.

[78] R.S. Stack, R.M. Califf, H.R. Phillips, D.B. Pryor, P.J. Quigley, R.P. Bauman, J.E. Tcheng, J.C. Greenfield, Jr., Interventional cardiac catheterization at Duke Medical Center, Am. J. Cardiol. 62(10 Pt 2) (1988) 3f-24f.

[79] S.G. Ellis, D.J. Kereiakes, D.C. Metzger, R.P. Caputo, D.G. Rizik, P.S. Teirstein, M.R. Litt, A. Kini, A. Kabour, S.O. Marx, J.J. Popma, R. McGreevy, Z. Zhang, C. Simonton, G.W. Stone, Everolimus-Eluting Bioresorbable Scaffolds for Coronary Artery Disease, N. Engl. J. Med. 373(20) (2015) 1905-1915.

[80] G.W. Stone, A. Abizaid, Y. Onuma, A. Seth, R. Gao, J. Ormiston, T. Kimura, B. Chevalier, O. Ben-Yehuda, O. Dressler, T. McAndrew, S.G. Ellis, D.J. Kereiakes, P.W. Serruys, Effect of Technique on Outcomes Following Bioresorbable Vascular Scaffold Implantation, Analysis From the ABSORB Trials (2017).

[81] M. Peuster, C. Hesse, T. Schloo, C. Fink, P. Beerbaum, C. von Schnakenburg, Long-term biocompatibility of a corrodible peripheral iron stent in the porcine descending aorta, Biomaterials 27(28) (2006) 4955-4962.

[82] R.O.N. Waksman, R. Pakala, R. Baffour, R. Seabron, D. Hellinga, F.O. Tio, Short-Term Effects of Biocorrodible Iron Stents in Porcine Coronary Arteries, J. Interv. Cardiol. 21(1) (2008) 15-20.

[83] Y. Qi, H. Qi, Y. He, W. Lin, P.Z. Li, L. Qin, Y. Hu, L. Chen, Q. Liu, H. Sun, Q. Liu, G. Zhang, S. Cui, J. Hu, L. Yu, D. Zhang, J. Ding, Strategy of Metal-polymer Composite Stent to Accelerate Biodegradation of Iron-based Biomaterials, ACS Appl. Mater. Interfaces (2017).

[84] A. Drynda, T. Hassel, F.W. Bach, M. Peuster, In vitro and in vivo corrosion properties of new iron–manganese alloys designed for cardiovascular applications, Journal of Biomedical Materials Research Part B: Applied Biomaterials 103(3) (2015) 649-660.

[85] B. Liu, Y.F. Zheng, Effects of alloying elements (Mn, Co, Al, W, Sn, B, C and S) on biodegradability and in vitro biocompatibility of pure iron, Acta Biomater. 7(3) (2011) 1407-1420.

[86] H. Yang, C. Wang, C. Liu, H. Chen, Y. Wu, J. Han, Z. Jia, W. Lin, D. Zhang, W. Li, W. Yuan, H. Guo, H. Li, G. Yang, D. Kong, D. Zhu, K. Takashima, L. Ruan, J. Nie, X. Li, Y. Zheng, Evolution of the degradation mechanism of pure zinc stent in the one-year study of rabbit abdominal aorta model, Biomaterials 145 (2017) 92-105.

[87] P.K. Bowen, R.J. Guillory, E.R. Shearier, J.-M. Seitz, J. Drelich, M. Bocks, F. Zhao, J. Goldman, Metallic zinc exhibits optimal biocompatibility for bioabsorbable endovascular stents, Materials Science and Engineering: C 56 (2015) 467-472.

[88] E. Mostaed, M. Sikora-Jasinska, A. Mostaed, S. Loffredo, A.G. Demir, B. Previtali, D. Mantovani, R. Beanland, M. Vedani, Novel Zn-based alloys for biodegradable stent applications: Design, development and in vitro degradation, J. Mech. Behav. Biomed. Mater. 60 (2016) 581-602.

[89] P.K. Bowen, J. Drelich, J. Goldman, Zinc Exhibits Ideal Physiological Corrosion Behavior for Bioabsorbable Stents, Adv. Mater. 25(18) (2013) 2577-2582.

[90] H. Yang, F. Zhang, J. Qian, J. Chen, J. Ge, Restenosis in Magmaris Stents Due to Significant Collapse, JACC Cardiovasc. Interv. 11(10) (2018) e77-e78.

[91] Y.C. Xin, C.L. Liu, X.M. Zhang, G.Y. Tang, X.B. Tian, P.K. Chu, Corrosion behavior of biomedical AZ91 magnesium alloy in simulated body fluids, J. Mater. Res. 22(7) (2007) 2004-2011.

[92] T.T. Yan, L.L. Tan, D.S. Xiong, X.J. Liu, B.C. Zhang, K. Yang, Fluoride treatment and in vitro corrosion behavior of an AZ31B magnesium alloy, Mater. Sci. Eng., C 30(5) (2010) 740-748.

[93] E. Willbold, A.A. Kaya, R.A. Kaya, F. Beckmann, F. Witte, Corrosion of magnesium alloy AZ31 screws is dependent on the implantation site, Mater. Sci. Eng., B 176(20) (2011) 1835-1840.

[94] H. Qin, Y. Zhao, Z. An, M. Cheng, Q. Wang, T. Cheng, Q. Wang, J. Wang, Y. Jiang, X. Zhang, G. Yuan, Enhanced antibacterial properties, biocompatibility, and corrosion resistance of degradable Mg-Nd-Zn-Zr alloy, Biomaterials 53(0) (2015) 211-220.

[95] T.A. Grunewald, A. Ogier, J. Akbarzadeh, M. Meischel, H. Peterlik, S. Stanzl-Tschegg, J.F. Loffler, A.M. Weinberg, H.C. Lichtenegger, Reaction of bone nanostructure to a biodegrading Magnesium WZ21 implant - A scanning small-angle X-ray scattering time study, Acta Biomater. 31 (2016) 448-457.

[96] X. Guan, M. Xiong, F. Zeng, B. Xu, L. Yang, H. Guo, J. Niu, J. Zhang, C. Chen, J. Pei, H. Huang, G. Yuan, Enhancement of osteogenesis and biodegradation control by brushite coating on Mg-Nd-Zn-Zr alloy for mandibular bone repair, ACS Appl. Mater. Interfaces 6(23) (2014) 21525-21533.

[97] D.T. Chou, D. Hong, P. Saha, J. Ferrero, B. Lee, Z. Tan, Z. Dong, P.N. Kumta, In vitro and in vivo corrosion, cytocompatibility and mechanical properties of biodegradable Mg-Y-Ca-Zr alloys as implant materials, Acta Biomater. 9(10) (2013) 8518-8533.

[98] S. Sandlöbes, M. Friák, S. Korte-Kerzel, Z. Pei, J. Neugebauer, D. Raabe, A rare-earth free magnesium alloy with improved intrinsic ductility, Sci. Rep. 7(1) (2017) 10458.

[99] D. Bian, W. Zhou, Y. Liu, N. Li, Y. Zheng, Z. Sun, Fatigue behaviors of HP-Mg, Mg-Ca and Mg-Zn-Ca biodegradable metals in air and simulated body fluid, Acta Biomater. 41 (2016) 351-60.

[100] T. Roland, D. Retraint, K. Lu, J. Lu, Fatigue life improvement through surface nanostructuring of stainless steel by means of surface mechanical attrition treatment, Scripta Mater. 54(11) (2006) 1949-1954.

[101] K. Hanada, K. Matsuzaki, X. Huang, Y. Chino, Fabrication of Mg alloy tubes for biodegradable stent application, Mater. Sci. Eng., C 33(8) (2013) 4746-4750.

[102] Y. Zhang, D. Kent, G. Wang, D. StJohn, M.S. Dargusch, The cold-rolling behaviour of AZ31 tubes for fabrication of biodegradable stents, J. Mech. Behav. Biomed. Mater. 39(0) (2014) 292-303.

[103] L. Wang, G. Fang, L. Qian, S. Leeflang, J. Duszczyk, J. Zhou, Forming of magnesium alloy microtubes in the fabrication of biodegradable stents, Prog. Nat. Sci.: Mater. Int. 24(5) (2014) 500-506.

[104] J. Wang, V. Giridharan, V. Shanov, Z. Xu, B. Collins, L. White, Y. Jang, J. Sankar, N. Huang, Y. Yun, Flow-induced corrosion behavior of absorbable magnesium-based stents, Acta Biomater. 10(12) (2014) 5213-5223.

[105] J.A. Grogan, D. Gastaldi, M. Castelletti, F. Migliavacca, G. Dubini, P.E. McHugh, A novel flow chamber for biodegradable alloy assessment in physiologically realistic environments, Rev. Sci. Instrum. 84(9) (2013).

[106] M.B. Kannan, R.K.S. Raman, Evaluating the stress corrosion cracking susceptibility of Mg-Al-Zn alloy in modified-simulated body fluid for orthopaedic implant application, Scripta Mater. 59(2) (2008) 175-178.

[107] L. Choudhary, R.K.S. Raman, J. Hofstetter, P.J. Uggowitzer, In-vitro characterization of stress corrosion cracking of aluminium-free magnesium alloys for temporary bio-implant applications, Materials Science & Engineering C-Materials for Biological Applications 42 (2014) 629-636.

[108] Y. Saito, H. Imamura, Airway stenting, Surg. Today 35(4) (2005) 265-70.

[109] T.G. Byrer, P.D. Frost, E.L. White, I. Battelle Memorial, S. United, The development of magnesium-lithium alloys for structural applications, NASA, WAshington, D.C., 1964.

[110] N. Angrisani, J. Reifenrath, F. Zimmermann, R. Eifler, A. Meyer-Lindenberg, K. Vano-Herrera, C. Vogt, Biocompatibility and degradation of LAE442-based magnesium alloys after implantation of up to 3.5 years in a rabbit model, Acta Biomater. 44 (2016) 355-365.

[111] B. Ullmann, J. Reifenrath, J.M. Seitz, D. Bormann, A. Meyer-Lindenberg, Influence of the grain size on the in vivo degradation behaviour of the magnesium alloy LAE442, Proc. Inst. Mech. Eng. H 227(3) (2013) 317-326.

[112] F. Witte, J. Fischer, J. Nellesen, C. Vogt, J. Vogt, T. Donath, F. Beckmann, In vivo corrosion and corrosion protection of magnesium alloy LAE442, Acta Biomater. 6(5) (2010) 1792-1799.

[113] S.S. Nene, B.P. Kashyap, N. Prabhu, Y. Estrin, T. Al-Samman, Biocorrosion and biodegradation behavior of ultralight Mg-4Li-1Ca (LC41) alloy in simulated body fluid for degradable implant applications, J. Mater. Sci. 50(8) (2015) 3041-3050.

[114] R.C. Zeng, W.C. Qi, F. Zhang, H.Z. Cui, Y.F. Zheng, In vitro corrosion of Mg-1.21Li-1.12Ca-1Y alloy, Prog. Nat. Sci.: Mater. Int. 24(5) (2014) 492-499.

[115] M.A. Leeflang, J.S. Dzwonczyk, J. Zhou, J. Duszczyk, Long-term biodegradation and associated hydrogen evolution of duplex-structured Mg-Li-Al-(RE) alloys and their mechanical properties, Mater. Sci. Eng., B 176(20) (2011) 1741-1745.

[116] W.R. Zhou, Y.F. Zheng, M.A. Leeflang, J. Zhou, Mechanical property, biocorrosion and in vitro biocompatibility evaluations of Mg-Li-(Al)-(RE) alloys for future cardiovascular stent application, Acta Biomater. 9(10) (2013) 8488-8498.

[117] R.C. Zeng, L. Sun, Y.F. Zheng, H.Z. Cui, E.H. Han, Corrosion and characterisation of dual phase Mg-Li-Ca alloy in Hank's solution: The influence of microstructural features, Corros. Sci. 79(0) (2014) 69-82.

[118] X.H. Liu, G.J. Du, R.Z. Wu, Z.Y. Niu, M.L. Zhang, Deformation and microstructure evolution of a high strain rate superplastic Mg-Li-Zn alloy, J. Alloys Compd. 509(39) (2011) 9558-9561.

[119] X.H. Liu, H.B. Zhan, S.H. Gu, Z.K. Qu, R.Z. Wu, M.L. Zhang, Superplasticity in a two-phase Mg-8Li-2Zn alloy processed by two-pass extrusion, Mater. Sci. Eng., A 528(19-20) (2011) 6157-6162.

[120] H. Takuda, H. Matsusaka, S. Kikuchi, K. Kubota, Tensile properties of a few Mg-Li-Zn alloy thin sheets, J. Mater. Sci. 37(1) (2002) 51-57.

[121] Y.N. Lin, H.Y. Wu, G.Z. Zhou, C.H. Chiu, S. Lee, Mechanical and anisotropic behaviors of Mg-Li-Zn alloy thin sheets, Mater. Des. 29(10) (2008) 2061-2065.

[122] Y. Liu, Y. Wu, D. Bian, S. Gao, S. Leeflang, H. Guo, Y. Zheng, J. Zhou, Study on the Mg-Li-Zn ternary alloy system with improved mechanical properties, good degradation performance and different responses to cells, Acta Biomater. 62(Supplement C) (2017) 418-433.

[123] O.I. Velikokhatnyi, P.N. Kumta, First Principles Study on Elastic Properties of Magnesium and Iron Based Bio-resorbable Alloys Mater. Sci. Eng., B Submited (2016).

[124] H. Hermawan, D. Dube, D. Mantovani, Degradable metallic biomaterials: design and development of Fe-Mn alloys for stents, J. Biomed. Mater. Res. A 93(1) (2010) 1-11.

[125] B. Wang, S.K. Guan, J. Wang, L.G. Wang, S.J. Zhu, Effects of Nd on microstructures and properties of extruded Mg-2Zn-0.46Y-xNd alloys for stent application, Mater. Sci. Eng., B 176(20) (2011) 1673-1678.

[126] S.R. Agnew, J.A. Horton, M.H. Yoo, Transmission electron microscopy investigation of ⟨c+a⟩ dislocations in Mg and α-solid solution Mg-Li alloys, Metall. Mater. Trans. A 33(3) (2002) 851-858.

[127] R.E. Lee, W.J.D. Jones, Microplasticity and fatigue of some magnesium-lithium alloys, J. Mater. Sci. 9(3) (1974) 469-475.

[128] S. Kamado, Deformability and strengthening of superlight Mg-Li alloys, Metall. Sci. Technol. 16(1-2) (1998) 45-54.

[129] D. Hardie, R.N. Parkins, Lattice spacing relationships in magnesium solid solutions, Philos. Mag. 4(43) (1959) 815-825.

[130] J. Kuhlmann, I. Bartsch, E. Willbold, S. Schuchardt, O. Holz, N. Hort, D. Hoche, W.R. Heineman, F. Witte, Fast escape of hydrogen from gas cavities around corroding magnesium implants, Acta Biomater. 9(10) (2013) 8714-8721.

[131] Y.W. Song, D.Y. Shan, R.S. Chen, E.H. Han, Corrosion characterization of Mg-8Li alloy in NaCl solution, Corros. Sci. 51(5) (2009) 1087-1094.

[132] C.A. Shaw, L. Tomljenovic, Aluminum in the central nervous system (CNS): toxicity in humans and animals, vaccine adjuvants, and autoimmunity, Immunol. Res. 56(2) (2013) 304-316.

[133] M. Kawahara, Effects of aluminum on the nervous system and its possible link with neurodegenerative diseases, J. Alzheimers Dis. 8(2) (2005) 171-82; discussion 209-15.

[134] Y. Ebina, S. Okada, S. Hamazaki, O. Midorikawa, Liver, kidney, and central nervous system toxicity of aluminum given intraperitoneally to rats: A multiple-dose subchronic study using aluminum nitrilotriacetate, Toxicol. Appl. Pharmacol. 75(2) (1984) 211-218.

[135] X. Zhang, G. Yuan, L. Mao, J. Niu, W. Ding, Biocorrosion properties of as-extruded Mg–Nd–Zn–Zr alloy compared with commercial AZ31 and WE43 alloys, Mater. Lett. 66(1) (2012) 209-211.

[136] J. Wang, F. Witte, T. Xi, Y. Zheng, K. Yang, Y. Yang, D. Zhao, J. Meng, Y. Li, W. Li, K. Chan, L. Qin, Recommendation for modifying current cytotoxicity testing standards for biodegradable magnesium-based materials, Acta Biomater. 21(0) (2015) 237-249.

[137] D. Hong, P. Saha, D.T. Chou, B. Lee, B.E. Collins, Z. Tan, Z. Dong, P.N. Kumta, In vitro degradation and cytotoxicity response of Mg-4% Zn-0.5% Zr (ZK40) alloy as a potential biodegradable material, Acta Biomater. 9(10) (2013) 8534-8547.

[138] E.-J. Park, J. Yi, K.-H. Chung, D.-Y. Ryu, J. Choi, K. Park, Oxidative stress and apoptosis induced by titanium dioxide nanoparticles in cultured BEAS-2B cells, Toxicol. Lett. 180(3) (2008) 222-229.

[139] J.M. Veranth, C.A. Reilly, M.M. Veranth, T.A. Moss, C.R. Langelier, D.L. Lanza, G.S. Yost, Inflammatory Cytokines and Cell Death in BEAS-2B Lung Cells Treated with Soil Dust, Lipopolysaccharide, and Surface-Modified Particles, Toxicol. Sci. 82(1) (2004) 88-96.

[140] V. Ansteinsson, A. Solhaug, J.T. Samuelsen, J.A. Holme, J.E. Dahl, DNA-damage, cell-cycle arrest and apoptosis induced in BEAS-2B cells by 2-hydroxyethyl methacrylate (HEMA), Mutation Research/Genetic Toxicology and Environmental Mutagenesis 723(2) (2011) 158-164.

[141] E.-J. Park, J. Choi, Y.-K. Park, K. Park, Oxidative stress induced by cerium oxide nanoparticles in cultured BEAS-2B cells, Toxicology 245(1–2) (2008) 90-100.

[142] W.C. Wang, C.Y. Kuo, B.S. Tzang, H.M. Chen, S.H. Kao, IL-6 augmented motility of airway epithelial cell BEAS-2B via Akt/GSK-3beta signaling pathway, J. Cell. Biochem. 113(11) (2012) 3567-75.

[143] L. Mao, L. Shen, J. Niu, J. Zhang, W. Ding, Y. Wu, R. Fan, G. Yuan, Nanophasic biodegradation enhances the durability and biocompatibility of magnesium alloys for the next-generation vascular stents, Nanoscale 5(20) (2013) 9517-9522.

[144] J. Fischer, D. Pröfrock, N. Hort, R. Willumeit, F. Feyerabend, Improved cytotoxicity testing of magnesium materials, Mater. Sci. Eng., B 176(11) (2011) 830-834.

[145] Z.H. Wang, J. Yan, J.A. Li, Q. Zheng, Z.G. Wang, X.N. Zhang, S.X. Zhang, Effects of biodegradable Mg-6Zn alloy extracts on apoptosis of intestinal epithelial cells, Mater. Sci. Eng., B 177(4) (2012) 388-393.

[146] Y. Chen, J. Yan, X. Wang, S. Yu, Z. Wang, X. Zhang, S. Zhang, Y. Zheng, C. Zhao, Q. Zheng, In vivo and in vitro evaluation of effects of Mg-6Zn alloy on apoptosis of common bile duct epithelial cell, BioMetals 27(6) (2014) 1217-1230.

[147] Z. Wang, J. Yan, J. Li, Q. Zheng, Z. Wang, X. Zhang, S. Zhang, Effects of biodegradable Mg-6Zn alloy extracts on apoptosis of intestinal epithelial cells, Materials Science and Engineering B-Advanced Functional Solid-State Materials 177(4) (2012) 388-393.

[148] Z. Wang, J. Yan, Q. Zheng, Z. Wang, J. Li, X. Zhang, S. Zhang, Effects of biodegradable Mg–6Zn alloy extracts on cell cycle of intestinal epithelial cells, J. Biomater. Appl. 27(6) (2013) 739-747.

[149] Z. Wang, X. Zhang, S. Chen, D. Wang, J. Wu, T. Liang, C. Liu, Lithium chloride inhibits vascular smooth muscle cell proliferation and migration and alleviates injury-induced neointimal hyperplasia via induction of PGC-1alpha, PLoS One 8(1) (2013) e55471.

[150] F. Witte, J. Fischer, J. Nellesen, H.A. Crostack, V. Kaese, A. Pisch, F. Beckmann, H. Windhagen, In vitro and in vivo corrosion measurements of magnesium alloys, Biomaterials 27(7) (2006) 1013-1018.

[151] Y. Jang, Z. Tan, C. Jurey, Z. Xu, Z. Dong, B. Collins, Y. Yun, J. Sankar, Understanding corrosion behavior of Mg-Zn-Ca alloys from subcutaneous mouse model: effect of Zn element concentration and plasma electrolytic oxidation, Mater. Sci. Eng., C 48 (2015) 28-40.

[152] P. Salunke, V. Shanov, F. Witte, High purity biodegradable magnesium coating for implant application, Materials Science and Engineering B-Advanced Functional Solid-State Materials 176(20) (2011) 1711-1717.

[153] A. Drynda, J. Seibt, T. Hassel, F.W. Bach, M. Peuster, Biocompatibility of fluoride-coated magnesium-calcium alloys with optimized degradation kinetics in a subcutaneous mouse model, Journal of Biomedical Materials Research Part A 101A(1) (2013) 33-43.

[154] Y. Jang, Z. Tan, C. Jurey, B. Collins, A. Badve, Z. Dong, C. Park, C.S. Kim, J. Sankar, Y. Yun, Systematic understanding of corrosion behavior of plasma electrolytic oxidation treated AZ31 magnesium alloy using a mouse model of subcutaneous implant, Materials Science and Engineering: C 45 (2014) 45-55.

[155] A.H.M. Sanchez, B.J.C. Luthringer, F. Feyerabend, R. Willumeit, Mg and Mg alloys: How comparable are in vitro and in vivo corrosion rates? – A Review, Acta Biomater. (0) (2014).

[156] F. Witte, V. Kaese, H. Haferkamp, E. Switzer, A. Meyer-Lindenberg, C.J. Wirth, H. Windhagen, In vivo corrosion of four magnesium alloys and the associated bone response, Biomaterials 26(17) (2005) 3557-63.

[157] J. Vormann, Magnesium: nutrition and metabolism, Mol. Aspects Med. 24(1–3) (2003) 27-37.

[158] M.M. Tomayko, C.P. Reynolds, Determination of subcutaneous tumor size in athymic (nude) mice, Cancer Chemother. Pharmacol. 24(3) (1989) 148-154.

[159] D. Zhao, T. Wang, X. Guo, J. Kuhlmann, A. Doepke, Z. Dong, V.N. Shanov, W.R. Heineman, Monitoring biodegradation of magnesium implants with sensors, JOM-J. Min. Met. S. 68(4) (2016) 1204-1208.

[160] D. Zhao, T. Wang, J. Kuhlmann, Z. Dong, S. Chen, M. Joshi, P. Salunke, V.N. Shanov, D. Hong, P.N. Kumta, W.R. Heineman, *In vivo* monitoring the biodegradation of magnesium alloys with an electrochemical H_2 sensor Acta Biomater. 36 (2016) 361-368.

[161] D. Noviana, D. Paramitha, M.F. Ulum, H. Hermawan, The effect of hydrogen gas evolution of magnesium implant on the postimplantation mortality of rats, J. Orthop. Transl. 5(Supplement C) (2016) 9-15.

[162] J. Kuhlmann, I. Bartsch, E. Willbold, S. Schuchardt, O. Holz, N. Hort, D. Hoeche, W.R. Heineman, F. Witte, Fast escape of hydrogen from gas cavities around corroding magnesium implants, Acta Biomater. 9(10) (2013) 8714-8721.

[163] D. Zhao, T. Wang, W.R. Heineman, Advances in H_2 sensors for bioanalytical applications, Trac-Trend Anal. Chem. 79 (2016) 269-275.

[164] D. Zhao, T. Wang, B. Hoagland, D. Benson, Z. Dong, S. Chen, D. Chou, D. Hong, J. Wu, P.N. Kumta, W.R. Heineman, Visual H_2 sensor for monitoring biodegradation of magnesium implants *in vivo*, Acta Biomater. 45 (2016) 399-409.

[165] R. Waksman, R. Pakala, P.K. Kuchulakanti, R. Baffour, D. Hellinga, R. Seabron, F.O. Tio, E. Wittchow, S. Hartwig, C. Harder, R. Rohde, B. Heublein, A. Andreae, K.H. Waldmann, A. Haverich, Safety and efficacy of bioabsorbable magnesium alloy stents in porcine coronary arteries, Catheter. Cardiovasc. Interv. 68(4) (2006) 607-619.

[166] T.L. Pinto Slottow, R. Pakala, R. Waksman, Serial imaging and histology illustrating the degradation of a bioabsorbable magnesium stent in a porcine coronary artery, Eur. Heart J. 29(3) (2008) 314.

[167] E. Wittchow, N. Adden, J. Riedmuller, C. Savard, R. Waksman, M. Braune, Bioresorbable drug-eluting magnesium-alloy scaffold: design and feasibility in a porcine coronary model, EuroIntervention 8(12) (2013) 1441-1450.

[168] D. Pierson, J. Edick, A. Tauscher, E. Pokorney, P. Bowen, J. Gelbaugh, J. Stinson, H. Getty, C.H. Lee, J. Drelich, J. Goldman, A simplified in vivo approach for evaluating the bioabsorbable behavior of candidate stent materials, J. Biomed. Mater. Res. B Appl. Biomater. 100(1) (2012) 58-67.

[169] A. Myrissa, N.A. Agha, Y. Lu, E. Martinelli, J. Eichler, G. Szakacs, C. Kleinhans, R. Willumeit-Romer, U. Schafer, A.M. Weinberg, In vitro and in vivo comparison of binary Mg alloys and pure Mg, Mater. Sci. Eng., C 61 (2016) 865-874.

[170] D. Xue, Y.H. Yun, Z. Tan, Z. Dong, M.J. Schulz, *In vivo* and *in vitro* degradation behavior of magnesium alloys as biomaterials, J. Mater. Sci. Technol. 28(3) (2012) 261-267.

[171] Q. Ge, M. Vedani, G. Vimercati, Extrusion of Magnesium Tubes for Biodegradable Stent Precursors, Mater. Manuf. Processes 27(2) (2012) 140-146.

[172] F. Liu, C. Chen, J. Niu, J. Pei, H. Zhang, H. Huang, G. Yuan, The processing of Mg alloy micro-tubes for biodegradable vascular stents, Materials Science and Engineering: C 48(0) (2015) 400-407.

[173] G. Fang, W.-j. Ai, S. Leeflang, J. Duszczyk, J. Zhou, Multipass cold drawing of magnesium alloy minitubes for biodegradable vascular stents, Materials Science & Engineering C-Materials for Biological Applications 33(6) (2013) 3481-3488.

[174] Q. Ge, D. Dellasega, G.A. Demir, M. Vedani, The processing of ultrafine-grained Mg tubes for biodegradable stents, Acta Biomater. (2013).

[175] M.B. Kannan, Improving the packing density of calcium phosphate coating on a magnesium alloy for enhanced degradation resistance, Journal of Biomedical Materials Research Part A (2012) n/a-n/a.

[176] J.X. Yang, Y.P. Jiao, F.Z. Cui, I.S. Lee, Q.S. Yin, Y. Zhang, Modification of degradation behavior of magnesium alloy by IBAD coating of calcium phosphate, Surface & Coatings Technology 202(22-23) (2008) 5733-5736.

[177] N. Erdmann, A. Bondarenko, M. Hewicker-Trautwein, N. Angrisani, J. Reifenrath, A. Lucas, A. Meyer-Lindenberg, Evaluation of the soft tissue biocompatibility of MgCa0.8 and surgical steel 316L in vivo: a comparative study in rabbits, Biomedical Engineering Online 9 (2010).

[178] J.L. Ruegemer, J.A. Perkins, K.S. Azarow, L.K. O'Bryant, R.E. Nielsen, R.W. Thomas, Effect of the Palmaz balloon-expandable metallic stent in the trachea of pigs, Otolaryngol. Head Neck Surg. 121(1) (1999) 92-7.

[179] J.P. Shaffer, J.N. Allen, The Use of Expandable Metal Stents to Facilitate Extubation in Patients With Large Airway Obstruction, CHEST Journal 114(5) (1998) 1378-1382.

[180] A. Korpela, P. Aarnio, H. Sariola, P. Törmälä, A. Harjula, Bioabsorbable Self-reinforced Poly-l-Lactide, Metallic, and Silicone Stents in the Management of Experimental Tracheal Stenosis, Chest 115(2) (1999) 490-495.

[181] P.R. Delaere, Z. Liu, R. Hermans, Laryngotracheal Reconstruction With Tracheal Patch Allografts, The Laryngoscope 108(2) (1998) 273-279.

[182] G. Coppit, J. Perkins, J. Munaretto, R. Nielsen, L. McKinney, K. Ulnick, The effects of mitomycin-C and stenting on airway wound healing after laryngotracheal reconstruction in a pig model, Int. J. Pediatr. Otorhinolaryngol. 53(2) (2000) 125-135.

[183] H. Olze, O. Kaschke, W.D. Müller, Untersuchungen zur Verbesserung des Designs eines alloplastischen epithelisierten Tracheaersatzes, HNO 45(6) (1997) 453-459.

[184] P. Macchiarini, E. Dulmet, V. de Montpreville, G.-M. Mazmanian, A. Chapelier, P. Dartevelle, Tracheal growth after slide tracheoplasty, The Journal of Thoracic and Cardiovascular Surgery 113(3) (1997) 558-566.

[185] J.R. Fuchs, B.A. Nasseri, J.P. Vacanti, Tissue engineering: a 21st century solution to surgical reconstruction, The Annals of Thoracic Surgery 72(2) (2001) 577-591.

[186] K. Kojima, L.J. Bonassar, A.K. Roy, C.A. Vacanti, J. Cortiella, Autologous tissue-engineered trachea with sheep nasal chondrocytes, The Journal of Thoracic and Cardiovascular Surgery 123(6) (2002) 1177-1184.

[187] B.J. Wiatrak, D.M. Albert, D.K. Holmes, R.T. Cotton, Cartilage graft epithelialization a preliminary study using a goat model, Archives of Otolaryngology–Head & Neck Surgery 119(7) (1993) 777-781.

[188] F.K. Hashem, M. Al Homsi, Z.Z. Mahasin, M.A. Gammas, Laryngotracheoplasty using the Medpor implant: an animal model, J. Otolaryngol. 30(6) (2001) 334-9.

[189] D. Noviana, D. Paramitha, M.F. Ulum, H. Hermawan, The effect of hydrogen gas evolution of magnesium implant on the postimplantation mortality of rats, J. Orthop. Transl. (2015).

[190] S. Windecker, P. Kolh, F. Alfonso, J.-P. Collet, J. Cremer, V. Falk, G. Filippatos, C. Hamm, S.J. Head, P. Jüni, A.P. Kappetein, A. Kastrati, J. Knuuti, U. Landmesser, G. Laufer, F.-J. Neumann, D.J. Richter, P. Schauerte, M. Sousa Uva, G.G. Stefanini, D.P. Taggart, L. Torracca, M. Valgimigli, W. Wijns, A. Witkowski, J.L. Zamorano, S. Achenbach, H. Baumgartner, J.J. Bax, H. Bueno, V. Dean, C. Deaton, Ç. Erol, R. Fagard, R. Ferrari, D. Hasdai, A.W. Hoes, P. Kirchhof, J. Knuuti, P. Kolh, P. Lancellotti, A. Linhart, P. Nihoyannopoulos, M.F. Piepoli, P. Ponikowski, P.A. Sirnes, J.L. Tamargo, M. Tendera, A. Torbicki, W. Wijns, S. Windecker, M. Sousa Uva, S. Achenbach, J. Pepper, A. Anyanwu, L. Badimon, J. Bauersachs, A. Baumbach, F. Beygui, N. Bonaros, M. De Carlo, C. Deaton, D. Dobrev, J. Dunning, E. Eeckhout, S. Gielen, D. Hasdai, P. Kirchhof, H. Luckraz, H. Mahrholdt, G. Montalescot, D. Paparella, A.J. Rastan, M. Sanmartin, P. Sergeant, S. Silber, J. Tamargo, J. ten Berg, H. Thiele, R.-J. van Geuns, H.-O. Wagner, S. Wassmann, O. Wendler, J.L. Zamorano, 2014 ESC/EACTS Guidelines on myocardial revascularization, The Task Force on Myocardial Revascularization of the European Society of Cardiology (ESC) and the European Association for Cardio-Thoracic Surgery (EACTS)Developed with the special contribution of the European Association of Percutaneous Cardiovascular … (2014).

[191] K. Gusieva, C.H.J. Davies, J.R. Scully, N. Birbilis, Corrosion of magnesium alloys: the role of alloying, Int. Mater. Rev. 60(3) (2015) 169-194.

[192] H.E. Friedrich, B.L. Mordike, Magnesium Technology: Metallurgy, Design Data, Automotive Applications, Springer Berlin Heidelberg2006.

[193] Y.-L. Zhou, Y. Li, D.-M. Luo, C. Wen, P. Hodgson, Microstructures, mechanical properties and in vitro corrosion behaviour of biodegradable Mg-Zr-Ca alloys, J. Mater. Sci. 48(4) (2013) 1632-1639.

[194] Z. Li, X. Gu, S. Lou, Y. Zheng, The development of binary Mg-Ca alloys for use as biodegradable materials within bone, Biomaterials 29(10) (2008) 1329-1344.

[195] E. Aghion, G. Levy, The effect of Ca on the in vitro corrosion performance of biodegradable Mg-Nd-Y-Zr alloy, J. Mater. Sci. 45(11) (2010) 3096-3101.

[196] E. Zhang, L. Yang, Microstructure, mechanical properties and bio-corrosion properties of Mg-Zn-Mn-Ca alloy for biomedical application, Materials Science and Engineering a-Structural Materials Properties Microstructure and Processing 497(1-2) (2008) 111-118.

[197] Y. Chino, M. Kobata, H. Iwasaki, M. Mabuchi, Tensile Properties from Room Temperature to 673 K of Mg-0.9 mass%Ca Alloy Containing Lamella Mg_2Ca, MATERIALS TRANSACTIONS 43(10) (2002) 2643-2646.

[198] Y. Wan, G. Xiong, H. Luo, F. He, Y. Huang, X. Zhou, Preparation and characterization of a new biomedical magnesium–calcium alloy, Mater. Des. 29(10) (2008) 2034-2037.

[199] D.H. StJohn, M. Qian, M.A. Easton, P. Cao, Z. Hildebrand, Grain refinement of magnesium alloys, Metallurgical and Materials Transactions A 36(7) (2005) 1669-1679.